UiT

**THE ARCTIC
UNIVERSITY
OF NORWAY**

Faculty of Science and Technology
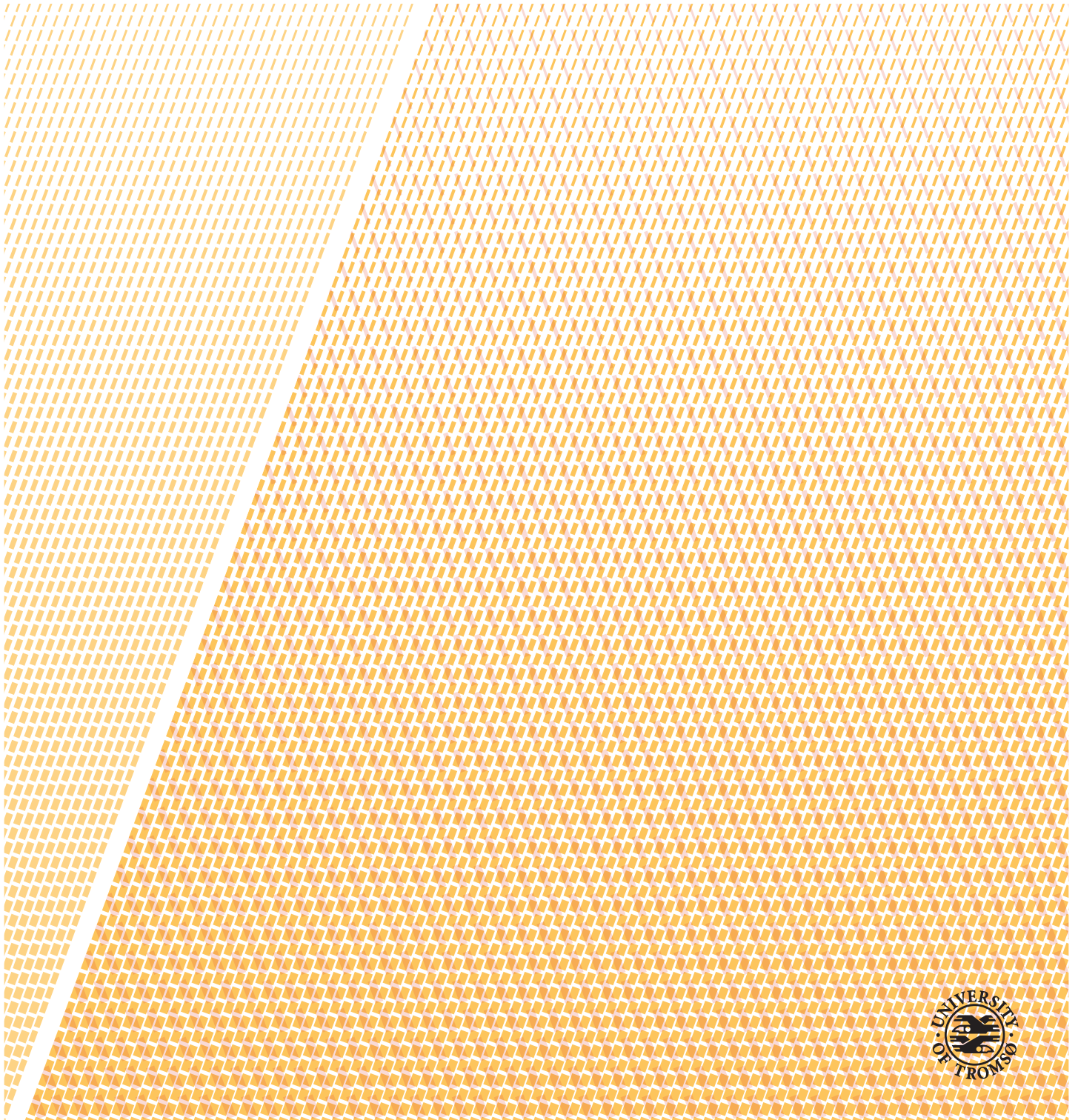Department of Physics and Technology

On polar lows and their formation

—

Patrick Johannes Stoll
A dissertation of the degree of Philosophiae Doctor, June 2020

Abstract

Polar lows are small, but extreme cyclones that develop in marine polar air mass. They feature one of the largest natural hazards in the polar regions. Their associated strong winds, high waves, substantial amounts of snow fall, low visibility and possibility for ice accumulation on ships and airplanes cause threats for coastal communities and marine operations.

Hence, accurate prediction of polar lows is of major importance. This, however, is a challenge for meteorological services due to the fast, non-linear development of these cyclones. The evaluation of weather-prediction models for polar-low situations is difficult, since polar lows appear in a large variety and the scientific community has not yet accepted a singular conceptual model describing their development. Further, a consistent global investigation of polar lows has not yet been performed.

In this thesis, the formation of polar lows is investigated. The aforementioned issues are targeted.

In order to compare the polar-low activity across ocean basins, the first global dataset of polar lows is derived (Paper I). For the derivation of the dataset, the characteristics of polar lows are compared to other storms. Most polar-low activity is found in the North-East Atlantic, namely the Nordic Seas and the Denmark Strait. The number of very intense polar lows was declining during the recent 40 years.

This thesis evaluates two modern weather-prediction models in forecasting a well-observed polar-low case (Paper II). Both models capture the polar low reasonably well for the analysis time, but show considerable issues at forecast times of more than one day. The polar low appears very sensible to the sea-surface temperature.

Additionally, the variety of polar lows is examined (Paper III). An earlier proposed classification scheme into forward and reverse-shear cases is extended by adding left and right-shear systems to the scheme. Polar lows in all four shear categories are characterised by a baroclinc cyclogenesis.

In conclusion, this thesis supports the perspective that polar lows are miniature versions of the baroclinic cyclones apparent in the mid-latitudes. The small scale and large growth rate of polar lows mainly arise from the low static stability and the low tropopause present in the marine polar air mass. The variety of polar lows is large since the synoptic-scale flow, in which polar lows are embedded, can take any orientation. Additionally, the release of latent heat significantly contributes to the intensification of polar lows. Therefore, the major conceptual model to describe polar-low formation is suggested to be moist-baroclinic instability.

Acknowledgements

First of all, I want to thank my PhD supervisor, Rune, to support me at all times and to give me the opportunity to find my way. It was a pleasure to be your PhD student. I am also truly grateful that I was part of a warm and happy research group. Sindre, Tuomas, Mathias, Kai, Hege, Johanne and Gregor, thanks to you I was happily coming to my office every morning and had good times also when my research was cumbersome.

Further, I want to thank Gunnar and Teresa for being my (quasi-)co-supervisors and Yurii. Thanks for your support with AROME-Arctic and interesting discussions about polar lows.

During my PhD, it was a great opportunity to participate in summer schools and courses, mainly organised by the research school CHESS. These courses, especially the people I met, highly encouraged by research. Also the conferences of the Polar Low Working Group and the European Geoscience Union motivated my research. I was glad to be part of a highly collaborative research field, which meteorology is.

This thesis would be considerably worse in both content and layout without python and latex. I want to thank their development groups for providing great open-source software. These are great examples the world is better when we share.

A thanks goes also to the Department of Physics and Technology for providing good administrative and IT support. I want to thank Geir for giving me the opportunity to reduce my working time to 80% for the last 1.5 years of my dissertation, such that I had some more time to enjoy the nature around Tromsø and to participate in the board of the local climbing club.

A big thanks goes to Laura, who supported me when I was struggling with my PhD. Also thanks to all my friends that shared fantastic moments and adventures with me. You are great.

Danke auch an meine Familie. Für Verständnis, dass ich weit weg bin. Ihr seid tief in meinem Herzen! Ein besonderer Dank geht an Hanna für die Unterstützung in einer endlosen Zeit des Schreibens und die schönen gemeinsamen Momente.

Last but not least, I want to thank mother Earth for providing a beautiful nature, the best place for inspiration. I deeply hope that we will take care for our planet.

Contents

List of Abbreviations

CAO cold air outbreak

DRV Diabatic Rossby Vortex

ECMWF European Centre for Medium-Range Weather Forecasts

EPLWG European Polar Low Working Group

MET Norwegian Meteorological Institute

PL polar low

PMC polar mesoscale cyclones

STARS Sea Surface Temperature and Altimeter Synergy for Improved Fore-casting of Polar Lows

1

Introduction

This chapter provides a general introduction to polar lows.

1.1 Motivation

A polar low (PL) is a small, but fairly intense storm. The combination of these two characteristics causes PLs to be threatening phenomena (Renfrew, 2015). They cause gale-force winds (Rojo et al., 2019; Wilhelmsen, 1985), high waves (Orimolade et al., 2016), massive amounts of snow fall, blowing snow, a low visibility of sometimes only a few metres, and severe avalanche danger. The conditions encountered during PLs can lead to ice accumulation on ships and airplanes (Samuelsen et al., 2015). Wilhelmsen (1985) argues that the harsh conditions encountered during PLs may have caused the capsizing of some vessels in the past. PLs also lead to major traffic issues, such as car accidents and closed roads due to rapid snow accumulation. Hence, the Norwegian Meteorological Institute (MET) recommends staying at home in situations of a strong incoming PL.

The small size of PLs makes them even more threatening. As opposed to large, so-called synoptic-scale cyclones (Fig. 1.1), which generally need a week in order to intensify, PLs develop very fast, often within a fraction of a day. Due to their fast development, PLs appear very suddenly, and their prediction is a major challenge for meteorological services. Some decades ago, their prediction was simply impossible, since the coarse resolution of the weather-forecasting models at that time could not simulate them. Nowadays, most extreme weather types can be warned of days in advance, but the location and strength of PLs remain still imprecise in the short-range forecast (e.g. Føre et al., 2012; Kristiansen et al., 2011).

Hence, even today, advances in the prediction of PLs are needed. In order to improve the capability of weather-forecast models for PL situations, two approaches are possible. The first is to increase the model resolution in order
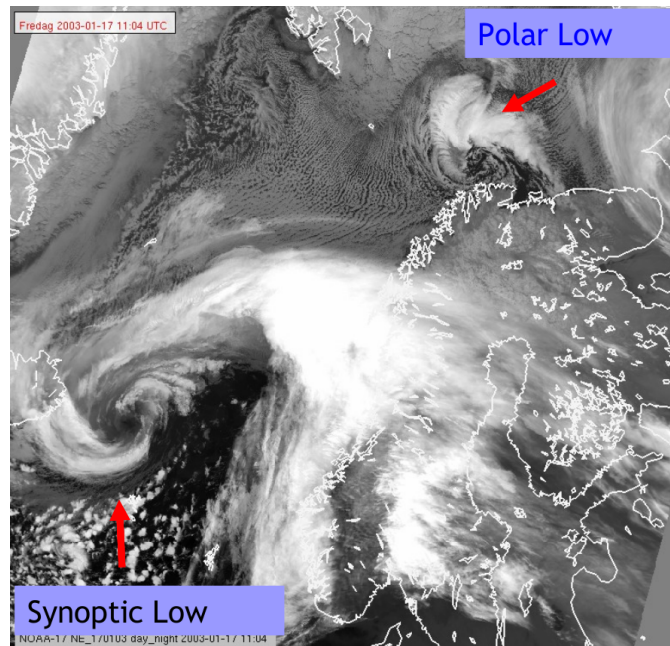
Figure 1.1: A satellite image displaying a polar low and a synoptic-scale low over the Nordic Seas on 17 January 2003 11 UTC. Reproduced with permission from Gunnar Noer (MET).

to improve the dynamical representation of the systems. However, this comes at large computational expenses, since the model dynamics are 4-dimensional. An increase in the resolution with a factor of two thus demands additional computational resources of approximately a factor of 16. The second approach is to identify the malfunctioning components in the model and to improve them - an endeavour that does not require increased computation power. In order to identify these components, a meteorological understanding of the PL development is required.

Ideal is, of course, the combination of both approaches. The meteorological services have increased the resolution of their weather-forecasting models considerably within the last decades. In contrast, research on the meteorological development of PLs does still not fully agree on a conceptual model describing the intensification of PLs (e.g. Jonassen et al., 2020; Renfrew, 2015).

1.2   Thesis outline

The general attention of my PhD is directed towards the investigation of PLs. A more specific outline of the scientific questions posed in this thesis is presented in Chapter 4. However, first the remaining introduction gives a general overview about the definition and appearance of PLs. Then, Chapters 2 and 3 provides a more detailed overview of the state-of-the-science on PLs and provide a background for the targeted scientific questions. These questions

are approached in the three papers of this thesis, which are summarized in Chapter 5. Chapter 6 contains a discussion about the papers and suggestions for future work on PLs. Finally, Chapter 7 provides the main conclusion of my PhD, which includes a general perspective on PLs.

1.3   Definition

Coastal communities at high latitudes have long been aware of the possibility of abrupt weather changes in situations of northerly flow (e.g. Dannevig, 1954). However, they could neither predict nor explain the phenomena, which we today call PL. The coarse network of weather stations in the polar regions was not capable to identify these small-scale systems. First in the 1970s with the appearance of satellites, their horizontal structure, displayed by their clouds, was identified (Lyall, 1972). Hence, meteorologists anticipated from cloud structures and coarse, synoptic weather maps if a small-scale, but threatening weather situation would develop (Businger and Reed, 1989; Forbes and Lottes, 1985; Rasmussen and Lystad, 1987).

Multiple names were suggested for these small-scale disturbances in polar air masses, such as "polar low", "Arctic instability low", "polar air depression", "mesoscale cyclone", "Arctic hurricane", "polar airstream cyclone" and "comma cloud" (Chapter 4 Johnson, 2015). These terms reveal somewhat different perspectives on the phenomenon.

In order to collaborate on research considering PLs and polar mesoscale systems, the European Polar Low Working Group (EPLWG) was founded. A consensus on the definition of the terms "polar mesoscale cyclone" and "polar low" was reached by the EPLWG in Paris in 1994 (Heinemann and Claud, 1997):

> The term "polar mesoscale cyclone" ("polar mesocyclone") is the generic term for all meso-alpha and meso-beta-scale cyclonic vortices poleward of the main polar front (scale definition according to Orlanski 1975). The term "polar low" should be used for intense maritime mesocyclones with scales up to about 1000 km with a near-surface wind speed exceeding 15m/s.

This provided a wide and general definition of polar mesoscale cyclones (PMC) as being meso-alpha (200 - 2000 km) or meso-beta (20 - 200 km) cyclones occurring in polar air masses. The polar front, or the jet stream, is considered to be the boundary of the polar air mass. All the above mentioned names are included within the PMC. PLs are a subclass of the most intense PMCs based on the strength of the near-surface wind. Today, the most commonly cited definition of PLs is formulated in Rasmussen and Turner (2003):

> A polar low is a small, but fairly intense maritime cyclone that
> forms poleward of the main baroclinic zone (the polar front or
> other major baroclinic zone). The horizontal scale of the polar low
> is approximately between 200 and 1000 km and surface winds near
> or above gale force (>15m/s).

This definition is almost similar to the previous one, but being more restrictive on the size of PLs. Both definitions are by intention fairly general as to include a wide range of systems. They do not include a dynamical intensification mechanism, and multiple interpretations exist about the term PL (see Introduction of Rasmussen and Turner, 2003). However, the following three conditions are generally to be satisfied for a phenomenon to be classified as PL:

- Mesoscale size

- Occurrence over open water

- Strong intensity as assessed by the near-surface winds stronger than $15\,\mathrm{ms}^{-1}$

- Development in the polar air mass, which is defined as the poleward side of the jet stream

1.4   Typical characteristics of polar low

Since the definition of PLs is formulated in a general manner, it is beneficial to give a broad overview over the characteristic meteorological conditions in which PLs are observed. These typical conditions have lead to the suggestion of additional criteria for the identification of PLs.

Open water within the polar air mass typically heats the atmosphere from below. This creates a low static stability (see Chapter 3.4.2) in the lower atmosphere and conditions conducive for convection. A measure of the low static stability is thus often applied for the detection of PLs (e.g. Bracegirdle and Gray, 2008; Kolstad, 2011; Zappa et al., 2014). This often expressed by a large temperature contrast between the sea surface and a certain atmospheric level.

Marine cold-air outbreaks, or just cold air outbreak (CAO), is the meteorological term describing situations, where the polar air mass that generally forms over sea ice or cold continents, floats over the warmer seas. In situations with strong air-sea temperature contrast, this outflow induces convection, often visible in satellite images as cloud streets (see Fig. 1.1 and 1.2(a) to the west of the PLs), or by cellular convection (see bottom left in Figure 1.4(b)). PLs tend to form on the outer flanks of these CAOs where the horizontal temperature contrast (baroclinicity) is large (Terpstra et al., 2016). The existence of a CAO is another
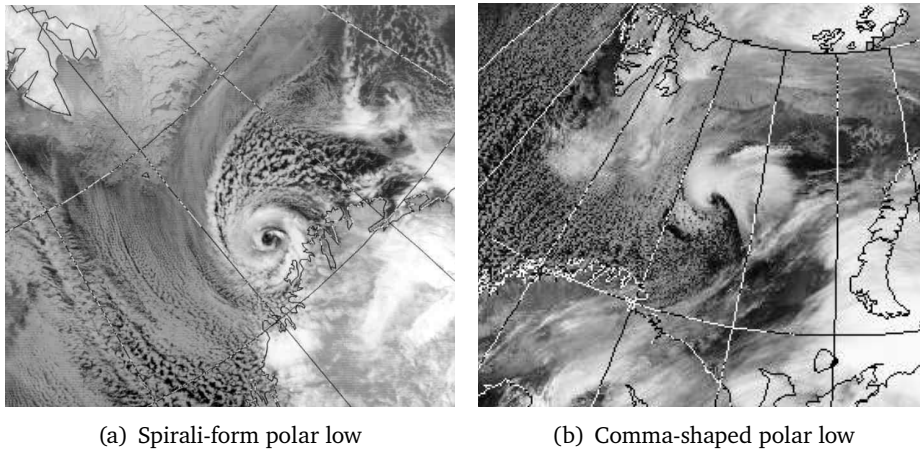
(a) Spirali-form polar low   (b) Comma-shaped polar low

Figure 1.2: Satellite images of (a) a spirali-form system occuring on 27 Feb 1987 08 UTC, and (b) a comma-shaped polar occurring on 19 Feb 2002 10 UTC. (Source: Dundee Satellite Receiving Station)

very common criteria for the detection of PLs (e.g. Bracegirdle, 2006).

Generally, PLs are observed to occur in the extended winter season (e.g. Blechschmidt, 2008; Noer et al., 2011; Wilhelmsen, 1985). The length and intensity of the season varies among the different ocean basins. The favourable condition with a high temperature contrast between the cold polar air mass and the sea surface in the neighbouring ocean basin mainly occur in winter. Several studies only investigate the winter season for the occurrence of PLs (e.g. Michel et al., 2018; Watanabe et al., 2016).

PLs were observed to have a typically a size in the range between 200 - 500 km and a lifetime between half a day and two days (Blechschmidt, 2008; Rojo et al., 2015). However, exceptions have been observed (e.g. Claud et al., 2004). One aim of Paper I was to identify among numerous suggested criteria the most effective ones for the identification of PLs.

1.5 Cloud structures

The primary source of data for the investigation of PLs has long been satellite imagery, such as displayed in Figures 1.1 - 1.4 (e.g. Rasmussen and Lystad, 1987). This was caused by the lack of other observations in the marine polar regions. Today, weather-prediction models are, at least in short-term forecasts, able to capture PLs and provide valuable additional information. Due to the long focus on satellite imagery the different cloud structures associated to PLs were thoroughly investigated (e.g. Forbes and Lottes, 1985). The cloud structure was argued to be connected to the physical mechanisms leading to the PL development (Rasmussen and Turner, 2003). We therefore give a short overview over the typical observed cloud structures associated to PLs.

Figure 1.3: Typical twitter warning from the MET for incoming polar lows. On 13 December 2015 a wave train of three polar lows developed in the Nordic Seas. Two of them were expected to threaten Northern Norway.

A lot of attention is given to the fact that some PLs develop a cloud spiral as shown in Figure 1.2(a). These spirals of convective bands with a pronounced eye in the centre resemble in the appearance to hurricanes, and therefore the term "Arctic hurricane" has been suggested for some PLs (e.g. Emanuel and Rotunno, 1989). However, the thorough investigation of a spirali-form PL revealed that the development of these PLs is considerably different from hurricanes (e.g. Føre et al., 2012; Kolstad et al., 2016).

More commonly PLs develop a comma-shaped cloud as presented in Figure 1.2(b) (Mokhov et al., 2007). The name comes from the resemblance of the cloud form with a ",". Often a cloud-free eye is forming near the comma head. The comma-shaped cloud is the typical appearance of synoptic-scale cyclones developing along the polar front, which is typically underneath the jet stream. Hence, comma-shaped PLs appear to be miniature versions of synoptic-scale cyclones with the difference that PLs develop in the polar air mass.

Rasmussen (1981, 1983) suggested the division of PLs into "real" PLs and comma-shaped clouds. Where the "real" or "true" PL are of spirali-form cloud signature. Rasmussen, however, also identifies that not all systems fit into either one of these cloud form. Therefore, a "PL spectrum" with the spirali-form on one end and the comma-shape on the other end was suggested in the 1980s (p.157ff Rasmussen and Turner, 2003). It was further observed that spirali-form PLs in their initial stages often have a comma-like cloud form (e.g Nordeng and
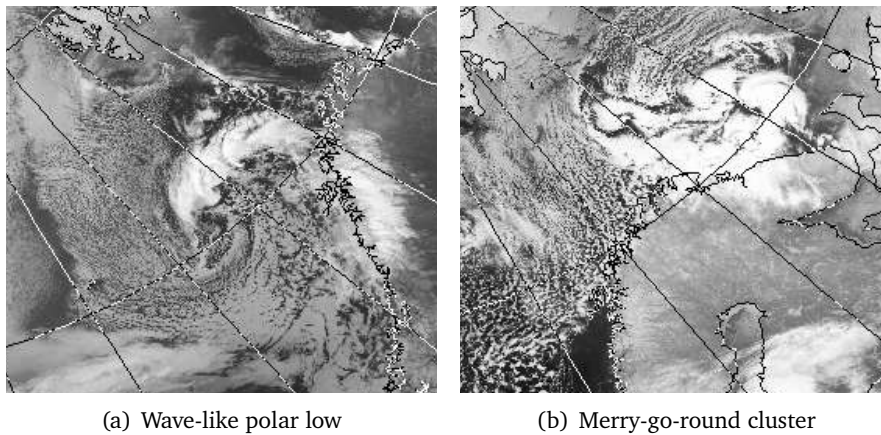
(a) Wave-like polar low   (b) Merry-go-round cluster

Figure 1.4: Satellite images of (a) a wave-type polar lows occurring on 1 April 2013 12 UTC, and (b) a merry-go-round cluster of polar lows on 12 March 2013 10 UTC. (Source: Dundee Satellite Receiving Station)

Rasmussen, 1992). Hence, some comma-shaped systems develop into spirals, but not all do.

Several PLs may develop simultaneously in vicinity of each other. Some arrangements of simultaneous development have been identified (e.g. Rojo et al., 2015). They can appear along a common frontal zone and form a wave-train of systems as shown in Figure 1.3. The systems within the wave-train likely develop by the same mechanism and hence may show a similar cloud structure, which is often of comma shaped. In some instances the comma-shaped clouds overlap and it appears that the PLs form one cloud, but they show individual eyes (e.g. Fig. 1.4(a)).

Another arrangement is the rotation of multiple PMCs around a common centre, which was given the name "merry-go-round" PL (Forbes and Lottes, 1985). These situations are rather seldom and have been investigated little. The rotation around the common centre appears to be rather minor. They are described to develop in the central part of an occluded synoptic-scale cyclone which developed a considerable upper-level cold core (Rasmussen and Turner, 2003).

2

Climatologies

This and the following chapter provide more detailed background on PLs. Here different derived lists of PLs, sometimes called PL climatologies, are presented. The focus is on the derivation of these lists and the different character of "subjective" and "objective" PL climatologies.

2.1   "Subjective" polar-low lists

A great amount of knowledge on about PLs have be gained by case studies (e.g. Bond and Shapiro, 1991; Harrold and Browning, 1969; Nordeng and Rasmussen, 1992). However, to deduce some kind of generality a lot of cases have to be examined. For this purpose, numerous lists of PLs have been collected in the last decades. The nature of these lists is "subjective" since the choice of systems that are included depends on the utilised data and the applied criteria for inclusion. Since the data are different from case to case and measures such as the strength of the system is often not directly measured these list depend on the interpretation of the producer.

The first PL climatologies were created by Wilhelmsen (1985) and Forbes and Lottes (1985) for the Nordic Seas. Wilhelmsen (1985) collected 33 cases that developed gale-force winds in the years 1978 to 1982 after analysis of weather stations and ships. Forbes and Lottes (1985) detected 133 PMCs that formed in December 1981 by infra-red satellite imagery. Most of them were to weak to be classified to be PLs.

Especially the Nordic Seas were highly investigated for PLs. Blechschmidt (2008) created a climatology with in total 90 cases in the years 2004-2005 based on satellite imagery retrieving the cloud structure and near-surface winds. Smirnova et al. (2015) produced a PL climatology with 637 cases of the years 1995-2009 based on visual inspection of satellite retrievals of the total atmospheric water content and the near-surface wind.

Climatologies based on satellite images have also been derived for other regions, such as the Gulf of Alaska for 1975 - 1983 (Businger, 1987), the North Pacific for 1976 - 1984 (Yarnal and Henderson, 1989), the Sea of Japan and North-West Pacific for the winter 1995/96 (Fu et al., 1999), and the Southern Hemisphere around Antarctica for 1977 - 1983 (Carleton and Carpenter, 1990).

Recently, Verezemskaya et al. (2017) manually tracked 1735 mesocyclones in the Southern Ocean for the winter 2004 from infra-red satellite images. Krinitskiy et al. (2018) used these tracks to train a convolutional neural network for detection mesocyclones in the Southern Hemisphere based on infra-red and water-vapour satellite images. This approach provides a mesocyclone climatology purely based on satellite data. However, in Chapter 2.1.2 some issues with purely satellite-based PL lists are presented.

2.1.1   STARS dataset

Probably the most frequently-used record of detected PLs is the Sea Surface Temperature and Altimeter Synergy for Improved Forecasting of Polar Lows (STARS) dataset developed by MET (Noer et al., 2011). The STARS dataset contains PL cases that developed in the Nordic Seas since November 1999 and is operationally updated. For the decision whether a system satisfies the PL definition the STARS dataset examines information from operationally-used weather-prediction models, satellite imagery and synoptic weather station. In recent years it was utilised as a basis for the investigation of PL development (e.g. Rojo et al., 2015; Terpstra et al., 2016), for evaluation of PL representation in different datasets (e.g. Laffineur et al., 2014; Smirnova and Golubkin, 2017), and the for the derivation of "objective" detection methods (e.g Zappa et al., 2014). Also Paper I and III of this thesis are based on PLs from the STARS dataset.

2.1.2   Difficulties of "subjective" lists

PLs were observed in all ocean basins at high latitudes. They are mainly developing in the extended winter season of both hemispheres. The number of PLs was observed to have an high inter-annual variability. Some describe PLs of being of different appearance for different ocean basins (e.g. Jonassen et al., 2020). However, the comparison of PLs in different ocean basins and the long-term investigation are prone to detection biases.

The "subjective" PL lists depend on the underlying dataset, the applied definition of PLs, and on the interpretation of the producer whether the detection criteria are satisfied.

The near-surface wind speed, that has to exceed $15\,\mathrm{ms}^{-1}$ in order for a system to be classified as PL, is seldomly directly measured on surfaces of open water. Generally satellite retrievals are utilised for the detection of PLs. However, satel-

lite imagery is not available at all times, which produces data gaps of sometimes multiple hours. Additionally, the cloud structure of PLs is sometimes hidden behind overlying high clouds and hence an existent PL might not be identifiable from a infra-red satellite image. (e.g. Furevik et al., 2015). The lacking data challenges the tracking of some PL centres. Therefore the examination of the PL development from satellite images alone can be difficult.

For this reason some of the aforementioned "subjective" lists also use other datasets than satellite imagery. Especially the STARS dataset combines the use of satellite retrievals and weather-prediction models.

The "subjective" PL lists are generally not comparable due to the large variety of the underlying datasets and applied methodologies for their production. To my knowledge neither a "subjective" PL list has been produced for multiple ocean basins nor for a time long enough to investigate the response of PLs to climate change. This is likely explained by extensive manual work that is required to compile such lists.

Due to advance of numerical weather-prediction models and atmospheric reanalysis, PLs are today reasonably well simulated. Hence it is now possible to detect PLs "objectively" from these model products.

2.2   "Objective" climatologies

An "objective" PL climatology is based on the automatic detection of PLs within a continuous dataset. Typically they rely on the following procedure: First, a dataset is required that resolves PLs. Only in recent years this was the case for atmospheric reanalysis datasets. Secondly, cyclonic systems have to be identified and tracked. And thirdly, from the tracked systems PLs are identified by the application of predefined detection criteria.

Multiple "objective" PL climatologies have been developed in the last decade for the North Atlantic (Bracegirdle and Gray, 2008; Zahn and von Storch, 2008a; Zappa et al., 2014) and Sea of Japan (Watanabe et al., 2016; Yanase et al., 2016). The derived "objective" climatologies range for multiple decades which makes them adequate to investigate for responses in the PL activity to climate change. Generally a change in the frequency of PLs connected to global warming has not been observed yet (e.g. Zahn and von Storch, 2008a).

The methodology of these "objective" PL climatologies was also applied to future climate projections. In climate scenarios with increased CO_2 concentration, Zahn and von Storch (2010) finds a considerably reduced amount of PLs in the North Atlantic. They observe a northward propagation of the main region of activity, but a general decline in the PL frequency due to increased atmospheric stability. In contrast, Landgren et al. (2019) finds a similar annual number of

PLs for a down-scaled present and future climate. Hence, it appears that more studies are necessary to give clarity whether and where the amount of PLs is expected to change in the future (Jonassen et al., 2020).

Most of the derived "objective" PL climatologies depend on different model dataset, different cyclone tracking algorithms and identification criteria. Hence a comparison of the climatologies for the different ocean basins is difficult. Here, the motivation for Paper I originated: to compare the PL activity all over the world. Kolstad (2011) had performed a global investigation that displayed regions with favourable conditions for PL development. However, Paper I directly examines the PL activity.

3

Development mechanisms

In general an atmospheric instability mechanism is required to intensify a small disturbance to the strength of a PL. Different concepts have been suggested in the past decades in order to explain the development of PLs.

Flow instabilities such as baroclinic and barotropic instability, as well as thermal instability that include the release of moisture were suggested to contribute to the development of PLs (Rasmussen and Turner, 2003). Multiple studies indicate that PLs are best explained by the combination of different concepts. Possibly moist baroclinic instability is the best candidate to give a general conceptual mechanism for PL development (Sardie and Warner, 1983; Terpstra et al., 2015).

Atmospheric instability mechanisms act on different atmospheric scales. Therefore, this chapter introduces the atmospheric scales. Afterwards, the chapter provides an overview of the different atmospheric instability mechanisms that have been suggested to explain PL development. This chapter ends with different suggestions of PL classification schemes.

3.1   Atmospheric scales

In meteorology, disturbances are broadly separated into three scales. The synoptic-scale (>2000 km), the micro-scale (<2 km), and in between the meso-scale. Both in the synoptic- and the micro-scale several terms can be disregarded in the governing equations of fluid dynamics due to the relative unimportance of some effects on large and small scales, respectively. Different, on the mesoscale, no such general simplifications can be made (Markowski and Richardson, 2011).

Single updrafts that are caused by thermal instability are occurring at the micro-scale. The organisation of convection to a storm involves the interaction of several mechanism and is happening at the mesoscale. The mesoscale can be

considered as the scale on which motions are driven by multiple mechanisms rather than a single dominant instability. Barotropic and symmetric instability are mechanisms often observed at the mesoscale (Markowski and Richardson, 2011).

At the synoptic-scale baroclinic instability is the major instability mechanism. It causes the formation of the dominant weather systems in the mid-latitudes, which are extratropical cyclones. Baroclinic instability organises roughly at an horizontal wavelength of four times the Rossby radius of deformation, L_R, given by

$$L_R = NH/f \tag{3.1}$$

with the Brunt-Väisälä frequency N, the scale height of the atmosphere H, and the Coriolis parameter f (Eady, 1949). The size of the baroclinically induced cyclone has an approximate size of half a wavelength, hence $2 \cdot L_R$. In the mid-latitudes, $2 \cdot L_R$ is typically in a range of 2000 - 3000 km. The typical scale of an mid-latitude, extra-tropical cyclone can be considered as the definition of the synoptic scale (Markowski and Richardson, 2011).

In the polar air mass, the tropopause is typically lower (smaller H), and the Coriolis parameter, f, is larger than in mid-latitudes. Additional, for polar air masses in marine environments the static stability is lower than normal (small N), as explained in Chapter 3.4.2. The combination of these factors lead to a considerably smaller Rossby radius of deformation in the marine polar air masses with $2 \cdot L_R \approx 500$ km, as demonstrated in Paper III. Hence, the scale of baroclinic disturbances is within the range of the mesoscale in the polar marine troposphere. The scale of the baroclinic disturbances in polar air masses is only slightly larger than the typical scale of PLs of around 300 km (Rojo et al., 2015).

3.2   Baroclinic instability

Baroclinic instability is the main mechanism leading to the development of extra-tropical cyclones. A situation, where isobars and isotherms (or isopycnals) cross each other, is called baroclinic, from baro = pressure and clinic = tilt. The intersection of the two is characterised by temperature advection.

The baroclinic development mechanism is sketched in Figure 3.1. It shows the upper-level (300 hPa), mid-level (700 hPa) and low-level (925 hPa) flow and thermal fields in the three rows.

In the initial stage (Figure 3.1a) the contours of geopotential height and equivalent potential temperature cross each other. A low-level temperature wave forms downstream of the an upper-level shortwave trough which amplify each other. The intensification can be good anticipated in the intensification stage
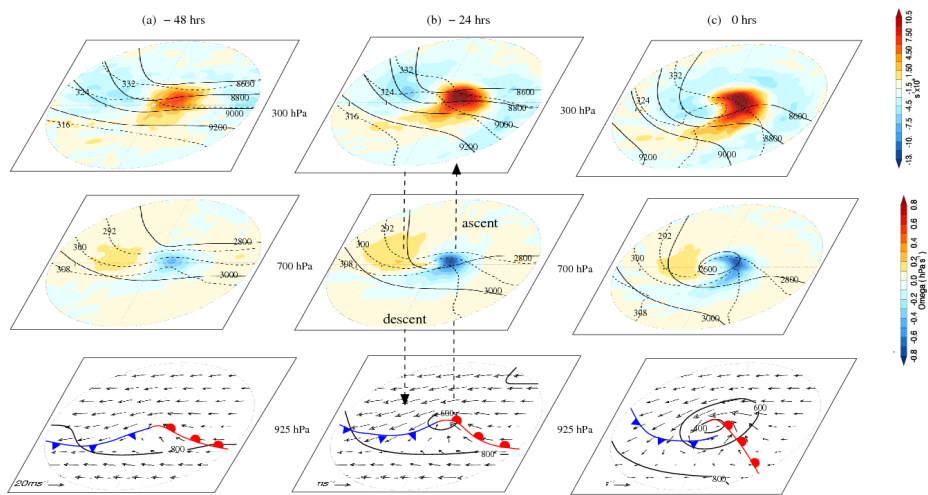
Figure 3.1: Horizontal composite fields of mid-latitude cyclones in system oriented frame with proagation direction to the right. (a) 48 and (b) 24 hours before the time of maximum intensity, and (c) at the time of maximum intensity. Bottom row: 925 hPa geopotential height (solid contours), system relative wind vectors and the location of the warm and cold front. Middle row: 700 hPa geopotential height (solid contours); equivalent potential temperature (dashed contours) and the vertical velocity (shadings, blue denotes upward motion). Top row: 300 hPa geopotential height (solid contours), equivalent potential temperature (dashed contours) and divergence (shadings, red denotes diverging flow). (Figure from Dacre et al., 2012)

(Figure 3.1b). Cold-air advection to the west of the surface low reduces the atmospheric thickness and hence deepens the upper-level trough. Warm-air advection to the east of the surface low increases the atmospheric thickness and intensifies the upper-level ridge above. Hence, the upper-level wave is amplified by the low-level temperature advection.

The upper-level wave causes convergence of air upstream and divergence downstream of the trough which forces descent and ascent of air below. The latter occurs at the location of the surface-level low and leads to vortex stretching, hence to intensification of the near-surface low pressure. The descent causes a surface-level high pressure anomaly to the west of the low which intensifies the surface wave. Additionally the upper-level trough causes warm-air and cold-air advection above the surface-level low and high pressure anomaly, respectively, which also amplifies the low-level cyclone.

Hence a positive feedback between the upper-level trough and the low-level cyclone develops. During the development the upper-level trough moves above the low-level cyclone (Figure 3.1c) and in the mature phase both become vertically aligned. This means that the positive feedback mechanism ends and the cyclone does not further intensify.

3.2.1   Different baroclinic life cycles

Considerable differences have been observed between cyclones developing by baroclinic instability. Hence several conceptual models have been suggested. They all develop a cold and a warm front, however the arrangements of the fronts varies. Also the role of conveyor belts and jet streaks is different (Semple, 2003), which lead to different cloud structures among the models. The two main conceptual models are the Norwegian cyclone model and the Shapiro-Keyser model (Wallace and Hobbs, 2006).

The concepts of these different cyclone models could improve the understanding for the different cloud forms associated to PLs, mainly comma- and spirali-types. Only seldom the spirali-form cloud was attributed to a Shapiro-Keyser development (e.g. Hewson et al., 2000; Shapiro et al., 1987). In general little attention has been given on the frontal configuration and the role of conveyor belts within PL development.

The Norwegian cyclone model was developed by the Bergen school of meteorology after the first world war Bjerknes and Solberg (1922). The international exchange of observational data made it possible to construct the large-scale picture of the evolution of fronts during the life cycle of cyclones. This model is since then used as the typical example for extra-tropical cyclogenesis (Fig. 3.2(a)).

According to this model, a low pressure anomaly develops within a frontal

(a) Norwegian cyclone model   (b) Shapiro-Keyser model
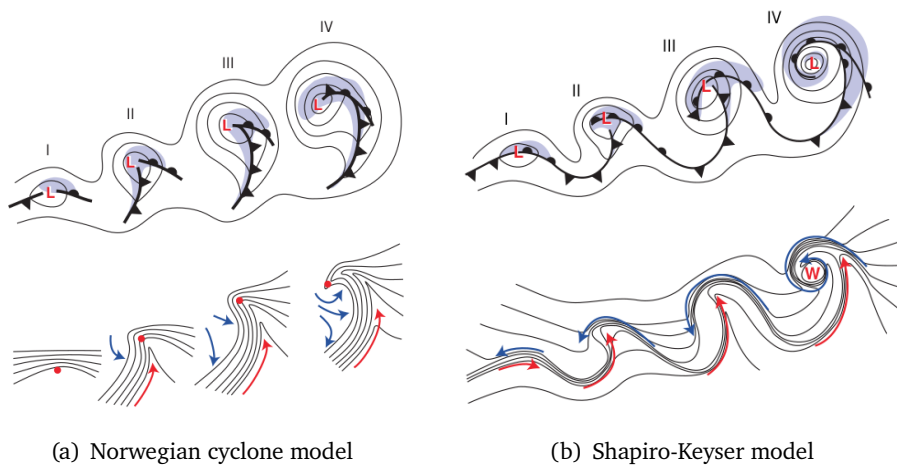
Figure 3.2: Schematic presentation of the four stages leading to the development of extratropical cyclones as envisioned by the (a) Norwegian cyclone model and (b) Shapiro-Keyser model. The panels I - IV show the four development stages of each model. (Top) isobars of the surface pressure (black contours), the frontal configurations (bolt black), the region of precipitation (blue shading). "L" denotes the location of the low-pressure centre. (Bottom) Isotherms (black) and the flow of the warm and cold air masses relative to the moving cyclone (red and blue arrows, respectively). The red dot in (a) denotes the cyclone centre, which lays within the cold air mass in stage IV. The "W" in (b) shows the secluded warm core. (From p.336 Wallace and Hobbs, 2006)

wave (stage I). It develops an intense cold front and a more gentle warm
front of advancing cold and warm air masses, respectively (stage II). Especially
the cold front rotates around the surface low and catches up with the warm
front to form an occluded front of typically weaker intensity (stage III). In the
mature stage (stage IV) the cyclone centre is embedded within the cold air
mass, hence the horizontal temperature contrast decrease and the intensity
reaches its maximum. The cloud form resembles a comma shape, with the
head near the low centre and the tail along the cold front.

However, some of the most intense extratropical cyclones exhibit considerable
departures from the Norwegian cyclone model. Hence a second model was
suggested by Shapiro and Keyser (1990) and depicted in Figure 3.2(b)). The
cyclone also initiates from a frontal wave (stage I). The fronts begin to circulate
and a frontal fracture occurs (stage II). The warm front continues to sharpen
and bends across the cold side of the low (bent back warm front). This leads to
the characteristic "T-bone" alignments of the fronts (stage III). The fronts coil
into a tight, mesoscale spiral which leads to a warm seclusion of the cyclone
core (stage IV). Hence different to comma-shaped cloud in the Norwegian
cyclone model, the associated cloud has spirali form in the later stages of the
Shapiro-Keyser model.

A third category of cyclogenesis was identified and referred to as open-wave
cyclones (Browning, 1994). These systems have a dominant cold front and never
develop an occluded front. The three kinds of cyclones, the Shapiro-Keyser, the
Norwegian and the open-wave cyclones were assigned to be Life cycle (LC) 1, 2
and 3, respectively (Shapiro et al., 1999). The determining factor appears to be
the large-scale horizontal wind shear (barotropic). This shear is of rather small
magnitude (around $10 \, \text{ms}^{-1}$ over 2000 km). Shapiro-Keyser systems (LC 1) are
observed to develop in a flow without barotropic shear. Cyclones following the
Norwegian model (LC 2) developed under the influence of cyclonic barotropic
shear. Open frontal-wave cyclones (LC 3) formed within an anticyclonic shear
(Wernli, 1995).

Also the large-scale diffluence was found to contribute to the type of the life
cycle. The flow is diffluent if streamlines are spreading apart in the downstream
direction and confluent if the streamlines converge (p.272 Wallace and Hobbs,
2006). From case studies and idealised simulations Schultz et al. (1998) show
that a diffluent flow leads to a development resembling the Norwegian cyclone
model and confluent flow to a Shapiro-Keyser-like development.

Generally, the Norwegian cyclone model is applied when explaining the baro-
clinic nature of PLs (e.g. Fig. 4.2 of Rasmussen and Turner, 2003). The Shapiro-
Keyser model is, however, only in seldom instances applied for giving a possible
explanation for the spirali-form cloud of some PLs [Hewson et al. (2000) and
p.309ff of Rasmussen and Turner (2003). PLs with a comma-shaped cloud sig-
nature are generally assigned to be of baroclinic origin. (Reed, 1979) describes

that comma clouds are often found poleward, but rather close to the polar front. Rasmussen and Turner (2003) (p.154) describes, that comma clouds are often found "downstream of an upper-tropospheric vorticity maximum in the region of 500 hPa positive vorticity advection". This so-called left-jet exit region is know to be favourable for cyclogenesis due to upper-level divergence (p. 202 Holton, 1973).

The region in the vicinity, but poleward of the polar front is characterised by large-scale cyclonic shear. It could be expressed that the westerly winds decrease in intensity with latitude. Hence, following the observations of Wernli (1995) the left-jet exit is a region, where the Norwegian cyclone model applies. Differently, spirali-form PLs are often observed to occur deep within the polar air mass (Johnson, 2015, Chapter 4). Here, the large-scale cyclonic shear is presumably small and hence rather the Shapiro-Keyser model could given an explanation for the spirali-form cloud signature. This could add to the typical interpretation that spirali-form PLs are often assigned to be of convective type (Johnson, 2015).

3.2.2   Upper-level forcing

Cyclone development is mainly initiated "top-down" (Wallace and Hobbs, 2006, p.337). Hence, the development is initiated by the dynamical process in the upper troposphere. In order for the cyclone to intensify, conditions in the upper and lower troposphere must be favourable and the upper and lower levels must dynamically couple. In this context, PL initialisation was often described by the advance of an upper-level short-wave trough over an low-level baroclinic zone (Johnson, 2015). This initialisation is schematically illustrated in Figure 3.3.

The fraction of upper and lower level contribution to the cyclogenesis varies among cyclones and also during the life cycle. Petterssen and Smebye (1971) identified two types of cyclones, and called them A and B. Deveson et al. (2002) introduced the fraction of the upper- to the lower-level forcing contribution to the vertical motion (U/L ratio) in the cyclone in order to objectively classify them into type A and B. They additionally extended the scheme to include a type C. Gray and Dacre (2006) introduced the thresholds of the lifetime average of U/L < 2 for type A, of 2 < U/L < 4 for type B and U/L > 4 for type C. The different cyclone types were characterised as follows (Fig. 3.4):

Type A cyclones are fundamentally driven by lower-level forcing, i.e. by thermal advection (Fig. 3.4a). These cyclones form in a baroclinic zone without a preexisting upper-level trough, although a trough develops during the intensification. The tilt between the upper-level trough and the low-level cyclone remains constant until the mature stage of the cyclone is reached.

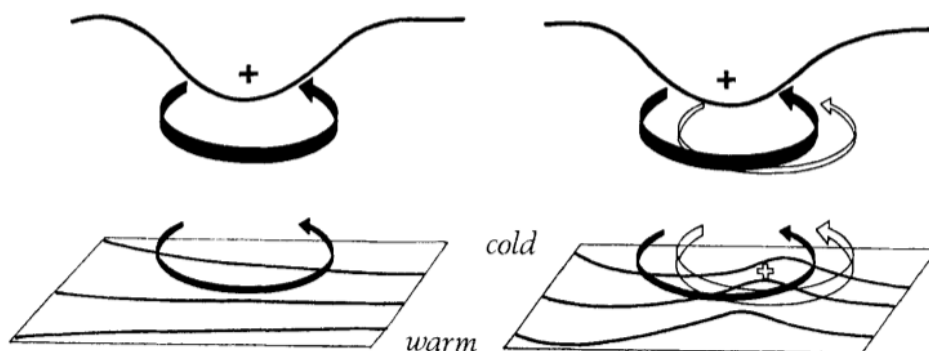Type B cyclones are dominantly forced from upper levels, i.e. by vorticity

Figure 3.3: Representation of cyclogenesis associated with the arrival of an upper-
level trough (upper solid line with "+") over a low-level baroclinic zone
(lower thin contours are isotherms). (Left) The upper-level circulation
(thick arrow) induces a weaker low-level circulation (thin arrow). (Right)
The low-level circulation causes warm-air advection to the right of the
upper-level anomaly (open "+"). This warm anomaly lead to expansion of
the atmospheric column and hence leads to a low-pressure anomaly, which
causes a low-level circulation (open arrow). The induced circulation at low
levels reinforces the one at upper levels (upper open arrow) and hence a
phase-locked intensification is initiated. (From Hoskins et al., 1985)

advection. They form when a preexisting upper-level trough moves over a
region of warm-air advection, as represented in Figure 3.3 and Fig. 3.4b. The
tilt between the upper-level trough and the low-level cyclone decreases as the
cyclone intensifies and aligns vertically in the mature stage.

Also type C cyclones possess large forcing by preexisting upper-level troughs,
however remains phase locked during their intensification (Fig. 3.4c). Plant
et al. (2003) describes that this type is dominated by the action of mid-level
latent heating, instead of a low-level temperature advection.

Bracegirdle and Gray (2008) applied this concept of cyclone types to a clima-
tology of PLs and found that PLs occur with approximately similar frequencies
in all three classes. It appears that some more investigation is necessary to
demonstrate that different dynamical mechanisms are active for PLs separated
into these three classes.

3.2.3   Diabatic Rossby Vortex

The Diabatic Rossby Vortex (DRV) describes the role of latent heating (diabatic)
in a moist-baroclinic framework. It was applied in order to explain the initial
stage in the rapid intensification of short-scale marine cyclones in mid-latitudes
(e.g. Moore et al., 2013; Wernli et al., 2002). The concept of the DRV is described
in Figure 3.5.

In this concept, low-level cyclonic disturbances grow in the absence of upper-
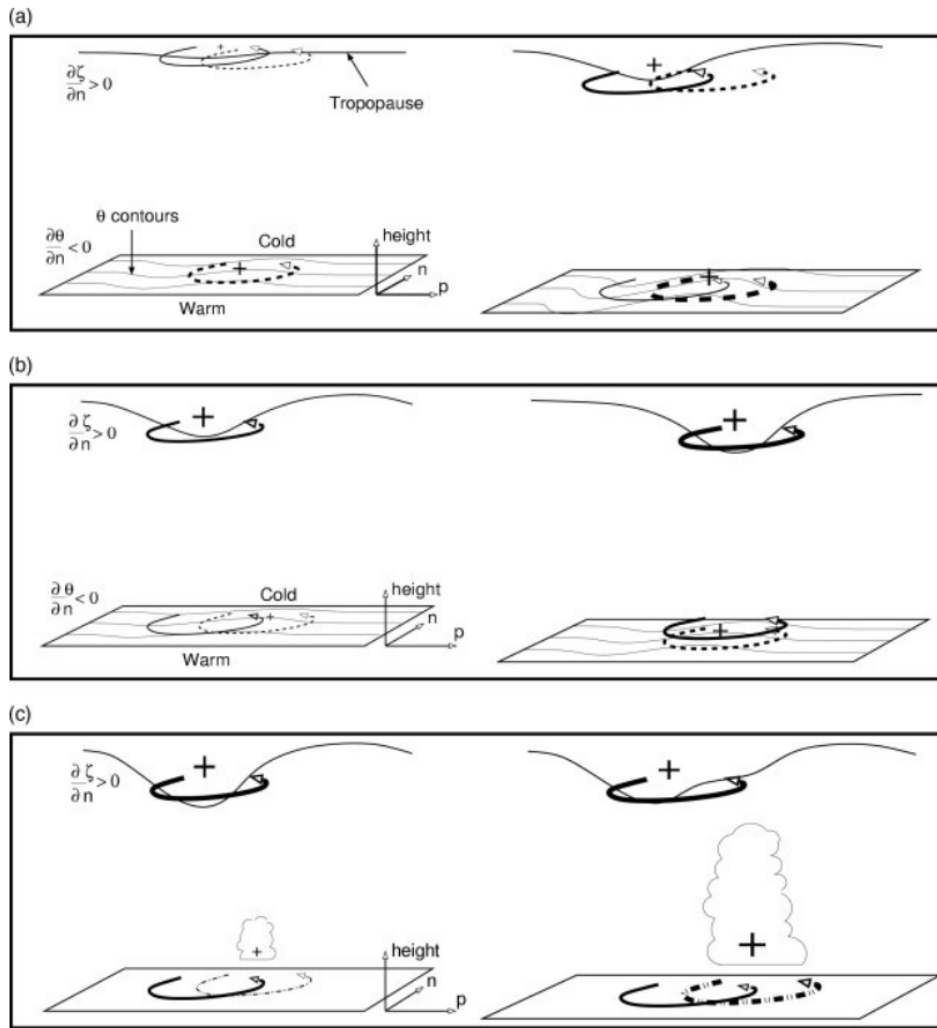
Figure 3.4: Conceptual depiction of the structure of the cyclone types A (top), B (middle) and C (top). In each panel the early (left) and mature (right) structure of the system is presented. The local and the induced circulations are shown by different line styles (solid for upper level, dashed for lower level and dot-dashed for mid-level latent heat release). The thickness indicates the strength of the circulations. The n-axis of the coordinate system is against the thermal gradient (towards cold air), the p-axis is along the thermal wind vector. (From Bracegirdle and Gray, 2008)

Figure 3.5: Schematic representation of the Diabatic Rossby Vortex. An initial low-level
circulation causes poleward warm-air advection on its eastern side (1a).
It induces upward transport of warm-moist air along isentropic surfaces,
since the potential temperature is conserved in adiabatic flow (2, red line).
When saturation is reached the moisture condensates and the latent heat
is released (3a). This release of heat reduces the height of the isentropic
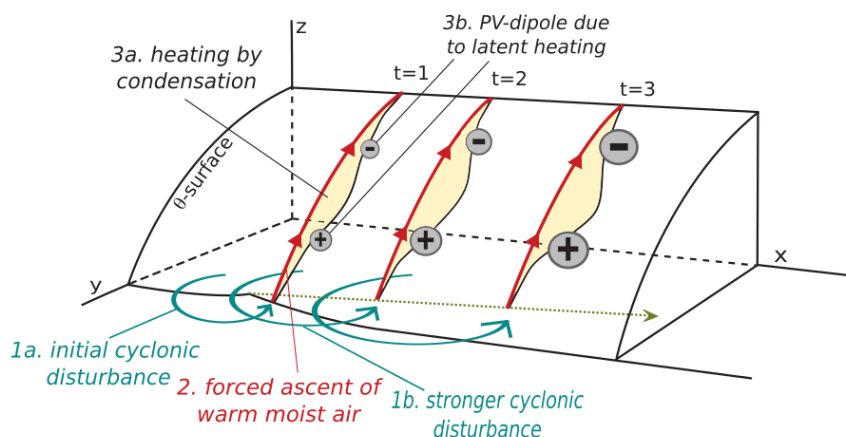surface (thin black line) which induces a positive potential vorticity (PV)
underneath the height of maximum heat release (3b, "+") and a negative
anomaly above ("-"). The positive low-level PV anomaly intensifies the
low-level circulation and hence induces a positive feedback (1b, green
circulation). (From Terpstra, 2014)

level forcing via the production of potential vorticity by latent heat release
(Moore et al., 2013). In order to amplify, the DRV requires a sufficient environ-
mental baroclinicity and moisture content. Terpstra et al. (2015) demonstrate
in simulations with a baroclinic channel model that disturbances in a marine-
polar environment can be conceptually described by the DRV concept. The low
moisture content in the cold polar air mass does not inhibit the intensification
since the vertical heating gradients are still sufficiently large due to a low
vertical extent, expressed by a low tropopause.

The DRV resembles the type C cyclogenesis from the previous section since for
both diabatic contributions are argued to be fundamental for intensification.
However, the DRV is considerably different from type C cyclogenesis since it
does not require upper-level forcing (Jonassen et al., 2020).

3.2.4   Forward and reverse shear

The typical mid-latitude cyclone develops in the polar front, a zone with
strong horizontal temperature gradients. Due to the thermal wind relation,
the westerly winds increase in their speed with height to form the jet stream,
hence a westerly vertical wind shear. Since, the thermal wind vector has the
same orientation as the horizontal mean wind vector this situation is called
forward shear (see Fig. 3.6). This situation is also displayed in the composite
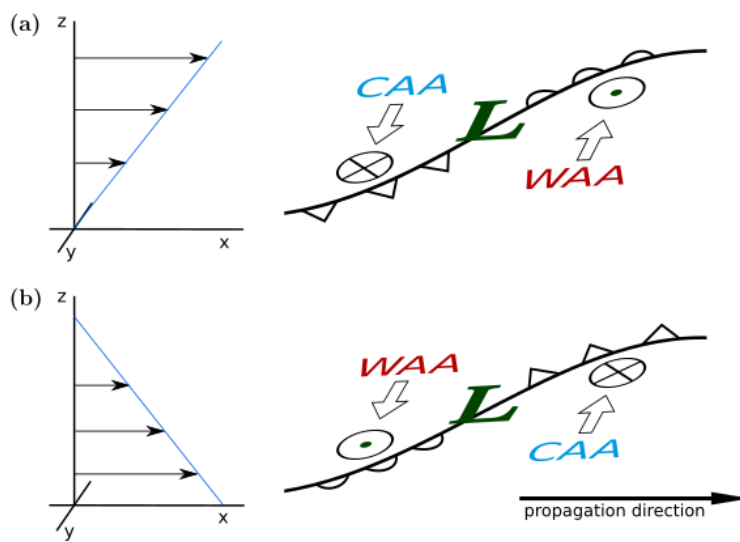
Figure 3.6: Schematic presentation of the baroclinic configuration for (a) forward and (b) reverse shear environments. (Left) Depiction of the horizontal wind vectors (arrows) at different heights. The change of the wind vector with height defines the vertical wind shear. The wind vectors are rotated towards the propagation direction (along x-axis). (Right) The low-level horizontal structure of the frontal wave around the low centre (L). Arrows indicate warm-air advection (WAA) and cold-air advection (CAA). The locations of maximum vertical motion is indicated by circles, with a dot presenting upward motion. (From Terpstra et al., 2016)

fields of mid-latitude cyclogenesis in Figure 3.1.

Duncan (1978) argued that disturbances are also able to grow in a reverse-shear condition. He defined reverse shear as the the condition when the mean wind is parallel, but opposite in direction to the thermal wind. In the reverse-shear situation the cold air is on the right side as seen from the cyclone propagation (which is in the same direction as the mean wind). The associated fields of cold and warm-air advection organise opposite to the forward-shear situation (see Figure 3.6b). The head of the comma-shaped cloud is typically located where the largest updrafts occur. Hence, the comma cloud is located ahead (behind) of the surface low for forward (reverse) shear PLs.

Terpstra et al. (2016) notes that many PLs develop along the outer edges of cold air outbreaks where the horizontal temperature gradient is high. The right flank of a CAO (as seen in direction of the flow) is characterised by forward-shear conditions. The left flank provides a reverse-shear situation. A situation of a simultaneous development of a forward and reverse-shear PL on each flanks of the CAO is depicted in Figure 3.7.

Terpstra et al. (2016) utilised the angle between the mean wind and the thermal wind vector (shear angle) to categorised the PLs from the STARS dataset (Ch. 2.1.1) into classes of forward (0 - 45°) and reverse shear (135 - 180°). Michel et al. (2018) applied the same methodology to a PMC dataset of the Nordic Seas. Terpstra et al. (2016) found an approximately similar amount of both types in the STARS dataset, whereas Michel et al. (2018) identified more than twice as many forward than reverse shear PMCs. In both studies the majority of cases were in an intermediate state with a shear angle between 45 and 135°. Terpstra et al. (2016) notes that a separation between the two classes at a shear angle of 90° would exhibit similar environmental characteristics, though less pronounced.

Some characteristic differences are found for the two shear environments (Michel et al., 2018; Terpstra et al., 2016). Forward-shear conditions are characterised by a baroclinic jet extending throughout the entire troposphere with a wind speed maximum at the tropopause. Reverse-shear conditions were found mainly on the western side of occluded synoptic-scale cyclones. For the Nordic Seas, PLs in a forward (reverse) shear environment occur in characteristic synoptic-scale conditions characterised by a ridge (trough) over Scandinavia, hence their propagation is primarily eastward (southward). Similar dominant propagation directions associated to the shear situations were observed for the Sea of Japan (Yanase et al., 2016).

Since the thermal wind is aligned with the mean horizontal wind for forward shear situations, these situation are characterised by an upper-level jet (see Fig. 3.6), whereas reverse-shear situations feature a low-level jet. Reverse-shear PLs were observed to produce higher near-surface winds, higher surface
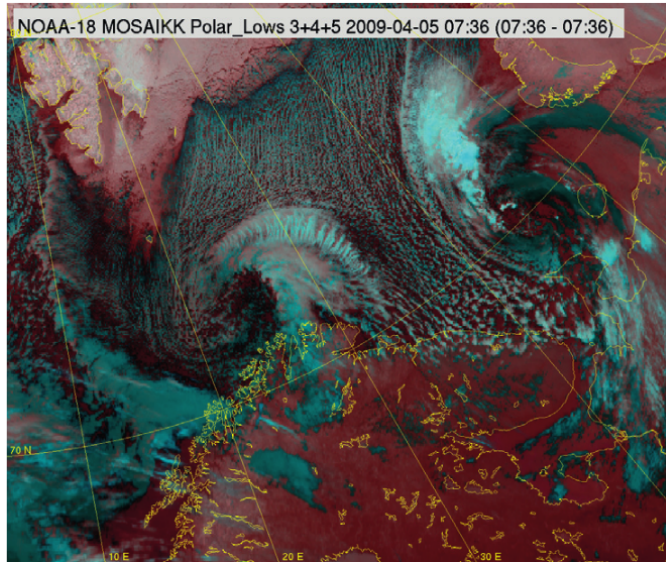
Figure 3.7: Satellite image of the simultaneous occurrence of a forward-shear (west) and reverse-shear (east) on each both sides of the southward directed cold-air outbreak. The cold-air outbreak is visible by the developing cloud streets, tightly spaced lines of clouds, in the middle of the image. (From http://polarlow.met.no)

turbulent heat fluxes and lower static stability than forward-shear PLs (Michel et al., 2018; Terpstra et al., 2016). The low-level jet can explain strong near surface winds, which cause large surface heat fluxes that are responsible for a low static stability. Hence different characteristics can be explained by the synoptic-scale environment, but may not be of primarily direct importance for the PL cyclogenesis.

Terpstra et al. (2016) suggested different initialisation of PLs associated with the two shear types. They argue that forward-shear PLs develop as mid-latitude cyclones by a wave interaction of upper and lower level, whereas reverse-shear PLs initiate as a secondary development associated with frontal instability as described by Schär and Davies (1990) and Joly and Thorpe (1990).

3.3   Barotropic instability

Barotropic instability is, as baroclinic instability, a mechanism that deprives it's energy from the mean flow, hence a flow instability (Markowski and Richardson, 2011). Baroclinic instability relies on a horizontal temperature gradient, which is equivalent to a vertical shear in the wind. In contrast, baroclinic instability is based on a horizontal shear in the velocity field, whereas the flow is uniform in the vertical (Vallis, 2017).
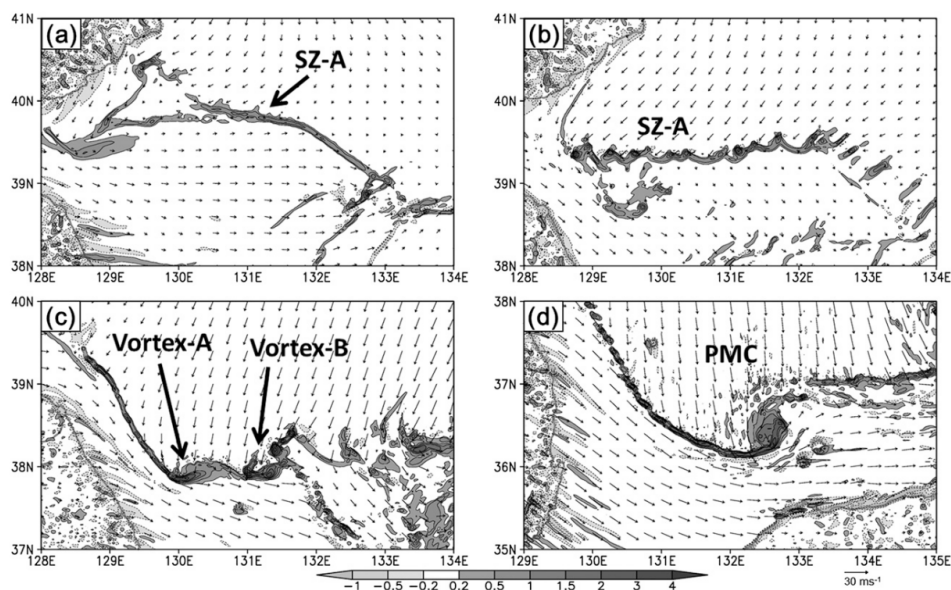
Figure 3.8: Simulated near-surface wind vectors and relative vorticity (shadings, unit $10^{-3}s^{-1}$) at different stages of a shear-line polar low that developed in the Sea of Japan at 29 - 30 Dec 2010. (a) A shear zone (SZ-A) formed between north-easterly and westerly winds that originated from different sides of the mountains of the Korean Peninsula, located to the North West of the map. (b) Early development stage: Numerous small convective vortices form in the shear zone. (c) Late development stage: Merging to a few larger vortices and intensification by barotropic instability. (d) Mature stage: Formation into a single polar mesoscale cyclone (PMC). (Figure 6 from Watanabe and Niino, 2014)

Reed (1979) argues that the jet is unlikely sharp enough to produce barotropic PLs. However, only recently Watanabe and Niino (2014) and Sergeev et al. (2017) described the development of shear-line PLs in which barotropic instability is discussed to contribute.

The evolution of a shear-line PL is described in Figure 3.8. This PL develops by the merging of small convective vortices that evolve along the shear zone. The shear line or convergence zone is caused by upstream topography. In Watanabe and Niino (2014) it is the mountains on the Korean Peninsula and in Sergeev et al. (2017) the topography of Svalbard.

In Sergeev et al. (2017) the shear zone is observed to have a horizontal wind gradient of $25\,\mathrm{ms}^{-1}$ over $50\,\mathrm{km}$, whereas the zone is mainly confined to the lowest 1 - 2 km of the atmosphere. It is common for PLs to develop along existing low-level confluence or shear zones (e.g. Jonassen et al., 2020). Especially reverse-shear PLs face strong low-level winds. Terpstra et al. (2016) suggests that mixed baroclinic-barotropic frontal instability as described by Joly and Thorpe (1990); Schär and Davies (1990) can describe the initialisation of these PLs.

Hence barotropic instability may play a role in the initialisation of PLs along frontal zones, however it is unlikely to be the dominant mechanism in the intensification to mature PLs (Businger and Reed, 1989).

3.4   Vertical instability

Different concepts exist to describe the formation of vertical motion in the atmosphere. These are presented in the following. Also the CISK and WISHE concepts, that were applied to describe "hurricane-like" PL development are introduced. However, both concepts appear inappropriate to fully explain the development of some PLs (Jonassen et al., 2020).

3.4.1   Dry-static instability

Consider a rising parcel of dry air. The parcel experiences decreasing pressure with height, and due to the ideal gas law decreasing temperature. This temperature decrease with height occurs at the dry-adiabatic lapse rate which is approximately $10\,\mathrm{K\,km^{-1}}$ (see Figure 3.9). The potential temperature, θ, of the parcel is defined to be constant for such adiabatic displacement. When the temperature decrease with height is faster than the dry-adiabatic lapse rate the atmosphere is **absolutely unstable**. Such conditions lead to spontaneous dry convection, such as thermals in situations of strong surface heating. Hence, absolute unstable conditions are immediately balanced and therefore do not occur on large scales.

A commonly applied proxy to estimate the static stability of the troposphere in PL situations is the temperature contrast between the sea surface and the $500\,\mathrm{hPa}$ level (SST$-T_{500}$). For example, Zahn and von Storch (2008a), Zappa et al. (2014) and Watanabe et al. (2016) use a threshold of SST$-T_{500} > 43\,\mathrm{K}$ for the identification of PLs. For typical extratropical cyclones the temperature contrast is considerably lower (Stoll et al., 2018; Yanase et al., 2016).

The value of SST$-T_{500} \gtrsim 43\,\mathrm{K}$ indicate that PLs typically occur in dry-stable conditions. Absolute unstable conditions in the polar air mass would occur at a value of SST$-T_{500} \gtrsim 50\,\mathrm{K}$ with the approximation that the $500\,\mathrm{hPa}$ level is elevated around $5\,\mathrm{km}$. This includes the assumption that the near-surface air has the same temperature as the sea surface. However, in cases of strong CAOs the low-level air can be more than $10\,\mathrm{K}$ colder than the sea surface (Fig. 3 Papritz and Spengler, 2017). Hence, the tropospheric stability is considerably higher than it appears when the sea-surface temperature is utilised.

In general, the investigation of dry-static stability can be more easily performed if the potential temperature is utilised, as in Kolstad (2011) and Stoll et al. (2018).
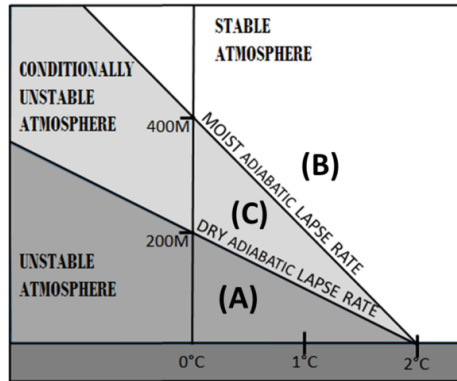
Figure 3.9: Depiction of the dry and moist-adiabatic lapse rates, which divide the atmosphere into stable, conditionally unstable and absolute unstable conditions. (Figure 1 from Feiccabrino et al., 2015)

Another measure for the static stability is the Brunt-Väisälä frequency

$$N = \sqrt{\frac{g}{\theta} \frac{\partial \theta}{\partial z}} \qquad (3.2)$$

which expresses the frequency of gravity waves (Holton, 1973). N is among the parameters to determine the scale at which baroclinic disturbances grow (see Equation 3.1). Typical tropospheric values for extra-tropical cyclones are $N \sim 0.01 \text{s}^{-1}$. However, for the marine polar air mass N can take half that value, as found in Paper III. A low static stability (small N) lead to a fast interaction of upper and low-level perturbations in the baroclinic model (Ch. 3.2).

3.4.2 Moist-static instability

Now consider a parcel of air saturated with water vapour. As the temperature of the rising parcel decreases some of the included water vapour condensates. The phase change releases heat, which is called latent heat of condensation. Therefore, the temperature decrease with height of the moist parcel, the moist-adiabatic lapse rate, is lower than for the dry parcel (see Figure 3.9).

A temperature decrease with height that is faster than the moist-adiabatic lapse rate is **conditional unstable**. The condition is that the air is saturated with water vapour. A faster environmental temperature decrease with height than the moist-adiabatic lapse rate is characterised by Convective Available Potential Energy (CAPE, see Markowski and Richardson, 2011). In contrast, if the temperature decrease with height is lower than the moist adiabiatic lapse rate, the atmosphere is absolutely stable.

During cold-air outbreaks deep conditionally unstable layers can develop (Renfrew, 2015). However, the instability condition, saturation of the air, is often (almost) satisfied near the sea surface, due to the provision of moisture by the open water. Therefore, the build-up of CAPE is prevented by the onset of

convection, and CAPE is consumed more or less as rapidly as it is produced (Linders and Saetra, 2010). Hence, it appears that the temperature profile in marine environments does not become steeper than the moist-adiabatic lapse rate, as also argued for by (Xu and Emanuel, 1989).

The moist-adiabatic lapse rate depends on the temperature and pressure. It is approximately $5\,\mathrm{K\,km^{-1}}$ in the lower troposphere at around 10°C . For temperatures of -30°C the moist-adiabatic converges towards the dry-adiabatic lapse rate. Hence, in the polar air mass conditional instability is nearly equivalent to absolute instability. Therefore, the static stability, N, which contributes to define the baroclinic scale and growth rate, can take considerably smaller values in the marine polar air mass than in warmer air masses. Hereby, a meteorological requirement for N to reach small values are low tropospheric temperatures.

3.4.3   Conditional instability of the second kind (CISK)

The air is typically unsaturated outside areas of convection, hence the instability condition is not satisfied. For this reason, Charney and Eliassen (1964) and Ooyama (1964) suggested a second concept for the initiation of convective instability, which is referred to as Conditional Instability of the Second Kind (CISK). After this concept, an initial forcing is required to cause convection in unsaturated, but conditionally-unstable air. The initial disturbance, generally a kind of low pressure anomaly, causes frictional convergence of the near-surface air. The convergence initiates vertical motion (see Figure 3.10a). Once the ascending air reaches saturation the instability condition of the previous chapter is satisfies, and the vertical motion is further accelerated.

This onsets a positive feedback loop (see Figure 3.10b). The vertical winds lead to latent heat release, which warm and hence expand the air and hereby cause the surface-level low-pressure anomaly to deepen. The growing low-pressure anomaly increases the frictional convergence, which enhances the vertical winds. For this mechanism CAPE must be available (e.g. Charney and Eliassen, 1964).

After this concept the atmosphere is not locally unstable, but unstable when combined with a low-pressure perturbation. For example thunderstorms and tropical cyclones require a disturbance for the initialisation. The CISK model is commonly applied to explain the development of tropical cyclones. Rasmussen (1979) suggested this model to describe the PL cyclogenesis.

However, Sardie and Warner (1983) finds that CISK theory alone is not sufficient to produce the observed growth rates of PLs. The CISK concept relies on significant reservoirs of CAPE. The existence of this reservoir in marine environments was questioned (e.g. Linders and Saetra, 2010; Xu and Emanuel, 1989). Therefore, this mechanism alone seems unlikely to explain PL intensification.
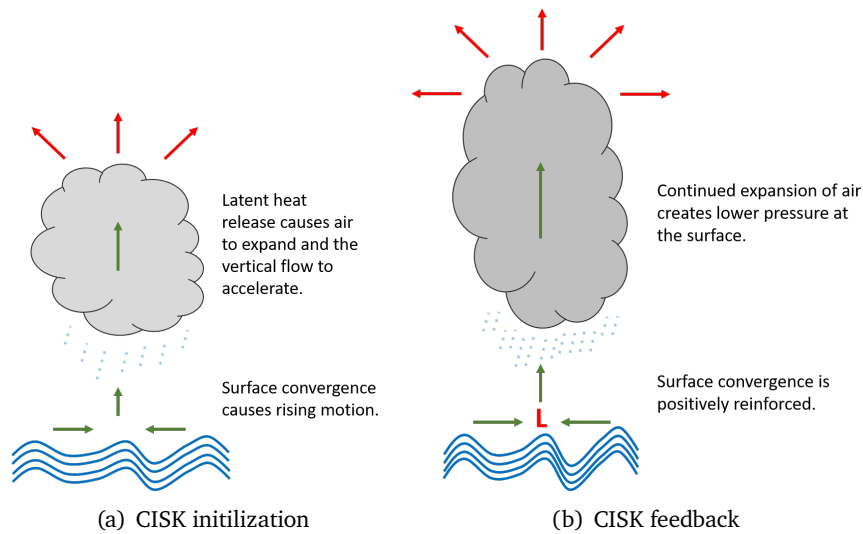
(a) CISK initilization   (b) CISK feedback

Figure 3.10: Conceptual presentation of the conditional instability of the second kind mechanism.

Still, CISK is instructive to conceptually describe the role of latent heat release in PL intensification. A CISK-like mechanism, however without pre-existing CAPE, can be included to the dry-baroclinic concept to form a moist-baroclinic framework, as suggested by Sardie and Warner (1983).

3.4.4 Wind-induced surface heat exchange (WISHE)

Another positive feedback mechanism that is often invoked in tropical cyclones is of the one of Wind-Induced Surface Heat Exchange (WISHE, Emanuel, 1986). This mechanism emphasises that the cyclone causes surface fluxes of heat and moisture from the sea surface. The sensible and latent heat fluxes in turn act to amplify the cyclone by destabilising the atmosphere and providing moisture for release by convection, respectively. Hence a positive feedback between the circulation and surface-heat fluxes.

This mechanism was applied by Emanuel and Rotunno (1989) to describe the intensification of PLs. Also Yanase and Niino (2007) shows that a WISHE-like vortex can grow within an idealised polar air mass. However, the WISHE-like vortex was very sensible to the initial, axis-symmetric disturbance and had only a slow growth rate. An axis-symmetric vortex is seldomly observed for PL cases (Mokhov et al., 2007).

Some PLs were observed to develop a spirali-form cloud structure in their mature stage (see Figure 1.4a). Hurricane-like characteristics were associated with spirali-form PLs (Emanuel and Rotunno, 1989; Rasmussen, 1979). However, the initial intensification stage of such PLs was observed to be characterised by baroclinic instability (Føre et al., 2012; Nordeng and Rasmussen, 1992).

Føre et al. (2012) and Kolstad et al. (2016) investigated whether the mature stage of a "hurricane-like" PL could be described by hurricane theory. Their sensitivity experiments provided little evidence for the relevance of the WISHE concept to describe the PL cyclogenesis: Intensification after the baroclinic stage was not observed, major updrafts occur on one side of the PL centre and downdrafts on the other side as characteristic for a baroclinic development (Fig. 10 of Kolstad et al., 2016), and latent heat release played only a minor role. The decay of the PL studied by Føre et al. (2012) and Kolstad et al. (2016) after deactivation of the sensible heat fluxes may be explained by a fast increase of the static stability, which causes a decoupling of the lower from the upper-level circulation and hence a decay of the PL.

When the sea-surface temperature was artificially increased by 6 K for the previously discussed "hurricane-like" PL, Kolstad and Bracegirdle (2017) observed a considerably prolonged non-baroclinic mature stage, however a structure that resemblance a hurricane was not clearly identified. It is remains questionable whether "hurricane-like" PLs occur in reality (Jonassen et al., 2020).

3.4.5   Symmetric instability

Symmetric instability is another form of vertical instability. In this concept the flow is unstable to slanted convection, as a combination of static and inertial instability (Markowski and Richardson, 2011). It appears that slantwise ascent, which leads to strati-form comma-shaped clouds is frequently observed for PLs (e.g. Harrold and Browning, 1969). Slantwise ascent is also part of the DRV concept (Ch.3.2.3). Hence, symmetric instability can be interpreted as a component contributing to the baroclinic development of PLs.

A criteria for symmetrical instability is:

$$\frac{Ri}{f}\left(f - \frac{\partial u_g}{\partial y}\right) < 1 \tag{3.3}$$

with the Coriolis parameter, f, the zonal component of the geostrophic wind u_g. Hence, symmetrical instability occurs at small Richardson numbers, Ri, and favourably at anticyclonic relative vorticity ($\partial u_g/\partial y > 0$). The Richardson number is used to predict fluid turbulence by comparing the strength of the static stability (inhibits turbulence) to the vertical shear in the flow (favours turbulence). It is defined by:

$$Ri \equiv \frac{\text{static stability}}{\text{vertical shear}} = \frac{N^2}{(\partial u_g/\partial z)^2} \tag{3.4}$$

Ri is small for low static stability (small N) and strong vertical shear (large $\partial u_g/\partial z$). A strong vertical shear is equivalent to a high baroclinicity, which together with a low static stability is often observed for PLs (see Paper III).

3.5   Polar-low classification

A large variety of PLs was observed (Rasmussen and Turner, 2003) and there-fore classification can help to identify similarities and differences among PLs.

As presented in Chapter 1.5, a "PL spectrum" ranging from baroclinic, comma-shaped on one side to convective, spirali-form, "hurricane-like" PLs on the other side, was suggested (p.157 Rasmussen and Turner, 2003). However, most PLs were observed to be located in the middle of the spectrum, as both baroclinic and convective processes contributed to the intensification (Renfrew, 2015). This combination may be termed moist-baroclinic instability.

Two more suggestions of PL classifications were already presented. Chapter 3.2.2 contained the suggestion by Bracegirdle and Gray (2008) to divide PLs by the fraction of upper versus lower-level contributions to the cyclone strength. Chapter 3.2.4 introduced the concept of separating PLs by their environmental vertical shear conditions, as suggested by Duncan (1978) and Terpstra et al. (2016). Both concepts are basically identifying subgroups of baroclinic instabil-ity.

3.5.1   Businger and Reed (1989) classification

Businger and Reed (1989) identified three elementary types of PL development based on distinctive synoptic-scale patterns, as well as different distributions and strength of the baroclinicity, static stability and surface heat fluxes:

1. **Short-wave/jet-streak type**: Characterised by a secondary vorticity max-imum and positive vorticity advection aloft, as well as deep, moderate baroclinicity, and modest surface fluxes.

2. **Arctic-front type**: Associated with ice boundaries and characterised by shallow baroclinicity and strong surface fluxes.

3. **Cold-low type**: Characterised by shallow baroclinicity, strong surface fluxes, and deep convection.

This classification was suggested in a time when PL investigation was mainly performed from cloud structures and synoptic weather maps, and therefore the classification includes a degree of subjectivity.

Bracegirdle (2006) notes that the first two types are of baroclinic nature, whereas the third type has a convective character. Terpstra et al. (2016) connects the first type to forward and the second type to reverse-shear situations. Hence, the shear angle provides an objective method to distinguish between the first two types. The cold-low type includes PLs with a spirali-form and merry-go-

round cloud structures (Ch. 1.5). "Hurricane-like" dynamics were associated to this type (Businger and Reed, 1989; Rasmussen and Turner, 2003). However, Grønås and Kvamstø (1995) notes that type 3 is infrequent in the Nordic Seas. Also Chapters 3.4.3 and 3.4.4 discuss that pure "hurricane-like" dynamics appear unlikely to account for the development of PLs.

An extension of the Businger and Reed (1989) classification to a "pragmatic" classification scheme with seven classes was suggested by Rasmussen and Turner (2003). However, many of the additional classes appear to be reducible to the three classes of Businger and Reed (1989). Rasmussen and Turner (2003) suggested classes of "trough systems" and "baroclinic waves (= forward shear)" which could be assigned to type 1. The "boundary layer fronts" and "reverse shear systems" could be associated to type 2. "Comma clouds" are possibly of type 1 or 2, depending on the shear angle. An additional suggested group in the "pragmatic" classification scheme are "orographic PLs" that form due to vortex stretching in the lee of land masses.

4

Objectives of this thesis

The previous chapter presented the different concepts suggested for PL cyclogenesis. It appears that there is a large variety of PLs.

The general scientific question behind my thesis is: What are the main processes that lead to PL development? As outlined in Chapter 1.1, a better meteorological understanding of PLs is required to eventually improve the prediction of PLs.

In the previous chapters, different open questions in the PL research were outlined:

1. How can PLs best be detected? Or differently formulated: What characterises PLs? (Ch. 1.4 + 2)

2. How does PL activity compare in different ocean basins? (Ch. 2)

3. How do state-of-the-art weather prediction models capture the development of PLs? (Ch. 1.1)

4. How sensible are PLs to diabatic contributions and the sea-surface temperature? (Ch. 3.4.4)

5. What is a useful classification of PLs? (Ch. 1.5 + 3.5)

6. How do PLs develop? (Ch. 3)

The investigation of PLs is approached in different ways in the three papers. Different scientific sub-questions are posed in each of the papers.

Paper I

The study performed in Paper I targets the first two outlined questions. Inspiration for this study came from the studies by Zappa et al. (2014) and Bracegirdle and Kolstad (2010). The first study demonstrate that PLs can be detected from the reanalysis data set ERA-Interim and provides a methodology for doing this. However, the parameter choice of Zappa et al. (2014) was not carefully tested. In order to test the parameters for PL detection, the later article provided an idea, which is as follows: (1) Use a subjective database of PLs and other cyclones to derive criteria to successfully separate between the two. (2) Apply these criteria to an entire cyclone database to filter out the PLs and hence to retrieve an objective PL climatology. Application of this methodology made it possible to derive a global climatology of PLs. This could then be used to compare the PL activity in different regions and possible changes over time.

Paper II

The second study aims to answer question 3 and 4. One PL case was investigated in this study since the extensive amounts of simulations required in the sensitivity experiments makes the approach not feasible for the investigation of a large number of cases.

This project was performed in close cooperation with MET since we use their weather-prediction model AROME-Arctic (Müller et al., 2017a). AROME-Arctic is operationally utilised for the forecast of PLs in the Nordic Seas. Therefore it is of importance to evaluate and eventually improve the quality of this model for prediction of PLs.

Paper III

The third study investigates questions 5 and 6. In order to approach the question how PLs develop it seemed a prerequisite to first group the PLs into classes of similar appearance.

However, multiple different classification schemes for PLs have been suggested (Ch. 3.5). The usefulness of the different classification schemes has not yet been compared or tested by an independent methodology. Unfortunately not all of the are easily and objectively applicable. For example Rasmussen's "pragmatic" classification requires an (subjective) interpretation of the meteorological situation in which the PL is embedded. The upper versus lower-level forcing classification by Bracegirdle and Gray (2008) requires the derivation of the quasi-geostrophic vertical motion attributed to forcing from different levels.

5

Summary of publications

This chapter provides a summary and discussion of the scientific work performed in connection with this thesis.

5.1   Paper I

P.J. Stoll, R.G. Graversen, G. Noer, K. Hodges,
"**An objective global climatology of polar lows based on reanalysis data.** ",
Quarterly Journal of the Royal Meteorological Society, 144:2099-2117, April 2018.

As mentioned before the aim of this study is twofold:

1. Derivation of a combination of model parameters that most clearly detects PLs.

2. Comparison of the the global PL activity across regions and time.

In this study, we first derive cyclone databases by applying the cyclone tracking algorithm of Hodges (1995) to the reanalysis datasets ERA-Interim and the Arctic System Reanalysis (ASR). We then utilise the STARS dataset of PLs to identify a representative amount of PLs within the cyclone database. In the next step, we test a large number of parameters to discriminate between PLs and other cyclones. The combination of the following three criteria is found to be successful for ERA-Interim (and ASR):

1. A difference of the mean SLP in a radius of 110 km (330 km) and the SLP of the system larger than 0.4 hPa (2.4 hPa),

2. A maximum potential temperature difference in a radius of 110 km between the sea surface and 500 hPa level above -9.4 K (-8.5 K), and
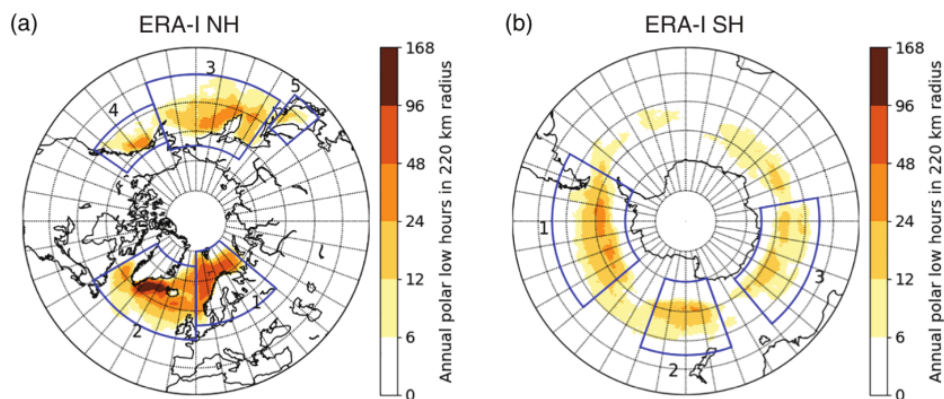
Figure 5.1: Maps of the polar-low activity for the (a) Northern and (b) Southern Hemisphere. The activity is measured by annual mean time that polar lows appear around a given location. (Figure 5 of Paper I)

3. The absence of tropopause (500 hPa) wind speed higher than $31.3\,\mathrm{m\,s^{-1}}$ ($29.6\,\mathrm{m\,s^{-1}}$) poleward of the system.

These criteria are all motivated by the dynamical nature of PLs as presented in Chapters 1.3 and 1.4. Criteria 1 is applied to identify intense PMCs, criteria 2 for the detection of CAOs associated with low static stability through the entire polar troposphere, and criteria 3 to guarantee the occurrence of the systems poleward of the polar front. The result that similar parameters are most effective for PL detection for both ERA-I and ASR gives confidence that the criteria have a universal character and are independent on the underlying model. The first criteria is not a standard model parameter, but the relative vorticity can be used instead since it is almost as successful for the identification of PLs.

We apply the three PL identification criteria to the derived ERA-Interim and ASR cyclone database and obtain the first global PL climatologies. The climatologies include PLs in all marine basins at high latitude with the main occurrence in the vicinity of the sea-ice edge and coastal zones (see Figure 5.1). The Denmark Strait and the Nordic Seas reveal as the regions with the highest PL activity. The climatologies confirm that the main PL season in the Northern Hemisphere is between November and March. In the Southern Hemisphere PLs develop between 50 - 65°S between April and October. The climatology of ERA-Interim ranging from 1979 to 2016 does not show significant hemispheric trends. However, regional trends are observed which suggest that the regions of activity has already adapted to global warming. Also a reduction of the most intense PLs is found.

The definition of PLs is formulated in a general way (Chapter 1.3). This is, among others, a reason which complicates the scientific investigation of PLs since it leads to different interpretations whether a system should be categorised as PL.

In contrast, the definition of tropical cyclones (hurricanes/ typhoons) is well formulated. The success of universal applicable criteria for the detection of PLs, as presented in Paper I, indicate that a more specific PL definition is possible. Such a definition could ease the discussion about PLs. The three detection criteria in Paper I could contribute to derive a specific definition of PLs.

A discussion on the general applicability of these criteria is given in Chapter 6.1. Also some ideas about how the global climatology can be tested and about future opportunities with this climatology are presented.

5.2   Paper II

P.J. Stoll, T.M. Valkonen, R.G. Graversen, G. Noer.
"**A well-observed polar low analysed with a regional and a global weather-prediction model**",
Quarterly Journal of the Royal Meteorological Society, 146:1740-1767, February 2020.

We investigate a PL that developed on 3 - 4 March 2008 and that was observed from three flights during the IPY-THORPEX campaign (Kristjánsson et al., 2011), a rarity for a PL. The aims of the study are twofold:

1. Validation of the AROME-Arctic model against observations from the flight campaign and satellite imagery. Additionally, examination of the benefits of the high-resolution regional weather-prediction model, AROME-Arctic, as compared to the coarser-resoluted global weather-prediction model European Centre for Medium-Range Weather Forecasts (ECMWF) HRES.

2. Investigation of the physical mechanisms underlying the development of this PL. Specifically, examination of the sensitivity of this PL to the sea-surface temperature.

AROME-Arctic is the currently operational short-range weather-forecasting model of the MET for the Nordic Seas utilised to deliver warnings for PLs (Müller et al., 2017b). It has a horizontal grid spacing of 2.5 km which is 10 times higher than of ECMWF HRES in 2008. The latter is a global medium-range weather prediction from the European weather service ECMWF. Validation of AROME-Arctic and ECMWF HRES against observations from the flight campaign and satellite data reveals that both models simulate the PL reasonably well. The cloud structures and the high local variability imprinted in the meteorological fields in the PL situation are more realistically represented by AROME-Arctic. However, the high local variability causes standard error statistics to be similar for AROME-Arctic and ECMWF HRES. Although the high local variability appears to be realistically represented by AROME-Arctic,

it may be out of phase with observations, which can lead to a double penalty by the standard error statistics. Hence, for the first time we apply a spatial verification technique to a PL case. This verification reveals that AROME-Arctic has improved skills at small scales for extreme values as compared to ECMWF HRES.

The comparison of the AROME-Arctic to the dropsonde also reveals some model biases. The model is observed to be too warm near the surface, which is likely attributed to a time-lacking update of the sea-surface temperature field in the simulation. The model has a higher vertical instability in the planetary boundary layer than apparent from measurements, which can be explained by the previously mentioned bias. The humidity profile indicates that the model overestimates the shallow convection, which is likely caused by the vertical instability bias. Hence the sea-surface-temperature bias might induce a whole chain of effects, which is a further motivation for the sensitivity experiments with the sea-surface temperature. Another model issue is that deep convective cells appear to be simulated too deep and confined, which is an indication that a deep-convective parametrization scheme could be beneficial also for non-hydrostatic, so-called "convective-permitting" models, as AROME-Arctic. We also analyse the forecast quality of the two models. It appears that forecast errors, especially in the location of the PL, grow faster in AROME-Arctic than in ECMWF HRES.

In the second part of the article, we analyse the PL development. The PL has two stages, an initial baroclinic and a convective mature stage. The initial baroclinic growth appears to be supported by sensible heat flux and condensational heat release. In the mature stage, latent heat release appears to maintain the system. At least two conditions must be satisfied for the convective stage to develop: i) The sensible heat flux has sufficiently destabilised the local environment around the PL, and ii) sufficient amount of moisture is available for condensational heat release. In this case more than half of the condensated moisture within the system originates from the surrounding. The PL is "pulled" towards the area of strongest condensational heating, following the Diabatic Rossby Vortex concept (Ch. 3.2.3).

Sensitivity experiments of the PL with perturbed sea-surface temperature, reveal that the maximum near-surface wind speed connected to the system increases by 1 - $2\,\mathrm{ms}^{-1}$ per K of surface warming. These values are approximately twice as high as a previous estimate obtained from a idealised model from Sætra et al. (2008). Additionally to increased maximum near-surface winds, also a second PL centre develops at the Arctic front in the experiments with highly increased temperatures.

5.3   Paper III

P.J. Stoll, R.G. Graversen, T. Spengler, A. Terpstra
"Polar lows as moist-baroclinic cyclones in four vertical-shear environments."
This paper is in final preparation for the submission to the journal Weather and Climate Dynamics.

The aim of this study is the investigation of the PL development mechanisms. Since PLs appear to be different from each other, we first classify PLs with regard to their local environment in which the cyclogenesis and system maintenance occur. For this purpose, self-organising maps are applied to 370 PLs which are obtained by matching mesoscale cyclone tracks from the reanalysis ERA-5 with PLs from the STARS dataset. Self-organising maps are a useful tool in order to represent patterns of coherent spatial variability in large datasets.

The classification reveals that PLs develop in various configurations of the thermal field as compared to the flow field (Fig. 5.2). This study hereby confirms the usefulness of the categorisation into forward and reverse-shear PLs in order to describe the dynamical configuration as suggested by Duncan (1978) and Terpstra et al. (2016). In Figure 5.2, forward shear is present in node 1 + 2 and reverse shear in node 9.

We expand the shear categorisation by right (node 3) and left-shear PLs (node 7) that propagate towards colder and warmer environments, respectively, hereby proposing in total four categories. Systems in all four shear categories arrange in a manner typical for baroclinic instability (see Figure 7 of Paper III). The low pressure anomaly tilts with height in the opposite direction to the thermal wind vector which lead to a dynamical coupling of the upper and lower-level pressure perturbations. A comma-like cloud (grey shadings in Figure 5.2) develops at the location of low-level warm-air advection (warm front) and contributes to the intensification of PLs in all shear orientations. Therefore, we suggest that the intensification is best be described by moist baroclinic instability. Surface fluxes of sensible and latent heat are argued to have no direct effect, but are required to provide a favourable environment for the moist-baroclinic growth.

We find no evidence for systems that intensify in an environment without baroclinicity. Hence, our results could not support the presence of a "hurricane-like" mechanism for the intensification of a significant amount of PLs, as suggested by Emanuel and Rotunno (1989).

The cloud structure is since long believed to be connected to physical development (e.g. Forbes and Lottes, 1985; Yanase and Niino, 2007). Therefore we use a version of the STARS dataset provided by Rojo et al. (2019), which includes the cloud structure at each time step when a given PL was detected by infra-red satellite imagery. The cloud information revealed that the baroclinic intensifica-
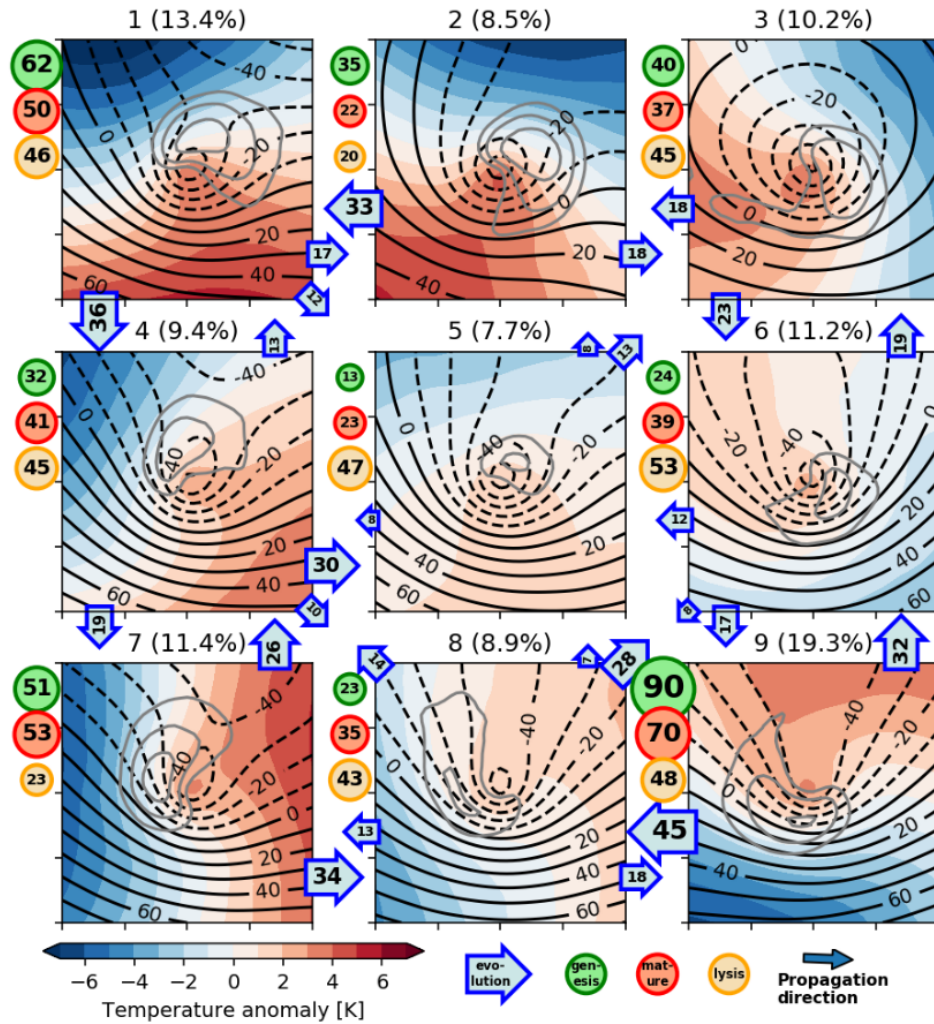
Figure 5.2: 9 typical arrangements (nodes) of the thermal field around polar lows revealed by self-organising maps (shadings: temperature anomaly fields at 850 hPa). The polar-low centre is located in the middle of each field and propagates towards the right. The tick distance along the x and y-axis is 250 km. Black contours display geopotential height anomaly at 850 hPa and grey contours the medium-level cloud cover (levels at 0.7, 0.8 and 0.9) associated to each node. The percentage depicts the fraction of polar-low time steps associated with each node. Numbers in the green, red and yellow circles count the genesis, mature and lysis time steps, respectively, encountered to each node. Blue arrows depict the number of polar-low evolutions from one to another node. (Figure 2 of Paper III)

tion stages of the PLs are more often connected to comma than to spirali-form clouds and that the opposite is apparent for the end stages of the PLs. This indicates that the cloud spiral may be explained as being the occlusion stage of a baroclinic cyclogenesis, as described by the Shapiro-Keyser cyclone model (Ch. 3.2.1). Some ideas on how this hypothesis might be tested are formulated in Chapter 6.3.

6

Discussion and future work

Each of the papers led to new questions, discussions and ideas. Some of these are expressed in this Chapter.

6.1   Discussion arising from Paper I

In Paper I, we develop a global climatology of PLs. A caveat of our methodology is that the criteria are derived on the basis of PLs from the North Atlantic only. Hence the obtained PL-identification criteria may be biased. The robustness of the criteria could be tested for other PL lists, e.g. that of Smirnova et al. (2015), and preferably from another ocean basin, e.g. Verezemskaya et al. (2017). However, these lists are less well-accepted than the STARS dataset.

Criticism about the use of general criteria for PL detection, as applied in Paper I, was formulated in Jonassen et al. (2020) (p.25): "The latter threshold [SST-T_{500}] varies regionally. For example, polar lows in the Pacific region tend to be more baroclinic and develop in more statically stable conditions (Businger 1985, 1987; Chen and von Storch 2013) than their Atlantic counterparts, rendering generic thresholds unsuitable for creating global polar low climatologies."

However, the three mentioned references by Jonassen et al. (2020) provide little evidence for fundamentally different static-stability conditions in the Pacific than in the Atlantic. Businger (1985) does not investigate PLs in the Pacific. Businger (1987) writes in the conclusion: "Comparing the compositing results for PLs over the Gulf of Alaska with those over the Norwegian and Barents Seas (see Businger, 1985), the signature of the environments conducive to the formation of PLs appear very similar in most of the variables studied for both regions. Strong negative-height and temperature anomalies were present at 500 mb on the key day in both regions. Low values of the 500-1000 mb thickness and low surface pressures were also present on the key day in both regions." In fact this conclusion indicates that common parameters are applicable.

The study from Chen and von Storch (2013) refers to Chen et al. (2012) in order to argue that the SST - T_{500} threshold is reduced from 43 K, as used by Zahn and von Storch (2008b) for the North Atlantic, to 39 K for the Pacific. Chen et al. (2012) investigated 10 PL cases from the North Pacific and apparently found it advantageous to reduce the SST - T_{500} threshold to 39 K to objectively identify the PLs. This is, however, no proof that PLs in the North Pacific are generally occurring in more statically stable conditions. Imagine one would pick 10 random PLs from the North Atlantic. One would likely only detect all of them if a SST - T_{500} threshold of 39 K instead of 43 K is applied. The result from the parameter distributions in Paper I (Table 2) show that 10% of the PLs from the STARS dataset have a SST - T_{500} that never exceeds 41.4 K.

Therefore, the global PL climatology from Paper I is based on a weaker threshold in the static stability than the commonly applied threshold of 43 K. The climatology is based on a threshold of $\theta_{SST} - \theta_{500} > -9.4$ K, which is approximately similar to SST - $T_{500} > 41.4$ K.

Hence, the argumentation from Johnson (2015) provides little evidence to generally reject the production of a global climatology.

In general, the static stability (SST - T_{500}) varies from case to case. The use of this criteria, as the use (or lack of use) of any criteria, can lead to biases in a climatology. This can happen within a singular ocean basin also. Terpstra et al. (2016) finds somewhat different values for SST - T_{500} at the genesis of forward (41.0 ± 3.6 K) than reverse shear PLs (45.2 ± 2.6 K) in the North Atlantic.

It could therefore be beneficial to take a general approach to develop a global PL climatology. This could be as follows: (1) Derive cyclones tracks, e.g. with the algorithm by Watanabe et al. (2016) which may be applied to ERA-5. (2) Obtain globally all PLs by applying a scale criteria (mesoscale), a polar-front criteria, and a intensity criteria (gale-force winds). The so-derived climatology would include all systems that satisfy the PL definitions formulated in Chapter 1.3.

Michel et al. (2018) used a comparable approach for the North-Atlantic, however by applying additional criteria and without a polar-front criteria. From (Michel et al., 2018, Fig. 4b) it appears that their PMC climatology does not reproduce the typical annual cycle of PLs for the North Atlantic. The climatology only slightly less PLs in October than in the peak winter months, which is inconsistent most other PL climatologies for the North Atlantic (Blechschmidt, 2008; Noer et al., 2011; Wilhelmsen, 1985, e.g.). Hence also the lack of criteria may lead to biases, for example to the inclusion of systems that are not be well embedded in the polar air mass.

Of high interest is the further investigation of a global PL climatology in order to investigate possible differences between PLs from the ocean basins. A direct

comparison of a representative amount of PLs from different ocean basins has to the authors knowledge not been performed yet. This comparison could for example reveal whether Pacific PLs develop in more baroclinic and statically stable environments than North Atlantic PLs, suggested by (Jonassen et al., 2020). The comparison could also reveal areas with typical shear structures of PLs, as identified in Paper III. Also other effects could be investigated. For example the role of orographic forcing, which was suggested to vary for different regions (Turner et al., 1993).

6.2   Ideas arising from Paper II

PLs are among the most chaotic phenomena and presents one of the major natural hazards in the polar regions. Hence, the forecast quality of PLs appears to be a useful measure for the examination of weather-prediction models applied in polar regions. In Paper II, two such models are compared regarding their capability to predict a PL. Until now, a direct comparison of multiple models for a representative amount of PLs has not been performed. Also the improvement in the last decades of the forecast models to predict PL cases has not been scientifically investigated. In the following an outline for such a study is given.

An evaluation of the models could be based on measures that capture the characteristics of PLs, such as the location, size and maximum intensity. Hence, one challenge is to derive a good estimate of the real characteristics of each PL. For the validation of weather-prediction models, this estimate is often given by the analysis time of the model.

For PLs the assumption that the analysis time is a good estimated of reality should first be tested, for example by comparing the characteristics of PLs from the model analysis with satellite imagery. If the model analysis captures a given PL, the forecast can be compared to the analysis. The deviation in the location, size and intensity of the PLs can be measured dependent on the forecast length. This can provide an estimate for the forecast time of PLs, which can be utilised to compare different models for their quality in predicting PLs. Also, the quality of model ensemble prediction systems could be evaluated following this methodology.

In light of the shear-based categorisation of Paper III, it could also be tested whether some types of PLs are predicted with a higher quality than others.

6.3   Ideas arising from Paper III

Paper III results in a classification of PLs based on their vertical shear angle. Terpstra et al. (2016) suggest that forward-shear PLs develop as mid-latitude cyclones by a wave interaction of upper and lower level, whereas reverse-shear PLs initiate as a secondary development associated with frontal instability (Joly and Thorpe, 1990; Schär and Davies, 1990). Our results from Paper III show that all shear types represent a deep baroclinic structure. However, the initiation of the shear types may be different. More investigation is needed to examine the PL genesis for the different shear types.

In Paper III, we formulated the hypothesis that the origin of spirali-form PLs may be a Shapiro-Keyser life cycle. This hypothesis needs to be tested. The frontal evolution of PLs could be investigated in order identify life cycles following the Norwegian cyclone model and the Shapiro-Keyser model. These life cycles could then be compared to the evolving cloud structures. High-resolution datasets, such as state-of-the-art weather prediction models or synthetic-aperture radar (SAR) retrievals may display the frontal structure at a sufficient resolution. Alternatively, the large-scale barotropic shear and the confluence of the environments could be measured and compared to the resulting cloud structures.

Since the resolution of ERA-5 may not be sufficient to reproduce the convective dynamics of "hurricane-like" PLs, the hypothesis that "hurricane-like" PLs do not exist needs to be evaluated. It is of interest to investigate whether a high-resolution, non-hydrostatic model, such as AROME-Arctic with a 2.5 km horizontal grid spacing, simulates "hurricane-like" PLs. MET is currently producing an Arctic reanalysis called CARA with this model (CAR). The investigation of CARA for PLs could give information whether a "PL spectrum" ranging from baroclinic to "hurricane-like" PLs actually exists.

An alternative approach for testing the existence a "PL spectrum" is the reexamination of cases where a hurricane mechanism was suggested to describe the intensification (e.g. Nordeng, 1990; Nordeng and Rasmussen, 1992; Rasmussen, 1979). The atmospheric models are considerably more advanced today than at the time when these mechanisms were suggested. The new models could reveal the cyclogenesis of these PLs in more detail.

7

Main conclusion

Specific conclusions from the thesis were presented in Chapter 5. Here a synthesis of the general, main conclusion of the thesis is provided in perspective to the general comprehension of PLs.

Multiple studies point towards that most PLs are fundamentally driven by moist-baroclinic instability (Bresch et al., 1997; Reed, 1979; Sardie and Warner, 1983; Terpstra et al., 2015). This can be conceptually described by the interaction of mobile upper-level with a low-level perturbation produced by thermal advection and diabatic heating (Bresch et al., 1997). The initial role of the upper and lower anomalies varies in different concepts. In the Diabatic Rossby Vortex concept applied by Terpstra et al. (2015) a low-level anomaly initiates the cyclogenesis and in concept by Montgomery and Farrell (1992) it is the upper-level anomaly. Still both are embedded in the moist-baroclinic framework.

A main conclusion of this thesis is a confirmation that the majority of PLs can be explained by baroclinic instability with support by condensational latent heat release. In Paper III, we show that PLs are arranged in multiple ways, which all express a baroclinic development. The PL in Paper II is mainly driven by baroclinic instability, where latent heat release provides an additional source of energy mainly active for the maintenance in the mature stage. Essential for the large growth rates observed during PL development is a low static stability. This is expressed by the effectiveness of the cold-air outbreak criteria derived in Paper I to distinguish between PLs and other cyclones.

Multiple other dynamical mechanisms have been suggested in the past. When reading literature about PLs, it may appear that other mechanisms are as important as baroclinic instability. For example the Encyclopedia of Atmospheric Sciences states: "In terms of dynamics, PLs are fundamentally baroclinic or convective in nature." (Renfrew, 2015). However, it is questionable whether other mechanisms lead to PL development in the absence of baroclinic instability. Therefore, it is relevant to clearly state that baroclinic instability appears to be the main concept to describe the intensification of the vast majority, possibly

even all PLs.

Hence, PLs appear to be a polar versions of typical mid-latitude, baroclinic
cyclones, as also formulated by Bresch et al. (1997). The smaller scale and
faster growth rate of PLs than mid-latitude cyclones arise from a considerably
smaller static stability, a lower tropopause and a somewhat higher Coriolis
parameter (Renfrew, 2015). However, the variety of PLs appears larger than of
mid-latitude cyclones. Typical synoptic, mid-latitude cyclones are embedded in
the planetary flow, which has a well defined meridional temperature gradient.
Hence, the mid-latitude cyclones are predominantly of forward-shear type
(e.g. Dacre et al., 2012). In contrast, PLs are secondary, mesoscale cyclones
embedded in a synoptic-scale flow, as already depicted by Dannevig (1954).
The synoptic-scale flow can take any orientation as compared to the thermal
field. Therefore a continuous spectrum across four vertical-shear environments
in which PLs develop is found in Paper III. PLs of different shear orientations
appear different at first, however, they all organise in a moist-baroclinic way, and
hence are fundamentally similar. Therefore, moist-baroclinicity is suggested as
the basic conceptual model for explaining PL cyclogenesis, whereas the large
variety of PLs is primarily expressed by their shear angle.

Bibliography

Copernicus Arctic Regional Reanalysis Service, `https://climate.copernicus.eu/copernicus-arctic-regional-reanalysis-service`, accessed: 2020-06-11.

Bjerknes, J. and Solberg, H.: Life cycle of cyclones and the polar front theory of atmospheric circulation, Geofyiske Publikasjoner, 3, 1922.

Blechschmidt, A.-M.: A 2-year climatology of polar low events over the Nordic Seas from satellite remote sensing, Geophysical Research Letters, 35, 2008.

Bond, N. A. and Shapiro, M.: Polar lows over the Gulf of Alaska in conditions of reverse shear, Monthly weather review, 119, 551–572, 1991.

Bracegirdle, T. J.: The role of convection in the intensification of polar lows, Ph.D. thesis, University of Reading, 2006.

Bracegirdle, T. J. and Gray, S. L.: An objective climatology of the dynamical forcing of polar lows in the Nordic seas, International Journal of Climatology, 28, 1903–1919, 2008.

Bracegirdle, T. J. and Kolstad, E. W.: Climatology and variability of Southern Hemisphere marine cold-air outbreaks, Tellus A, 62, 202–208, 2010.

Bresch, J. F., Reed, R. J., and Albright, M. D.: A polar-low development over the Bering Sea: Analysis, numerical simulation, and sensitivity experiments, Monthly weather review, 125, 3109–3130, 1997.

Browning, K.: Life cycle of a frontal cyclone, Meteorological Applications, 1, 233–235, 1994.

Businger, S.: The synoptic climatology of polar low outbreaks, Tellus A, 37, 419–432, 1985.

Businger, S.: The synoptic climatology of polar-low outbreaks over the Gulf of Alaska and the Bering Sea, Tellus A: Dynamic Meteorology and Oceanography, 39, 307–325, 1987.

Businger, S. and Reed, R. J.: Cyclogenesis in cold air masses, Weather and Forecasting, 4, 133–156, 1989.

Carleton, A. M. and Carpenter, D. A.: Satellite climatology of 'polar lows' and broadscale climatic associations for the Southern Hemisphere, International Journal of Climatology, 10, 219–246, 1990.

Charney, J. G. and Eliassen, A.: On the growth of the hurricane depression, Journal of the Atmospheric Sciences, 21, 68–75, 1964.

Chen, F. and von Storch, H.: Trends and variability of North Pacific polar lows, Advances in Meteorology, 2013, 2013.

Chen, F., Geyer, B., Zahn, M., and von Storch, H.: Toward a Multi-Decadal Climatology of North Pacific Polar Lows Employing Dynamical Downscaling., Terrestrial, Atmospheric & Oceanic Sciences, 23, 2012.

Claud, C., Heinemann, G., Raustein, E., and McMurdie, L.: Polar low le Cygne: satellite observations and numerical simulations, Quarterly Journal of the Royal Meteorological Society, 130, 1075–1102, 2004.

Dacre, H., Hawcroft, M., Stringer, M., and Hodges, K.: An extratropical cyclone atlas: A tool for illustrating cyclone structure and evolution characteristics, Bulletin of the American Meteorological Society, 93, 1497–1502, 2012.

Dannevig, P.: Meteorologi for flygere, Aschehoug, 1954.

Deveson, A., Browning, K., and Hewson, T.: A classification of FASTEX cyclones using a height-attributable quasi-geostrophic vertical-motion diagnostic, Quarterly Journal of the Royal Meteorological Society, 128, 93–117, 2002.

Duncan, C.: Baroclinic instability in a reversed shear-flow, Meteorological Magazine, 107, 17, 1978.

Eady, E. T.: Long waves and cyclone waves, Tellus, 1, 33–52, 1949.

Emanuel, K. A.: An air-sea interaction theory for tropical cyclones. Part I: Steady-state maintenance, Journal of the Atmospheric Sciences, 43, 585–605, 1986.

Emanuel, K. A. and Rotunno, R.: Polar lows as arctic hurricanes, Tellus A, 41, 1–17, 1989.

Feiccabrino, J., Graff, W., Lundberg, A., Sandström, N., and Gustafsson, D.: Meteorological knowledge useful for the improvement of snow rain separation in surface based models, Hydrology, 2, 266–288, 2015.

Forbes, G. S. and Lottes, W. D.: Classification of mesoscale vortices in polar airstreams and the influence of the large-scale environment on their evolutions, Tellus A: Dynamic Meteorology and Oceanography, 37, 132–155, 1985.

Føre, I., Kristjánsson, J. E., Kolstad, E. W., Bracegirdle, T. J., Saetra, Ø., and

Røsting, B.: A 'hurricane-like'polar low fuelled by sensible heat flux: high-resolution numerical simulations, Quarterly Journal of the Royal Meteorological Society, 138, 1308–1324, 2012.

Fu, G., Qin-Yu, L., and Zeng-Mao, W.: General features of polar lows over the Japan Sea and the Northwestern Pacific, Chinese Journal of Oceanology and Limnology, 17, 300–307, 1999.

Furevik, B. R., Schyberg, H., Noer, G., Tveter, F., and Röhrs, J.: ASAR and ASCAT in polar low situations, Journal of Atmospheric and Oceanic Technology, 32, 783–792, 2015.

Gray, S. L. and Dacre, H. F.: Classifying dynamical forcing mechanisms using a climatology of extratropical cyclones, Quarterly Journal of the Royal Meteorological Society, 132, 1119–1137, 2006.

Grønås, S. and Kvamstø, N. G.: Numerical simulations of the synoptic conditions and development of Arctic outbreak polar lows, Tellus A, 47, 797–814, 1995.

Harrold, T. and Browning, K.: The polar low as a baroclinic disturbance, Quarterly Journal of the Royal Meteorological Society, 95, 710–723, 1969.

Heinemann, G. and Claud, C.: Report of a workshop on" theoretical and observational studies of polar lows" of the European Geophysical Society Lows Working Group, Bulletin of the American Meteorological Society, 78, 2643, 1997.

Hewson, T., Craig, G., and Claud, C.: Evolution and mesoscale structure of a polar low outbreak, Quarterly Journal of the Royal Meteorological Society, 126, 1031–1063, 2000.

Hodges, K.: Feature tracking on the unit sphere, Monthly Weather Review, 123, 3458–3465, 1995.

Holton, J. R.: An introduction to dynamic meteorology, American Journal of Physics, 41, 752–754, 1973.

Hoskins, B. J., McIntyre, M. E., and Robertson, A. W.: On the use and significance of isentropic potential vorticity maps, Quarterly Journal of the Royal Meteorological Society, 111, 877–946, 1985.

Johnson, R.: A Half Century of Progress in Meteorology: A Tribute to Richard Reed, Springer, 2015.

Joly, A. and Thorpe, A. J.: Frontal instability generated by tropospheric potential vorticity anomalies, Quarterly Journal of the Royal Meteorological Society,

116, 525–560, 1990.

Jonassen, M. O., Chechin, D., Karpechko, A., Lüpkes, C., Spengler, T., Tepstra, A., Vihma, T., and Zhang, X.: Dynamical processes in the Arctic atmosphere, in: Physics and Chemistry of the Arctic Atmosphere, pp. 1–51, Springer, 2020.

Kolstad, E. W.: A global climatology of favourable conditions for polar lows, Quarterly Journal of the Royal Meteorological Society, 137, 1749–1761, 2011.

Kolstad, E. W. and Bracegirdle, T.: Sensitivity of an apparently hurricane-like polar low to sea-surface temperature, Quarterly Journal of the Royal Meteorological Society, 143, 966–973, 2017.

Kolstad, E. W., Bracegirdle, T. J., and Zahn, M.: Re-examining the roles of surface heat flux and latent heat release in a "hurricane-like" polar low over the Barents Sea, Journal of Geophysical Research: Atmospheres, 121, 7853–7867, 2016.

Krinitskiy, M., Verezemskaya, P., Grashchenkov, K., Tilinina, N., Gulev, S., and Lazzara, M.: Deep Convolutional Neural Networks Capabilities for Binary Classification of Polar Mesocyclones in Satellite Mosaics, Atmosphere, 9, 426, 2018.

Kristiansen, J., Sørland, S. L., Iversen, T., Bjørge, D., and KØLtzow, M. Ø.: High-resolution ensemble prediction of a polar low development, Tellus A: Dynamic Meteorology and Oceanography, 63, 585–604, 2011.

Kristjánsson, J. E., Barstad, I., Aspelien, T., Føre, I., Godøy, Ø., Hov, Ø., Irvine, E., Iversen, T., Kolstad, E., Nordeng, T., et al.: The Norwegian IPY–THORPEX: Polar lows and Arctic fronts during the 2008 Andøya campaign, Bulletin of the American Meteorological Society, 92, 1443–1466, 2011.

Laffineur, T., Claud, C., Chaboureau, J.-P., and Noer, G.: Polar lows over the Nordic Seas: Improved representation in ERA-Interim compared to ERA-40 and the impact on downscaled simulations, Monthly Weather Review, 142, 2271–2289, 2014.

Landgren, O. A., Batrak, Y., Haugen, J. E., Støylen, E., and Iversen, T.: Polar low variability and future projections for the Nordic and Barents Seas, Quarterly Journal of the Royal Meteorological Society, 145, 3116–3128, 2019.

Linders, T. and Saetra, Ø.: Can CAPE maintain polar lows?, Journal of the atmospheric sciences, 67, 2559–2571, 2010.

Lyall, I.: The polar low over Britain, Weather, 27, 378–390, 1972.

Markowski, P. and Richardson, Y.: Mesoscale meteorology in midlatitudes, vol. 2, John Wiley & Sons, 2011.

Michel, C., Terpstra, A., and Spengler, T.: Polar Mesoscale Cyclone Climatology for the Nordic Seas Based on ERA-Interim, Journal of Climate, 31, 2511–2532, 2018.

Mokhov, I., Akperov, M., Lagun, V., and Lutsenko, E.: Intense arctic mesocyclones, Izvestiya, Atmospheric and Oceanic Physics, 43, 259–265, 2007.

Montgomery, M. T. and Farrell, B. F.: Polar low dynamics, Journal of the atmospheric sciences, 49, 2484–2505, 1992.

Moore, R. W., Montgomery, M. T., and Davies, H.: Genesis criteria for diabatic Rossby vortices: A model study, Monthly weather review, 141, 252–263, 2013.

Müller, M., Batrak, Y., Kristiansen, J., Køltzow, M. A., Noer, G., and Korosov, A.: Characteristics of a Convective-Scale Weather Forecasting System for the European Arctic, Monthly Weather Review, 145, 4771–4787, 2017a.

Müller, M., Homleid, M., Ivarsson, K.-I., Køltzow, M. A., Lindskog, M., Midtbø, K. H., Andrae, U., Aspelien, T., Berggren, L., Bjørge, D., et al.: AROME-MetCoOp: a nordic convective-scale operational weather prediction model, Weather and Forecasting, 32, 609–627, 2017b.

Noer, G., Saetra, Ø., Lien, T., and Gusdal, Y.: A climatological study of polar lows in the Nordic Seas, Quarterly Journal of the Royal Meteorological Society, 137, 1762–1772, 2011.

Nordeng, T. E.: A model-based diagnostic study of the development and maintenance mechanism of two polar lows, Tellus A, 42, 92–108, 1990.

Nordeng, T. E. and Rasmussen, E. A.: A most beautiful polar low. A case study of a polar low development in the Bear Island region, Tellus A, 44, 1992.

Ooyama, K.: A dynamical model for the study of tropical cyclone development, Geofisica Internacional (Mexico), 4, 187–198, 1964.

Orimolade, A., Furevik, B., Noer, G., Gudmestad, O., and Samelson, R.: Waves in polar lows, Journal of Geophysical Research: Oceans, 121, 6470–6481, 2016.

Papritz, L. and Spengler, T.: A Lagrangian climatology of wintertime cold air outbreaks in the Irminger and Nordic Seas and their role in shaping air–sea heat fluxes, Journal of Climate, 30, 2717–2737, 2017.

Petterssen, S. and Smebye, S. J.: On the development of extratropical cyclones,

Quarterly Journal of the Royal Meteorological Society, 97, 457–482, 1971.

Plant, R., Craig, G. C., and Gray, S.: On a threefold classification of extratropical cyclogenesis, Quarterly Journal of the Royal Meteorological Society, 129, 2989–3012, 2003.

Rasmussen, E.: The polar low as an extratropical CISK disturbance, Quarterly Journal of the Royal Meteorological Society, 105, 531–549, 1979.

Rasmussen, E.: An investigation of a polar low with a spiral cloud structure, Journal of the Atmospheric Sciences, 38, 1785–1792, 1981.

Rasmussen, E.: A review of meso-scale disturbances in cold air masses, in: Mesoscale meteorology—theories, observations and models, pp. 247–283, Springer, 1983.

Rasmussen, E. and Lystad, M.: The Norwegian polar lows project: a summary of the international conference on polar lows, 20-23 May 1986, Oslo, Norway, Bulletin of the American Meteorological Society, 68, 801–816, 1987.

Rasmussen, E. A. and Turner, J.: Polar lows: Mesoscale Weather Systems in the Polar Regions, Cambridge University Press: Cambridge, UK, 2003.

Reed, R. J.: Cyclogenesis in polar air streams, Monthly Weather Review, 107, 38–52, 1979.

Renfrew, I.: SYNOPTIC METEOROLOGY | Polar Lows, in: Encyclopedia of Atmospheric Sciences (Second Edition), edited by North, G. R., Pyle, J., and Zhang, F., pp. 379 – 385, Academic Press, Oxford, 2015.

Rojo, M., Claud, C., Mallet, P.-E., Noer, G., Carleton, A. M., and Vicomte, M.: Polar low tracks over the Nordic Seas: a 14-winter climatic analysis, Tellus A, 67, 2015.

Rojo, M., Claud, C., Noer, G., and Carleton, A. M.: In situ measurements of surface winds, waves, and sea state in polar lows over the North Atlantic, Journal of Geophysical Research: Atmospheres, 124, 700–718, 2019.

Rojo, M., Noer, G., and Claud, C.: Polar Low tracks in the Norwegian Sea and the Barents Sea from 1999 until 2019, https://doi.org/10.1594/PANGAEA. 903058, supplement to: Rojo et al. (2019), 2019.

Sætra, O., Linders, T., and Debernard, J.: Can polar lows lead to a warming of the ocean surface?, Tellus A: Dynamic Meteorology and Oceanography, 60, 141–153, 2008.

Samuelsen, E. M., Løset, S., and Edvardsen, K.: Marine icing observed on KV Nordkapp during a cold air outbreak with a developing polar low in the Barents sea., Proceedings of the 23rd International Conference on Port and Ocean Engineering under Arctic Conditions; 2015 Jun 14–18; Trondheim, Norway, 2015.

Sardie, J. M. and Warner, T. T.: On the Mechanism for the, Development of Polar Lows, Journal of the Atmospheric Sciences, 40, 869–881, 1983.

Schär, C. and Davies, H. C.: An instability of mature cold fronts, Journal of the atmospheric sciences, 47, 929–950, 1990.

Schultz, D. M., Keyser, D., and Bosart, L. F.: The effect of large-scale flow on low-level frontal structure and evolution in midlatitude cyclones, Monthly weather review, 126, 1767–1791, 1998.

Semple, A. T.: A review and unification of conceptual models of cyclogenesis, Meteorological Applications, 10, 39–59, 2003.

Sergeev, D., Renfrew, I., Spengler, T., and Dorling, S.: Structure of a shear-line polar low, Quarterly Journal of the Royal Meteorological Society, 143, 12–26, 2017.

Shapiro, M., Wernli, H., Bao, J.-W., Methven, J., Zou, X., Doyle, J., Holt, T., Donall-Grell, E., and Neiman, P.: A planetary-scale to mesoscale perspective of the life cycles of extratropical cyclones: The bridge between theory and observations, in: The life cycles of extratropical cyclones, pp. 139–185, Springer, 1999.

Shapiro, M. A. and Keyser, D.: Fronts, jet streams and the tropopause, in: Extratropical cyclones, pp. 167–191, Springer, 1990.

Shapiro, M. A., Fedor, L. S., and Hampel, T.: Research aircraft measurements of a polar low over the Norwegian Sea, Tellus A, 39, 272–306, 1987.

Smirnova, J. E. and Golubkin, P. A.: Comparing polar lows in atmospheric reanalyses: Arctic System Reanalysis versus ERA-Interim, Monthly Weather Review, 2017.

Smirnova, J. E., Golubkin, P. A., Bobylev, L. P., Zabolotskikh, E. V., and Chapron, B.: Polar low climatology over the Nordic and Barents seas based on satellite passive microwave data, Geophysical Research Letters, 42, 5603–5609, 2015.

Stoll, P. J., Graversen, R. G., Noer, G., and Hodges, K.: An objective global climatology of polar lows based on reanalysis data, Quarterly Journal of the Royal Meteorological Society, 2018.

Terpstra, A.: Dynamical perspectives on the formation and intensification of polar lows, 2014.

Terpstra, A., Spengler, T., and Moore, R. W.: Idealised simulations of polar low development in an Arctic moist-baroclinic environment, Quarterly Journal of the Royal Meteorological Society, 141, 1987–1996, 2015.

Terpstra, A., Michel, C., and Spengler, T.: Forward and reverse shear environments during polar low genesis over the North East Atlantic, Monthly Weather Review, 144, 1341–1354, 2016.

Turner, J., Lachlan-Cope, T. A., and Thomas, J. P.: A comparison of Arctic and Antarctic mesoscale vortices, Journal of Geophysical Research: Atmospheres, 98, 13 019–13 034, 1993.

Vallis, G. K.: Atmospheric and oceanic fluid dynamics, Cambridge University Press, 2017.

Verezemskaya, P., Tilinina, N., Gulev, S., Renfrew, I. A., and Lazzara, M.: Southern Ocean mesocyclones and polar lows from manually tracked satellite mosaics, Geophysical Research Letters, 44, 7985–7993, 2017.

Wallace, J. M. and Hobbs, P. V.: Atmospheric science: an introductory survey, vol. 92, Elsevier, 2006.

Watanabe, S.-i. I. and Niino, H.: Genesis and development mechanisms of a polar mesocyclone over the Japan Sea, Monthly Weather Review, 142, 2248–2270, 2014.

Watanabe, S.-i. I., Niino, H., and Yanase, W.: Climatology of polar mesocyclones over the Sea of Japan using a new objective tracking method, Monthly Weather Review, 144, 2503–2515, 2016.

Wernli, H., Dirren, S., Liniger, M. A., and Zillig, M.: Dynamical aspects of the life cycle of the winter storm 'Lothar' (24–26 December 1999), Quarterly Journal of the Royal Meteorological Society, 128, 405–429, 2002.

Wernli, J. H.: Lagrangian perspective of extratropical cyclogenesis, Ph.D. thesis, ETH Zurich, 1995.

Wilhelmsen, K.: Climatological study of gale-producing polar lows near Norway, Tellus A, 37, 451–459, 1985.

Xu, K.-m. and Emanuel, K. A.: Is the tropical atmosphere conditionally unstable?, Monthly Weather Review, 117, 1471–1479, 1989.

Yanase, W. and Niino, H.: Dependence of polar low development on baro-
    clinicity and physical processes: An idealized high-resolution numerical
    experiment, Journal of the Atmospheric Sciences, 64, 3044–3067, 2007.

Yanase, W., Niino, H., Watanabe, S.-i. I., Hodges, K., Zahn, M., Spengler, T., and
    Gurvich, I. A.: Climatology of polar lows over the Sea of Japan using the
    JRA-55 reanalysis, Journal of Climate, 29, 419–437, 2016.

Yarnal, B. and Henderson, K. G.: A climatology of polar low cyclogenetic regions
    over the North Pacific Ocean, Journal of Climate, 2, 1476–1491, 1989.

Zahn, M. and von Storch, H.: A long-term climatology of North Atlantic polar
    lows, Geophysical Research Letters, 35, 2008a.

Zahn, M. and von Storch, H.: Tracking polar lows in CLM, Meteorologische
    Zeitschrift, 17, 445–453, 2008b.

Zahn, M. and von Storch, H.: Decreased frequency of North Atlantic polar lows
    associated with future climate warming, Nature, 467, 309–312, 2010.

Zappa, G., Shaffrey, L., and Hodges, K.: Can polar lows be objectively identi-
    fied and tracked in the ECMWF operational analysis and the ERA-Interim
    reanalysis?, Monthly Weather Review, 142, 2596–2608, 2014.

/8

Paper I:

An objective global climatology of polar lows based on reanalysis data.

P.J. Stoll, R.G. Graversen, G. Noer, K. Hodges,

Quarterly Journal of the
Royal Meteorological Society   RMetS

An objective global climatology of polar lows based on reanalysis data

Patrick J. Stoll[1] | Rune G. Graversen[1] | Gunnar Noer[2] | Kevin Hodges[3]

[1]Arctic University of Norway, Tromsø, Norway
[2]Norwegian Meteorological Institute, Tromsø, Norway
[3]Department of Meteorology, University of Reading, UK

Correspondence
Patrick J. Stoll, Department of Physics and Technology, Arctic University of Norway, 9037 Tromsø, Norway.
Email: patrick.stoll@uit.no

Here we present an objective global climatology of polar lows. In order to obtain objective detection criteria, the efficacy of several parameters for separating polar lows from other cyclones has been compared. The comparison and the climatology are based on the ERA-Interim reanalysis from 1979 to 2016 and the high-resolution Arctic System Reanalysis from 2000 to 2012. The most effective parameters in separating polar lows from other extratropical cyclones were found to be the difference between the sea-level pressure at the centre of the low and its surroundings, the difference in the potential temperature between the sea surface and the 500 hPa level, and the tropopause wind speed poleward of the system. Other parameters often used to identify polar lows, such as the 10 m wind speed and the temperature difference between the sea surface and the 700 hPa level, were found to be less effective. The climatologies reveal that polar lows occur in all marine basins at high latitudes, but with high occurrence density in the vicinity of the sea-ice edge and coastal zones. The regions showing the highest degree of polar-low activity are the Denmark Strait and the Nordic Seas, especially for the most intense polar lows. In the North Atlantic and Pacific, the main polar-low season ranges from November to March. In the Southern Hemisphere, polar lows are mainly detected between 50 and 65°S from April to October, indicating that this hemisphere compared to its northern counterpart has a two months longer, but less intense, polar-low season. No significant hemispheric long-term trends are observed, although some regions, such as the Denmark Strait and the Nordic Seas, experience significant downward and upward trends in polar lows, respectively, over the last decades. For intense polar lows, a significant declining trend has been observed for the Northern Hemisphere.

KEYWORDS

Arctic hurricane, detection/identification criteria, long-term trend, mesoscale cyclone, marine cold-air outbreak, polar low, tracking algorithm

1 | INTRODUCTION

Polar lows (PLs) are intense mesoscale cyclones occurring over the oceans at high latitudes. Due to their strong winds, they are a threat to fishing, maritime operations, and to life in coastal zones of the polar regions. They are often associated with high amounts of snowfall, so that at landfall they can cause increased avalanche danger and traffic chaos. Furthermore, PLs may lead to fast accumulation of ice on aircrafts and ships (Samuelsen *et al.*, 2015). In particular, PLs can be dangerous since they often develop rapidly, so hazardous conditions occur suddenly.

Probably the most cited definition of a polar low was formulated by Rasmussen and Turner (2003):

"A polar low is a small, but fairly intense maritime cyclone that forms poleward of the main baroclinic zone (the polar front or other major baroclinic zone). The horizontal scale of the polar low is approximately between 200 and 1000 km and has surface winds near or above gale force."
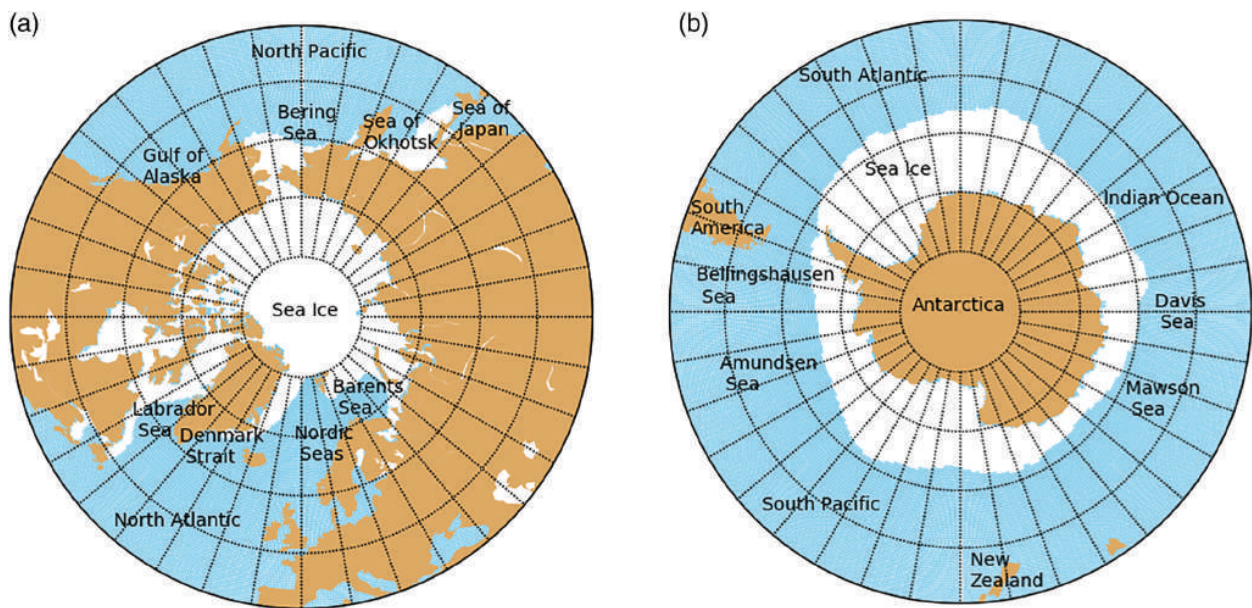
FIGURE 1 Map of the polar regions of the (a) Northern and (b) Southern Hemispheres. White denotes areas with an average sea ice cover above 20% during the main polar low season, being for (a) November–April and for (b) April–October, for the years 1979–2016 from ERA-I

Some PLs are referred to as Arctic hurricanes due to their clear central "eye" surrounded by deep convective cloud bands (e.g. Emanuel and Rotunno, 1989). However, in contrast to their tropical counterparts, the definition of a PL is vague, and the transition between a PL and the weaker form of a polar mesoscale cyclone is fluid. The scientific community does not agree on criteria for the classification of a cyclone as a PL. This study aims to develop a set of objective identification criteria for the detection of PLs in reanalyses by examining a broad range of previously suggested parameters and to investigate a global PL climatology based on these criteria.

Different PL climatologies have been developed by inspection of satellite images, starting from the late 1970s and early 1980s for the Nordic Seas (Figure 1; Wilhelmsen, 1985). For the same region, and for the years 2000–2012, Noer et al. (2011) developed the Sea Surface Temperature and Altimeter Synergy for Improved Forecasting of Polar Lows (STARS) database. Recently Smirnova et al. (2015) proposed a new PL climatology of this region based on satellite passive microwave data for 1995–2009 and referred to here as the Smirnova database. This database includes considerably more cases than does the STARS database. This reveals the key problem when investigating and comparing PL climatologies: they are generally based on different criteria and methodologies. Two meteorologists might come to different conclusions on whether a system is classified as a PL or not, based on a vague notion of what a PL is.

The Nordic Seas are probably the region most often investigated with respect to PL activity, but some other studies have developed climatologies based on satellite images for other regions, such as the Gulf of Alaska for 1975–1983 (Businger,

1987), the North Pacific for 1976–1984 (Yarnal and Henderson, 1989), the Sea of Japan and Northwest Pacific for the winter 1995/96 (Fu et al., 1999), and in the Southern Hemisphere (SH) for 1977–1983 (Carleton and Carpenter, 1990). However, the subjective nature of PL identification makes comparisons between different climatologies difficult.

Global atmospheric reanalyses can be used to overcome this subjective identification problem. Laffineur et al. (2014) showed that global reanalyses include some PLs, but only a small fraction of the STARS PLs were identified as sea-level pressure (SLP) minima in reanalysis datasets. By using the European Centre for Medium-Range Weather Forecasts (ECMWF) reanalysis (ERA-I; Dee et al., 2011), only 13 out of 29 STARS PLs for the period December 1999 to May 2002 were found, although this analysis showed a considerable improvement compared to using the older ERA-40 reanalysis, where only six systems were identified. Laffineur et al. (2014) also showed that by downscaling ERA-I with a 12 km resolution model, 22 of the 29 STARS PLs were detected. Kolstad (2011) attempted to circumvent the issue of the under-representation of PLs in coarse-resolution global reanalysis datasets by compiling a climatology of conditions favourable for PL development. Two criteria were considered, one for the low-level static stability and the other for the upper-level forcing, to obtain the duration over which both criteria are satisfied simultaneously in a given region.

Although global reanalyses show deficits in representing mesoscale systems, Zappa et al. (2014) and Bromwich et al. (2016) showed that it is generally possible to identify a considerable number of PLs in ERA-I. They show that 55% (19 out of 34) of the STARS PLs of the period 2008–2011 could be automatically detected by objective criteria based

on the 850 hPa vorticity, the 10 m wind speed and a measure for the static stability. Michel *et al.* (2018) detected about 60% of all STARS PLs in ERA-I with an automatic tracking algorithm based on the Laplacian of the SLP. In the higher-resolution ECMWF operational analysis, Zappa *et al.* (2014) detected 70% (23 out of 34) of the events. Investigations by Smirnova and Golubkin (2017) estimate that ERA-I represents 48% (22 out of 46) of the PLs during the cold seasons 2000/2001–2003/2004 from the STARS database, but only 26% (41 out of 158) from the Smirnova database. Further, they show that the recently developed high-resolution Arctic System Reanalysis (ASR) version 1 (Bromwich *et al.*, 2016) represents 89% (41 out of 46) of the PLs from the STARS dataset and 66% (104 out of 158) from the Smirnova dataset. The improvement is explained by the improved representation of mesoscale systems in this high-resolution reanalysis (Smirnova and Golubkin, 2017). The conclusion from this comparison of different reanalysis products indicates a considerable improvement of ASR over ERA-I in terms of PL representation; the ECMWF operational analysis used by Zappa *et al.* (2014) and ERA-I downscaled with a 12 km resolution mesoscale model as performed by Laffineur *et al.* (2014) are still missing a higher proportion of STARS PLs than ASR. Although the studies used different time periods and methodology, ASR could be regarded as one of the most reliable and consistent datasets for PL representation in the Arctic.

Yanase *et al.* (2016) has also explored PLs in reanalyses, developing an objective PL climatology for the Sea of Japan based on the Japanese reanalysis JRA-55, from 1979 to 2015, and based on the same approach as Zappa *et al.* (2014). Using a different approach, Zahn and von Storch (2008) created a PL climatology for the North Atlantic sector for the years 1948–2006 by downscaling the global NCEP/NCAR reanalysis with a regional climate model with a resolution of about 50 km. Chen and von Storch (2013) applied the same methodology for the North Pacific sector for the years 1948–2010.

Objective PL climatologies depend crucially on criteria applied in order to detect PLs from the whole variety of cyclonic features that are present in the data. Commonly, a threshold for the strength of the SLP minima, or for the vorticity extrema, are imposed, to ensure a certain intensity of the system. Some other additional criteria which are often applied are presented in the following.

Because PLs develop only over sea areas and dissipate rapidly after making landfall, presence over open water is commonly set as a criterion. The PL definition of Rasmussen and Turner (2003) includes a condition for near or above gale force surface winds, which is generally considered as the maximum of the near-surface wind speed in a certain radius around the PL centre. Often, a threshold of 15 m s^{-1} in a radius of 2.5° around the centre, is applied (e.g. Yanase *et al.*, 2016). However, global reanalyses such as ERA-I have been shown to under-represent maximum wind speeds associated with

PLs (e.g. Zappa *et al.*, 2014), making a strict application of the wind criteria problematic. In ASR the near-surface wind were observed to be more realistic (Smirnova and Golubkin, 2017).

Even though the definition of Rasmussen and Turner (2003) does not mention the occurrence of PLs in marine cold-air outbreaks (MCAOs), there seems to be a general agreement within the scientific community that an MCAO is required for a cyclone to be classified as a PL. This is partly taken into account in the widely applied static-stability criterion, given by a difference between the sea-surface temperature (SST) and the overlying atmospheric temperature, either at 500 hPa (Zahn and von Storch, 2008; Zappa *et al.*, 2014), at 700 hPa (Bracegirdle and Gray, 2008; Kolstad, 2011) or at 850 hPa (e.g. Papritz *et al.*, 2015). Commonly, a threshold of $SST - T_{500} > 43$ K is used, although Terpstra *et al.* (2016) and Smirnova and Golubkin (2017) argue that this threshold excludes a considerable number of PL cases. Bracegirdle and Gray (2008) investigated different temperature parameters, and found the difference between the wet-bulb potential temperature at 700 hPa and the SST to be the most effective of their considered parameters to separate PLs from other cyclones. To our knowledge the study of Bracegirdle and Gray (2008) was the first to objectively compare the effectiveness of different parameters for PL detection. As indicated above, the research community does not agree on a set of parameters and thresholds for objective PL detection, and a comprehensive comparison of criteria is still lacking. In addition, an important part of the PL definition formulated by Rasmussen and Turner (2003) – the formation poleward of the main baroclinic zone – to our knowledge has previously not been used as a criterion for PL detection.

This study aims to objectively compare the efficacy of different parameters for the identification of PLs and to apply the derived criteria to the development of an objective, global PL climatology. The paper is structured as follows. After presenting the methods and data in section 2, the results are divided into two parts. In section 3, the efficacy of the different parameters for PL identification from reanalysis datasets based on the subjective STARS dataset is compared, and in section 4 the obtained global PL climatologies based on the application of the most effective derived criteria are analysed. The paper ends with a discussion and conclusion in section 5.

2 | DATA AND METHODS

2.1 | Reanalysis datasets

The ERA-I is a time-consistent and homogeneous global, atmospheric reanalysis product at a T255 horizontal spectral resolution, which corresponds to a grid spacing of about 80 km, and with 60 vertical sigma levels of which 12 are below 850 hPa (Dee *et al.*, 2011). ERA-I is produced using four-dimensional variational data assimilation (4D-Var) with

TABLE 1 Parameters compared for their efficacy to identify PLs from the large set of cyclones

Parameter	Symbol	Type	r (° lat)
Intensity criteria			
T40–T100 filtered relative vorticity at 850 hPa	$\xi_{f,850}$	point	0
Maximum 10 m wind speed within radius r	U_{10m}	max	1, 2, 3
Sea level pressure	SLP $\star$	point	0
Difference of the mean SLP within radius r and the SLP of the cyclone centre	$\overline{SLP} - SLP$	mean – point	1, 2, 3, 5
Marine cold air outbreak criteria			
Mean temperature at 500 and 700 hPa within radius r	T_{500}, T_{700} $\star$	mean	1
Mean sea-surface temperature within radius r	SST $\star$	mean	1
Mean equivalent potential temperature at 700 and 850 hPa within radius r	$\theta_{e,700}, \theta_{e,850}$ $\star$	mean	1
Mean and maximum difference between the SST and T_{500}/T_{700} within radius r	$SST - T_{500/700}$	mean, max	1
Difference in the potential temperature at the sea surface and $p = 500/700/850$ hPa	$\theta_{SST} - \theta_p$	mean, max	1, 2, 3
Difference in the equivalent potential temperature at the same levels	$\theta_{e,SST} - \theta_{e,p}$	mean, max	1, 2, 3
MCAO criterion used by Kolstad and Bracegirdle (2008) with $p = 500/700$ hPa	$MCAO_{1,p}$	mean, max	1
MCAO criterion used by Bracegirdle and Kolstad (2010) at 700 hPa	$MCAO_2$	mean, max	1
Mean and minimum potential temperature of the tropopause within radius r	θ_{tr} $\star$	mean, min	1, 3, 5
Difference in the potential temperature of the sea surface and the tropopause	$\theta_{SST} - \theta_{tr}$	mean, max	1, 3
Maximum tropopause pressure within radius r	p_{tr}	max	3, 4, 5
Mean planetary boundary layer height within radius r	PBH	mean	1, 2, 3
Maximum gradient of the 850 hPa equivalent potential temperature within radius r	$\nabla\theta_{e,850}$ $\star$	max	3, 4, 5
Mean of the total column water within radius r	water $\star$	mean	1
Polar-front criteria			
Maximum tropopause wind speed poleward of the cyclone centre	$U_{tr,p}$ $\star$	max	Poleward
Maximum 500 hPa wind speed poleward of the cyclone centre	$U_{500,p}$ $\star$	max	Poleward
Maximum of the gradient of the $\theta_{e,850}$ poleward of the cyclone centre	$\nabla\theta_{e,850,p}$ $\star$	max	Poleward

Parameters are grouped after their type: the intensity criteria, the marine cold-air outbreak (MCAO) criteria, and the polar-front criteria. Generally the parameters are larger for PLs than for average cyclones, but parameters denoted with * are typically smaller. A radius (r) of 1° lat is equivalent to 110 km.

a 12 h window. The analysis data are provided and retrieved with a 6-hourly time step and a horizontal spacing of 0.5°. To obtain a reasonable time resolution for the tracking of mesoscale cyclones, the time resolution of the vorticity fields is increased to become 3-hourly by using the 3 h and 9 h forecasts starting at 0000 and 1200 UTC every day. Other fields are not extended to 3-hourly resolution, since not all (compare Table 1) can be retrieved from the ERA-I forecast. For this study full-year data for 1979–2016 for both hemispheres are used.

The recently released Arctic System Reanalysis (ASR) version 2 is a regional reanalysis of the greater Arctic (north of ∼40° N) based on the Weather Research and Forecasting Model (WRF) version 3.6.0 with adaptations relevant for polar regions (Bromwich *et al.*, 2017). It has a horizontal grid resolution of 15 km, has 71 vertical eta levels, of which 25 are below 850 hPa, and is produced from 2000 to 2012. ERA-I is used for the lateral boundary condition and for spectral nudging above 100 hPa. ASR applies 3D-Var with a 3 h window to include additional *in-situ* measurements, GPS radio occultation and radiance data from numerous satellite platforms, including 10 m ocean wind speed information. The output fields from ASR are provided 3-hourly on a polar stereographic grid.

2.2 | STARS polar low list

The STARS dataset version 2 provides a list of 185 PL tracks over the Nordic Seas from January 2001 to March 2011 (Noer *et al.*, 2011). The PLs are subjectively identified by forecasters at the Norwegian Meteorological Institute by inspection of satellite infrared data, scatterometer winds and the operational weather forecasting model HIRLAM 4 (Rojo *et al.*, 2015; Terpstra *et al.*, 2016), for evaluation of PL occurrence in different datasets (e.g. Laffineur *et al.*, 2014; Smirnova and Golubkin, 2017), and the evaluation of objective detection methods (e.g Zappa *et al.*, 2014).

2.3 | Tracking algorithm

Several methods are applied for the automatic detection and tracking of PLs in models and reanalyses. They are based on the detection of local minima in the SLP (e.g. Zahn and von Storch, 2008), of local maxima in the Laplacian of the SLP (e.g. Michel *et al.*, 2018), or on local extrema in the relative vorticity (e.g. Zappa *et al.*, 2014). To our knowledge no study has found particular evidence for the advantage of one method over another for the detection of PLs. For extratropical cyclones in general, Neu *et al.* (2013) found little evidence for differences in statistics between the detection algorithms based on vorticity and SLP.

In this study, the objective tracking algorithm (Hodges, 1995; 1999) is applied to the relative vorticity at 850 hPa. The algorithm detects cyclonic features from which PLs will be identified. Tracking routines for PLs often utilize a spatial bandpass filter to focus on the mesoscale nature of PLs, and hence to remove planetary-, synoptic- and micro-scale local features. In order to retain global wavenumbers 40–100 (equivalent to mesoscale features with scales of 200–1000 km), the spherical harmonic fast spectral transform (for ERA-I), and the discrete cosine transform filter (for ASR) is applied. The former method only applies to global data and can therefore not be used for ASR. A spectral taper is also utilized in order to suppress Gibbs oscillations (Hoskins and Sardeshmukh, 1984). However, synoptic-scale systems are not completely excluded by this filter. The same algorithm has recently been used for the detection of PLs by Zappa et al. (2014) in the Nordic Seas and by Yanase et al. (2016) in the Sea of Japan. However, in this study it is applied to reanalysis datasets covering the globe and the greater Arctic.

The algorithm tracks local maxima in the T40 - 100 filtered vorticity at 850 hPa ($\xi_{f,850}$) in the Northern Hemisphere (NH) above $2 \times 10^{-5} s^{-1}$ from the 3-hourly fields by first initializing tracks based on a nearest-neighbour method and then minimizing a cost function in order to produce the smoothest set of tracks. In the SH, cyclones are tracked in the same way for vorticity minima below $-2 \times 10^{-5} s^{-1}$. The identified tracks are henceforth referred to as TRACK cyclones. They include all kinds of cyclonic features, such as mesoscale lows, frontal zones, orographic shear zones and remnants of synoptic-scale lows that have not fully been removed by the filter. For systems with several small cyclonic cells, such as dual PLs, only the most intense system within a radius of 220 km is considered. A link to the dataset of the TRACK cyclones is given in the acknowledgements.

2.4 | Representation of STARS PLs in TRACK cyclones

In section 3, PLs will be compared to all tracked cyclones. For this, the TRACK cyclones that correspond to a PL from the STARS dataset are identified. A STARS PL has a corresponding TRACK cyclone if it matches within a radius of less than 250 km at more than half of its time steps with the same TRACK cyclone. A STARS-matched PL is defined as the part of the corresponding TRACK cyclone where the matching is satisfied. These STARS-matched PL are investigated in the following.

The distance of 250 km was chosen from consideration that the $\xi_{f,850}$ extrema in the reanalysis dataset can be displaced in comparison to the subjectively detected PL centre in the satellite images. Bracegirdle and Gray (2008) estimate that displacement errors between subjectively identified polar mesoscale cyclones and features from a model-based cyclone database in the order of 300 km can occur, but applied a radius of 200 km by arguing that the maximum displacement seldomly occurs. The sensitivity of the matching was examined

with a radius of 200 and 300 km and almost the same results were obtained as for a radius of 250 km.

It was also decided that a STARS PL has to match at more than half of its time steps with the same TRACK cyclone, in contrast to all time steps, since the initialization and decaying time can vary for cyclones between the datasets. Nevertheless, as presented below, most STARS PLs that match with one TRACK cyclone do so for all time steps.

2.4.1 | ERA-I

In ERA-I, only PLs from the STARS dataset with a duration of at least 6 h are considered, so that they are represented in at least one time step in the 6-hourly ERA-I analysis data. Note that only the vorticity is extended to 3-hourly time resolution, as described in section 2.1, to obtain a time resolution sufficient for tracking of mesoscale cyclones. As a result, 138 out of the 185 STARS PLs are of a duration of at least 6 h, out of which 109 are matched with a TRACK cyclone in ERA-I. Of these, 76 PLs matched for all the STARS time steps, and the remaining 33 for more than half of the STARS time steps. Three pairs out of the 109 STARS PLs are associated with the same TRACK cyclones within an overlapping time window. This is due to multiple PL events documented in the STARS dataset.[1] These three pairs are merged, such that 106 STARS-matched PLs remain for ERA-I.

Occurrence over open water is commonly required as criterion for PLs. For example, Zappa et al. (2014) excludes in their detection algorithm TRACK cyclones with an ocean fraction smaller than 75% within a radius of 1°. For the comparison in section 3, only the time steps where the TRACK cyclone is located over open water are included. Open water is here defined as within a circle of radius of 220 km (equivalent to 2° latitude) with more than 75% of the grid cells having water, as opposed to both land and sea ice. Of the 106 STARS-matched PLs, 94 have at least one time step occurring over open water. These 94 STARS-matched PLs are used for the development of the PL criteria in section 3. The 12 excluded cases occur close to the coast or the ice edge in the matching time steps, and are represented closer to the land or ice in ERA-I than in the STARS dataset. Analyses using different radii and fractions of water cover compared to the chosen values show negligibly small differences in PL exclusion.

2.4.2 | ASR

Since all the ASR data are obtained at 3-hourly time resolution, PLs from the STARS dataset with a duration of at least 3 h are considered. Out of the 185 STARS PLs, 163 are of a duration of at least 3 hr, and of these, 139 match with a TRACK cyclone in ASR. Out of these, 115 PLs match for all STARS time steps, and the remaining 24 for more than half

---

[1]STARS PL numbers: 7 and 8, 84 and 85 from the northern list, and 19 and 20 from the southern list.

of the STARS time steps. The same three pairs of PLs as in ERA-I are identified as multiple PLs and merged, so that 136 STARS-matched PLs remain from ASR. Out of these, 123 have at least one time step with occurrence over open water, and these remaining 123 STARS-matched PLs are used in section 3.

The comparison of the PL representation between the two reanalyses reveals that the matching is more often satisfied in ASR (139 out of 163 = 85%) than in ERA-I (109 out of 138 = 79%), that it is more often satisfied in all time steps in ASR (115 out of 139 = 83%) than in ERA-I (76 out of 109 = 70%), and that the STARS-matched PLs in ASR more often have at least one time step occurring over open water (123 out of 136 = 90%) than in ERA-I (94 out of 106 = 87%). This shows the improved PL representation in ASR in comparison to ERA-I, even though ASR includes 3–6 hourly events that are often less well represented in reanalysis than longer-lasting systems.

3 | DEVELOPMENT OF POLAR LOW IDENTIFICATION CRITERIA

In this section, different parameters are compared for the full set of extratropical cyclones and the subset of STARS-matched PLs, in order to find effective criteria to separate the PLs from other cyclones. These criteria will be applied in section 4 for the detection of PLs in the reanalysis datasets. Therefore, the distribution of different parameters of the STARS-matched PLs and the large set of all TRACK cyclones, where the latter represent the whole variety of cyclonic systems including PLs, are compared. In the following the prefix "TRACK" and "STARS-matched" are often skipped.

Table 1 summarizes the parameters considered in order to separate the PLs from other cyclones. Here, all parameters are compared that have been found in the literature relating to PL detection from model products. Some additional parameters that were considered as being possibly useful for PL detection, as for example the planetary boundary-layer height (PBH), the gradient in the equivalent potential temperature at 850 hPa ($\nabla\theta_{e,850}$), the total column water, and the maximum tropopause wind speed poleward of the system ($U_{tr,p}$). Although it is still possible that other parameters not considered here may show higher skills for PL detection, we believe that the parameter list of Table 1 covers the state-of-the-art knowledge of parameters important for PLs.

Note that the wind speed $U = \sqrt{u^2 + v^2}$ in this article always refers to the magnitude in the horizontal wind vector with zonal and meridional wind components u and v. The potential temperature of air with temperature T at pressure p is calculated by $\theta = T(p_0/p)^\kappa$ with reference pressure $p_0 = 1000$ hPa and the Poisson constant for dry air $\kappa = 2/7$. For the potential temperature at the sea surface (θ_{SST}), $p = SLP$ is used. The equivalent potential temperature is

calculated by $\theta_e = \theta \exp(L_v r_v/C_p T)$ with the water vapour mixing ration r_v, the latent heat of vaporization $L_v = 2.501 \times 10^6$ J kg^{-1} and the heat capacity of dry air $C_p = 1.006 \times 10^3$ J kg^{-1}.

Poleward properties are obtained from grid cells of higher latitude along the same longitude for ERA-I with spherical coordinates, and from grid cells of higher latitude within longitudes of $\pm 1°$ compared to the cyclone centre for ASR, having a stereographic projection.

For most parameters, the mean and maximum value within different radii are compared, to find the most effective set-up. The parameters are separated into three categories: intensity, MCAO and polar-front criteria, where the latter determines whether the system is poleward of the polar front. Each parameter is put into the category where it shows the highest dependence on the other parameters within the category. A high dependence of two parameters is found if, applied as criteria, they exclude the same cyclones. Therefore, some parameters that generally would not be considered as MCAO criteria are put into that category. Examples of these parameters are the maximum tropopause pressure (p_{tr}), as suggested by Kolstad (2011), and the potential temperature at the tropopause (θ_{tr}), as suggested by Terpstra *et al.* (2016). These are both applied to identify areas of upper-level forcing. Another example is $\nabla\theta_{e,850}$, which is investigated for the efficacy to exclude systems close to the main baroclinic zone. However, the classification of the parameters into different types of criteria is done for clarity reasons only and does not influence the result of obtaining the most skilful PL identification parameters.

Within the intensity criteria, the filtered vorticity ($\xi_{f,850}$) and the difference of the mean SLP within a circle of radius r and the SLP of the cyclone centre ($\overline{SLP} - SLP$), both consider intensity within the mesoscale. The $\xi_{f,850}$ is the spectrally filtered value, and $\overline{SLP} - SLP$ measures the depth of the low compared to the local surroundings.

The tropopause properties, such as the potential temperature (θ_{tr}), the pressure (p_{tr}) and the wind speed (U_{tr}), are taken from the 2 PVU level. For ASR, only a selection of the parameters from Table 1 were investigated, since some, such as the tropopause properties and the PBH, were not directly available, and others, such as the equivalent potential temperature, were not expected to lead to improved criteria, based on the investigations with ERA-I.

The comparison includes two MCAO criteria suggested from recent studies:

$$MCAO_{1,p} = \frac{\theta_{SST} - \theta_p}{SLP - p},$$

applied by Kolstad and Bracegirdle (2008) at the pressure level $p = 700$ hPa and here also at $p = 500$ hPa, and

$$MCAO_2 = \frac{L}{Z_{700}}(\ln\theta_{SST} - \ln\theta_{700})$$

from Bracegirdle and Kolstad (2010), with Z_{700} being the geopotential height at 700 hPa and $L = 7.5 \times 10^5$ m, a scaling
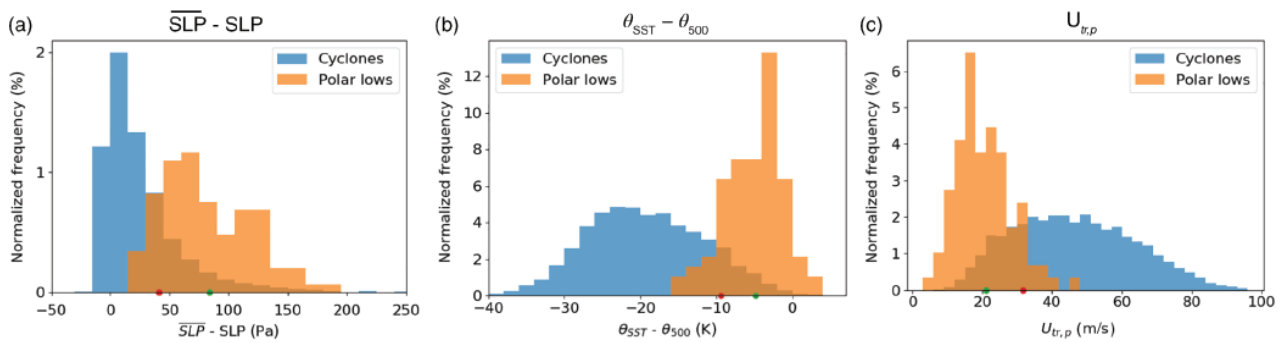
FIGURE 2 Normalized distributions of (a) the difference between the mean SLP within a radius of 110 km and the SLP of the cyclone centre, (b) the maximum potential temperature difference between the sea surface and the 500 hPa level within a radius of 110 km, and (c) the tropopause wind speed poleward of the system, for all types of cyclone (blue) and the STARS-matched PLs of ERA-I (orange). Also shown are the mean (green dot) and in (a, b) the 10th percentile (red dot) and in (c) the 90th percentile (red dot) of the PL distributions. These criteria were found to be the most effective for discrimination between PLs and other cyclones in ERA-I

height. The latter parameter is, together with p_{tr}, used by Kolstad (2011) to identify areas with favourable PL conditions.

In the following, the maximum value of these parameters during the lifetime of the STARS-matched PLs and all cyclones, including PLs, are computed, and their distributions are compared. The more the distributions differ from each other, the better the variable is for separating PLs from non-PL cyclones. Here, it is implicitly assumed that only a small number of the cyclones are PLs. Note that, for variables that are found to be smaller for PLs than for all cyclones, such as SLP, SST, $T_{500/700}$, $\theta_{e,700/850}$, θ_{tr}, $\nabla\theta_{e,850}$, water, $U_{tr,p}$ and $U_{500,p}$, the minimum values during the lifetime are compared.

3.1 | ERA-I

It was chosen to compare the identified 94 STARS-matched PLs to all TRACK cyclones occurring in potentially PL active regions and seasons, since the aim is to find effective parameters to distinguish between the two. For ERA-I, all cyclones over open water north of 30° N in the time ranges January–April and October–December 2003, representing the PL active season, are taken for the comparison. This sample includes 8301 cyclones. Because of the large number of cyclonic events, it is assumed that one year of cyclones is representative of the distribution of all cyclones in the same season during the whole dataset. This assumption is supported by a comparisons of the cyclone distributions for a few parameters for the whole timespan of the dataset from 1979 to 2016 and for the year of 2003 only (not shown). The year 2003 is an arbitrary choice.

3.1.1 | The measure for the efficacy of different parameters for PL detection

Examples of the comparison between the distributions of the parameters $\overline{\text{SLP}} - \text{SLP}$, $\theta_{SST} - \theta_{500}$ and $U_{tr,p}$ for PLs and cyclones are shown in Figure 2. For these three parameters, the distributions for all cyclones and PLs differ considerably, with PLs showing deeper lows, lower static stability,

and lower maximum tropopause wind poleward of the system.

A comparison of the efficacy of all included parameters to distinguish between PLs and cyclones is summarized in Table 2. For parameters where the mean and maximum values over different radii are tested, the table includes only the most effective set-up for distinguishing between PLs and cyclones. The efficacy of a parameter for PL detection is measured as follows. The 10th percentile of the parameters for the PLs (red dot in Figure 2 and fourth column in Table 2) are calculated. For parameters that are generally found to be lower for PLs than for cyclones, such as SLP, the 90th percentile is calculated instead. Then, the fraction of cyclones that remain below (above) this boundary is calculated and presented in column 5 of Table 2. If the 10th (90th) percentile threshold excludes a large proportion of the cyclones, the variable is regarded as being effective for distinguishing PLs from other cyclones.

It was chosen to take the nth percentile instead of the mean minus $m \times$ the standard deviation since the distribution may not be normal (e.g. Figure 2a). The 10th percentile was chosen from an intention to falsely exclude only a few PLs, but at the same time to disregard as many cyclones as possible. Application of the 5th percentile instead of the 10th leads to slightly weaker criteria, whereby too few cyclones are excluded. However, it leads to the same conclusions regarding the most effective parameters.

3.1.2 | Most effective criteria – the PL-IC

The three most effective parameters of each category are found to be

(a) intensity criteria: a difference of the mean SLP within a radius of 110 km and the SLP of the cyclone centre, $\overline{\text{SLP}} - \text{SLP} > 0.4$ hPa;

(b) MCAO criteria: a maximum difference of the potential temperature at the sea surface and 500 hPa within a radius of 110 km, $\theta_{SST} - \theta_{500} > -9.4$ K; and

TABLE 2 Comparison of the efficacy of different parameters for the selection of PLs from the large set of all cyclones in ERA-I

Parameter	Type	Radius (km)	10th percentile of polar lows	Excluded cyclones (%)	Excluded cyclones after two criteria (%)	Excluded cyclones after three criteria (%)
Intensity criteria						
$\xi_{f,850}$	point	0	$> 5.04 \times 10^{-5} \, \text{s}^{-1}$	71.4	58.3	22.4
U_{10m}	max	220	$> 13.3 \, \text{m s}^{-1}$	43.3	27.0	7.7
SLP $\star$	point	0	$< 1006.7 \, \text{hPa}$	49.1	16.1	2.7
$\overline{\text{SLP}} - \text{SLP}$ ††	mean–point	110	$> 0.4 \, \text{hPa}$	77.9	63.7	0
$\overline{\text{SLP}} - \text{SLP}$	mean–point	330	$> 2.3 \, \text{hPa}$	74.9	53.3	2.2
Marine cold air outbreak criteria						
T_{500} $\star$	mean	110	$< 241.4 \, \text{K}$	81.0	52.6	2.7
T_{700} $\star$	mean	110	$< 260.3 \, \text{K}$	72.5	45.9	2.7
$\theta_{e,700}$ $\star$	mean	110	$< 292.5 \, \text{K}$	68.3	44.6	1.1
$\theta_{e,850}$ $\star$	mean	110	$< 290.9 \, \text{K}$	61.6	41.5	3.3
SST $\star$	mean	110	$< 281.8 \, \text{K}$	51.4	19.1	10.4
$\text{SST} - T_{500}$	max	110	$> 41.4 \, \text{K}$	82.3	69.9	6.6
$\text{SST} - T_{700}$	max	110	$> 22.8 \, \text{K}$	73.6	67.7	13.7
$\theta_{\text{SST}} - \theta_{500}$ ††	max	110	$> -9.4 \, \text{K}$	88.5	72.3	0
$\theta_{\text{SST}} - \theta_{700}$	max	110	$> -4.1 \, \text{K}$	79.5	66.0	7.7
$\theta_{\text{SST}} - \theta_{850}$	mean	220	$> 0.0 \, \text{K}$	72.2	64.0	14.2
$\theta_{e,\text{SST}} - \theta_{e,500}$	mean	110	$> -3.1 \, \text{K}$	65.3	46.7	6.6
$\theta_{e,\text{SST}} - \theta_{e,700}$	max	110	$> 4.3 \, \text{K}$	63.0	62.5	19.7
$\theta_{e,\text{SST}} - \theta_{e,850}$	max	110	$> 5.8 \, \text{K}$	55.3	63.4	24.6
$\text{MCAO}_{1,500}$	max	110	$> -20.0 \times 10^{-5} \, \text{K Pa}^{-1}$	86.9	70.4	0
$\text{MCAO}_{1,700}$	max	110	$> -14.1 \times 10^{-5} \, \text{K Pa}^{-1}$	79.2	66.3	8.7
MCAO_2	max	110	> -4.0	79.0	66.5	8.7
θ_{tr} $\star$	mean	330	$< 300.7 \, \text{K}$	86.1	56.0	9.3
$\theta_{\text{SST}} - \theta_{tr}$	mean	330	$> -19.0 \, \text{K}$	88.5	65.3	11.5
p_{tr}	max	330	$> 382 \, \text{hPa}$	53.5	13.1	4.4
PBH	mean	330	$> 902 \, \text{m}$	53.7	45.9	16.4
$\nabla\theta_{e,850}$ $\star$	max	550	$< 7.9 \times 10^{-2} \, \text{K km}^{-1}$	37.3	29.1	23.5
water $\star$	mean	110	$< 10.8 \, \text{kg m}^{-2}$	60.8	46.5	3.8
Polar-front criteria						
$U_{tr,p}$ $\star$ ††	max	polew	$< 31.3 \, \text{m s}^{-1}$	77.6	31.7	0
$U_{500,p}$ $\star$	max	polew	$< 24.8 \, \text{m s}^{-1}$	69.6	34.0	9.8
$\nabla\theta_{e,850,p}$ $\star$	max	polew	$< 7.2 \times 10^{-2} \, \text{K km}^{-1}$	31.9	19.0	20.2

The first column expresses the used parameter. The second column inficates whether the value taken is at a point, or the maximum or mean value within the radius given by column 3. For $U_{tr,p}$, $U_{500,p}$ and $\nabla\theta_{e,850,p}$ the maximum value poleward of the system is considered. The fourth column presents the value of the 10th percentile of the PLs, meaning that 90% of the PLs have a higher value. Parameters which are lower for PLs than for all cyclones are marked with $\star$, and the 90th percentile is calculated instead. The fifth column shows the fraction of cyclones below the 10th (above the 90th) percentile. The higher the value, the more effective is the parameter. The most effective parameter of each category is denoted by †† in the first column. These are the PL identification criteria (PL-IC). The sixth column presents the fraction of cyclones that are excluded by the 10th (90th) percentile of PLs after the PL-IC from the other two categories have been applied. The seventh column gives the fraction of cyclones after application of the PL-IC, which are below (above) the 10th (90th) percentile. Values around 10% or below show that this criterion would not contribute to an improved separation of PLs from all cyclones.

(c) polar-front criteria: a maximum tropopause wind poleward of the system, $U_{tr,p} < 31.3 \, \text{m s}^{-1}$.

In the following, these three parameters are referred to as the PL identification criteria (PL-IC). Column 6 in Table 2 depicts the fraction of cyclones that have not been excluded by the PL-IC of the other two categories, and that are excluded by applying the 10th percentile threshold of the parameter. It is found that $\overline{\text{SLP}} - \text{SLP} > 0.4 \, \text{hPa}$ and $\theta_{\text{SST}} - \theta_{500} > -9.4 \, \text{K}$ exclude about 63.7 and 72.3% of the cyclones that have not been excluded by the other two PL-IC. $U_{tr,p} < 30.7 \, \text{m s}^{-1}$ excludes about 31.7% of the cyclones satisfying the other two

PL-IC. The high proportion of cyclones excluded by each of the PL-IC after application of the other two PL-IC shows that these criteria are non-redundant. However, each PL-IC excludes a lower fraction of cyclones after the other two PL-ICs have been applied (column 6) than if they would not have been applied (column 5), meaning that the PL-IC are not completely independent of each other.

These three PL-IC are found to be sufficient for PL detection. The last column of Table 2 shows the proportion of cyclones being excluded by the different parameters after application of all three PL-IC. Note that, for the PL-IC

themselves, no additional cyclones are excluded, since these parameters were already used for exclusion. The additional application of parameters with a value around or below 10% in the last column would exclude about as many PLs as cyclones, and those parameters therefore do not contribute to a better identification of PLs. This applies for most of the additional parameters. Some examples are presented in Figure 3 for the distributions of the 10 m wind speed (U_{10m}), the total column water, $\theta_{e,SST} - \theta_{e,700}$, $\xi_{f,850}$, $\nabla\theta_{e,850}$, and p_{tr}, which all show differences between PLs and cyclones (Figure 3a–c,g–i). After application of the PL-IC, the distributions of PLs and cyclones for most other parameters become similar (Figure 3d–f,j–l). For example, using $\theta_{e,SST} - \theta_{e,850}$ as an extra criterion to the PL-IC would exclude an additional 24.6% cyclones (value in last column of Table 2), but Figure 3f depicts that none of the additional excluded cyclones is far away from the exclusion threshold (red dot). This implies that $\theta_{e,SST} - \theta_{e,850}$ as an additional criterion would not exclude cyclones significantly different from the STARS-matched PLs. The same argument is valid for $\theta_{e,SST} - \theta_{e,700}$.

Two other parameters, $\xi_{f,850}$ and $\nabla\theta_{e,850}$, exclude more than 20% of the remaining cyclones as additional criteria (see value in last column of Table 2). The comparison of the distributions of these two parameters with and without application of the PL-IC (Figure 3g,h and j,k) shows that the distributions of the remaining cyclones and PLs are more similar, but not identical. These two parameters were tested as additional PL-IC and, in order not to exclude too many of the matched PLs, the exclusion threshold was lowered from the 10th to the 5th percentile. The characteristics of the resulting climatology with the three PL-IC (presented in section 4), and the resulting climatology with $\xi_{f,850}$ and $\nabla\theta_{e,850}$ as additional criteria are similar to each other (not shown). Since it is considered advantageous to use as few criteria as possible, it was decided to not include $\xi_{f,850}$ and $\nabla\theta_{e,850}$ as PL-IC.

The fact that, after application of the three PL-IC, the identified cyclones show a similar distribution in almost all parameters to the 94 STARS-matched PLs gives confidence that the criteria perform well for PL detection and that the identified cyclones can be considered to be PLs (e.g. Figure 3e,f). A time step of a cyclone that satisfies all three PL-IC in the following discussion will be called a PL point. Most of the STARS PLs (72 out of 94 = 76.6%) include at least one PL point, while only a small proportion of the large set of cyclones (183 out of 8301 = 2.2%) include a PL point.

3.1.3 | Intensity criteria

In the following, the different parameters within each type of criteria are compared, starting with the intensity criteria. Within the intensity criteria, the filtered vorticity $\xi_{f,850}$ (Figure 3g) and a measure for the local depth of the low $\overline{SLP} - SLP$ (Figure 2a) are both effective parameters, with the latter being slightly better than the former. The $\overline{SLP} - SLP$

was found to be the most effective, if the mean was calculated within a radius of 110 km, probably since this best considers the mesoscale nature of PLs. Most of the cyclones excluded by the $\xi_{f,850}$ criterion are also excluded by the application of the $\overline{SLP} - SLP$ criterion (comparison of Figure 3g,j and the values in the last two columns of Table 2 for $\xi_{f,850}$). However, the distribution of $\xi_{f,850}$ for the identified cyclones is shifted slightly towards weaker systems compared with the PL distribution (Figure 3j). This shows that the two intensity criteria are strongly related, but not completely redundant.

The maximum 10 m wind speed (U_{10m}) was found considerably less effective in identifying PLs than $\overline{SLP} - SLP$ and $\xi_{f,850}$. The U_{10m} distributions for PLs and cyclones are relatively similar to each other (Figure 3a). After application of the PL-IC, the distributions of the identified cyclones and STARS-matched PLs are similar (Figure 3d). The 10th percentile of U_{10m} for PLs is found to be 13.3 m s^{-1}, lower than the threshold of 15 m s^{-1}, which represents gale force, commonly used for detecting PLs from low-resolution reanalyses (e.g. Zappa et al., 2014; Yanase et al., 2016).

It was noticed by e.g. Zappa et al. (2014) that the wind criterion of 15 m s^{-1} excludes a relevant number of PLs (for their study region, 9 out of 34 = 26%), and for our analysis it was found to exclude a comparable fraction (26 out of 94 = 28%). This can partly be explained by an under-representation of strong winds associated with PLs in ERA-I, as for example found by Smirnova and Golubkin (2017). Another possible reason for the better performance of $\overline{SLP} - SLP$ and $\xi_{f,850}$ compared to U_{10m} is the occurrence of PLs in synoptic-scale MCAOs, which are often associated with large-scale wind speeds in the order of 10 m s^{-1}. The first two parameters are considering the occurrence of PLs within a synoptic-scale phenomenon, while the U_{10m} can almost be satisfied by the MCAO itself.

3.1.4 | Marine cold air outbreak criteria

In the following the parameters representing the MCAO criteria are compared. The $\theta_{SST} - \theta_{500}$ is the most effective parameter for PL identification within the MCAO criteria.

Static stability measures, such as SST $-T_p$, $\theta_{SST} - \theta_p$ and MCAO$_1$, perform in general better for discrimination between PLs and other cyclones when the upper-level value is obtained from the $p = 500$ hPa level instead of from the 700 or 850 hPa level. This result is not in contradiction with lower-level temperature differences, for instance $\theta_{SST} - \theta_{850}$ as applied by Papritz et al. (2015), being more effective for the identification of MCAOs, since the outbreaking air often stays below a strong inversion layer. However, for PLs, deep instability and convection are observed. The outbreaking air is warmed by the sea surface and lifted through the inversion layer until it reaches the upper troposphere (Noer et al., 2011).

MCAO$_1$ and MCAO$_2$, which are formulae dependent on the ratio of the θ differences to pressure/height difference
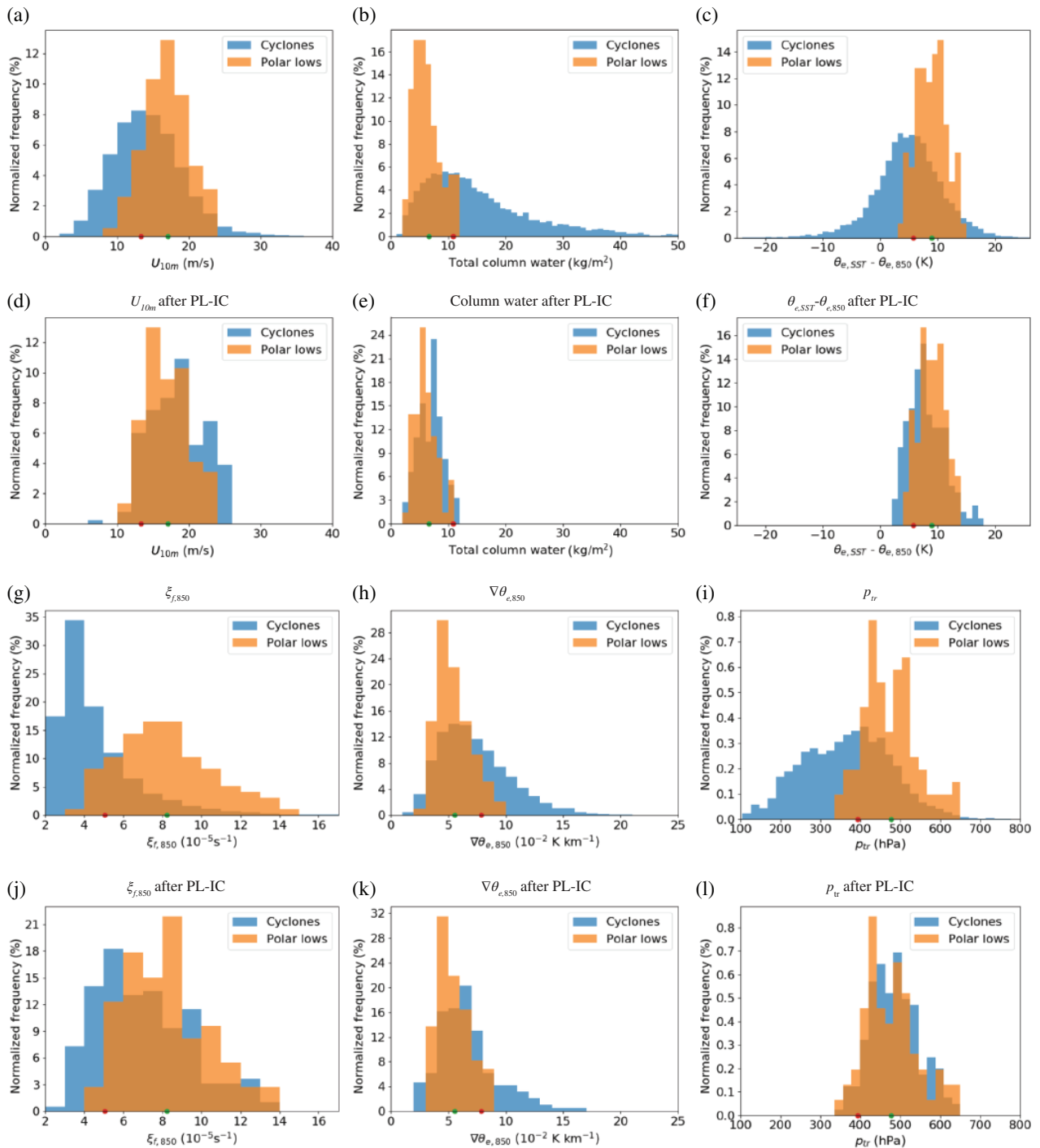
FIGURE 3 Normalized distribution of the (a) maximum 10 m wind speed within a radius of 220 km, (b) mean atmospheric column water within a radius of 110 km, (c) the maximum equivalent potential temperature difference between the sea surface and 700 hPa within a radius of 110 km, (g) the filtered vorticity at 850 hPa, (h) maximum gradient of the equivalent potential temperature within a radius of 550 km, and (i) maximum tropopause pressure within a radius of 330 km around the system for all types of cyclone (blue) and PLs (yellow) of ERA-I. For (a, c, g, i) the green and red dots mark the mean and the 10th percentile of the PLs. For (b, h) they mark the mean and the 90th percentile. (d)–(f) and (j)–(l) are as (a)–(c) and (g)–(i) respectively, but only for PLs and cyclones that satisfy the three PL-IC

between the levels, do not show improvement compared with the difference in θ between the same two levels.

Bracegirdle and Gray (2008) did a similar study to investigate the efficacy of some MCAO criteria for PL detection on the basis of a subjective dataset. They found that the difference in temperature between the 700 hPa level and the sea surface is more effective than between the 500 hPa level and the sea surface. However, they investigated a different

temperature parameter and used only a small subjective database of 58 polar mesoscale cyclones (both PLs and weaker systems) during the three months December 2001 to February 2002.

The comparison reveals that potential temperature performs better at identifying the PLs than the temperature difference between two levels. The former includes the sea-level pressure, making it a more accurate measure of the static stability. Since PLs often coincide with lower SLP than other cyclones (Table 2), static stability based on θ rather than on T becomes more distinct for PLs than cyclones. Interestingly, the equivalent potential temperature difference, an even more accurate parameter for the vertical stability since it includes moisture, is not as effective at identifying the PLs. This may be explained by the occurrence of PLs in cold environments where the atmosphere holds very little moisture and therefore considering θ_e instead of θ has only a small effect. In warmer environments, where midlatitude cyclones develop, and where the atmospheric water content is larger, moisture contributes more to the static instability.

The temperatures at 500 and 700 hPa also perform well at distinguishing between PLs and other cyclones, but slightly less well than the differences in potential temperature between the same level and the sea surface. The SST on its own does not seem to be a successful parameter for discrimination. This leads to the suggestion that the upper-level temperature is more important than the SST for identification of PLs.

A commonly used threshold for the static stability is $\mathrm{SST} - T_{500} > 43$ K evaluated as a mean within a 1° radius (e.g. Zappa *et al.*, 2014). Our methodology of calculating the 10th percentile from the PLs would suggest a weaker threshold of 39.7 K for this parameter (not shown). A threshold of 43 K for this parameter would exclude 30.9% of the PLs and therefore appears to be too high. Also, Terpstra *et al.* (2016) noted that this threshold excludes a considerable number of PLs in the North Atlantic.

Kolstad (2011) suggested the use of the maximum value of the tropopause pressure (p_{tr}) within a radius of 400 km to identify areas of upper-level forcing, a mechanism that Kolstad (2011) argued to be necessary for PL development. By taking the 5th percentile of a subjective PL dataset, Kolstad (2011) suggests a threshold of $p_{tr} > 470$ hPa for the detection of PL favourable regions. In our study, the threshold defined by the 10th percentile of the STARS-matched PLs is $p_{tr} > 382$ hPa, which is considerably weaker than the threshold from Kolstad (2011). In our study p_{tr} is found to be less effective than other parameters for PL identification (also Figure 3i).

Terpstra *et al.* (2016) use the potential temperature at the tropopause (θ_{tr}) to indicate upper-level potential vorticity anomalies. This parameter appears effective to distinguish between PLs and other cyclones, but slightly weaker than $\theta_{SST} - \theta_{500}$ and redundant after application of the three PL-IC (Table 2). The difference in the potential temperature of the sea surface and the tropopause ($\theta_{SST} - \theta_{tr}$) has the same

score for cyclone exclusion as $\theta_{SST} - \theta_{500}$, and the only reason for choosing the latter is that it excludes more cyclones after the other two PL-IC have been applied (column 6 in Figure 2).

Whether the PBH could be an effective discriminator was also tested, since PLs are often found to be connected to a higher PBH than other cyclones (column 5 in Table 2). The high PBH is believed to be induced by the convection associated with the PLs. Another parameter, the total column water, in general shows lower values for PLs than for cyclones (Figure 3b), which can be explained by the occurrence of PLs in cold environments. However, both parameters appear to be less effective than most of the other stability measures.

Most of the static-stability parameters perform best for PL detection when the maximum value within a rather small radius (here 110 km) is utilized. However, the difference from using a calculated mean over a larger radius is small (not shown).

3.1.5 | Polar-front criteria

Three parameters are compared as polar-front criteria. One parameter is the maximum gradient in the equivalent potential temperature at 850 hPa poleward of the system ($\nabla\theta_{e,850,p}$). Since the main baroclinic zone is generally in the vicinity of the jet stream by the thermal wind relation, the other two parameters are based on the maximum wind speed poleward of the cyclone in the tropopause ($U_{tr,p}$) and at the 500 hPa level ($U_{500,p}$). The comparison reveals that the inspection of the strength of the jet stream is more effective than the temperature gradient in the lower troposphere. The tropopause wind speed is more effective as a single parameter, while the 500 hPa wind speed performs slightly better after the other two PL-IC are applied.

3.2 | ASR

For ASR, 15018 cyclones for the months of January–April and October–December for 2003 in the ASR domain are considered for comparison to the 123 identified STARS-matched PLs. As discussed above, fewer parameters are included in the comparison for ASR than for ERA-I.

The same procedure as for ERA-I is applied to the parameters in ASR, to investigate their efficacy in distinguishing between PLs and other cyclones. Results are summarized in Table 3. The 10th percentile boundary from PLs for the same parameters in ERA-I and in ASR (column 4 in Tables 2 and 3) are in general reasonably close to each other. This gives confidence that the same criteria can be used independently of the underlying dataset. Differences in thresholds can be due to a larger number of the STARS PLs being recognized in ASR than in ERA-I (123 versus 94), and due to a difference in resolution of the two datasets. The precise comparison of the number of the excluded cyclones in ERA-I and ASR

TABLE 3 As Table 2, but for ASR

Parameter	Type	Radius (km)	10th percentile of polar lows	Excluded cyclones (%)	Excluded cyclones after two criteria (%)	Excluded cyclones after three criteria (%)
Intensity criteria						
$\xi_{f,850}$	point	0	$> 4.27 \times 10^{-5}\,\mathrm{s}^{-1}$	77.2	63.7	22.9
U_{10m}	max	220	$> 17.4\,\mathrm{m\,s}^{-1}$	66.8	53.1	19.8
$\overline{\mathrm{SLP}} - \mathrm{SLP}$	mean – point	110	$> 0.44\,\mathrm{hPa}$	73.7	60.9	10.7
$\overline{\mathrm{SLP}} - \mathrm{SLP}$ ††	mean – point	330	$> 2.38\,\mathrm{hPa}$	83.3	69.0	0
Marine cold air outbreak criteria						
T_{500} ★	mean	110	$< 240.4\,\mathrm{K}$	84.8	67.2	6.8
T_{700} ★	mean	110	$< 259.6\,\mathrm{K}$	75.1	59.4	7.6
SST ★	mean	110	$< 281.5\,\mathrm{K}$	54.9	24.5	15.6
$\mathrm{SST} - T_{500}$	max	110	$> 42.0\,\mathrm{K}$	85.3	77.4	4.5
$\mathrm{SST} - T_{700}$	max	110	$> 23.2\,\mathrm{K}$	74.1	73.4	10.7
$\theta_{\mathrm{SST}} - \theta_{500}$ ††	max	110	$> -8.5\,\mathrm{K}$	91.2	80.5	0
$\theta_{\mathrm{SST}} - \theta_{700}$	max	110	$> -3.4\,\mathrm{K}$	80.9	75.7	6.8
Polar-front criteria						
$U_{500,p}$ ★ ††	max	polew	$< 29.6\,\mathrm{m\,s}^{-1}$	61.6	26.4	0
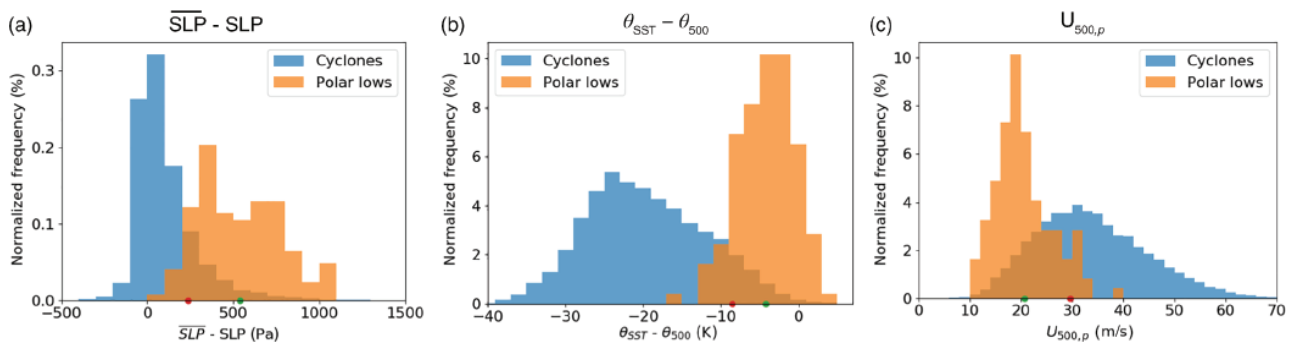
FIGURE 4 Normalized distribution of the (a) difference between the mean SLP in a radius of 330 km and the SLP of the cyclone centre, (b) mean potential temperature difference between the sea surface and 500 hPa within a radius of 110 km, and (c) the 500 hPa wind speed poleward of the system for all types of cyclones and PLs of ASR. The green and red dots are as in Figure 2. These criteria were found to be most effective for discrimination between PLs and cyclones in ASR

by the 10th percentile threshold of different parameters (column 5 in Tables 2 and 3) has to be done with caution due to at least two reasons. Firstly, ASR includes cyclones of shorter minimum duration than does ERA-I (3-hourly versus 6-hourly), and secondly, in ERA-I, all cyclones north of 30° N are included, while ASR includes cyclones in its whole domain, which is bounded by varying latitudes between 25 and 40° N (Figure 5c). Even though these limitations exist, the difference in the efficacy of the single parameters from ERA-I and ASR lies within 10%.

For ASR, the most effective of the investigated parameters for the exclusion of cyclones within each type of criteria are

(a) the difference in the mean SLP within a radius of 330 km and the SLP of the cyclone centre, $\overline{\mathrm{SLP}} - \mathrm{SLP} > 2.38\,\mathrm{hPa}$;
(b) the maximum difference of the potential temperature at the sea surface and 500 hPa within a radius of 110 km, $\theta_{\mathrm{SST}} - \theta_{500} > -8.5\,\mathrm{K}$; and
(c) the wind speed at 500 hPa poleward of the system, $U_{500,\mathrm{p}} < 29.6\,\mathrm{m\,s}^{-1}$.

The distributions of these three parameters for all types of cyclones and PLs are shown in Figure 4. They are the PL-IC for ASR and are only slightly different from those for ERA-I.

The $\overline{\mathrm{SLP}} - \mathrm{SLP}$ is more effective in ASR than in ERA-I if the mean is calculated over a larger radius. However, differences in the efficacy of different radii are relatively small. The threshold of $\overline{\mathrm{SLP}} - \mathrm{SLP}$ is dependent on the radius over which the mean is calculated, and the thresholds are in general close to each other for ASR and for ERA-I for the same radius.

The main difference within the compared parameters between ERA-I and ASR is observed for U_{10m}, where the 10th percentile threshold for PLs in ASR is much higher ($17.4\,\mathrm{m\,s}^{-1}$) than in ERA-I ($13.3\,\mathrm{m\,s}^{-1}$). This can be explained by a better representation of the near-surface wind in ASR connected to PLs, as observed by Smirnova and Golubkin (2017). But even though the U_{10m} is more realistically represented in ASR than in ERA-I, both $\overline{\mathrm{SLP}} - \mathrm{SLP}$ and $\xi_{f,850}$ are found to be more skilful for PL identification.
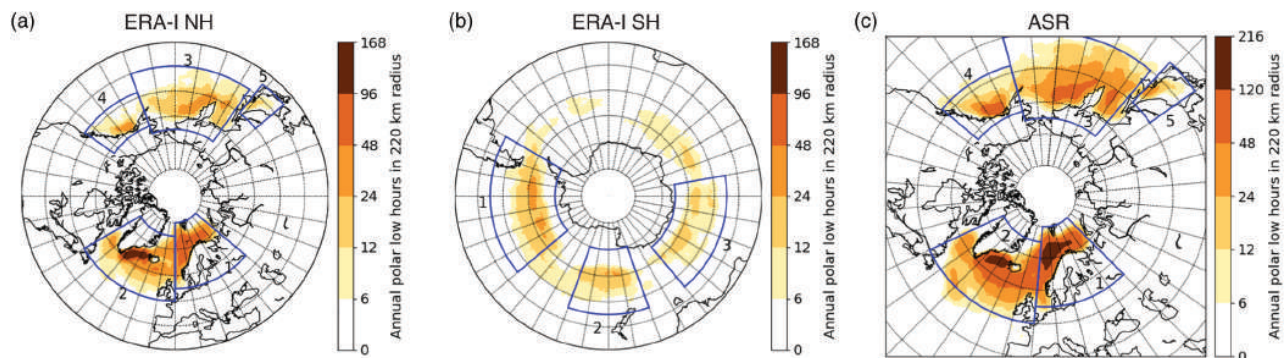
FIGURE 5 Spatial distribution of the average annual time of PL activity (h) within a radius of 220 km for (a) the NH from ERA-I, (b) the SH from ERA-I, and (c) the NH from ASR

The $\theta_{SST} - \theta_{500}$ parameter is for both datasets more effective than the other MCAO criteria. The threshold of $\theta_{SST} - \theta_{500} > -8.5$ K is stricter than in ERA-I, where -9.4 K is applied. This might be explained by the smoothing of local maxima due to the coarser resolution in ERA-I than in ASR. For other considered parameters within the MCAO criteria, the same findings as for ERA-I are obtained. The efficacy of these compared parameters for PL identification do not seem to depend much on the resolution of the dataset. This may be due to the large-scale character of MCAOs.

In ASR, $U_{500,p}$ is the only parameter included as a polar-front criterion. The fraction of excluded PLs by $U_{500,p}$ as an additional criterion suggests that this parameter improves the PL identification. Since in ERA-I the efficacy of $U_{tr,p}$ and $U_{500,p}$ are similar to each other, ASR is nudged by ERA-I at the upper boundary, and tropopause parameters for ASR are not directly accessible, it was considered sufficient to use $U_{500,p}$ for ASR.

As for ERA-I, the other parameters considered show distributions that are comparable for the STARS-matched PLs and the identified cyclones after the application of the three PL-IC (distributions are not shown, but see last column of Table 3), giving confidence that the PL-IC for ASR are sufficient for PL identification, and that the identified cyclones can be considered PLs. Most of the STARS-matched PLs (93 out of $123 = 75.6\%$) include at least one time step where the three PL-IC are satisfied, called PL points, while only a small proportion of the cyclones include a PL point (297 out of 15018 $= 2.0\%$). Thus, in ASR, a slightly smaller proportion of subjective PLs are excluded by the PL-IC, and a slightly lower proportion of the cyclones are classified as PLs as compared to ERA-I. This is an indication that the identified cyclones in ASR include fewer falsely excluded and falsely included PLs than in ERA-I.

4 | ANALYSIS OF THE CLIMATOLOGIES

In order to detect PLs, the PL-IC derived in section 3 are applied to all cyclones which occur over open water poleward

of 30° for ERA-I and in the complete domain of ASR for the whole time span of the two reanalyses. To the knowledge of the authors, no PL has been reported between 30° S and 30° N, and systems occurring within these latitudes would not be classified as being PLs, since the polar front is far poleward over open sea.

From the identified PLs, two climatologies are derived. One for the timespan 1979–2016 for ERA-I and one for 2000–2012 for ASR. In the following, these two climatologies are first briefly inspected and then analysed further in terms of their spatial and temporal distributions.

4.1 | Inspection of the climatologies

One way to test the climatologies is to investigate for "false hits." Inspection of some randomly picked PL cases from the climatologies reveals that most of these can be classified as being PLs or the weaker form of polar mesoscale cyclones. Since the transition between being a PL and a mesoscale cyclone is fluid, a decision for a system being a PL is subjective. The counting of "true hits" and "false hits" strongly depends on a subjective decision on whether a system is regarded as a PL or not, hence this type of analysis was not performed. However, only a small fraction of the cases in the climatologies are clear-cut PLs. The climatology also includes some cases of occluded synoptic-scale systems with convective signatures. These could possibly be excluded by applying a constraint on the size of the system. This is challenging for PLs, since automatic size calculation of cyclones is often based on closed isobars (e.g. Rudeva and Gulev, 2007). PLs, occurring in a pressure gradient that causes the MCAO, are not always local SLP minima, especially not in low-resolution reanalysis datasets such as ERA-I (Laffineur *et al.*, 2014).

The number of PLs in the derived climatologies can be compared to the STARS and Smirnova datasets. The STARS dataset includes 185 PLs in the Nordic Seas for the years 2000–2011. The climatologies include 911 PLs for ERA-I and 1321 PLs for ASR for the same time period and approximately the same area as STARS. A possible explanation for

this difference is that the STARS dataset includes only clear PL cases, while the climatologies include a large number of cases whose status as PL would be debated among meteorologists. It is noted that other PL climatologies, such as the Smirnova database, find a considerably higher PL density. The Smirnova dataset includes 637 PLs for the time period of 1995/1996–2008/2009 in the Nordic Seas. The derived climatology for ERA-I shows 709 cases for the same time period and approximately the same area as the Smirnova dataset. This reveals that other studies have found a similar PL density as those derived here.

An objective study of the "false misses" is impossible, since no accepted global PL dataset exists. However, a comparison with some existing PL climatologies is performed. Of the vaguely described 27 PLs in the period 1979–1982 from Wilhelmsen (1985), 22 PLs are identified in the climatology based on ERA-I. A one-to-one comparison cannot be performed due to the inaccurate description of the PL tracks in Wilhelmsen (1985). Of the list presented in Yanase *et al.* (2016), eight of the 19 PLs can be recognized in ERA-I and, of the eight PLs in the years 2000–2012, four can be found in ASR and two in ERA-I. This reveals that the derived climatologies do not include all cases of other subjective PL datasets, but they recognize a relevant proportion of them. It also should be noted that observational studies are subjective in nature.

4.2 | Spatial distribution of PLs

Another factor giving confidence in the climatologies is that the spatial and the temporal distributions are comparable to existing climatologies, as will be discussed in the following. The spatial annual-averaged distribution of PL duration is presented in Figure 5 for (a) the NH and (b) SH from ERA-I, and (c) from ASR. The PL duration is calculated by multiplying the number of detected PL points by application of the PL-IC derived in section 3 by the time resolution of the dataset, which is 6 h for ERA-I and 3 h for ASR. This presentation of the average annual PL duration per area was chosen rather than the number of PLs, since the PL duration is considered to be a better measure of the PL activity in a region. A long-lasting PL contributes more to the PL activity than a short-lasting one, which is taken into account in the PL duration.

The spatial distribution of the climatologies in the NH between the two reanalyses shows similar patterns. They are in good agreement with that presented for the North Atlantic by Zahn and von Storch (2008), and for the North Pacific by Chen and von Storch (2013), even though different methodologies are used.

High PL density is often found in areas where Kolstad (2011) and Fletcher *et al.* (2016) detected a high frequency of MCAOs, e.g. in the Barents Seas and the Sea of Okhotsk, although this is not always the case. For example, these two studies found a relatively low frequency of MCAOs in the

Denmark Strait, which is here found as one of the major PL regions. Kolstad (2011) identified the Labrador Sea as the region with the most favourable PL conditions in the North Atlantic (section 1), while the Norwegian Sea south of 70° N shows rather unfavourable PL conditions, both in disagreement with our results. As opposed to the Kolstad (2011) approach, Zahn and von Storch (2008), Zappa *et al.* (2014), Yanase *et al.* (2016) and this study identify individual cyclones and apply criteria to determine whether they can be regarded as PLs.

Some regions of intense PL activity can be recognized. In ERA-I, the Denmark Strait, between the southern tip of Greenland and Iceland, is identified as the region with the highest, and the Nordic Seas as the region with the second highest PL density of both hemispheres. This finding agrees with Zahn and von Storch (2008), who found that the Denmark Strait had the highest activity within the North Atlantic. In ASR, the Nordic Seas are recognized as having slightly higher PL activity than the Denmark Strait. This indicates that these two areas have the highest PL activity of the entire globe. Within the Nordic Seas, the highest PL density is identified in an area around 72° N, 15° E, also known as "Tromsø flake," which is in agreement with Noer *et al.* (2011).

The results suggest that more PLs occur in the North Atlantic (64%) than in the North Pacific (36%). On the Pacific side, the Gulf of Alaska, the Bering Sea, the Sea of Okhotsk and the Sea of Japan are found to be PL active regions. PLs in the North Pacific occur as far south as 40° N, while in the North Atlantic PLs are rarely identified south of 50° N. In general, increased PL density is observed close to land masses or sea-ice edges and the density decreases in the direction of open sea. Yarnal and Henderson (1989) presented comparable maps of observed comma-cloud and spiral-form systems for the North Pacific with comma-cloud systems being observed as far south as 40° N, and with the occurrence of spiral systems often present in the vicinity of land masses. The maps generally show high agreement with the density maps of the derived climatologies. Yanase *et al.* (2016) objectively identified PLs in the Sea of Japan and presented a spatial distribution of the PLs at their maximum intensity, similar to the results derived here from ERA-I and ASR. Kolstad (2011) identified the same area in the Sea of Japan and the Sea of Okhotsk as favourable for PL development in the North Pacific, but did not recognize the areas to the east of this as being PL active.

In the SH, most PL activity is found between 50 and 65° S, with three areas showing increased activity: (a) the Bellingshausen and Amundsen Sea, (b) the sea south of New Zealand and (c) the Mawson and Davis Sea southwest of Australia. (a) and (b) are the regions where Kolstad (2011) found PL favourable conditions in the SH, but the third region was not identified in that study. Carleton and Carpenter (1990) identified more PLs at lower latitudes up to 30° S, although their identification of PLs is based on satellite imagery and does not include criteria on intensity or the occurrence in an MCAO.
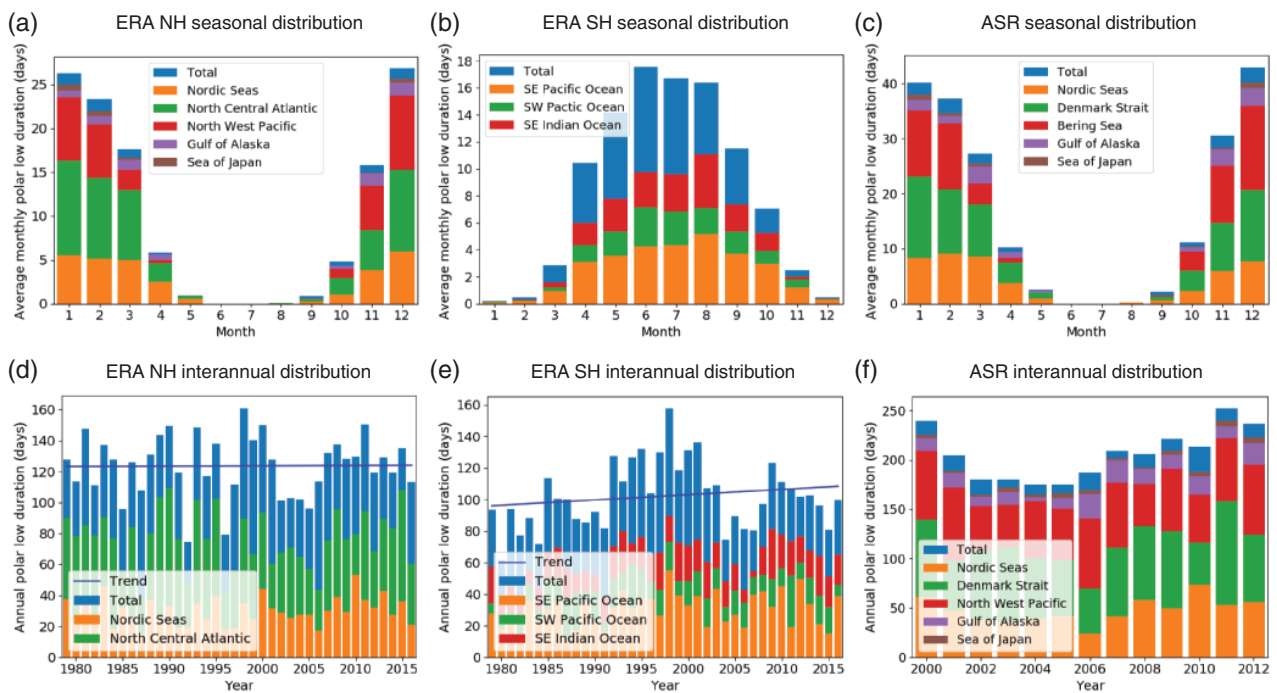
FIGURE 6 Average monthly time of PL activity in the (a) NH and (b) SH from ERA-I and (c) from ASR for its whole domain. The average is normalized to months with a duration of 30 days. Note that two PLs occurring simultaneously count twice to the PL duration. Colours denote the contribution of specific regions marked by boxes in Figure 5. (d)–(f) the annual PL duration of each year for the same regions and datasets. Note different scales

The density of PL occurrence is in general lower than in active regions in the NH. Nevertheless, due to a larger ocean area, the SH has only 17% less PL activity than the NH in ERA-I.

4.3 | Temporal distribution of PLs

The average seasonal distributions of PL duration in ERA-I for the NH and SH and ASR are presented in Figure 6a–c. PLs occur in the extended winter seasons of both hemispheres. In the NH, this is five months from November to March, with the maximum activity in January, some cases in April and October, and a few cases in May and September.

The hemispheric seasonal PL distribution cannot be compared with the literature since, to our knowledge, no global PL climatology has yet been developed. However, seasonal distributions for different regions can be compared. This comparison has to be considered with caution, since the domains are often chosen differently. Also, other studies often count the PLs, whereas here the duration of PL activity is presented.

For the Nordic Sea (defined by box 1 in Figure 5a), our climatology reveals a similarly high PL activity from November to March, with some PLs occurring in October and April, and less activity of PLs in September and May. Noer *et al.* (2011) and Smirnova *et al.* (2016) present seasonal PL distributions for the Nordic Seas that in general show similar PL activity for the same time period as found here. However, they also find local extrema in PL frequency in the main season, such as a distinct and strong maximum in March. In agreement with

our results, Zahn and von Storch (2008) observe the highest PL activity for the North Atlantic in December and January, without local maxima in other months. Months of extrema in PL frequency in climatologies of short duration are possibly explained by the high interannual variability of PL occurrence (Figure 5d).

The seasonal distribution of PLs in the North Pacific is in general in good agreement with the distribution presented by Chen and von Storch (2013). The PL season in the Northwest Pacific and the North Atlantic are comparable, except for considerably fewer PL occurrences in the former region in March. In the Sea of Japan, PLs are mainly detected in December to February with few cases in autumn and spring, in good agreement with Yanase *et al.* (2016).

In the SH, the PL season is seven months long, ranging from April to October with some cases in March and November, and a few cases even in the SH summer (December to February). Since none of the months in the SH shows as high PL frequency as in the NH, it can be concluded that the PL season in the SH is longer and less intense than in the NH.

The time series of the annual PL duration in ERA-I and ASR are presented in Figure 6d–f. The annual PL frequency for ASR and ERA-I for the NH show same years of high and low PL activity. In general, PL activity shows a very high interannual variability, as noted by e.g. Zahn and von Storch (2008), with the active years of each hemisphere having more than twice as many PL hours as the calm years.

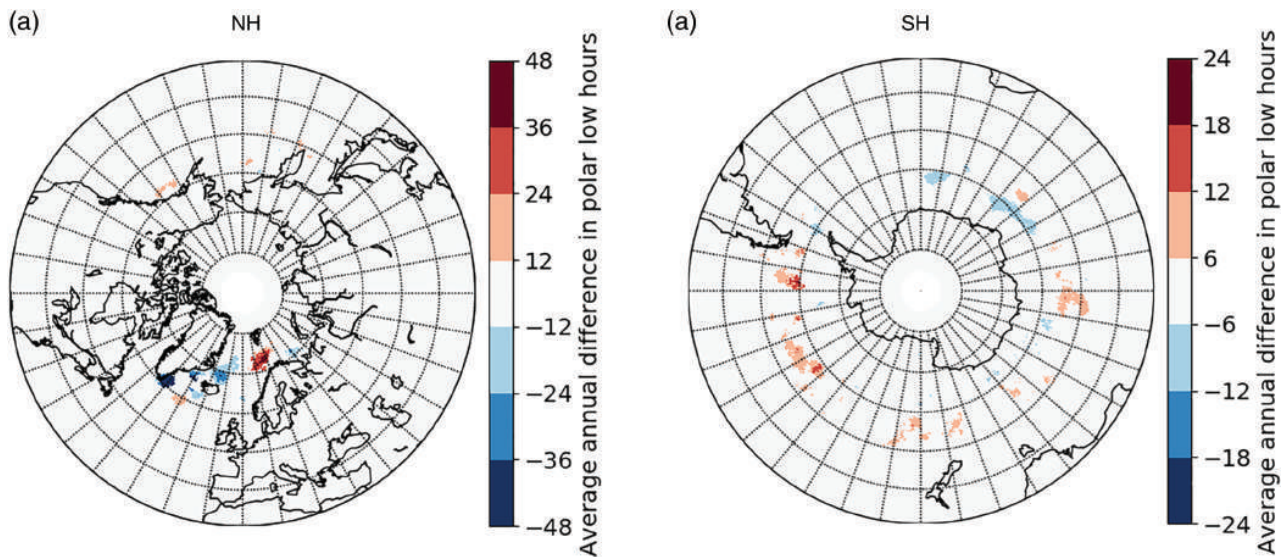The trend in PL activity is negligible for the NH from ERA-I (0.42 PL hours per year with *p*-value of 0.95 by a two

FIGURE 7 Difference of the average annual time of polar low activity between 2001–2016 and 1979–1994 in a 220 km radius for ERA-I. Red (blue) shading indicates areas with higher (lower) PL occurrence in the last 15 years. Only significant change with a *p*-value smaller than 5% by a two-sided *t*-test is displayed

sided *t*-test). ASR is regarded as being too short for an investigation of a trend. For the SH, ERA-I shows an increasing trend of 7.8 PL hours per year, which is not significant, with a *p*-value of 0.28. More interesting for the SH is the decade from 1992 to 2001 which shows strongly increased PL activity. The seven most PL active years between 1979 and 2016 fall into this 10-year period.

In Figure 7 the difference in PL occurrence in ERA-I in the last versus the first 15 years is compared, to identify regions of significant increase and decrease of PL activity. The strongest decline in PL activity is observed east of Greenland's southern tip, and the highest increase on the Tromsø flake south of Svalbard, both with a change of up to 2 days of PL occurrence per year. In the Southern Ocean, increased PL activity is observed on the northern side of PL active areas, while partly reduced activity is recognized closer to Antarctica, leading to the suggestion that PL activity is propagating away from the continent. However, note that *p*-values smaller than 5% by the *t*-test can still be obtained by coincidence.

4.4 | Intense PLs

A climatology of the most intense PLs was also derived. In order to detect these systems, the 10th percentile threshold used in section 3 is replaced by a threshold of the 50th percentile for both the intensity and the MCAO criteria, while the same polar-front criterion is used as before. Hereby the most intense PLs that develop in strong MCAOs are detected. For ERA-I (and ASR) this results in the detection criteria of $\overline{\text{SLP}} - \text{SLP} > 0.71\,\text{hPa}$ (5.07 hPa) and $\theta_{\text{SST}} - \theta_{500} > -4.4\,\text{K}$ ($-4.0\,\text{K}$). The set of these thresholds excludes 73 of 94 (89 of 123) STARS PLs and retains only 21 of 8301 (21 of 15018) cyclones in the NH of the year 2003 for ERA-I (and ASR). Hence only about 20% of the earlier

identified PLs, now referred to as "all PLs," of the NH, are detected with these stricter thresholds.

The spatial distributions of intense PLs, presented in Figure 8a–c, resemble the distributions of all PLs depicted in Figure 5, with the difference that regions of high activity, being the Nordic Seas and the Denmark Strait, stand out more clearly. About 4 times more intense PLs develop in the NH as compared to the SH. In the NH most (about 75%) of the intense PLs occur in the North Atlantic.

The seasonal distributions of intense PLs, shown in Figure 8d–f, are in general more restricted to the winter months December–March in the NH and June–August in the SH. The time series of the annual duration of intense PLs in the NH, depicted in Figure 8g, has a significant decaying trend of -1.1 PL hours per year ($p = 0.034$), which is equivalent to a reduction of approximately 10% between 1979 and 2016. This decaying trend is twice as strong in the central North Atlantic as in the Nordic Seas.

A possible explanation for the decrease in intense PLs is a decline in the strength of MCAOs. From climate model projections, Kolstad and Bracegirdle (2008) found a weakening of MCAOs for the end of the 21st century compared with the end of the 20th century. However, to the knowledge of the authors, no study has observed a decay in the strength of MCAOs over the past decades.

5 | DISCUSSION AND CONCLUSION

For the first time, an objective global PL climatology has been developed. The climatology is based on ERA-I and ranges from 1979 to 2016. A second climatology is derived from the higher-resolution ASR reanalysis for the greater Arctic from 2000 to 2012. Both climatologies are developed by applying constraints on cyclone tracks identified by a tracking
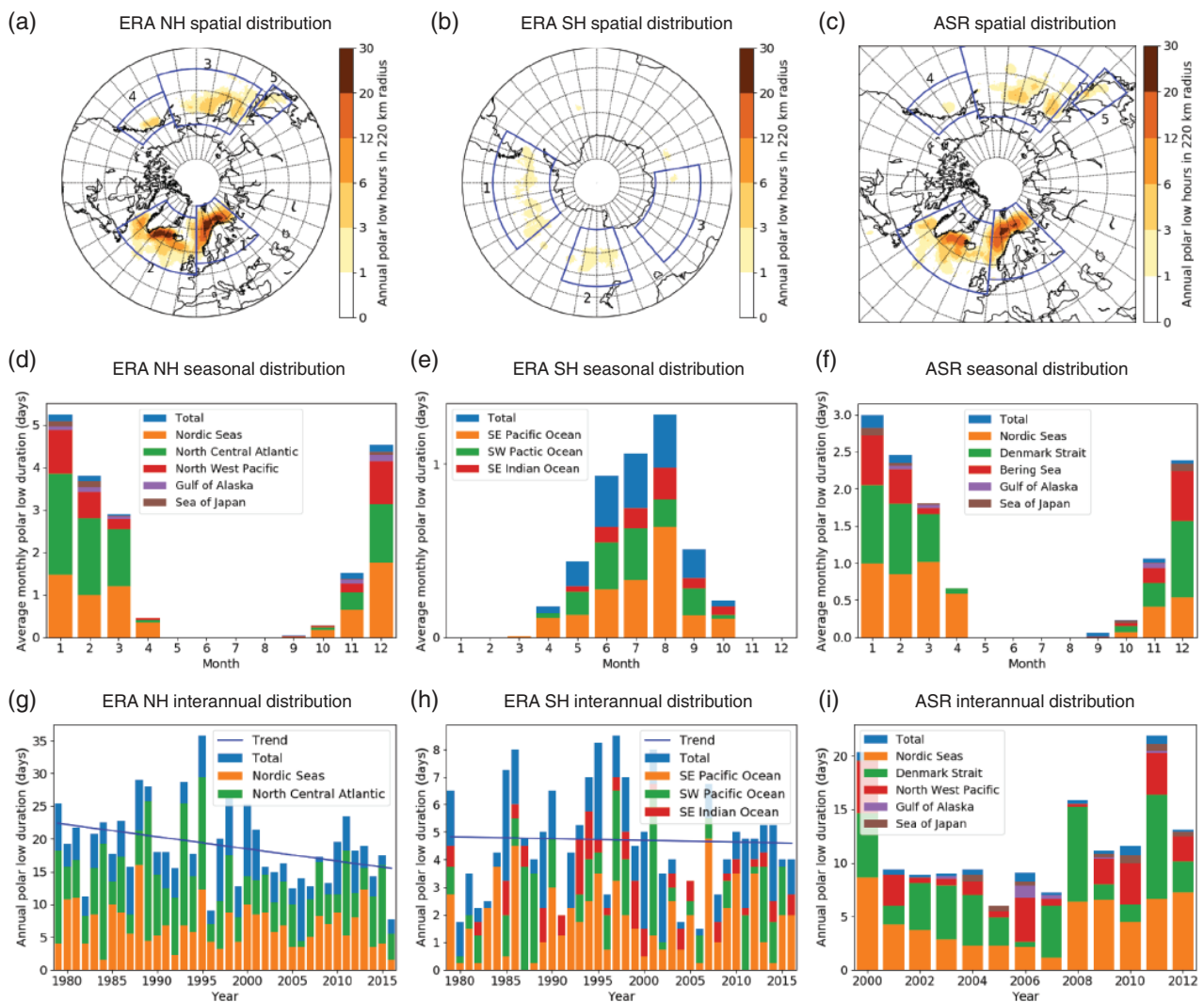
FIGURE 8 Spatial and temporal distributions of the most intense PLs. (a)–(c) are as Figure 5, and (d)–(i) are as Figure 6

algorithm based on spectrally filtered 850 hPa vorticity data (Hodges, 1995; 1999). The criteria were objectively developed by finding parameters that were most effective in distinguishing between PLs from the subjective STARS database (Noer *et al.*, 2011) and all kinds of mid- and high-latitude cyclones.

For ERA-I (and ASR), the criteria were found to be

(a) a difference larger than 0.4 hPa (2.38 hPa) of the mean SLP within a radius of 110 km (330 km) and the SLP of the system; (as earlier)

(b) a maximum potential temperature difference above −9.4 K (−8.5 K) within a radius of 110 km between the sea surface and 500 hPa level; and

(c) the absence of a tropopause (500 hPa) wind of magnitude higher than 31.3 m s^{-1} (29.6 m s^{-1}) poleward of the system.

Criterion (a) is applied to identify intense mesoscale systems, criterion (b) for the detection of MCAOs with connected deep convection, and criterion (c) to guarantee the occurrence of

the systems poleward of the polar front. The result that the same parameters are found to be most effective for PL detection for both ERA-I and ASR, with thresholds only slightly stricter for ASR than for ERA-I, gives confidence that the criteria can be applied to other datasets as well.

Several other parameters (summarized in Table 1) were investigated for ERA-I and ASR, but none of them were found to improve the detection of PLs as additional criteria. Importantly, a constraint on the near-surface wind speed, a commonly applied intensity criterion, is found to be much less effective for PL detection than criterion (a), a measure for the depth of the low. This applies for ERA-I, where maximum winds connected to mesoscale systems are under-represented, but also for ASR, even though it was found to better represent near-surface wind speeds (e.g. Smirnova and Golubkin, 2017). It is therefore suggested to avoid the 10 m wind speed for the detection of PLs from reanalyses.

The application of an MCAO criterion for PL detection is generally agreed upon, and it may be included in the PL definition by Rasmussen and Turner (2003), presented in

section 1. Often, a temperature difference larger than 43 K between the sea surface and the 500 hPa level is utilized. Our analysis suggests that potential temperature performs better for PL detection than the actual temperature, and that the commonly used threshold of $SST - T_{500} > 43$ K is too strict, since it excludes a considerable proportion of PLs, which was also noted by Terpstra *et al.* (2016). A comparison of the temperature difference between the sea surface and three atmospheric pressure levels reveals that the 500 hPa is more useful for PL identification than the 700 and 850 hPa levels. This result is in disagreement with Bracegirdle and Gray (2008), although they used different temperature measures and a smaller set of polar mesoscale cyclones, which includes systems that are too weak to be considered as PLs. Here, a new criterion is suggested, ensuring that only systems poleward of the polar front are detected. This criterion excludes about one third of the otherwise falsely detected cyclones and is therefore regarded as being important.

The investigation of our obtained climatologies reveals that they detect a significant fraction of the subjectively identified PLs from STARS and other satellite-based PL datasets. Not all systems identified in our climatologies would be classified as definite PLs, but only a few could be excluded by experts as clearly non-PLs. This expresses the classical PL problem of not having an absolute objective definition. In this study, as in other studies where PLs are identified objectively, all conditions for a PL have to be satisfied at the same time step, without considering the evolution of the cyclone. A more sophisticated approach would be to include all time steps of the system, when deciding whether or not it should be classified as a PL. The use of cyclone-tracking algorithms, as done in this study, gives the opportunity to apply this approach.

Due to the higher resolution of the ASR data compared to ERA-I, the ASR climatology is regarded as better than that based on ERA-I, although ASR has the disadvantage of having a shorter temporal coverage and a domain only for the NH. The two climatologies show similar spatial and temporal PL distributions. The Denmark Strait and the Nordic Seas are found to be the two most active PL regions. Also, other regions in the North Atlantic, the North Pacific and the Southern Seas between 65° and 50° S were found to be PL active. It is observed that high PL activity occurs often in the vicinity of the sea-ice edge or the coast. The PL season generally ranges from November to March, with few cases in October and April for the NH. In the SH, the PL season is about two months longer, from April to October, with a few cases in March and November, but less active. The annual PL activity is about 17% lower in the SH than in the NH. The most intense PLs are mainly constrained to the two most active PL regions and the core winter season.

The total annual PL occurrence for both hemispheres shows high interannual variability, but no significant trend during the period of ERA-I. However, in the SH a decade (1992–2001) of increased intensity was identified, and some regions in both hemispheres show changes in PL occurrence.

The strongest decreasing trend is observed in the Denmark Strait and the highest increasing trend in the Nordic Seas to the south of Svalbard. Also, for the most intense PLs in the NH, a significant decaying trend was observed.

The derived PL climatologies can be used for further investigation of different PL types and of typical synoptic-scale patterns associated with PL development in different regions. It will be of interest to investigate the PL representation in the recently produced high-resolution global reanalysis ERA-5 and to derive a PL climatology based on this reanalysis once it is fully released. Also of relevance would be to compare how the derived criteria depend on the underlying subjective PL list, such as the STARS or Smirnova datasets.

ORCID

Patrick J. Stoll https://orcid.org/0000-0003-1120-2049

REFERENCES

Bracegirdle, T.J. and Gray, S.L. (2008) An objective climatology of the dynamical forcing of polar lows in the Nordic Seas. *International Journal of Climatology*, 28(14), 1903–1919.

Bracegirdle, T.J. and Kolstad, E.W. (2010) Climatology and variability of southern hemisphere marine cold-air outbreaks. *Tellus A*, 62(2), 202–208.

Bromwich, D.H., Wilson, A.B., Bai, L.S., Moore, G.W.K. and Bauer, P. (2016) A comparison of the regional Arctic system reanalysis and the global ERA-Interim reanalysis for the Arctic. *Quarterly Journal of the Royal Meteorological Society*, 142, 644–658.

Bromwich, D.H., Wilson, A.B., Bai, L., Liu, Z., Barlage, M., Shih, C.F., Maldonado, S., Hines, K.M., Wang, S.H., Woollen, J., Kuo, B., Lin, H.-C., Wee, T.-K., Serreze, M.C. and Walsh, J.E. (2017) The Arctic System Reanalysis, version 2. *Bulletin of the American Meteorological Society*, 99, 805–828.

Businger, S. (1987) The synoptic climatology of polar-low outbreaks over the Gulf of Alaska and the Bering Sea. *Tellus A*, 39(4), 307–325.

Carleton, A.M. and Carpenter, D.A. (1990) Satellite climatology of 'polar lows' and broadscale climatic associations for the Southern Hemisphere. *International Journal of Climatology*, 10(3), 219–246.

Chen, F. and von Storch, H. (2013) Trends and variability of North Pacific polar lows. *Advances in Meteorology*, 2013(170387). https://doi.org/10.1155/2013/170387.

Dee, D.P., Uppala, S.M., Simmons, A.J., Berrisford, P., Poli, P., Kobayashi, S., Andrae, U., Balmaseda, M.A., Balsamo, G., Bauer, P., Bechtold, P., Beljaars, A.C.M., van de Berg, L., Bidlot, J., Bormann, N., Delsol, C., Dragani, R., Fuentes, M., Geer, A.J., Haimberger, L., Healy, S.B., Hersbach, H., Hólm, E.V., Isaksen, L., Kållberg, P., Köhler, M., Matricardi, M., McNally, A.P., Monge-Sanz, B.M., Morcrette, J.-J., Park, B.-K., Peubey, C., de Rosnay, P., Tavolato, C., Thépaut, J.-N. and Vitart, F. (2011) The ERA-Interim reanalysis: configuration and performance of the data assimilation system. *Quarterly Journal of the Royal Meteorological Society*, 137, 553–597.

Emanuel, K.A. and Rotunno, R. (1989) Polar lows as Arctic hurricanes. *Tellus A*, 41(1), 1–17.

Fletcher, J., Mason, S. and Jakob, C. (2016) The climatology, meteorology, and boundary layer structure of marine cold air outbreaks in both hemispheres. *Journal of Climate*, 29(6), 1999–2014.

Fu, G., Qin-Yu, L. and Zeng-Mao, W. (1999) General features of polar lows over the Japan Sea and the northwestern Pacific. *Chinese Journal of Oceanology and Limnology*, 17(4), 300–307.

Hodges, K. (1995) Feature tracking on the unit sphere. *Monthly Weather Review*, 123(12), 3458–3465.

Hodges, K. (1999) Adaptive constraints for feature tracking. *Monthly Weather Review*, 127(6), 1362–1373.

Hoskins, B.J. and Sardeshmukh, P.D. (1984) Spectral smoothing on the sphere. *Monthly Weather Review*, 112, 2524–2529.

Kolstad, E.W. (2011) A global climatology of favourable conditions for polar lows. *Quarterly Journal of the Royal Meteorological Society*, 137, 1749–1761.

Kolstad, E.W. and Bracegirdle, T.J. (2008) Marine cold-air outbreaks in the future: an assessment of IPCC AR4 model results for the Northern Hemisphere. *Climate Dynamics*, 30(7–8), 871–885.

Laffineur, T., Claud, C., Chaboureau, J.P. and Noer, G. (2014) Polar lows over the Nordic Seas: improved representation in ERA-Interim compared to ERA-40 and the impact on downscaled simulations. *Monthly Weather Review*, 142(6), 2271–2289.

Michel, C., Terpstra, A. and Spengler, T. (2018) Polar mesoscale cyclone climatology for the Nordic Seas based on ERA-Interim. *Journal of Climate*, 31(6), 2511–2532.

Neu, U., Akperov, M.G., Bellenbaum, N., Benestad, R., Blender, R., Caballero, R., Cocozza, A., Dacre, H.F., Feng, Y., Fraedrich, K., Grieger, J., Gulev, S., Hanley, J., Hewson, T., Inatsu, M., Keay, K., Kew, S.F., Kindem, I., Leckebusch, G.C., Liberato, M.L.R., Lionello, P., Mokhov, I.I., Pinto, J.G., Raible, C.C., Reale, M., Rudeva, I., Schuster, M., Simmonds, I., Sinclair, M., Sprenger, M., Tilinina, M.D., Trigo, I.F., Ulbrich, S., Ulbrich, U., Wang, X.I. and Wernli, H. (2013) Imilast: a community effort to intercompare extratropical cyclone detection and tracking algorithms. *Bulletin of the American Meteorological Society*, 94(4), 529–547.

Noer, G., Saetra, Ø., Lien, T. and Gusdal, Y. (2011) A climatological study of polar lows in the Nordic Seas. *Quarterly Journal of the Royal Meteorological Society*, 137, 1762–1772.

Papritz, L., Pfahl, S., Sodemann, H. and Wernli, H. (2015) A climatology of cold air outbreaks and their impact on air–sea heat fluxes in the high-latitude South Pacific. *Journal of Climate*, 28(1), 342–364.

Rasmussen, E.A. and Turner, J. (2003) *Polar Lows; mesoscale weather systems in the polar regions*. Cambridge University Press, Cambridge, UK.

Rojo, M., Claud, C., Mallet, P.E., Noer, G., Carleton, A.M. and Vicomte, M. (2015) Polar low tracks over the Nordic Seas: a 14-winter climatic analysis. *Tellus A*, 67. https://doi.org/10.3402/tellusa.v67.24660.

Rudeva, I. and Gulev, S.K. (2007) Climatology of cyclone size characteristics and their changes during the cyclone life cycle. *Monthly Weather Review*, 135(7), 2568–2587.

Samuelsen, E.M., Løset, S. and Edvardsen, K. (2015) Marine icing observed on kv Nordkapp during a cold air outbreak with a developing polar low in the Barents Sea. In: *Proceedings of the 23rd International Conference on Port and Ocean Engineering under Arctic Conditions*, 14–18 June 2015, Trondheim, Norway

Smirnova, J.E. and Golubkin, P.A. (2017) Comparing polar lows in atmospheric reanalyses: Arctic System Reanalysis versus ERA-Interim. *Monthly Weather Review*, 145, 2375–2383.

Smirnova, J.E., Golubkin, P.A., Bobylev, L.P., Zabolotskikh, E.V. and Chapron, B. (2015) Polar low climatology over the Nordic and Barents Seas based on satellite passive microwave data. *Geophysical Research Letters*, 42(13), 5603–5609.

Smirnova, J.E., Zabolotskikh, E.V., Bobylev, L.P. and Chapron, B. (2016) Statistical characteristics of polar lows over the Nordic Seas based on satellite passive microwave data. *Izvestiya, Atmospheric and Oceanic Physics*, 52(9), 1128–1136.

Terpstra, A., Michel, C. and Spengler, T. (2016) Forward and reverse shear environments during polar low genesis over the Northeast Atlantic. *Monthly Weather Review*, 144, 1341–1354.

Wilhelmsen, K. (1985) Climatological study of gale-producing polar lows near Norway. *Tellus A*, 37(5), 451–459.

Yanase, W., Niino, H., Watanabe, S.i.I., Hodges, K., Zahn, M., Spengler, T. and Gurvich, I.A. (2016) Climatology of polar lows over the Sea of Japan using the JRA-55 reanalysis. *Journal of Climate*, 29(2), 419–437.

Yarnal, B. and Henderson, K.G. (1989) A climatology of polar low cyclogenetic regions over the North Pacific Ocean. *Journal of Climate*, 2(12), 1476–1491.

Zahn, M. and von Storch, H. (2008) A long-term climatology of North Atlantic polar lows. *Geophysical Research Letters*, 35(22). https://doi.org/10.1029/2008GL035769.

Zappa, G., Shaffrey, L. and Hodges, K. (2014) Can polar lows be objectively identified and tracked in the ECMWF operational analysis and the ERA-Interim reanalysis?. *Monthly Weather Review*, 142(8), 2596–2608.

/9

Paper II:

A well-observed polar low analysed with a regional and a global weather-prediction model.

P.J. Stoll, T.M. Valkonen, R.G. Graversen, G. Noer.

A well-observed polar low analysed with a regional and a global weather-prediction model

Patrick J. Stoll[1] | Teresa M. Valkonen[2] | Rune G. Graversen[1] | Gunnar Noer[3]

[1]Department of Physics and Technology, Arctic University of Norway, Tromsø, Norway

[2]Norwegian Meteorological Institute, Oslo, Norway

[3]Norwegian Meteorological Institute, Tromsø, Norway

Correspondence
P. J. Stoll, Department of Physics and Technology, The Arctic University of Norway, 9037 Tromsø, Norway.
Email: patrick.stoll@uit.no

Funding information
Norwegian Research Council, Grant/Award Number: 280573

Abstract

The capability of a regional (AROME-Arctic) and a global (ECMWF HRES) weather-prediction model are compared for simulating a well-observed polar low (PL). This PL developed on 3–4 March 2008 and was measured by dropsondes released from three flights during the IPY-THORPEX campaign. Validation against these measurements reveals that both models simulate the PL reasonably well. AROME-Arctic appears to represent the cloud structures and the high local variability more realistically. The high local variability causes standard error statistics to be similar for AROME-Arctic and ECMWF HRES. A spatial verification technique reveals that AROME-Arctic has improved skills at small scales for extreme values. However, the error growth of the forecast, especially in the location of the PL, is faster in AROME-Arctic than in ECMWF HRES. This is likely associated with larger convection-induced perturbations in the former than the latter model. Additionally, the PL development is analysed. This PL has two stages, an initial baroclinic and a convective mature stage. Sensible heat flux and condensational heat release both contribute to strengthen the initial baroclinic environment. In the mature stage, latent heat release appears to maintain the system. At least two conditions must be met for this stage to develop: (a) the sensible heat flux sufficiently destabilises the local environment around the PL, and (b) sufficient moisture is available for condensational heat release. More than half of the condensed moisture within the system originates from the surroundings. The propagation of the PL is "pulled" towards the area of strongest condensational heating. Finally, the sensitivity of the PL to the sea-surface temperature is analysed. The maximum near-surface wind speed connected to the system increases by $1–2\,\mathrm{m\cdot s^{-1}}$ per K of surface warming and a second centre develops in cases of highly increased temperature.

KEYWORDS

polar low, mesoscale cyclone, AROME-Arctic, baroclinic instability, cold-air outbreak, diabatic processes, ECMWF HRES, HARMONIE-AROME, IPY-THORPEX

---

1 | INTRODUCTION

Polar lows (PLs) are small but intense cyclones developing in cold air masses that flow over large water surfaces, known as cold-air outbreaks (CAOs; Rasmussen and Turner, 2003). The associated strong winds, high waves and substantial snowfall are a threat for coastal communities and maritime operations at high latitudes. The Northeast Atlantic is one of the areas with the most frequent PL occurrence (Stoll *et al.*, 2018).

PLs are mesoscale cyclones with a typical diameter of 200–600 km (Rojo *et al.*, 2015). They develop and intensify rapidly, generally within a few hours. Hence, hazardous conditions associated with PLs appear at short notice. In contrast to synoptic-scale cyclones, their lifetime rarely exceeds two days (Rojo *et al.*, 2015).

Because of their fast development and due to the sparse observation network in polar regions, the prediction of PLs is a challenge for meteorological services (Furevik *et al.*, 2015). Numerical weather prediction (NWP) models still have issues to correctly represent important details of convection and the stable atmospheric boundary layer of cold air masses (Holtslag *et al.*, 2013). These two processes are relevant during and before, respectively, the PL development. Up-to-date regional NWP models show substantial differences in their representation of convection connected to CAOs (Field *et al.*, 2017).

Detailed measurements of the development of PLs are rare. Only a handful of flight campaigns have been performed (Shapiro *et al.*, 1987; Douglas *et al.*, 1991; Douglas *et al.*, 1995; Brümmer *et al.*, 2009). In February and March 2008, in connection with the International Polar Year (IPY) of The Observing System Research and Predictability Experiment (THORPEX), several flight missions were conducted in the Northeast Atlantic (Kristjánsson *et al.*, 2011). Two PL cases and several other Arctic marine boundary-layer phenomena were observed by an aircraft. To the knowledge of the authors, the only PL observed by multiple flights was that monitored during the IPY-THORPEX campaign on 3–4 March 2008. This, commonly referred to as the THORPEX PL, is among the most investigated PLs, and is also scrutinised in this study.

Føre *et al.* (2011) described this PL based on dropsonde data obtained from the flights, satellite images and the weather-prediction model HIRLAM (High-Resolution Limited-Area Model), operational at the Norwegian Meteorological Institute (MET Norway) at that time. Føre and Nordeng (2012) use the Weather Research and Forecasting model (WRF) with 3 km horizontal grid-spacing and non-hydrostatic dynamical core to investigate the effect of surface energy fluxes and condensational heat release on the intensification of the PL. Wagner *et al.* (2011) performed WRF simulations with 2 km grid-spacing and

compared these to lidar and dropsonde measurements obtained from the flight campaigns. Innes *et al.* (2011) used the Met Office Unified Model (UM) with grid-spacing of 12, 4 and 1 km to investigate the effect of the model grid-spacing on the PL simulation. They found that the 4 km version performed considerably better than the 12 km version, while the 1 km simulation did not improve the representation of the PL with that particular model.

Føre *et al.* (2011) and Kristjánsson *et al.* (2011) suggested using the observations retrieved from the IPY-THORPEX campaign for model validation. In this study, the state-of-the-art regional weather-prediction model, AROME-Arctic (Müller *et al.*, 2017a), is validated against this dataset. AROME-Arctic (Applications of Research to Operations at MEsoscale for the European Arctic) has been used operationally at MET Norway since 2015. AROME-Arctic (AA) is the first operational model for the European Arctic with a non-hydrostatic core that permits convection. The model system from which AA originates is utilised by numerous other European meteorological services for operational weather forecasting (Bengtsson *et al.*, 2017). This model system is also currently employed for the production of the first regional reanalysis of the European Arctic. Section 2.1 gives more details on the model.

At present, AA is the main tool for forecasting PLs that develop in the Nordic Seas and offer a threat to the Norwegian coast. Due to the non-hydrostatic, convective-permitting dynamics, AA is expected to be more suited for simulating the development of PLs than previous hydrostatic models. Müller *et al.* (2017a) conclude that a PL which occurred on 8 December 2016 was represented with higher accuracy in AA than in the operational High RESolution global weather-prediction model (HRES) of the European Centre for Medium-Range Weather Forecasts (ECMWF; ECMWF, 2018). More details to ECMWF HRES are given in Section 2.2. However, in that study the models were only compared for their performance in simulating the near-surface wind speeds. The model representation of the three-dimensional dynamical structure of a PL has not yet been investigated for AA.

The capability of AA to accurately simulate the THORPEX PL is evaluated in the first part of this study, with the explicit purpose of revealing the strengths and weaknesses of the model. Furthermore, the representation of this PL by AA is compared to the performance of the weather-prediction model HRES.

In the second part of the study, the focus is on the development mechanisms of the PL in question. However, this is connected to the first, since a better understanding of the PL evolution eases the identification of the model components that need improvement to increase the forecast quality of PLs.

Multiple development mechanisms, such as baroclinic instability, shear instability, upper-level potential vorticity forcing, orographic vortex generation, convection, and diabatic processes have been recognised as being important for the intensification of PLs (Rasmussen and Turner, 2003; Terpstra *et al.*, 2015). Often, the mentioned mechanisms interact nonlinearly, implying that the role of every single component is difficult to examine (Bracegirdle, 2006).

The importance of the different mechanisms varies among PL cases, which is the major reason why no standard model for PL development has been developed. Furthermore, the importance of the different mechanisms changes during the lifetime of a PL. Some PLs were observed to develop initially in a baroclinic environment and subsequently to intensify by convective processes (e.g. Nordeng and Rasmussen, 1992). The PL investigated in this study follows such development.

Various idealised numerical simulations have been performed in order to understand the development of PLs. For example, Terpstra *et al.* (2015) applied a baroclinic channel model adapted for high-latitude conditions to demonstrate that a low-level disturbance requires a "diabatic boost" in order to amplify quickly. The occurrence of this "boost" depends on sufficient humidity and baroclinicity and weak static stability. They conceptually described the growing perturbation in the context of the Diabatic Rossby Vortex (DRV), where potential vorticity is produced below the source of latent heating.

Yanase and Niino (2005; 2007) showed in idealised experiments that the cloud structure can be associated with the dominant development mechanism. Simulations with a strong baroclinic environment lead to cyclones with comma-shaped clouds. In the absence of baroclinicity, spiral-form convective clouds develop, as seen in "hurricane-like" PLs (e.g. Nordeng and Rasmussen, 1992).

Also, NWP models have been utilised for investigation of the physical development mechanisms of PLs. Often sensitivity experiments with perturbed surface heat fluxes and condensational heat release are performed to investigate their relevance. Yanase *et al.* (2004) showed, using the Meteorological Research Institute Nonhydrological Model (MRI-NHM) with 5 km grid-spacing, that the rapid development of a PL in the Sea of Japan was mainly caused by condensational heating, whereas the surface fluxes maintained the favourable environment for the PL development.

Innes *et al.* (2011), Wagner *et al.* (2011), and Føre and Nordeng (2012) investigated the development of the THORPEX PL with sensitivity experiments. We also perform several sensitivity experiments, some of which are comparable to those in these studies. However, the earlier studies mainly examine the evolution of sea-level pressure

of the PL. In this study, we analyse the PL development based on multiple relevant variables, whereby new conclusions are drawn. Additionally, we undertake new experiments to investigate the influence of the sea-surface temperature (SST) on the PL evolution. PLs develop over surfaces of open water, and the sensitivity to SST has previously been tested only in an idealised axisymmetric model (Linders *et al.*, 2011). The investigation of the effect of the SST on the PL development is of high interest for weather prediction, since it elucidates the influence of inaccurate SST fields on the forecast. In NWPs, the SST is typically set constant during the forecast. However, strong cold-air advection during which PLs occur can lead to rapidly varying SSTs (e.g. Sætra *et al.*, 2008), violating a constant SST assumption.

To summarise, the research questions posed in this study are two-fold:

1. How well does the regional NWP model AA capture the development of the well-observed THORPEX PL? How does it perform compared to the global NWP model ECMWF HRES?
2. What are the important physical mechanisms for the development of this PL? How sensitive is this PL to the sea-surface temperature?

The paper is organised as follows. In Section 2, the AA and HRES models, the observational datasets, and the applied methods are presented. Then, research questions 1 and 2 are approached in Sections 3 and 4, respectively. Finally, discussions and conclusions are provided in Section 5.

2 | DATA AND METHODS

In this study, the operational weather-forecast models, AROME-Arctic and ECMWF HRES, are compared and validated against satellite and dropsonde data from the IPY-THORPEX campaign. The models and observational datasets are introduced in the Sections 2.1 to 2.4. In Sections 2.5 to 2.7 we present the techniques applied for validation of the models in Section 3 and the comparison of the sensitivity experiments in Section 4.

2.1 | AROME-Arctic

The AROME model was developed by Météo France (Seity *et al.*, 2011), as part of the Aire Limitée Adaptation Dynamique Développement International (ALADIN) consortium. A collaboration of the ALADIN and
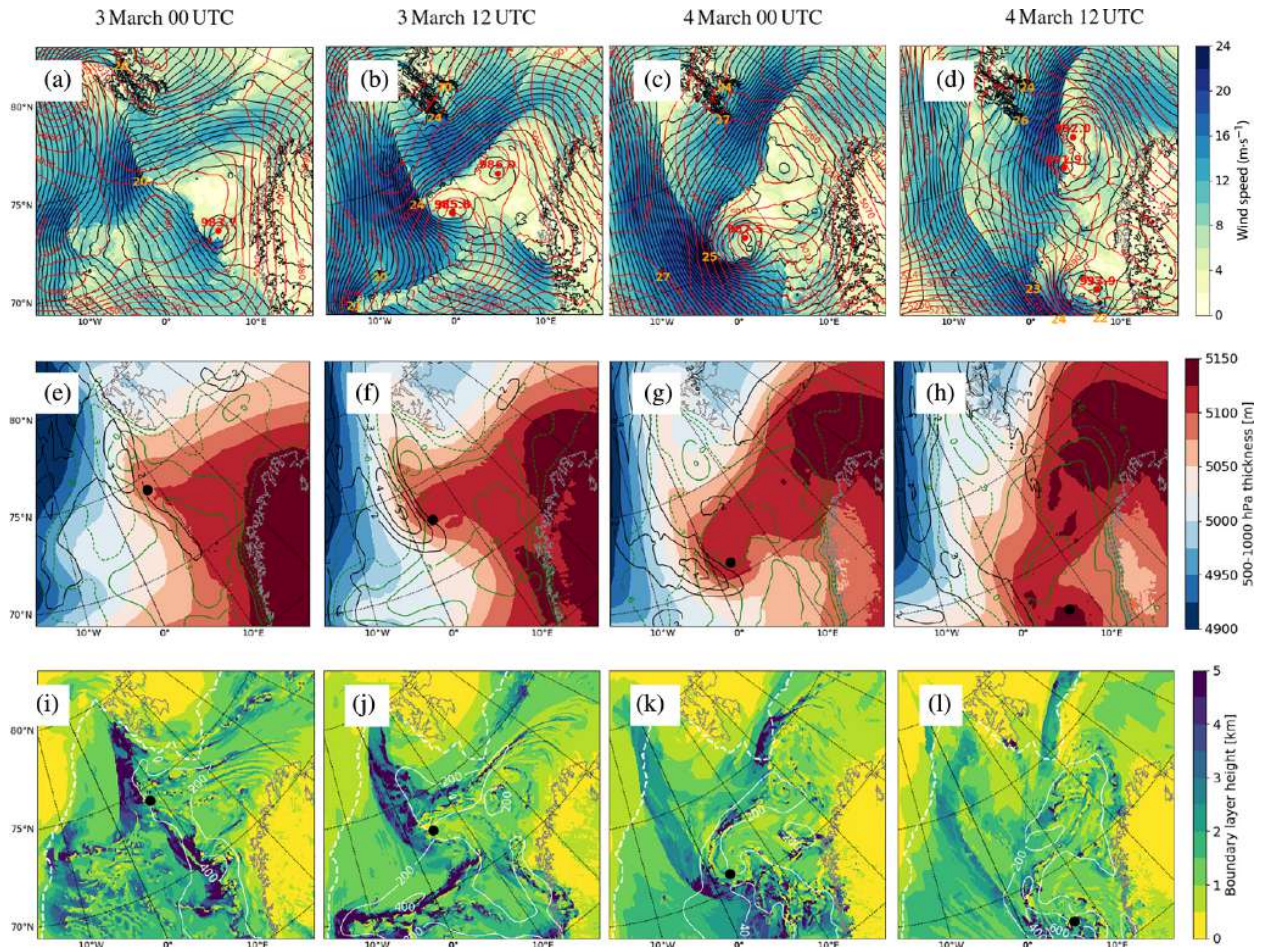
FIGURE 1 Fields from the AROME-Arctic analysis at 0000 and 1200 UTC on 3–4 March 2008. (a–d) horizontal wind speed (colour shading, m·s^{-1}), the sea-level pressure (black contours, spacing 2 hPa), and the 500 hPa geopotential height (m, red contours). Yellow and red numbers denote maximum wind speeds (m·s^{-1}) and the minimum sea-level pressure (hPa), respectively. (e–h) 500–1,000 hPa thickness (m, colour shading), as a measure of the atmospheric temperature, the baroclinicity expressed by $\nabla\theta_{850}$ (K·(100 km)$^{-1}$, black contours), and the static stability expressed by $\theta_{e,SST} - \theta_{e,500}$ (K, green contours), where positive values depict conditionally unstable conditions. (i–l) planetary boundary-layer height (km, colour shading), CAPE (J·kg^{-1}, white contours), and the location of the ice edge (white dashed line). The position of the PL centre is denoted by a black dot in (e–l)

HIRLAM consortia further adapted AROME into the HIRLAM–ALADIN Research on Mesoscale Operational NWP in Euromed (HARMONIE)-AROME model system (Bengtsson et al., 2017).

The HARMONIE-AROME model system is utilised by numerous meteorological services for operational weather forecasts after adaptation for local conditions (e.g. Müller et al., 2017b). MET Norway implemented a configuration of this model system, called AROME-Arctic (AA), for the European Arctic with the centre around Svalbard in November 2015 (Müller et al., 2017a). For experiments in this study, version 40h1.1 of the model system is applied, which was operational for AA from 2016 until early 2019. We display only the southern half of the domain of AA (e.g. Figure 1) since the THORPEX PL evolved in that

area. The full domain is presented in Figure 1 of Müller et al. (2017b).

AA has a horizontal model grid-spacing of 2.5 km and 65 vertical hybrid levels, of which 32 are below 3 km. The model includes a non-hydrostatic dynamical core that permits convection. AA uses 3D-Var upper-air data assimilation of conventional and satellite observations and optimal interpolation of near-surface temperature, humidity and snow depth, both within a 3 hr cycle. Every hour, it obtains lateral and upper-boundary data from ECMWF HRES, which is presented in the next subsection. Operationally, AA retrieves data from the HRES forecast starting 12 hr earlier, because the recent HRES version is still in production. Since we reproduce an old case, we utilise the HRES forecast with the same initialisation time as the

TABLE 1   List of the performed experiments with AROME-Arctic and the main results

Name	Description	Main result
CTR = SIM-03-00	Control run; start at 0000 UTC on 3 March 2008.	PL well simulated, especially within first 24 hr of the simulation.
SIM-"day"-"hour"	Simulations starting "day" March "hour" UTC.	Realistic short-term forecasts. After 24 hr the simulations deviate.
noFLX	No turbulent heat fluxes in the domain.	The PL "consumes" the baroclinicity and decays thereafter.
noFLX-A	No turbulent fluxes in limited area (box in Figure 10e).	The local fluxes around the PL centre are most important.
2FLX	Doubled turbulent fluxes in the bulk scheme.	The convective mature stage develops considerably stronger.
noQH	No latent heat flux in the domain.	Initially comparable to CTR; no intensification in the mature stage.
noTH	No sensible heat flux in the domain.	The vortex develops weaker; the PL develops no mature stage.
noCond	No condensational heat release in the domain.	Initially reduced baroclinicity; the PL develops no mature stage.
+2/4/6 SST	Sea-surface temperature increased by 2, 4, 6 °C.	Faster and enhanced PL development; two cores develop.
−2/4/6 SST	Sea-surface temperature reduced by 2, 4, 6 °C.	Suppressed PL development after the baroclinicity is "consumed."

Note: The sensitivity experiments are started at the same time as the control run.

AA simulation. This removes differences between the AA and HRES simulations with same initialization time which originate from old boundary data of AA.

The PL developed in the morning of 3 March 2008 to the south of Svalbard and made landfall in the afternoon of 4 March 2008 in central Norway. In order to obtain accurate initial conditions for the AA simulations, a spin-up phase is started at 0000 UTC on 1 March 2008 from interpolation of the ECMWF HRES analysis. After that the model is updated 3-hourly with assimilation of observations. The main AA simulation, also referred to as the control run (CTR) and SIM-03-00, is initiated from the cycle at 0000 UTC on 3 March, just before the THORPEX PL developed, and forecasts for 48 hr until 0000 UTC on 5 March. Similar forecasts are also initiated from the consecutive cycles at 0600, 1200 and 1800 UTC on 3 and 4 March and referred to as SIM-"day"-"hour," where "day" and "hour" indicate the time of initialisation. These simulations are used for the validation of the forecast performance of the model (Section 3). In order to investigate different physical mechanisms, several sensitivity experiments are performed, beginning at the same time as CTR (Section 4). The different experiments are briefly summarised in Table 1. In experiments where the surface flux components are investigated (e.g. noTH, noQH, noFLX and 2FLX), an artificial factor was implemented into the bulk formula.

2.2 | ECMWF HRES

ECMWF HRES produces a global weather forecast for 10 days into the future. In this study, data from the model that was in operation in March 2008, is used. It is based on the ECMWF Integrated Forecast System (IFS) cycle 32r3 with a horizontal spectral resolution of T799, corresponding to a grid-spacing of about 25 km, and includes 91 vertical levels (ECMWF, 2018). The model runs twice a day, starting from 0000 and 1200 UTC. The initial state is updated by 4D-VAR data assimilation with a 12 hr window. In this study, HRES simulations from 2–4 March 2008 are compared to AA.

2.3 | Satellite data

For the qualitative validation of the PL, the model products are validated against different satellite retrievals. The U.S. National Oceanic and Atmospheric Administration (NOAA) Advanced Very High Resolution Radiometer (AVHRR) measures radiation emitted from Earth. Channel 4 retrieves infrared radiation within the spectral band of 10.3–11.3 μm, from which the emission temperature can be determined. The latter is equivalent to the cloud-top temperature in the case of cloud cover, and to the surface temperature otherwise.

QUIKSCAT (U.S. Quick Scatterometer mission carrying the SeaWinds scatterometer) is a specialised microwave radar that measures the near-surface wind vector on a swath width of 1,800 km over sea surfaces under all weather conditions (Verhoef *et al.*, 2016). The instrument measured the wind speed with a horizontal resolution of 25 km and an accuracy of 2 m·s^{-1} between June 1999 and November 2009.

2.4 | IPY-THORPEX dropsondes

The IPY-THORPEX campaign included a total of 12 flight missions between 27 February and 17 March 2008 with a total of 150 released dropsondes (Kristjánsson *et al.*, 2011). Three of the flight missions focused on the PL investigated here, with 20, 15, and 20 released dropsondes, respectively. The sondes were dropped from an altitude of about 7 km and measured the pressure, temperature, horizontal wind and relative humidity with an accuracy of 1 hPa, 0.1 K, 0.5 m·s^{-1} and 5%, respectively.

2.5 | Verification techniques

Simple error statistics – the BIAS and mean absolute error (MAE) – are calculated by comparison of the model data to the dropsondes released in the THORPEX flights. In order to exclude effects assigned to the high local variability of AA, the local average in a circle with a radius of 12.5 km, approximately the grid-spacing of HRES, is calculated for AA and presented as AA-avg. However, traditional metrics are sensitive to exact matches of observations and simulations (Ebert, 2008). Since models can have a high quality without capturing the exact location of meteorological features, spatial verification methods have been introduced for model evaluation. Different types, such as scale separation, object-oriented, field deformation and "fuzzy" verification techniques have been developed (Gilleland *et al.*, 2010).

The former three approaches are normally applied to gridded observation data, often for precipitation verification (e.g. Gilleland *et al.* (2009). This study utilises gridded observation data from satellites for infrared radiation and scatterometer wind fields. However, examples of spatial verification with these fields are rare for case-studies. Alternatively, some "fuzzy" verification techniques are commonly applied to point observations, such as the dropsondes. Fuzzy verification utilises a spatial window surrounding the location of the observation. Within this window, the data can be treated in various ways (Ebert, 2008). Here, a simple approach of Atger (2001) is applied: for a given threshold, if both the observation and at least one

grid cell within the window satisfy the threshold, a hit is obtained. Following this logic, a contingency table of hits, misses, false alarms and correct rejections can be derived which is utilised for the calculation of a skill score. Following Ebert (2008), the Hanssen and Kuipers (HK) score is calculated as:

$$HK = \text{hit rate } - \text{ false alarm rate}$$
$$= \frac{\text{hits}}{\text{hits} + \text{misses}} - \frac{\text{false alarm}}{\text{false alarm} + \text{correct rejection}}.$$

A multi-event contingency table is derived by varying the threshold and the radius of the window size (scale) and displaying the result in a two-dimensional table (Ebert, 2008). Also, the equitable threat score (ETS) is applied and gives qualitatively similar results and is therefore not displayed here.

2.6 | Tracking of the polar low centre

Both for the model forecast validation (Section 3.5) and the sensitivity experiments (Section 4), the propagation of the PL is analysed. An automatic tracking procedure is applied to detect the system objectively. It consists of three steps:

- Local maxima of the filtered relative vorticity at 850 hPa are labelled as cyclone centres.
- Consecutive cyclone centres that propagated at less than 130 km·h^{-1} are merged in time to their nearest neighbour.
- The THORPEX PL is detected as the cyclone centres that propagate through the box bounded by 65°N–71°N and 5°W–10°E between hours 20 and 30 of the experiment. Satellite images reveal that the THORPEX PL was the only cyclonic system propagating through that box during that time.

Comparison of the retrieved tracks to the location of the THORPEX PL in satellite images reveals that this tracking procedure is sufficient. The detection proves insensitive to the pressure level of the vorticity, as long as the level is chosen from the lower troposphere (below 700 hPa). The maximum propagation speed may appear to be high, but was chosen because the THORPEX PL moved with a speed of up to 90 km·h^{-1} at the later stages (Wagner *et al.*, 2011), and because the centre of the PL, recognised by the applied detection algorithm, was adjusted to the location of strongest vorticity.

A Gaussian filter is applied on the relative vorticity within a radius of 100 km, cutting at one standard deviation. The size of the radius was employed after the following consideration. The smaller the filter radius, the

more individual convective cells are recognised. The larger the filter radius, the more circulation cells, including multiple PLs, are merged. In some simulations, the PL tends to split into a dual PL after more than 24 hr of forecast time (e.g. Figure 2l). For the comparison applied here, it was considered most instructive to summarise the characteristics of the PL as a single system. However, in simulations with a pronounced division of the PL centre (e.g. +6 SST in Figure 10c below), an individual investigation of the centres is insightful. The chosen filter radius of 100 km takes this into account. In cases of multiple centres within a small distance, the procedure detects an intermediate position between the centres.

2.7 | Variables in the vicinity of the polar low

After detection of the THORPEX PL, several variables are computed in order to analyse the evolution. The strength of the THORPEX PL is measured in three ways:

(a) the filtered relative vorticity at 850 hPa in the centre,

(b) the maximum wind speed at 10 m within 400 km around the centre, and

(c) the minimum sea-level pressure (SLP) within 100 km of the centre.

The location of the minimum SLP and the vorticity maximum do not coincide perfectly. In some cases, the PL does not even have a well-defined local minimum in SLP. The near-surface wind speed is influenced by the strength of both the PL and the synoptic-scale CAO. Stoll *et al.* (2018) show that the wind speed and SLP are both less effective criteria for measuring the strength of PLs than is the vorticity. However, the near-surface wind speed is likely the most relevant variable for human activities. The SLP is widely utilised as an intensity measure (e.g. Føre *et al.*, 2011), but in the present study it is demonstrated to be of little value.

The roles of the three diabatic components, the sensible and latent surface heat flux and the latent heat release by condensation, are compared. The latent heat release by condensation is deduced from the precipitation rate by using the specific latent heat for deposition, since the precipitation is almost purely in the solid phase. The mean in each of the three diabatic components within a circle of radius 300 km around the PL centre is computed in order to compare their strengths. This is necessary since the condensational heating occurs locally in convective cells, whereas surface heat fluxes are more continuous, mainly in regions of strong near-surface winds.

The gradient in the potential temperature at 850 hPa ($\nabla\theta_{850}$) is used to investigate the baroclinic development of the PL, and in the following is referred to as the baroclinicity. A Gaussian filter with 100 km radius is applied to θ_{850} prior to the calculation of the gradient in order to detect meso-α-scale baroclinic zones and to exclude temperature variations caused by small-scale convective cells. The maximum baroclinicity within a distance of 400 km of the PL centre is computed for the analysis of the evolution of the PL. Also, horizontal fields of the planetary boundary-layer height are presented. This variable is computed by AA as the lowest atmospheric level where turbulent kinetic energy is below 0.01 m^2·s^{-2}.

Conclusions presented in the following were tested and confirmed to be insensitive to variations in the above-mentioned length-scales.

3 | MODEL VALIDATION

In this section, the capability of the weather-prediction models AA and HRES for simulating the THORPEX PL are evaluated. First, the development of the THORPEX PL in the AA simulations is described and qualitatively evaluated against satellite images (Section 3.1). Then, the representation of the PL is qualitatively (Section 3.3) and quantitatively (Section 3.4) compared between AA and HRES. Finally, the forecast qualities of the two models are compared (Section 3.5).

3.1 | Evolution of the THORPEX polar low

The evolution of the THORPEX PL is described by investigating model fields from the analysis of AA (Figure 1), and additionally by comparing the pseudo-satellite images from the analysis of AA (second column of Figure 2) to actual satellite retrievals (first column of Figure 2). The development of the THORPEX PL is also described in Føre *et al.* (2011) and Wagner *et al.* (2011). Here, a somewhat different perspective is presented by the inclusion of additional fields, such as the baroclinicity, the static stability, the planetary boundary-layer height and the convective available potential energy.

On 2 March 2008, a synoptic-scale low moved eastward across the Norwegian Sea, causing a CAO to its western side. At 0000 UTC on 3 March, the synoptic-scale low was positioned off the coast of Northern Norway (Figure 1a; 70°N, 12°E). On the western flank of the low pressure a frontal zone developed (Figure 1a; 70–78°N, 10°E). The front separated the cold air masses over the Arctic sea ice and warmer air masses over Scandinavia and developed a significant temperature gradient (Figure 1e, black contours). Along the front, the boundary layer was convective and hence reached up to 5 km altitude (Figure 1i). To the
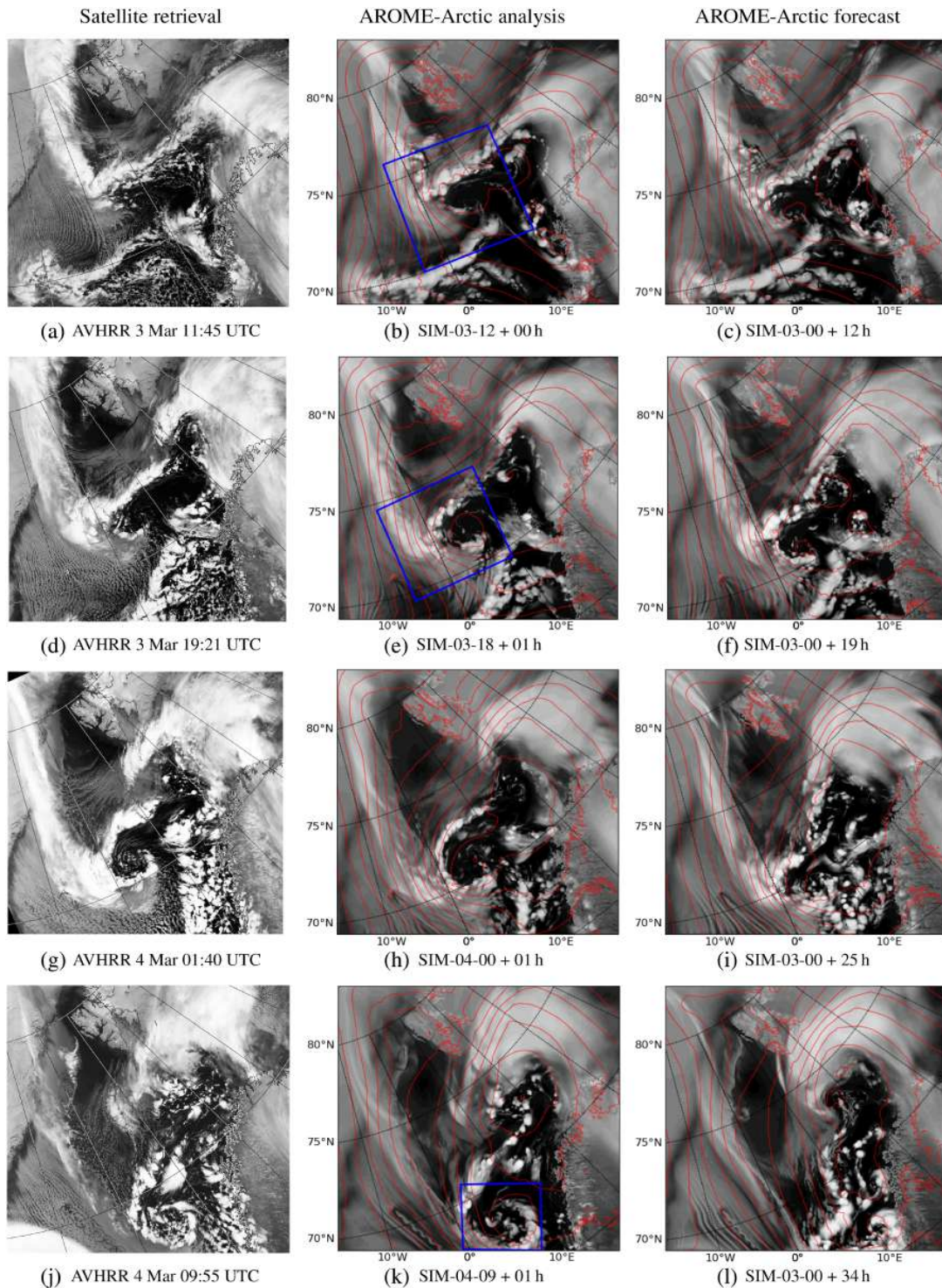
Satellite retrieval AROME-Arctic analysis AROME-Arctic forecast

(a) AVHRR 3 Mar 11:45 UTC (b) SIM-03-12 + 00 h (c) SIM-03-00 + 12 h

(d) AVHRR 3 Mar 19:21 UTC (e) SIM-03-18 + 01 h (f) SIM-03-00 + 19 h

(g) AVHRR 4 Mar 01:40 UTC (h) SIM-04-00 + 01 h (i) SIM-03-00 + 25 h

(j) AVHRR 4 Mar 09:55 UTC (k) SIM-04-09 + 01 h (l) SIM-03-00 + 34 h

FIGURE 2 (a, d, g, j) Satellite images displaying the emission temperature, equivalent to the cloud-top temperature obtained by AVHRR channel 4, and retrieved from the NERC satellite retrieving station, Dundee, UK. Pseudo-satellite images expressing the cloud-top temperature from the AROME-Arctic analysis or 1 hr forecast (b, e, h, k), and from the AROME-Arctic forecast starting at 0000 UTC on 3 March 2008 (c, f, i, l). In the latter, the lead time of the simulations is displayed in the sub-caption by "+ h." The red contours in the model fields denote the sea-level pressure with a spacing of 4 hPa. The blue boxes in (b,e,k) show the areas that are presented in Figures S1–S3, respectively

west of the front, the wind was northerly and cold, and to the east, the wind was warmer and easterly (Figure 1a,e). The front propagated westward, and at 1200 UTC on 3 March, it lay along the 2°E meridian to the west of Svalbard (Figure 1b). The satellite and pseudo-satellite images from the model (Figure 2a,b) depict a frontal cloud band. The baroclinicity of the southern part of the frontal zone, which was connected to the synoptic-scale low, decayed in intensity. In contrast, the baroclinicity of the northern part of the front amplified (Figure 1e,f), and along this frontal zone, the PL was initiated.

A secondary convergence zone formed on 3 March along 74°N to the south of Svalbard, caused by easterly winds north and southeasterly winds south of the zone (Figure 2a,b). The PL intensified around noon on 3 March in the baroclinic zone at the intersection point of the two convergence zones (Figure 2b,e). The horizontal temperature gradient increased and was maintained at approximately 5 K per 100 km (Figure 1e,f). The comma-shaped cloud structure, visible until the night of 4 March (Figure 2d,g), with the comma-head to the west of the PL center, indicate a baroclinic intensification of the PL (Yanase and Niino, 2007). The upper-level low is located to the south of the low-level center (Figure 1a,b; 72°N, 5°E). Low-level cold-air advection below the upper-level low amplifies the upper-level disturbance. The upper-level low in turn causes upper-level warm air advection above the surface low, which strengthen the low-level vortex. This is the amplification mechanism of baroclinic instability, characterised by a vertical tilt in the pressure perturbations. 1. 1 In the following, the stage of the PL until 0000 UTC on 4 March is referred to as the initial baroclinic stage.

At the end of the baroclinic stage, at 0000 UTC on 4 March, the PL formed an eye-like cloud structure (Figure 2g) with a warm core, and the baroclinicity decayed (Figure 1g). Also, the SLP and the geopotential height at 500 hPa aligned vertically, an indication of a quasi-barotropic system (Figure 1c). The highest wind speed associated with the PL occurred on the western side of the centre at the edge of the CAO. This region is referred to as the western eye-wall.

On the morning of the 4 March, the PL propagated southeastward into an area that was conditionally unstable for deep convection, indicated by $\theta_{e,SST} - \theta_{e,500} > 3$ K (Figure 1g) and by CAPE values above $400 \, \mathrm{J \, kg^{-1}}$ (Figure 1k). In this environment, the PL intensified further, and strong winds of $25 \, \mathrm{m \cdot s^{-1}}$ occurred in the western eye-wall (Figure 1c). The PL developed into a spiral-like system of convective clouds (Figure 2j,k). This cloud signature indicates that convective processes were of major importance for the system (Yanase and Niino, 2007). The time from 0000 UTC on 4 March, where the PL reached

the highest intensity, is below referred to as the convective mature stage. Later, it will be shown that latent heat release by condensation was significant at this stage (Figure 12a).

The PL propagated further southeastward along the edge of the domain of AA from 1200 UTC on 4 March and made landfall on the coast of Norway at approximately 65°N around 1800 UTC on 4 March.

## 3.2 | AROME-Arctic validation against satellite images

The comparison of the satellite images with the pseudo-satellite images produced by AA, both depicted in Figure 2, reveals that the clouds are generally captured well in the AA analysis. Examples are the correct position and structure of the frontal zones and the spiral-form clouds of the PL in the mature stage. The cloud structure appears in balance with the model dynamics at the analysis time of the model. This can be seen by the lack of abrupt changes in the cloud representation within the first hours of the model simulations (not presented in detail, but indicated from a comparison of Figures 2b,c).

AA develops deep convective towers, visible as circular blobs (e.g. Figure 2e around 73°N, 3°E). In the satellite images, deep convection appears less confined and spread over larger areas (e.g. compare Figures 2g,h at 68°N, 10°E), indicating that some deep convection occurs on scales lower than the effective resolution of the model.

In the shallow CAO to the west of the frontal zone along 2°E, the model correctly simulates cloud streets (Figure 2e,h,k lower-left corner). However, the spacing between the cloud streets is about 25 km (10 grid cells, not shown), which is approximately the effective resolution of the model, and which is larger than the observed spacing of about 15 km in the satellite images (Figure 2d,g,j lower-left corner). The satellite images show that the convection in the CAO evolves into shallow convective cells during the night of 4 March (Figure 2g lower left side), whereas AA still simulates cloud streets at this time (Figure 2h). Since cloud streets are favoured over cellular convection when the vertical wind shear is large (Markowski and Richardson, 2010), AA may overestimate the vertical shear in the lowest model levels, which might be caused by an inaccurate boundary-layer parametrization.

Other interesting features captured by AA, which are not connected to the PL development, are lee vortices, visible as wave-breaking-like disturbances in the satellite image, induced by Jan Mayen, an island with a 2.2 km high mountain, located at 8°W, 71°N. These vortices can be observed in the lee of isolated terrain obstacles, when the lower atmosphere is strongly stratified, so that

FIGURE 3 The outgoing long-wave radiation (shading) from the (a) AROME-Arctic and (b) HRES simulations starting at 0000 UTC on 4 March, averaged over the first 3 hr of the forecasts, to be compared with the satellite image in Figure 2g. Red contours depict the sea-level pressure (spacing 3 hPa) after 3 hr of model integration

(a) AA SIM-04-00 +0h-3h

(b) HRES-04-00 +0h-3h
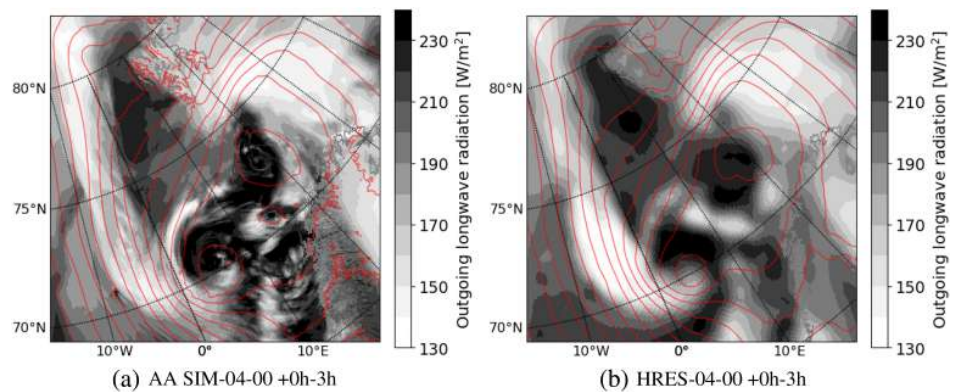
the flow has to pass around the obstacle (section 13.3 in Markowski and Richardson, 2010). In the model, the island initialises an oscillation in the cloud street passing the mountain (Figure 2j,k). However, the effective resolution of the model appears to be insufficient to simulate the wave-breaking of the oscillation.

High clouds, connected to the jet stream, which were observed over Northern Scandinavia (see the high gradient in the geopotential height in Figure 1b), are depicted by the model, but more smoothly than observed (e.g. Figure 2a,b right side). AA has only a few model levels above 10 km altitude and is highly steered by HRES at this height. The latter has a model grid-spacing of 25 km and therefore does not resolve fine-scale structures. Locally, deviation in this high-cloud cover can lead to large differences in the local radiative balance (Valkonen *et al.*, 2020). Since the deviation in the high-cloud cover is located more than 500 km to the east of the system it has no influence on the radiative budget of the PL.

3.3 | Qualitative comparison between AROME-Arctic and ECMWF HRES

After having shown a reasonable agreement of the AA analysis to satellite images, in this and the next Section the representation of the Thorpex PL in AA and ECMWF HRESis compared, first qualitatively and then quantitatively.

3.3.1 | Cloud structure

The emission temperature displayed in Figure 2 is not a standard output parameter from ECMWF models. However, the outgoing long-wave radiation (OLR) at the top of the atmosphere can be used instead, because the emission temperature largely determines it. The OLR from the models is typically stored as the accumulation since the start

of the simulation, whereas the pseudo-satellite images, shown earlier, depict instantaneous patterns. Therefore, the OLR from AA (Figure 3a) appears more smooth than the pseudo-satellite image (Figure 2h). Since ECMWF provides the output from HRES at 3 hr intervals, the mean OLR is displayed within 3 hr period of model integration .

The comparison of the OLR between the two NWP models reveals close agreement in the representation of the comma-shaped cloud of the PL (around 72°N, 5°E), other large-scale cloud patterns (e.g. the high clouds over the Barents Sea in the upper right corner of Figure 3a,b), and areas of cloud-free conditions. However, AA better captures the shallow convection in the CAO to the west of the PL (Figure 3 lower-left corner). Also, AA resolves individual convective clouds in much more detail than HRES (e.g. Figure 3a lower edge around 10°E). These clouds that can cause a considerable amount of precipitation.

3.3.2 | Near-surface winds

Despite differences in the cloud cover, the SLP and near-surface wind fields are quite similar in the two models at near-analysis time. Especially in the initial baroclinic stage of the PL, differences in the fields are small (not shown). Also in the convective mature stage around 0600 UTC on 4 March, which is investigated in the following, the pressure field is very similar in the two models (Figure 4d,g); e.g. the synoptic-scale low at 73°N, 20°E has a comparable depths in sea-level pressure. However, the centre of the PL is 1.5 hPa deeper in AA than in HRES. Smoothing of AA to HRES resolution with a Gaussian filter of 12.5 km radius shrinks the difference in the centre pressure to 0.7 hPa. Hence, large parts of the pressure differences are attributed to the small-scale dynamics of AA.

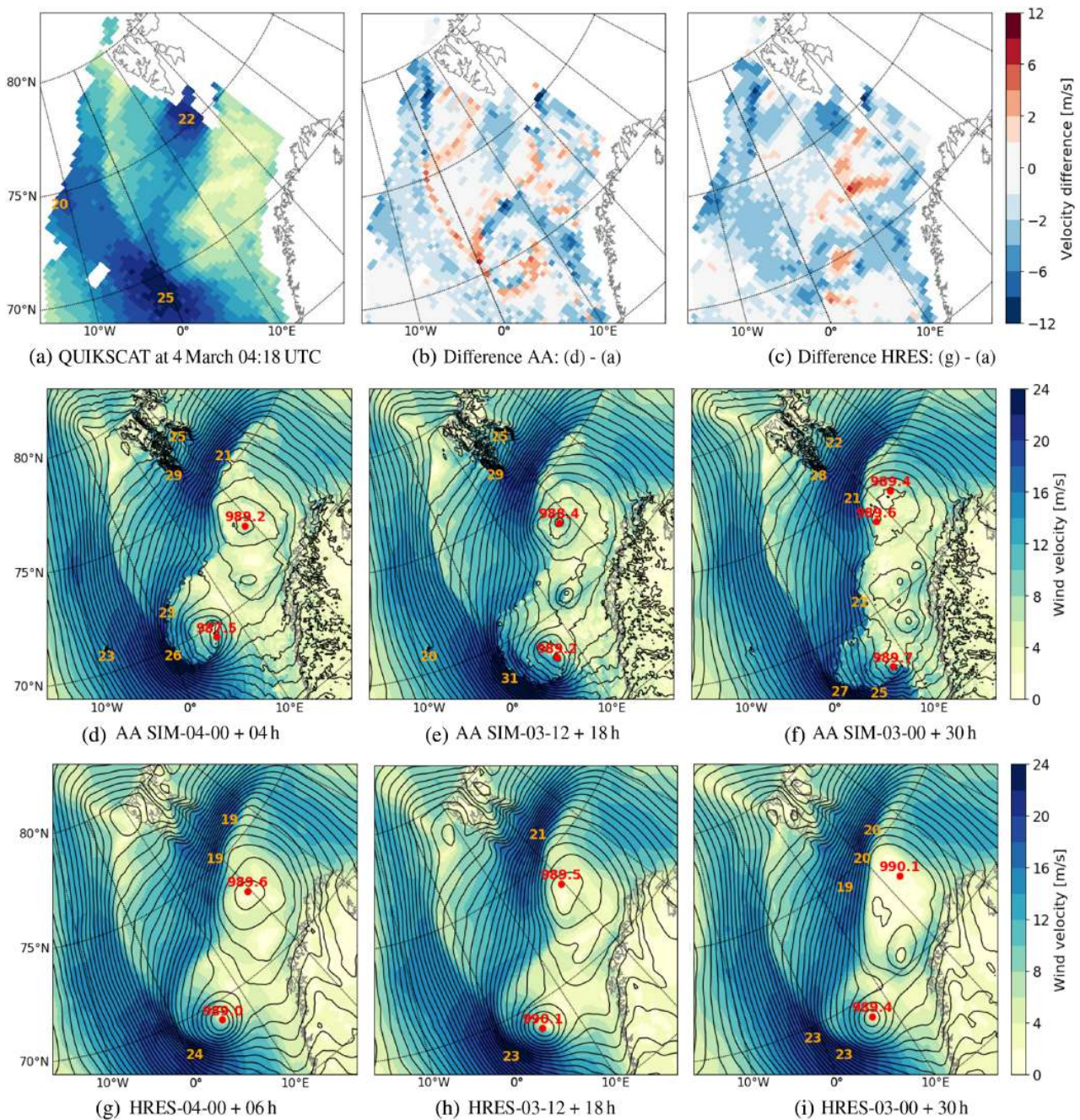AA and HRES compare well to the scatterometer wind field retrieved from QUIKSCAT (Figure 4a–c). The RMSE

FIGURE 4 (a) The 10 m wind speed (m·s^{-1}, colour shading, scale as for (d–i)) retrieved from QUIKSCAT at 0418 UTC on 4 March at the mature stage of the Thorpex PL. (d–i) The 10 m wind speed (colour shading) and sea-level pressure (contours, spacing 1 hPa) of the models AA and HRES for 0600 UTC on 4 March 2008 (but 0400 UTC for (d)). (d, g) show the near-analysis fields, (e, h) the 18 hr and (f, i) 30 hr forecasts from AA and HRES, respectively. (b, c) show the difference between the near-analysis and the QUIKSCAT satellite retrieval in (a). Red dots and numbers denote the local minima in sea-level pressure (hPa), and orange numbers the local maxima in the wind speed

of the near-surface wind fields of both models against QUIKSCAT is 1.8 m·s^{-1}. Comparable results are also found from scatterometer wind retrievals for other times (not shown).

The highest wind speed connected to this PL is observed in the western eye-wall of the PL at the edge

of the shallow CAO. The CAO is associated with the synoptic-scale situation with a low at 73°N, 20°E and both models reproduce this flow (Figure 4). The PL intensifies the flow of the CAO. Both models capture this wind intensification to the southwest of the PL. The maximum wind speed develops slightly stronger in AA (26 m·s^{-1})

than observed by QUIKSCAT (25 m·s⁻¹), and is slightly weaker in HRES (24 m·s⁻¹). AA captures the wind speed in the shallow CAO (Figure 4b,c between 10 and 0°W) better than HRES, which underestimates the wind speed by approximately 3 m·s⁻¹. This might be attributed to improved low-level dynamics in AA, due to the increased resolution.

The largest deviation of AA from QUIKSCAT occurs at the location of the fronts, which are displaced by around 30 km (Figure 4b, red line near 0°E). The fronts are considerably sharper in AA than in QUIKSCAT. Due to its coarse resolution of 25 km, QUIKSCAT underestimates the gradient of the wind speed. Furevik *et al.* (2015) for example observe a wind gradient of 11 m·s⁻¹ over a distance of 1 km in the front of a PL. Hence some of the deviations between AA and QUIKSCAT may not be associated with model deficiencies. No conclusions on wrong model dynamics of AA can be drawn from this comparison. Otherwise, the resolution of HRES appear insufficient to fully capture the flow close to the PL centre: HRES overestimates the wind speed in the almost calm centre by about 3 m·s⁻¹ (Figure 4c at 70°N, 4°E) and underestimates the wind around the centre by about 4 m·s⁻¹.

In both models, large differences from QUIKSCAT are observed in the calm sector to the east of the PL (e.g. Figure 4b,c at 70°N, 11°E). The models simulate too week winds in this area which is associated with deep cellular convection (Figure 2g). As mentioned before, none of the models correctly simulate these cells (e.g. Figure 3).

3.3.3 | Qualitative comparison to dropsondes

In order to provide a more detailed validation of the models, comparison with the dropsonde data is performed. This is done qualitatively in this subsection and quantitatively in the next section. First, the qualitative analysis is performed since it highlights the challenge of model verification with the utilised observational dataset.

Examples of horizontal cross-sections of the specific humidity for both models at 850 hPa are depicted in Figure 5a,b at the time of the second THORPEX flight, at the end of the baroclinic stage of the PL. The large-scale humidity field at 850 hPa is similar for AA and HRES, but also considerable differences are recognised (Figure 5a,b). AA shows more moisture than HRES in the baroclinic zone along the 0°meridian. In this zone, the relative humidity is exceeding 90% in AA, whereas HRES rarely simulates values close to saturation.

AA simulates small-scale convective cells (e.g. Figure 5a, around 69°N, 5°E) with the relative humidity

often reaching saturation. This causes a high local variability of the humidity field. HRES reaches near saturation only in the frontal and orographic zones, but has considerably drier conditions in areas of cellular convection (Figure 5b). This arises from the advanced skills of the convection-permitting dynamics of AA.

An enlargement of the central region of the PL simulated by AA, with the observed values of the dropsondes, is presented in Figure 5c. AA shows high local variability within this region. AA and the dropsonde observations appear to have similar values, and they also appear to have a similar spatial variability of the values. Hence it is concluded that AA captures the humidity reasonably well.

In order to validate the 3D structure of the PL in more detail, vertical cross-sections AA in equivalent potential temperature, relative humidity and wind for AA are presented in Figure 6, together with dropsonde data. The cross-section goes through the main baroclinic zone during the second flight between dropsondes 5 and 9 (red line in Figure 5c). In general, AA and the dropsondes agree well on the vertical structure of the meteorological fields and on showing high local variability in the vertical direction.

AA captures the shallow CAO (west of 2°W) with low temperature and increasing humidity from the surface towards the cloud top at approximately 800 hPa (Figure 6a,b). In the baroclinic zone around 0° E, strong temperature gradients are simulated, and the observations approximately agree. The strongest winds of up to 30 m·s⁻¹ are measured and simulated in this zone (dropsonde 7) at around 900 hPa (Figure 6c). From the low-level baroclinic zone, the isentropes (here surfaces of constant equivalent potential temperature) tilt towards the west with height in both model and observations. Along this tilt, frontal updraught is simulated, leading to increased relative humidity. Model and observations highlyagree in the frontal dynamics, which are causing the comma-shaped cloud.

To the east of the front, AA simulates strong convective updraughts of the order of 1 m·s⁻¹ at 700 hPa between dropsondes 7 and 8, high RH of almost 100% up to 600 hPa and a conditionally unstable situation from the surface to the tropopause (450 hPa). The dropsondes largely agree with this convective behaviour.

Føre *et al.* (2011) argue that this PL is to a large degree forced by upper-level potential vorticity. They partly base their argument on a tropopause downfold, which they observe by interpolatiing dropsondes 5 to 9 of the second flight (their figure 8a). In Figure 6a, the equivalent potential temperature for the same cross-section is displayed. Dropsonde 7 reports higher temperatures than dropsondes 6 and 8 between 700 and 400 hPa. Føre *et al.* (2011) argues that this indicates the tropopause downfold. However, dropsonde 7 is located close to the warm core of the
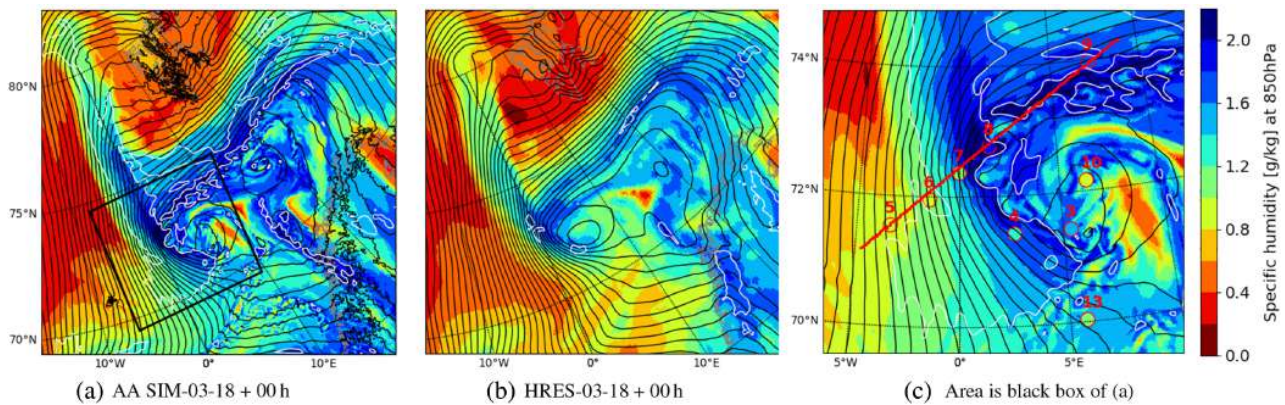
(a) AA SIM-03-18 + 00 h   (b) HRES-03-18 + 00 h   (c) Area is black box of (a)

FIGURE 5   The specific humidity at 850 hPa (colour shading), sea-level pressure (black contours, spacing 1 hPa) and relative humidity at 850 hPa (white contour at 90%) from (a) AROME-Arctic and (b) ECMWF HRES analysis at 1800 UTC on 3 March 2008. (c) Magnification of the area indicated by the black box in (a). In red circles the observations from the dropsondes released during the second THORPEX flight are depicted using the same colour code. Red numbers label the dropsondes, and the red line indicates the location of the cross-section presented in Figure 6
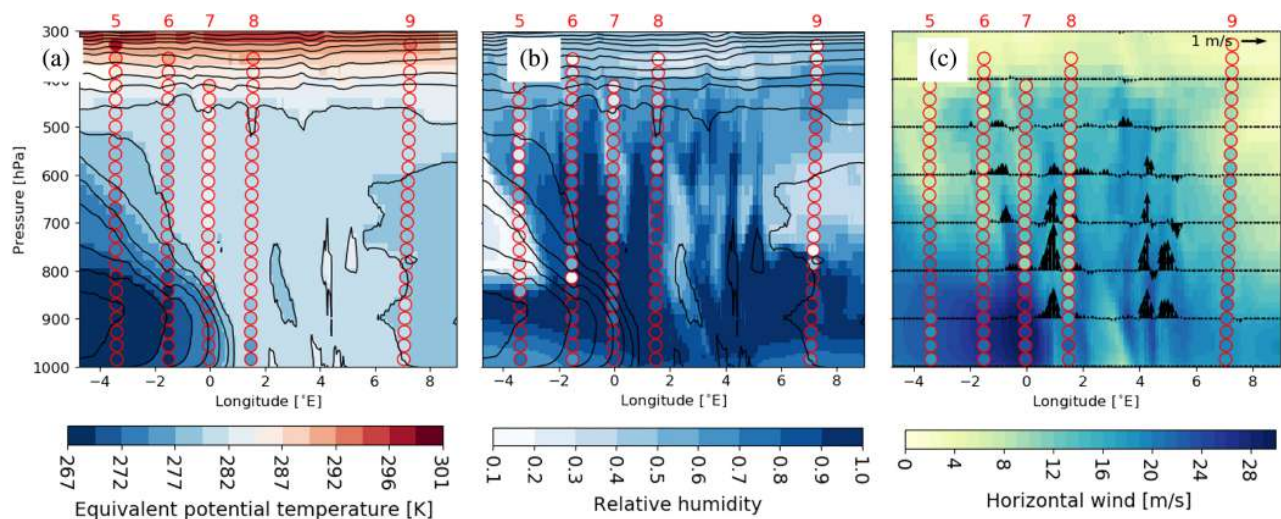

FIGURE 6   Vertical cross-section from the AA analysis at 1800 UTC on 3 March, along the line in Figure 5a during the second flight showing in colour shading (a) equivalent potential temperature), (b) relative humidity and (c) horizontal wind speed, all with data from the dropsondes in red circles. The black contours in (a,b) also depict the equivalent potential temperature with 2 K spacing.In (c) the black vertical arrows display the simulated vertical velocity. The numbers at the top label the dropsondes

PL in a convectively active region. Hence, the increased temperature for this dropsonde might be caused by adiabatic warming in the downdraught of a deep convective cell, i.e., a local tropospheric circulation not affecting the tropopause. The lidar profiles presented in figure 8 of Wagner *et al.* (2011) support this argument. An interpolation of the dropsonde data, as applied in Føre *et al.* (2011), can be misleading since it does not consider the high local variability, and the spatial extent of the interpolated values is easily exaggerated. Also, AA does not show a signal of a tropopause downfolding at the time of the

second flight but, as discussed above, the occurrence of this downfolding during the second flight is questioned here.

More horizontal cross-sections of the two models are presented in Supporting Figures S1–S4. Simulated variables (potential temperature, relative humidity and the horizontal wind velocity at 950, 850, 700 and 500 hPa) from the two models are compared to the corresponding dropsonde data of the three flights. The conclusion is qualitatively the same as for the humidity. Both models simulate the 3D structure of the PL reasonably well.

TABLE 2 Error statistics of the near-analysis time of AROME-Arctic and ECMWF HRES at different pressure levels compared to all the dropsondes released during the three flights

Level (hPa)	Model	T_{BIAS} (K)	T_{MAE} (K)	RH_{BIAS} (%)	RH_{MAE} (%)	U_{BIAS} (m·s^{-1})	U_{MAE} (m·s^{-1})
950	AA	0.47	0.76	–4.1	8.4	–0.55	2.76
	AA-avg	0.49	0.76	–4.4	7.9	–0.46	2.38
	HRES	–0.37	0.84	–4.7	9.0	0.11	2.23
850	AA	–0.22	0.64	7.4	14.7	–0.01	2.54
	AA-avg	–0.24	0.61	9.4	14.3	0.10	2.33
	HRES	–0.06	0.67	–7.4	15.9	–0.66	1.91
700	AA	–0.20	0.35	–1.1	19.1	–0.15	2.28
	AA-avg	–0.18	0.35	–1.2	17.0	–0.04	2.30
	HRES	–0.24	0.47	–9.1	15.5	–0.02	1.96
500	AA	–0.05	0.31	–0.9	14.5	0.14	2.03
	AA-avg	–0.05	0.32	–0.6	13.7	0.13	1.96
	HRES	–0.05	0.29	6.3	12.2	–0.18	1.97

Note: The BIAS and mean absolute error (MAE) in temperature (*T*), relative humidity (*RH*) and horizontal wind speed (*U*) are shown. AA-avg gives the values of AROME-Arctic at an approximate resolution of HRES by taking the local average within a radius of 12.5 km around the dropsonde. The model fields in these meteorological fields and the measured values by the dropsondes are depicted in Figures S1–S4.

AA shows much higher local variability than HRES in the potential temperature and relative humidity (Figures S2 and S4). High local variability was also observed in the lidar profile obtained by the aircraft passing the THORPEX low (Wagner *et al.*, 2011). Hence this variability appears realistic.

3.4 | Quantitative comparison between AROME-Arctic and ECMWF HRES

In the following, AA and ECMWF HRES are compared to the dropsondes released during the THORPEX flight campaign.

3.4.1 | Statistical scores as compared to dropsondes

In the previous sections, different fields were compared by visual inspection. Now, error statistics, such as the BIAS and mean absolute error (MAE), obtained by comparison to all the dropsondes released in the three THORPEX flights are compared for the model products (Table 2).

The MAE is in general about the same for AA at near-analysis time as for HRES. AA and HRES perform approximately equally well for the compared variables (temperature, horizontal wind speed and relative humidity) at different pressurelevels. Smoothing the AA data by applying a local average in a circle of radius

12.5 km (approximately the grid-spacing of HRES), slightly improves the MAE for AA, especially in the relative humidity and wind speed. However the skill is still similar to HRES.

The high variability of the meteorological fields makes the objective model validation challenging. For some dropsondes, model and observation are considerably different, e.g. Figure 5 dropsondes 4 and 7. For these locations, the model simulates high variability, and a small displacement creates large differences in the values. For example, the convective cells and the frontal zone of the PL are observed to be slightly displaced in AA. In classical error scores, such as the mean absolute error, the displacement of a correctly simulated feature is penalised twice: firstly since the feature is not captured at the correct location and secondly since it is simulated at a wrong location. Hence, the error statistics are weaker than if the feature had not been present in the model at all. Smoothing of AA corrects for some of this problem, as the error scores improve. However, this also degrades some of the skills of AA to simulate local extreme values. Therefore a spatial verification technique of the two models is applied and is now presented.

3.4.2 | Fuzzy verification

A "fuzzy" verification technique, which relaxes the requirement for exact collocation of observations and model simulations, is employed. Multi-event contingency

tables (Ebert, 2008) utilising the Hanssen and Kuipers (HK) score are displayed in Figure 7 for AA and HRES simulations compared to dropsonde observations from all three flights.

AA generally has highest skills on a scale of 10–20 km (Figure 7a,d), whereas HRES performs best over scales of 40–80 km (Figure 7b,e). At large scales, the models lose accuracy since the False Alarm Rate becomes as large as the Hit Rate. AA loses accuracy at smaller scales (40–80 km) than HRES (160–320 km), since the high local variability of AA generates lots of false alarms. HRES has higher skills at larger scales since the method considers displacement of features but the false alarms do not increase considerably due to a low local variability of HRES as compared to AA (e.g. compare Figure 5a,b). For the displayed fields, the skill score of AA improves slightly (around 0.1) if AA is smoothed to the HRES grid-spacing since the False Alarm Rate is reduced (not shown).

For the relative humidity, AA performs better than HRES for a scale of 10 km (Figure 7c). This indicates that AA has improved the representation of convective cells relative to HRES. Also in the wind speed, AA has very high skills at small scales (≤ 20 km) and large intensities (≥ 20 m·s^{-1}, Figure 7d) and is considerably advanced compared to HRES (Figure 7f). This means that AA considerably improves the capture of local extreme winds.

The fuzzy verification gives some indication of the strength and weaknesses of the models. However, it does not reveal which of the observed weather features are correctly reproduced by the models. Therefore, the qualitative validation that was previously presented is of importance.

3.4.3 | Comparison of vertical profiles

Now, the average vertical profiles of AA and HRES analysis are validated against the dropsondes released in each of the three THORPEX flights independently. The averaging is expected to correct for some of the random displacement errors between observation and models.

The average of the vertical profiles of each flight in potential temperature, relative humidity and the horizontal wind of the dropsondes and the corresponding AA and HRES grid cells containing the dropsonde is presented in Figure 8a,c,e. Figure 8b,d,f presents the BIAS and MAE of the profiles. In general, the analyses of AA and HRES agree reasonably well with the dropsonde data.

For the initial stages of the PL during the first two flights, the highest wind speeds are both observed and modelled at low levels, and the wind speed decays towards mid-levels. This wind profile is a signature of

a reverse-shear baroclinic system with a low-level jet (Terpstra *et al.*, 2016). At the mature stage (Flight 3) the wind speed and direction are almost constant in the vertical, an indication that the system is quasi-barotropic. The models capture this behaviour and do not show significant differences from the dropsondes.

For temperature, AA is warmer than the dropsondes close to the surface by 0.6–1.3 K during the first two flights. The near-surface temperature BIAS is almost as large as the MAE, meaning that the model is too warm at most dropsonde locations. This is likely attributed to overestimated surface sensible heat fluxes in the model, which might be caused by a SST warm BIAS. The strong and cold winds are cooling the sea surface, whereas in the model the SST is fixed during the simulation and only updated once a day in model cycles starting at 0000 UTC. This delayed update of the SST can cause a near-surface warm BIAS in the model. In Section 4 it is found that the PL development is quite sensitive to SST perturbations.

At approximately 850–800 hPa, this warm BIAS vanishes. Hence, on average AA is more unstable in the boundary layer than is indicated by the observations, which is also the case during the third flight (Figure 8b,d,f). Also, HRES appears to be more unstable below 900 hPa.

In terms of relative humidity, AA is on average too dry close to the surface and too moist around 800 hPa at the first two flights. This humidity profile indicates that AA overestimates shallow convection. The reduced stability in AA might explain the exaggerated convection. The near-surface dry BIAS of AA likely leads to overestimated surface latent-heat fluxes. During flight 3 both AA and HRES are considerably drier than the dropsondes through the whole troposphere, mainly around 700 hPa where the relative humidity is on average 25% lower than observed. This indicates that deep convection, different from shallow convection, is under-represented in the models. It is possible that AA would benefit from a deep convection parametrization.

3.5 | Forecast error growth

Until now, the analysis times of AA and HRES have been validated. Now short-term forecasts of the two weather-forecasting models are compared for this PL.

In the third column of Figure 2, the pseudo-satellite images of the AA simulations initiating at 0000 UTC on 3 March (SIM-03-00) are presented in order to validate the forecast quality. Also, simulations initiated at earlier and later times are compared to satellite images, but not presented here. The clouds are in general captured well by
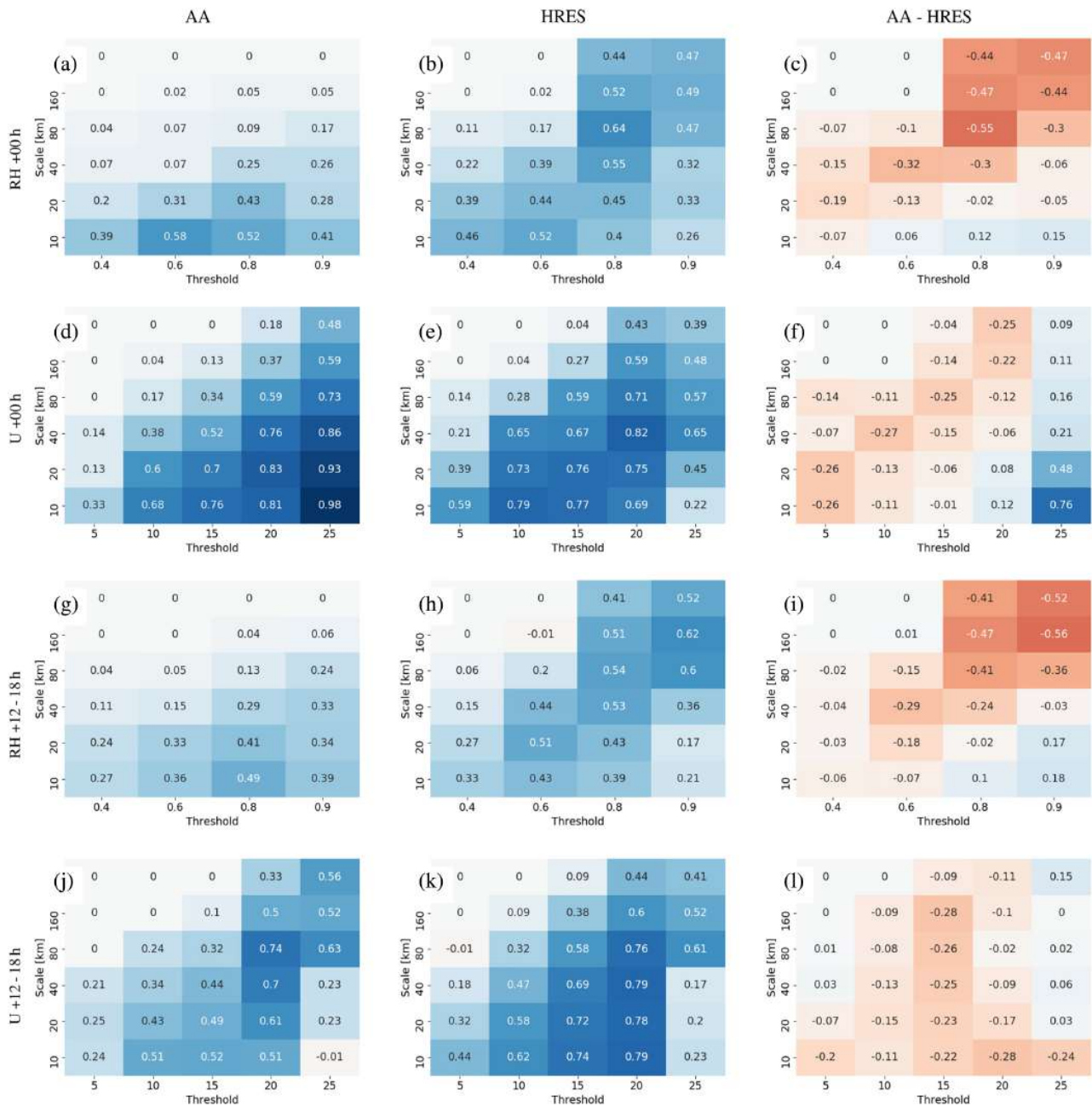
FIGURE 7 The multi-event contingency table (Atger, 2001) with the Hanssen and Kuipers (HK) score calculated for (a, d, g, j) AROME-Arctic and (b, e, h, k) HRES simulations at near-analysis time (+00 hr) and for short forecasts (+12–18 hr) compared to dropsonde observations from all three flights at pressure levels 950, 850, 700 and 500 hPa for (a, b, g, h) relative humidity (RH) and (d, e, j, k) wind speed (*U*). The HK score (Hit Rate minus False Alarm Rate) is 1 for a perfect model, 0 for no skill and can take negative values for higher False Alarm Rates than Hit Rates. The threshold defines the level above which an observion , or the simulated value at the location of the observation, is a hit, for RH in % and for U in m·s⁻¹. The scale defines the radius within which a hit is searched in the models. (c, f, i,l) show the differences between the HK scores of AA and HRES

AA, both in structure and placement within the first 24 hr of the simulation. For longer forecast times, the evolution of the PL starts to deviate from the observations. On the morning of 4 March, the PL is observed to be a singular

spiral-like system (Figure 2j). In contrast, after 30 hr of model integration in SIM-03-00, the PL has divided into two centres (Figure 2l), a leading one (at 69°N, 7°E) and one at the intersection point of the fronts (68°N, 0°E).
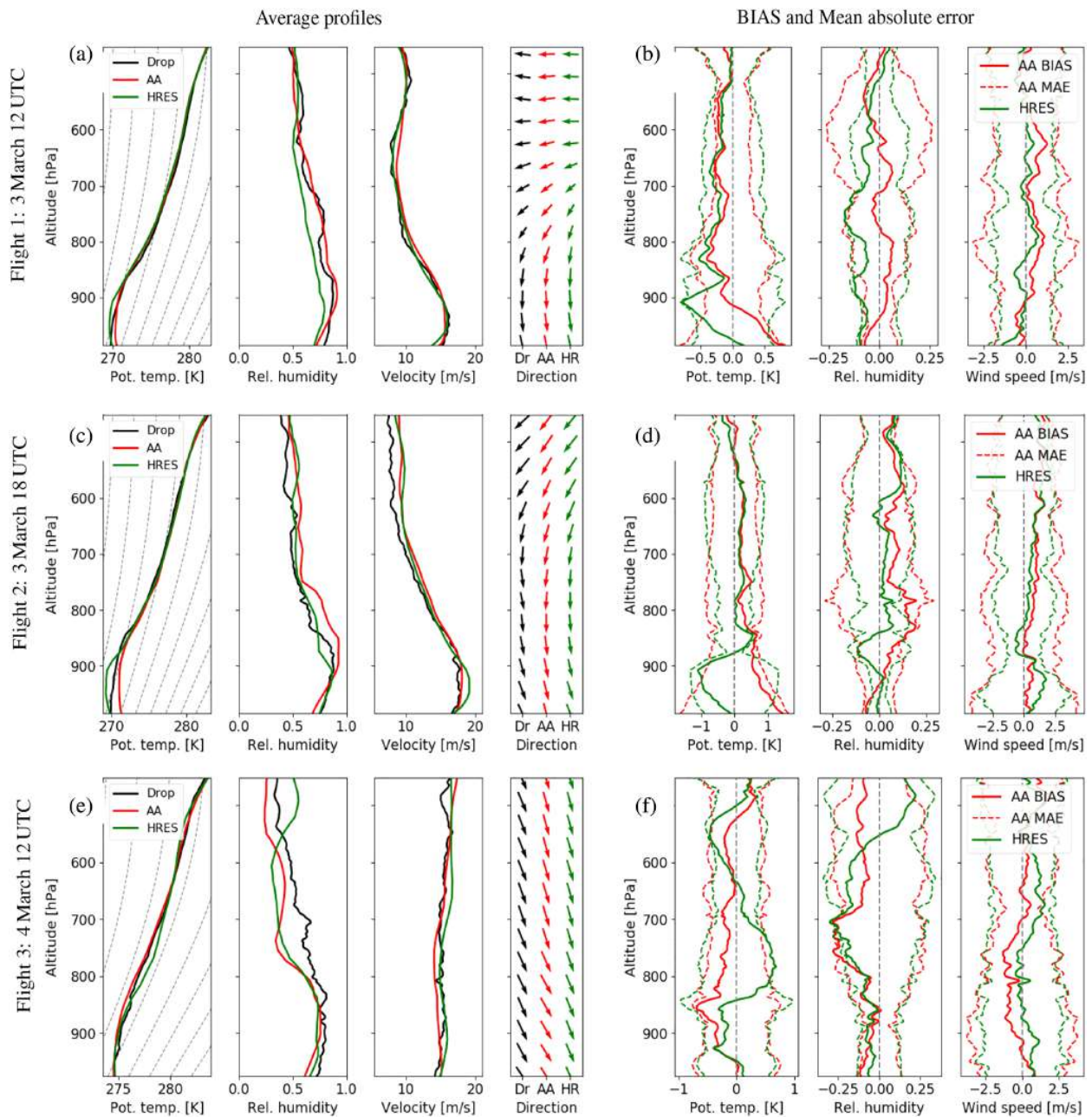
FIGURE 8 (a, c, e) Average of the potential temperature, relative humidity, horizontal wind speed and wind direction from the THORPEX dropsondes (black) released during the three flights, and from the analysis of the AA (red) and HRES (green) at grid cells containing the dropsonde at the corresponding time. The area within which the dropsondes are released are displayed by blue boxes in Figure 2. The position and measured values of the dropsondes with simulated model fields for some vertical levels are also shown in Figures S1–S4. In the potential temperature plots, moist adiabats are displayed with grey dashed lines. (b, d, f) The BIAS (solid line) and mean absolute error (MAE, dashed line) for AA (red) and HRES (green) compared to the dropsondes released during each of the flights shown in the first column. Also –MAE is added to highlight when a negative BIAS explains the total MAE

The development of two centres originates within the domain. Already after 19 hr of integration (Figure 2f), a false leading centre with a closed isobar develops around 71°N, 5°E ahead of the frontal intersection at 72°N, 0°E, where the observed PL develops.

Tracks of the PL centre for different AA simulations are presented in Figure 9a. As described in Section 2.6, the detection of the PL centre is constrained to condense the system to one if the separation of the centres is small enough. In the simulation starting 12 hr earlier, SIM-02-12,
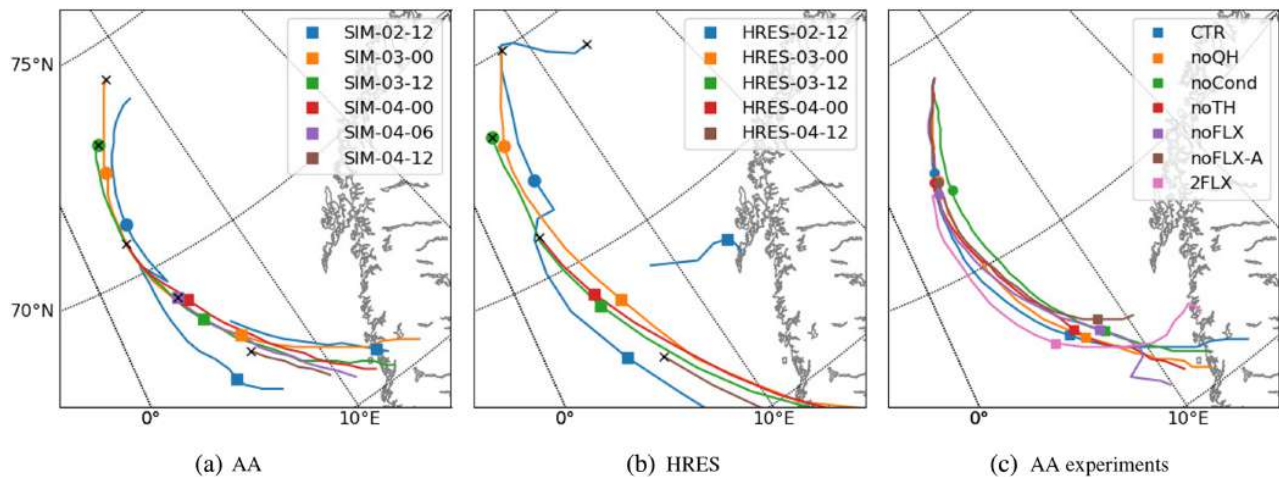
FIGURE 9 The tracks of the PL centre, defined by the local maxima in the filtered vorticity, for simulations at different initial times for (a) AROME-Arctic and (b) ECMWF HRES. Coloured circles and boxes denotes the location of each centre at 1200 UTC on 3 March and 0600 UTC on 4 March, respectively. The location at analysis times is indicated by black crosses. Note that the tracks are influenced by the boundary of the domain for the final time steps of the PL in AA. (c) depicts the tracks of the different sensitivity experiments performed with AA

the split of the PL is considerably more pronounced than in SIM-03-00, and the centre at the frontal intersection moves out of the domain (Figure 9a; the track of SIM-02-12 disappears at 66°N, 7°E since the vorticity centre leaves the domain). A split of the PL develops also in HRES-02-12 (Figure 9b) which shows that this erroneous development is an artefact across models. However, HRES-03-00, differently from SIM-03-00, correctly simulates one PL centre, and predicts its location quite accurately for the mature stage. AA generally overestimates the propagation speed of the PL in the forecasts. Already at 1200 UTC on 3 March, AA forecasts the PL considerably further to the south than observed (Figure 9a; compare orange and blue circles to the green circle with the "x", displaying the analysis time). The displacement grows until 0600 UTC on 4 March, which means that AA overestimates the propagation speed of the system. The sensitivity experiments presented in the next section reveal that suppressing condensational heat release increases the propagation speed of this PL (Figure 9c), even though it weakens the large-scale flow (Figure 10i). More discussion about this is given in Section 4.6. Hence, the faster propagation of the PL in the AA forecast might be caused by erroneous representation of convective processes, as discussed earlier.

The spatial verification of AA and HRES against dropsondes is also applied to 12–18 hr forecasts (Figure 7g–l). It reveals that AA loses some of its skill in the small scales after short forecast times. This is most pronounced in the wind speed for high values (compare Figure 7d,j), but also appears in the small scales in the humidity (compare Figure 7a,g). HRES appears not to

lose skill in the short-term forecast when compared to the analysis. At the analysis time, AA is considerably improved over HRES for high wind speed at small scales (Figure 7f). AA loses these advantages already after short forecast times of 12–18 hrs (Figure 7l). It appears that the error growth is faster for AA than for HRES. Some of this error growth is attributed to a larger displacement of the PL for short-term forecasts by AA than by HRES (compare green and red point in Figure 9a,b).

In Figure 4e,f,h,i, near-surface wind fields in the 18 and 30 hr forecasts of AA and HRES are depicted for the mature stage of the PL. The development of the PL is quite different for the AA forecasts when compared to the near-analysis. The 18 hr forecast simulates maximum wind speeds in the vicinity of the PL of up to 31 m·s^{-1} (Figure 4e), whereas 25 m·s^{-1} is observed by the QUIKSCAT instrument (Figure 4a). The 30 hr forecast experiences the separation and the overestimated propagation speed of the centre (Figure 4f). In contrast, HRES forecasts appear to differ considerably less for different lead times (Figure 4g–i). This is in accordance with Køltzow *et al.* (2019), who find that model errors grow faster for near-surface fields in high-resolution models, such as AA, than in HRES. An explanation could be given by the conceptual model of three-stage error growth suggested by Zhang *et al.* (2007): (a) convective instability causes fast error growth on small scales, which saturates within approximately 1 hr due to the complete displacement of convective cells, (b) the errors expand in space and influence the large-scale balanced flow, and (c) baroclinic

instability leads to slow growth of the balanced large-scale error component.

In AA, the model error caused by displaced convective cells is larger than for HRES, where convection is fully parametrized and therefore smoothed. Also, the qualitative validation presented earlier indicates that in AA convection is more confined than observed. Hence, larger initial perturbations are influencing the large-scale flow and eventually growing by baroclinic instability. Due to a high Coriolis parameter at high latitudes and a more shallow troposphere than in midlatitudes, this growth can be faster in PL active regions. Possibly the forecast quality of convective-permitting models could be improved by emphasising a subgrid-scale convective parametrization.

4 | SENSITIVITY EXPERIMENTS

The previous section reveals that AA performs a high-quality simulation of the PL within the first 24 hr of the model integration. Forecasts of more than 18 hr show some deviation from the observations, but the PL is still reasonably well predicted.

In this section, the development mechanisms of the PL are further investigated. For this, several sensitivity experiments are performed. The aim is to improve physical understanding of the PL development and to identify the critical components for accurate forecasts of PLs. Hence, the role of surface turbulent heat fluxes and latent heat release are investigated. Some of the forecast error in AA might be associated with a lack of updates to the SST, as discussed in the previous section. Therefore, the sensitivity of the PL to the SST is tested. All experiments are initiated at 0000 UTC on 3 March and integrated for 48 hr, until the landfall of the PL. A summary of the experiments and their main results is given in Table 1.

The wind field of the PL in the mature stage, at 0300 UTC on 4 March, in the different sensitivity experiments are displayed in Figure 10. The development of the PL in the different experiments is compared in Figure 11 by three intensity parameters, (a) the filtered vorticity, (b) the maximum wind speed, and (c) the minimum sea-level pressure, as well as by the maximum baroclinicity ($\nabla \theta_{850}$) in the vicinity of the PL centre. Additionally, the evolution of the sensible and latent surface heat flux and the latent heat release by condensation around the PL are depicted in Figure 12. Section 2.7 provides details about the computation of these parameters.

Wagner *et al.* (2011) and Føre and Nordeng (2012) mainly utilise the SLP for analysis of the PL evolution in the sensitivity experiments. However, the SLP has to be considered with caution. The SLP of the PL centre

is constant until 2100 UTC on 3 March (Figure 11a or Føre and Nordeng, 2012). Afterwards, the SLP rises even though the vorticity and wind speed are still increasing. This demonstrates that the local SLP is a misleading measure of the strength of the PL, since the SLP strongly depends on the synoptic-scale environment. The SLP of the synoptic-scale low is strongly affected in the sensitivity experiments (e.g. noFLX and 2FLX in Figure 10d,f). Hence, comparing the SLP among simulations can lead to wrong conclusions on the evolution of the PL itself. Therefore the SLP is only occasionally discussed in the following.

Føre and Nordeng (2012) perform experiments with delayed deactivation of different fluxes, which we generally consider valuable, but only when combined with a careful analysis. Because an immediate response of the SLP is lacking, they conclude that all the investigated diabatic components have a small direct effect on the PL. They also conclude, from growing SLP perturbations after long simulation times, that effects of different heat fluxes become more important at later stages of the PL. However, the SLP is a synoptic-scale field that is changing slowly and perturbations accumulate over time. For this reason, only the time derivative of the SLP difference from the control run could allow such conclusions. Other variables, like the wind speed and the vorticity that are investigated here, reveal the effects on the PL more directly. Hence due to inclusion of additional intensity measures, the analysis of the sensitivity experiments performed here is more comprehensive than the analysis in the previously mentioned studies. Additionally, the strength of the baroclinicity, turbulent fluxes and condensational heat release in the vicinity of the PL are included. In this way, the cause and effect of the diabatic components are distinguishable.

4.1 | Control run

In the control run (CTR), the vorticity of the PL increases until 0300 UTC on 4 March (27 hr into the simulation), the mature stage of the PL (Figure 10). Afterwards, the vorticity decays. The strongest winds associated with the PL, of up to 27 m·s^{-1}, are simulated between 22 and 32 hr into the simulation.

The baroclinicity ($\nabla \theta_{850}$) is high (>5K/100 km) until 1800 UTC on 3 March – called the initial baroclinic stage – and then steadily decreases in the mature stage (Figure 11a). After 0600 UTC on 4 March, the baroclinic zone is along the edge of the domain, and therefore these values are not displayed. However, a simulation with a domain further south, initialised from interpolation of the ECMWF HRES without the spin-up phase, reveals a
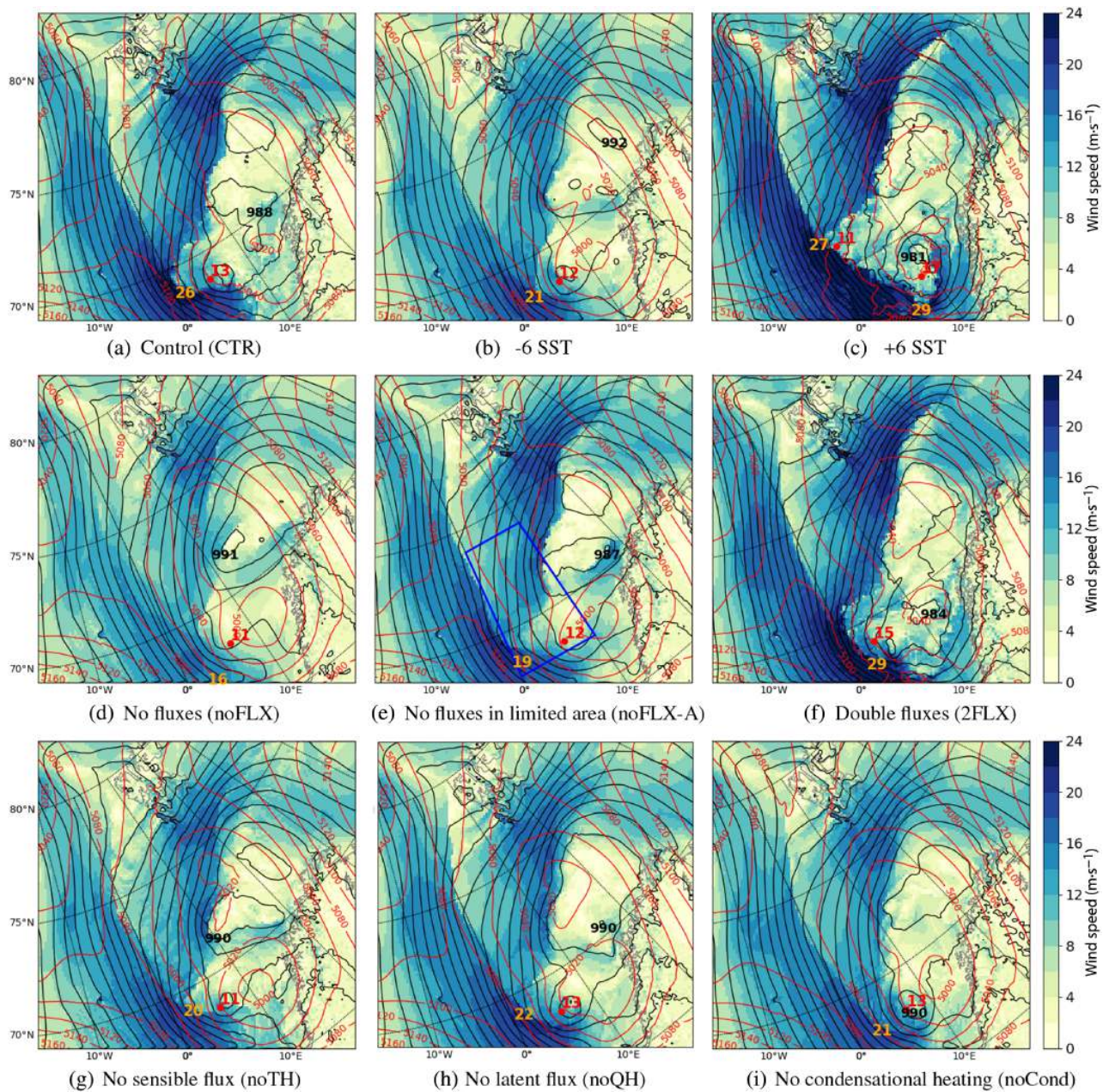
FIGURE 10 The 10 m wind speed (colour shading), sea-level pressure (black contours, spacing 2 hPa) and 500 hPa geopotential height (m, red contours) after 27 hr of model integration for different simulations starting at 0000 UTC on 3 March 2008. Red dots denote local maxima in the filtered relative vorticity at 850 hPa which defines the centres of the PL, and the red number indicates the strength in $10^{-5}\,\text{s}^{-1}$. The orange number depicts the maximum wind speed within 400 km of the PL centre. Black numbers show sea-level pressure minima

comparable decay of the baroclinicity in the mature stage of the PL (not shown).

Both turbulent heat fluxes around the PL increase in the baroclinic stage of the PL and eventually decrease in the mature stage after 0000 UTC on 4 March (Figure 12a). The sensible heat flux is approximately 40% higher than the latent heat flux until the middle of the mature stage of the PL at 0600 UTC on 4 March. At this stage, the air

masses around the PL are warmed considerably compared to the initial stage, so they can hold more moisture.

Interestingly, the release of latent heat by condensation is smaller than the sensible heat flux in the baroclinic stage but then it triples within 6 hr in the convective mature stage. It is also recognised that the latent heat release is higher than the surface latent heat flux by 20–30% in the baroclinic stage and more than double in theconvective
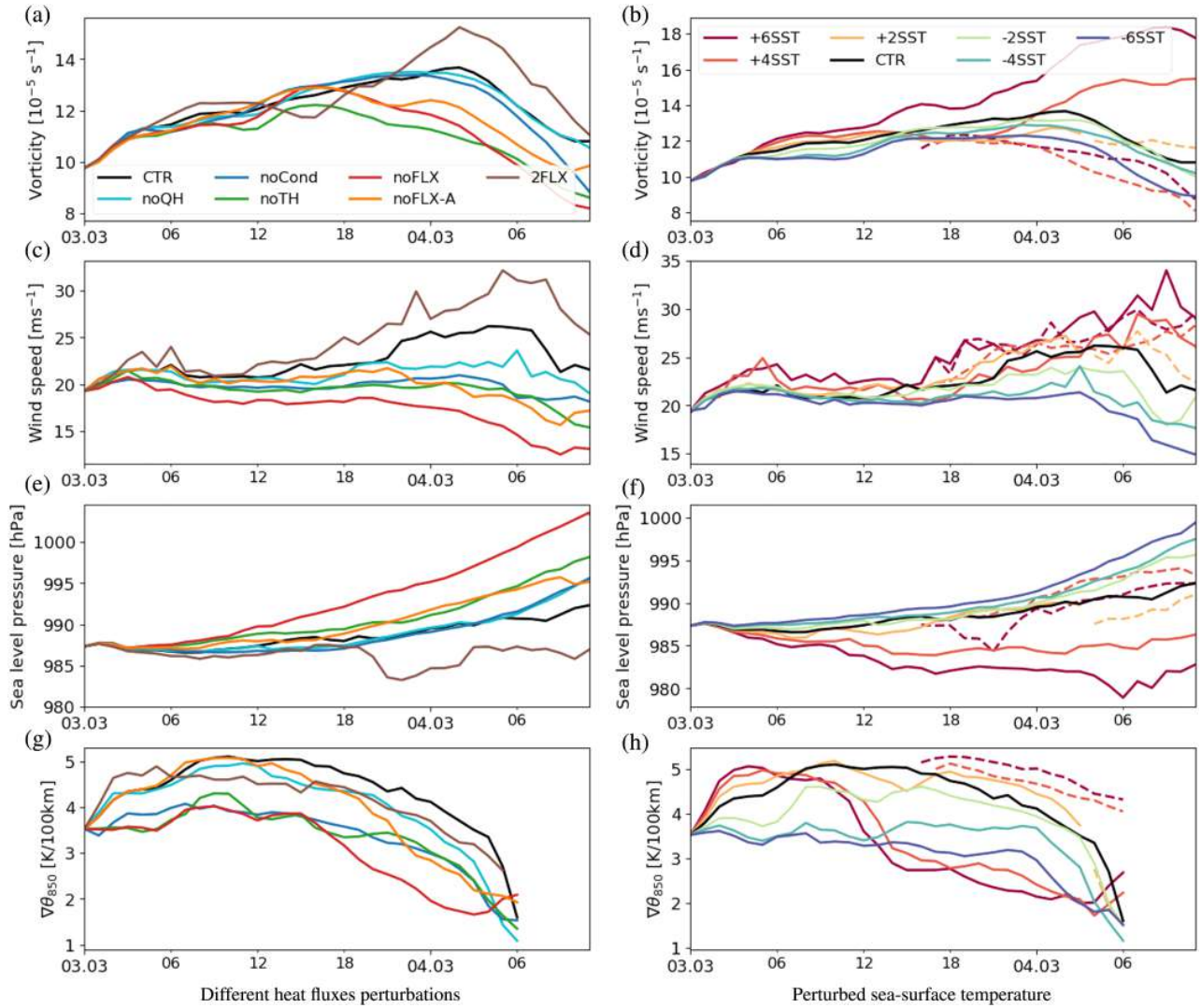
FIGURE 11 The evolution of the intensity of the PLs, as shown in Figure 10, in experiments with (a, c, e, g) perturbed fluxes, and (b, d, f, h) perturbed sea-surface temperature. The intensity is expressed as (a, b) the filtered vorticity of the centre, (c, d) the maximum wind speed within 400 km, and (e, f) the minimum sea-level pressure within 100 km distance of the vorticity centre of the PL. (g, h) show the evolution of the maximum baroclinicity ($\nabla\theta_{850}$) within 400 km distance of the PL centre. In (a, c, e, g) for +4/6SST where the PL develops two separate centres, the solid lines show the intensity of the leading centre and dashed lines of the secondary centre. Note different scales in the strength of the parameters between the two columns.

stage. This indicates that a substantial amount of the moisture is transported into the PL.

Føre and Nordeng (2012) conclude that low-level baroclinic energy conversion dominates the PL development, while other processes have a minor direct impact on the PL intensity. Here, we suggest that baroclinicity initiates and intensifies the PL, and convection maintains the PL in the mature phase of the PL from 0000 UTC on 4 March. In the following, more supporting evidence is given for this hypothesis.

4.2 | No turbulent fluxes

The role of heat fluxes from the surface is investigated in an experiment (noFLX) without both turbulent heat flux components, the sensible and the latent heat flux, over water surfaces (Figure 12d).

The maximum wind speed in the first 18 hr, measured in the western eye-wall of the PL, is somewhat weaker (4 m·s^{-1}) than in CTR. The local wind amplification is hampered since the sharp frontal structure at the western

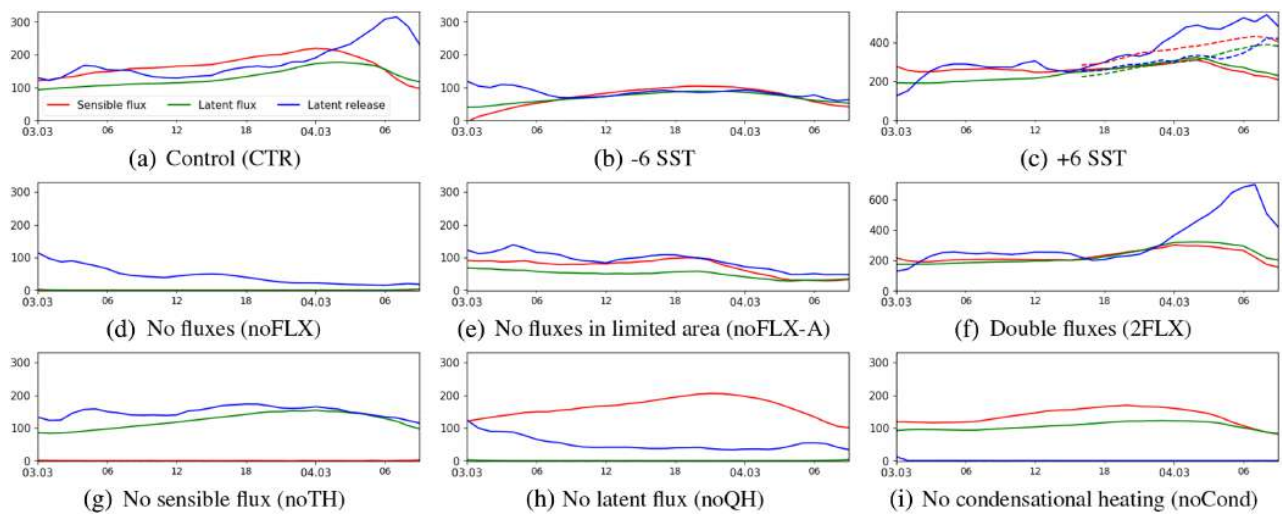**FIGURE 12** The sensible and latent surface heat fluxes and latent heat release in condensation ($W \cdot m^{-2}$) during the evolution of the PL for the different sensitivity experiments. The mean in each variable is calculated within a circle of 300 km radius around the PL centre. Note that the western eye-wall, the area of strongest surface heat fluxes, propagates along the edge of the domain after 0300 UTC on 4 March, which partly explains the reduced fluxes at that time. Note also the different vertical scales in (c) and (f). In (c) the dashed lines depict values for the secondary centre

side of the PL does not develop in the experiment without turbulent fluxes (Figure 10d). Since the baroclinicity ($\nabla\theta_{850}$) is weakened in noFLX within the first 18 hr, it is suggested that turbulent fluxes act to maintain the baroclinicity. Papritz and Spengler (2015) argue that surface sensible heat flux and latent heat release are among the main processes for the development of baroclinicity. The experiments presented later reveal that these two components are also important for the baroclinicity for this PL case.

After 18 hr of simulation, the vorticity and wind speed of the PL decay quickly, and only a moderate trough is present at 0300 UTC on 4 March (Figure 10d). Hence it is concluded that the turbulent fluxes are responsible for maintenance and further intensification of the system. These results are in accordance with Wagner *et al.* (2011) and Føre and Nordeng (2012) who performed comparable sensitivity experiments with different models without heat fluxes in simulations starting at 0600 UTC and 1200 UTC, respectively, on 3 March. They also found that the deactivation of surface heat fluxes leads to a weakening of the PL in terms of increasing SLP in the centre and prevention of convection. As here, Føre and Nordeng (2012) argue that the initial baroclinicity is "consumed" without surface heat fluxes.

4.3 | Doubled turbulent fluxes

A sensitivity experiment (2FLX) is performed where the turbulent fluxes calculated by the bulk formula are

doubled in the model simulation. This leads approximately to a doubling of the latent heat flux. In contrast, the sensible heat flux is only increased by approximately 50% because the near-surface vertical temperature gradient is reduced faster than in CTR.

In 2FLX, the PL develops similarly to CTR within the first 18 hr of the model integration, the initial baroclinic stage (Figure 11a). The baroclinicity is weaker in 2FLX because the near-surface air is heated more in the shallow CAO than on the warm and calm side of the front (not shown). Presumably, this hampers an even stronger development of the PL in the baroclinic stage in 2FLX. Interestingly, the baroclinicity develops the strongest when the turbulent fluxes are as strong as simulated in CTR. Both an increase and a decrease of the surface fluxes reduce the baroclinicity. In noFLX, the baroclinicity is "consumed," whereas in 2FLX, the baroclinicity is maintained but at a weaker level than in CTR.

From 0000 UTC on 4 March, during the convective mature stage, the intensification of the PL is strongly enhanced in 2FLX. This is indicated by an increase in the vorticity, an increase of the maximum wind speed from 27 (in CTR) to 36 $m \cdot s^{-1}$ (in 2FLX) and a decrease of the SLP by approximately 5 hPa until the PL encounters landfall. In this phase, the latent heat release is approximately doubled compared to CTR, leading to vortex intensification. Hence, in conclusion, the increased heat fluxes have a minor effect in the initial baroclinic stage. However, the accumulation of additional moisture leads to enhanced development in the convective stage when the latent heat is released.

4.4 | No turbulent fluxes in an area around the centre

In noFLX-A, the heat flux is turned off in a fixed area (0–10°E and 68–74°N, see blue box in Figure 10e) through which the centre is propagating within the first 27 hr with a distance of approximately 100 km to the boundary of the area10. The PL develops comparably to CTR in the initial baroclinic stage until 1800 UTC on 3 March, even though surface fluxes in the near vicinity of the PL are suppressed. In the mature stage, the omitted fluxes in the limited area prevent the PL intensifying further and developing a centre (Figure 10e). Most of the CAO, where the highest wind speed is measured, are receiving the same heat flux in noFLX-A as in CTR. For this reason, the wind strength is about the same as in CTR for the first 21 hr. Subsequently, the wind speed decays in noFLX-A, since the PL does not develop a mature stage in this experiment.

After 27 hr of model integration, at the time of highest intensity of the PL in CTR, the system leaves the area of suppressed heat fluxes (Figure 10e). However, the latent heat release does not increase in noFLX-A when the PL leaves this area, and the trough does not intensify in this experiment. In the baroclinic stage, the system appears not to accumulate enough moisture and not to develop a local statically unstable environment to further intensify convectively in the mature stage. This is in accordance to Terpstra *et al.* (2015) who conclude that interdependent thresholds in the humidity and instability are necessary for a diabatic boost of the PL development.

In conclusion, even though the PL receives some moisture from the surrounding, the local heat fluxes, particularly those leading to the accumulation of moisture and the destabilisation of the boundary layer in the baroclinic stage, are required for the development of the PL into the convective mature stage.

4.5 | Surface sensible and latent heat fluxes and latent heat release

First we give some considerations to the role of the two latent heat components. In the experiment without surface latent heat flux (noQH), moisture is still present from the initial conditions and to some extent by the boundary conditions. This moisture leads to a mean latent heat release of approximately $50 \, W \cdot m^{-2}$ around the PL (Figure 12h), approximately one third of the mean heat release of CTR in the baroclinic phase. In noCond the condensational heat release is completely suppressed. Consequently, the PL is weaker than in noQH, mainly as regard the wind speed, but also for the convective mature phase when it comes to vorticity. In general, it seems more meaningful to

investigate the effect of the heat release by condensation than the surface fluxes of latent heat. The former measures the consumption of "fuel," whereas the latter measures the production of the "fuel," which is not necessarily consumed.

Now the role of the different diabatic components is investigated. From the baroclinic phase, the vorticity of the PL is weakened similarly in the experiments without sensible heat flux (noTH) and with both flux components suppressed (noFLX; Figure 11a). Differently, effects on the vorticity are only recognisable later in the mature phase for suppressed condensational heat release (noCond), and negligible for suppressed latent heat flux (noQH). Hence, in the initial baroclinic stage, the sensible heat flux mainly favours the vortex intensification of this PL.

In contrast, for both noTH and noCond, the wind development is weaker than in CTR but stronger than in noFLX (Figure 11c). This means that the maximum wind speed is dependent on both sensible heat flux and latent heat release. Hence, the two diabatic components act differently on the intensity measures. Also for both noTH and noCond, the baroclinicity is weakened as in noFLX. Hence, the sensible heat flux and condensational heat release appear to be important for increasing and maintaining the baroclinicity in the initial stage of the PL (Figure 11g).

In noQH, the wind speed and baroclinicity are less influenced in the initial stage than in noCond, because the moisture present still condenses. First in the mature stage, the wind speed development is weaker in noQH than in CTR. Both in noQH and noCond the intensification of the PL in the convective mature stage, which is fuelled by latent heat release, is hampered. In noCond the latent energy is not released (by construction) and in noQH too little moisture accumulates in the baroclinic stage.

Interestingly, even though the latent heat flux is approximately the same in noTH as in CTR, the PL does not develop a convective mature stage in noTH, as the latent heat release and wind speed do not increase. This raises two suggestions: (a) the PL has to reach a certain strength before the engine of latent heat release can maintain the system in the mature stage, and (b) a destabilisation of the boundary layer by sensible heat flux is required to make latent heat release an effective intensification mechanism. Both effects may be coexisting and interacting. This suggests that all diabatic components are required to accomplish the full PL development.

These results are mainly in accordance with Føre and Nordeng (2012), but we come to opposite conclusions in two respects: (a) from theoretical considerations, the surface latent heat flux cannot be more important than the condensational heat release for the development of
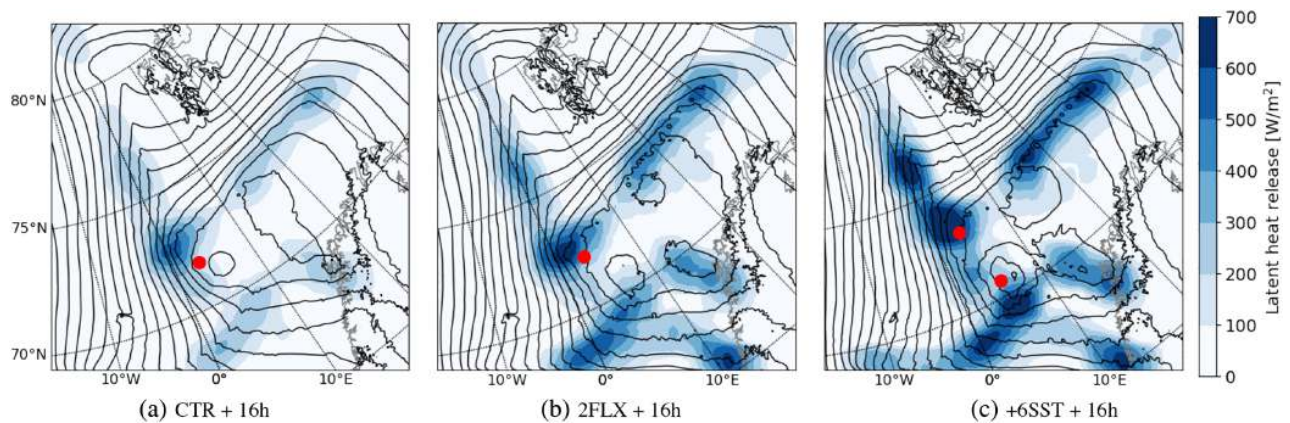
FIGURE 13   The latent heat release by condensation (colour shading) and sea-level pressure (contours, spacing 2 hPa) for (a) CTR, (b) 2FLX and (c) +6SST, all after 16 hr model integration. The red dot denotes the location of the vorticity centre of the PL. The latent heat release is derived from the precipitation rate and smoothed with a Gaussian filter of 100 km radius

dynamical systems, which is also observed for this PL, and (b) sensible heat flux is more relevant than the latent heat flux for the development of the PL in the baroclinic stage.

4.6 | Role of latent heat release on the polar low track

It is observed that the PL is "pulled" towards the area of the strongest convection. In Figure 9c the tracks of the PL in the different sensitivity experiments are displayed. At 1200 UTC on 3 March only small differences are visible in the location since the perturbations had little time to grow. However, in the experiment without condensational heat release, the PL at this time is already deflected towards the east. This deflection is explained by convection and the associated latent heat release by condensation mainly occurring on the western side of the PL (Figure 13a). The heating induces a positive potential vorticity anomaly below this heat source, hence at low levels, following the Diabatic Rossby Vortex concept (Terpstra *et al.*, 2015). This process "pulls" the PL towards the area of the strongest latent heating and hence reduces the propagation speed of the PL. Therefore, in the experiment without condensational heating, the missing "drag" from the convection leads to a faster propagation of the PL until 0600 UTC on 4 March.

Likewise, in the experiments noFLX, noFLX-A and noQH (where latent heat release in the vicinity of the PL is dampened), the PL has also propagated faster until 0600 UTC on 4 March (Figure 9c). In contrast, the PL was slowed down in 2FLX where latent heat release is amplified (Figure 13b). This is especially recognisable since the large-scale flow is decreased in noCond and noFLX (Figure 10), which would decrease the propagation speed

of the PL, and the opposite for 2FLX. In noFLX-A, the large-scale flow is little affected, but, as for the before mentioned experiments, the PL propagates faster due to reduced local convection. The sensible heat flux, different to the latent heat release by condensation, has a negligible influence on the PL track (compare noTH to CTR).

4.7 | Perturbation of the sea-surface temperature

In order to examine the sensitivity of the PL to the sea-surface temperature (SST), experiments are performed with perturbed SST from −6 to +6 °C with 2 °C increments. This generally provides more realistic perturbations of the surface fluxes than the experiments with adapted flux components (e.g. noTH, noQH, noFLX and 2FLX). The increase (decrease) of the SST by 6 °C leads to approximately a doubling (halving) of both heat flux components in the area of the PL development (Figure 12a–c).

The initial baroclinic stage is highly influenced by the SST perturbations (Figure 11b,d,f,h). For higher (lower) SSTs, the baroclinicity is considerably stronger (weaker) than in CTR. The large-scale baroclinic environment is enhanced (weakened) by increased (decreased) SSTs, as the warm area over the sea becomes warmer (colder) by increased (decreased) heat fluxes, while the cold region, which is determined by the conditions over the Arctic sea ice, is unaffected. Interestingly, the baroclinicity does not exceed a value of approximately $5 \, \mathrm{K \cdot (100 \, km)^{-1}}$ for any experiment (Figure 11h), even though the baroclinic development is faster for increased SST, as can be seen in higher vorticity and wind speeds in Figure 11b,d for the initial stage. Likely at the threshold of $5 \, \mathrm{K \cdot (100 \, km)^{-1}}$, the baroclinicity

is produced and consumed at approximately the same rate.

The Arctic front develops considerably more strongly for increased SSTs (compare CTR to +6SST in Figure 13a,c at 69°N, 0–7°E). The initial PL centre in +6SST connects to the diabatic heating associated with the Arctic front. Since the front lies ahead of the PL, the initial centre is accelerated and "pulled" out of the baroclinic zone. Therefore the baroclinicity of the initial PL centre is low from 1200 UTC on 3 March in +6SST. Some hours later, the PL centre in +6SST intensifies further and develops into a convective system with mean values of latent heat release above $300\,\mathrm{W}{\cdot}\mathrm{m}^{-2}$ around the centre and of more than $500\,\mathrm{W}{\cdot}\mathrm{m}^{-2}$ from 0000 UTC on 4 March, approximately twice as high as in CTR (Figure 12a,c).

Also in +2FLX the Arctic front is enhanced as compared to CTR, but is considerably less than in +6SST (Figure 13). The initial PL centre does not connect the Arctic front as in +6SST, possibly since the latent heat release in the front close to the PL centre is too weak to "pull" the PL centre out of the baroclinic zone.

In +4/6SST, a second PL centre develops around 1600 UTC on 3 March at the intersection point between the baroclinic front (73–77°N, 2°E) and the convergence zone (74°N, 2–30°E in Figure 13c). It is accompanied by high baroclinicity which slowly decays, whereas latent heat release is increasing (dashed lines in Figures 11h and 12c). This also indicates a transition into a convective system for the secondary centre. However, this transition is not finalised before the PL reaches the edge of the domain. This second centre is significantly slowed down by the strong latent heat release at the intersection point behind the centre (Figures 13c and 10c).

In the mature stage, the difference in the PL intensity for various SST perturbations is very pronounced. It is estimated that 1 °C of SST increase leads to enhanced near-surface winds of 1–$2\,\mathrm{m}{\cdot}\mathrm{s}^{-1}$ (Figure 11b). The intensity of the PL appears to increase nonlinearly with the warming of the sea surface. Different observations capture this.

- The perturbation of the vorticity and SLP nonlinearly increase with higher SSTs. The vorticity of +6SST almost doubles compared to CTR, whereas the vorticity of −6SST is only slightly lower than in CTR. The difference in SLP between CTR and −6SST is approximately 4 hPa in the mature stage of the PL, whereas the difference between CTR and +6SST is about 10 hPa. However, note that the SLP perturbations are partly caused by a deepening of the synoptic low.
- The kinetic energy increases with the square of the velocity. The wind speed increases at least linearly with

increased SST, and the area of stronger winds expands for increased SST (Figure 10k,l)

- With highly increased SSTs (+4/6SST), the PL develops a second centre (Figure 10c). The intensity of the second centre is displayed by dashed lines in Figures 11b and 12c. It reaches the same intensity as the first centre in terms of the wind speed.

The experiments performed here suggest a much higher sensitivity of the PL intensity to the SST thanwas obtained by simulation of an axisymmetric non-hydrostatic idealised model by Linders *et al.* (2011). They obtain an increase of the wind speed of about $0.6\,\mathrm{m}{\cdot}\mathrm{s}^{-1}$ and a decrease of the core pressure of $-0.6\,\mathrm{hPa}$ per °C increase in SST. The increase/decrease rates obtained here are more than twice as high.

The high sensitivity of the PL development to the SST suggests that updated sea surface fields are essential for a realistic simulation of PLs. A coupled atmosphere–ocean weather prediction model could be beneficial for the forecast of PLs, especially since the strong heat fluxes can lead to a modification of the SSTs. One would expect that the CAO leads to a cooling of the ocean surface. However for one PL event, Sætra *et al.* (2008) demonstratedthat turbulent mixing of warm sub-surface currents by strong winds led to a rapid surface warming of 1–2 °C within a few hours. This SST warming is a positive feedback for further PL intensification.

5 | DISCUSSION AND CONCLUSION

In the first part of the study, the capability of the regional weather-prediction model AROME-Arctic (AA) for representing the THORPEX PL, which occurred on 3–4 March 2008 in the Norwegian Sea, is validated against observations and compared to the performance of the global model ECMWF HRES. In the second part of the study, the development mechanisms involved in this PL are investigated by sensitivity experiments with AA.

5.1 | Model validation

The comparison of the simulated cloud fields of AA with satellite images reveals the high quality of the model. AA captures the observed cloud types with a comparable structure at approximately the correct location, which is a large improvement over HRES. However, AA tends to simulate the deep and shallow convective cells more discretely than observed. The model appears to include too much

convection in the model dynamics but to underestimate subgrid-scale convection.

The near-surface wind fields of both models compare well to the scatterometer wind field from QUIKSCAT. The largest differences between AA and the satellite product occur in the zones of dislocated fronts. In this zone, the sharpness of the front in AA appears more appropriate than both QUIKSCAT and HRES.

This PL was also measured by dropsondes released from three flights during the IPY-THORPEX campaign. A one-to-one comparison of the vertical profiles from the dropsondes to the model grid cells is inappropriate, because the correct simulation of a local feature, such as a convective cell, at a wrong location, leads to a double punishment in classical error scores. Therefore, the skills in error statistics, such as the mean absolute error, are similar for AA and HRES, even though AA improves in the qualitative validation. For this reason, a "fuzzy" verification technique, which relaxes the requirement for spatial collocation of observations and simulations, is applied to the dropsonde data. This reveals that AA has higher skill than HRES for small scales (≤ 10 km) and for high intensities (e.g. for wind speeds ≥ 20 m·s^{-1}).

A few more conclusions are drawn from the comparison of AA to the dropsondes:

- The model has a near-surface warm BIAS in the initial baroclinic stage. The BIAS is likely caused by the lack of updating of the SST boundary fields in the model.
- The model is statically too unstable in the planetary boundary layer (Figure 8a,c compare the potential temperature profile to the moist adiabats), which might be caused by the near-surface warm BIAS.
- The humidity profiles indicate that shallow convection is too strong in the model. This could be induced by too weak stability of the boundary layer. Hence, an erroneous SST field appears to cause the misrepresentation of a range of other variables in the model.
- The model might overestimate the depth of deep convective cells, possibly because the implicit treatment of the model produces cells that are too confined. A deep convective parametrization scheme could relax this problem.

For predictions beyond 18 hr, AROME-Arctic deviates more from reality than the ECMWF operational model. This is in accordance with Køltzow *et al.* (2019), who also observe that error growth is faster in AA than in ECMWF HRES. Some of the faster error growth is associated with a larger dislocation of the PL in AA forecasts than in HRES forecasts. From sensitivity experiments, it is concluded that erroneous representation of convection (and connected latent heat release) has a considerable influence on the displacement of the PL in AA.

In this study, only the deterministic forecast of the models is validated. A comparison of several ensembles of each model could give additional information about the model uncertainty. Also, a comprehensive study of more PL cases would be relevant in order to examine the forecast time upto which the high-resolution AA provides more accurate predictions than ECMWF HRES.

5.2 | Polar low development

The second focus of this study is the investigation of the development of this PL. The wind profile, cloud structure, strength of baroclinicity and heat fluxes indicate that the PL initially develops in a baroclinic zone, a remnant of an occluded synoptic-scale low. As it intensifies, the baroclinicity decreases, and the PL develops into a quasi-barotropic convective system with strong latent heat release and a warm core.

There are two general remarks on the common practice of the analysis of PLs:

- The sea-level pressure used as an intensity proxy of a PL has little relevance because it is mainly determined by the synoptic-scale environment. Most other studies that have investigated this PL have focused mainly on this parameter for the comparison of sensitivity experiments.
- The surface latent heat flux has no direct influence on the PL development. It merely creates the potential for latent heat release by condensation. The latter is of significant interest for the investigation of PLs.

Sensitivity experiments, summarised in Table 1, are performed with AA in order to study the PL in more detail. The vortex of the PL develops surprisingly similarly within the first 18 hr of the simulation in all experiments. We conclude that, in the initial baroclinic stage, the vortex development is mainly driven by the synoptic-scale environment and has limited sensitivity to different diabatic effects. However, the surface sensible heat flux and condensational heat release both contribute to enhance the baroclinicity. If these heat sources are suppressed, the PL weakens from the end of the baroclinic stage. In the initial baroclinic stage, both the sensible heat flux and the latent heat release locally intensify the near-surface wind by approximately 2 m·s^{-1}. Both diabatic contributions lead to a sharpening of the frontal zones.

In the mature stage, the baroclinicity is low, and latent heat release appears to maintain and intensify the PL, hence it is of a convective nature. At this stage, only

less than half of the consumed moisture is locally produced. The convective mature stage does not develop in the absence of sensible heat flux, latent heat flux, or latent heat release. Instead, the PL intensity decreases. Also, if the turbulent fluxes are suppressed in a limited area, through which the PL propagates in the initial baroclinic stage, the PL does not intensify further. The vortex intensifies in the mature stage when the surface fluxes or the SST are increased. Therefore, we conclude that the development of the mature stage depends on the sensible heat flux having destabilised the local environment around the PL core sufficiently, and enough moisture having accumulated for condensational heat release. It is also observed that the PL is "pulled" towards the area of the strongest convection. Following the Diabatic Rossby Vortex concept, the latent heat release associated with the convection induces a positive potential vorticity anomaly at low levels. This anomaly intensifies the PL and "pulls" the centre towards the area of latent heating. Hence, the propagation of the PL is influenced by the location of the convective area.

Sensitivity experiments with perturbed SST reveal an increased maximum in near-surface wind speed connected to the PL of $1-2\,\mathrm{m\cdot s^{-1}}$ per K warming of the sea surface. This estimate is more than twice as high as the one provided by idealised experiments by Sætra *et al.* (2008). Further, the intensity of the PL increases nonlinearly with higher SSTs. For increased SSTs of 4 and 6 °C, a secondary PL centre develops after the first centre has propagated out of the baroclinic zone. The development of coupled atmosphere–ocean weather prediction systems with more sophisticated SSTs might considerably improve the predictions of PLs.

We conclude that baroclinicity provides the cradle for this PL, and diabatic processes in a conditionally unstable environment further intensify the system in the mature stage. The correct simulation of the latter stage appears to be more challenging for NWP models than the initial baroclinic stage.

ORCID

Patrick J. Stoll ![ORCID] https://orcid.org/0000-0003-1120-2049

REFERENCES

Atger, F. (2001) Verification of intense precipitation forecasts from single models and ensemble prediction systems. *Nonlinear Processes in Geophysics*, 8(6), 401–417.

Bengtsson, L., Andrae, U., Aspelien, T., Batrak, Y., Calvo, J., de Rooy, W., Gleeson, E., Hansen-Sass, B., Homleid, M., Hortal, M., Ivarsson, K.-I., Lenderink, G., Niemelǎ, S., Nielsen, K.P., Onvlee, J., Rontu, L., Samuelsson, P., Muñoz, D.S., Subias, A., Tijm, S., Toll, V., Yang, X. and Køltzow, M.Ø. (2017) The HARMONIE-AROME model configuration in the ALADIN-HIRLAM NWP system. *Monthly Weather Review*, 145(5), 1919–1935.

Bracegirdle, T.J. (2006). The role of convection in the intensification of polar lows. PhD thesis, University of Reading, UK.

Brümmer, B., Müller, G. and Noer, G. (2009) A polar low pair over the Norwegian Sea. *Monthly Weather Review*, 137(8), 2559–2575.

Douglas, M.W., Fedor, L.S. and Shapiro, M.A. (1991) Polar low structure over the northern Gulf of Alaska based on research aircraft observations. *Monthly Weather Review*, 119(1), 32–54.

Douglas, M.W., Shapiro, M.A., Fedor, L.S. and Saukkonen, L. (1995) Research aircraft observations of a polar low at the East Greenland ice edge. *Monthly Weather Review*, 123(1), 5–15.

Ebert, E.E. (2008) Fuzzy verification of high-resolution gridded forecasts: a review and proposed framework. *Meteorological Applications*, 15(1), 51–64.

ECMWF (2018) *Changes in ECMWF model.* Available at: https://www.ecmwf.int/en/forecasts/documentation-and-support/changes-ecmwf-model; accessed 19 February 2020.

Field, P.R., Brožková, R., Chen, M., Dudhia, J., Lac, C., Hara, T., Honnert, R., Olson, J., Siebesma, P., de Roode, S., Tomassini, L., Hill, A. and McTaggartâĂŘCowan, R. (2017) Exploring the convective grey zone with regional simulations of a cold air outbreak. *Quarterly Journal of the Royal Meteorological Society*, 143, 2537–2555.

Føre, I., Kristjánsson, J.E., Saetra, Ø., Breivik, Ø., Røsting, B. and Shapiro, M. (2011) The full life cycle of a polar low over the Norwegian Sea observed by three research aircraft flights. *Quarterly Journal of the Royal Meteorological Society*, 137, 1659–1673.

Føre, I. and Nordeng, T.E. (2012) A polar low observed over the Norwegian Sea on 3–4 March 2008: high-resolution numerical experiments. *Quarterly Journal of the Royal Meteorological Society*, 138, 1983–1998.

Furevik, B.R., Schyberg, H., Noer, G., Tveter, F. and Röhrs, J. (2015) ASAR and ASCAT in polar low situations. *Journal of Atmospheric and Oceanic Technology*, 32(4), 783–792.

Gilleland, E., Ahijevych, D., Brown, B.G., Casati, B. and Ebert, E.E. (2009) Intercomparison of spatial forecast verification methods. *Weather and Forecasting*, 24(5), 1416–1430.

Gilleland, E., Ahijevych, D.A., Brown, B.G. and Ebert, E.E. (2010) Verifying forecasts spatially. *Bulletin of the American Meteorological Society*, 91(10), 1365–1376.

Holtslag, A.A.M., Svensson, G., Baas, F., Basu, S., Beare, B., Beljaars, A.C.M., Bosveld, F.C., Cuxart, J., Lindvall, J., Steeneveld, G.J., Tjernstrøom, M. and Van De Wiel, B.J.H. (2013) Stable

atmospheric boundary layers and diurnal cycles: challenges for weather and climate models. *Bulletin of the American Meteorological Society*, 94(11), 1691–1706.

Innes, H.M., Kristiansen, J., Kristjánsson, J.E. and Schyberg, H. (2011) The role of horizontal resolution for polar low simulations. *Quarterly Journal of the Royal Meteorological Society*, 137, 1674–1687.

Køltzow, M., Casati, B., Bazile, E., Haiden, T. and Valkonen, T. (2019) A NWP model intercomparison of surface weather parameters in the European Arctic during the year of polar prediction Special Observing Period Northern Hemisphere 1. *Weather and Forecasting*, 43, 959–983.

Kristjánsson, J.E., Barstad, I., Aspelien, T., Føre, I., Godøy, Ø., Hov, Ø., Irvine, E., Iversen, T., Kolstad, E., Nordeng, T.E., McInnes, H., Randriamampianina, R., Reuder, J., Saetra, Ø., Shapiro, M., Spengler, T. and Ólafsson, H. (2011) The Norwegian IPY-THORPEX: polar lows and Arctic fronts during the 2008 and Andøya campaign. *Bulletin of the American Meteorological Society*, 92(11), 1443–1466.

Linders, T., Saetra, Ø. and Bracegirdle, T.J. (2011) Limited polar low sensitivity to sea-surface temperature. *Quarterly Journal of the Royal Meteorological Society*, 137, 58–69.

Markowski, P. and Richardson, Y. (2010) *Mesoscale Meteorology in Midlatitudes*. John Wiley & Sons, Chichester, UK.

Müller, M., Batrak, Y., Kristiansen, J., Køltzow, M.A.Ø., Noer, G. and Korosov, A. (2017a) Characteristics of a convective-scale weather forecasting system for the European Arctic. *Monthly Weather Review*, 145(12), 4771–4787.

Müller, M., Homleid, M., Ivarsson, K.-I., Køltzow, M.AØ., Lindskog, M., Midtbø, K.H., Andrae, U., Aspelien, T., Berggren, L., Bjørge, D., Dahlgren, P., Kristiansen, J., Randriamampianina, R., Ridal, M. and Vignes, O. (2017b) AROME-MetCoOp: a Nordic convective-scale operational weather prediction model. *Weather and Forecasting*, 32(2), 609–627.

Nordeng, T.E. and Rasmussen, E.A. (1992) A most beautiful polar low. A case study of a polar low development in the Bear Island region. *Tellus A*, 44(2), 81–99.

Papritz, L. and Spengler, T. (2015) Analysis of the slope of isentropic surfaces and its tendencies over the North Atlantic. *Quarterly Journal of the Royal Meteorological Society*, 141, 3226–3238.

Rasmussen, E.A. and Turner, J. (2003) *Polar Lows: Mesoscale Weather Systems in the Polar Regions*. Cambridge University Press, Cambridge, UK.

Rojo, M., Claud, C., Mallet, P.-E., Noer, G., Carleton, A.M. and Vicomte, M. (2015) Polar low tracks over the Nordic Seas: a 14-winter climatic analysis. *Tellus A*, 67. https://doi.org/10.3402/tellusa.v67.24660

Sætra, O., Linders, T. and Debernard, J.B. (2008) Can polar lows lead to a warming of the ocean surface?. *Tellus A*, 60(1), 141–153.

Seity, Y., Brousseau, P., Malardel, S., Hello, G., Bénard, P., Bouttier, F., Lac, C. and Masson, V. (2011) The AROME-France convective-scale operational model. *Monthly Weather Review*, 139(3), 976–991.

Shapiro, M.A., Fedor, L.S. and Hampel, T. (1987) Research aircraft measurements of a polar low over the Norwegian Sea. *Tellus A*, 39(4), 272–306.

Stoll, P.J., Graversen, R.G., Noer, G. and Hodges, K. (2018) An objective global climatology of polar lows based on reanalysis data. *Quarterly Journal of the Royal Meteorological Society*, 144(716), 2099–2117.

Terpstra, A., Michel, C. and Spengler, T. (2016) Forward and reverse shear environments during polar low genesis over the North East Atlantic. *Monthly Weather Review*, 144(4), 1341–1354.

Terpstra, A., Spengler, T. and Moore, R.W. (2015) Idealised simulations of polar low development in an Arctic moist-baroclinic environment. *Quarterly Journal of the Royal Meteorological Society*, 141, 1987–1996.

Valkonen, T.M., Stoll, P.J., Batrak, Y., Køltzow, M., Schneider, T.M., Stigter, E.E., Aashamar, O.B., Støylen, E. and Jonassen, M. (2020) Evaluation of a sub-kilometre NWP system in an Arctic fjord-valley system in winter. (unpublished manuscript)

Verhoef, A., Vogelzang, J. and Stoffelen, A. (2016). Reprocessed Sea-Winds L2 winds validation report. Technical Report SAF/OSI/C-DOP2/KNMI/TEC/RP/221. KNMI, De Bilt, Netherlands.

Wagner, J.S., Gohm, A., Dörnbrack, A. and Schäfler, A. (2011) The mesoscale structure of a polar low: airborne lidar measurements and simulations. *Quarterly Journal of the Royal Meteorological Society*, 137, 1516–1531.

Yanase, W., Fu, G., Niino, H. and Kato, T. (2004) A polar low over the Japan Sea on 21 January 1997. Part II: a numerical study. *Monthly Weather Review*, 132(7), 1552–1574.

Yanase, W. and Niino, H. (2005) Effects of baroclinicity on the cloud pattern and structure of polar lows: a high-resolution numerical experiment. *Geophysical Research Letters*, 32(2). https://doi.org/10.1029/2004GL020469

Yanase, W. and Niino, H. (2007) Dependence of polar low development on baroclinicity and physical processes: an idealized high-resolution numerical experiment. *Journal of the Atmospheric Sciences*, 64(9), 3044–3067.

Zhang, F., Bei, N., Rotunno, R., Snyder, C. and Epifanio, C.C. (2007) Mesoscale predictability of moist baroclinic waves: convection-permitting experiments and multistage error growth dynamics. *Journal of the Atmospheric Sciences*, 64(10), 3579–3594.

SUPPORTING INFORMATION

Additional supporting information may be found online in the Supporting Information section at the end of this article.

/10

Paper III:

Polar lows as moist-baroclinic cyclones in four vertical-shear environments.

P.J. Stoll, R.G. Graversen, T. Spengler, A. Terpstra.
in final preparation for the submission to Weather and Climate Dynamics.

Polar lows as moist-baroclinic cyclones in four vertical-shear environments.

Patrick Johannes Stoll[1], **Rune Grand Graversen**[1,2], **Thomas Spengler**[3], **and Annick Terpstra**[3]

[1]Department of Physics and Technology, Arctic University of Norway, Tromsø, Norway
[2]Norwegian Meteorological Institute, Norway
[3]Geophysical Institute, University of Bergen, and Bjerknes Centre for Climate Research, Bergen, Norway

Correspondence: Patrick Johannes Stoll (patrick.stoll@uit.no)

Abstract. By applying self-organising maps, polar lows are classified with regard to their environment in which the cyclogenesis and system maintenance occurs. The method is applied to 370 polar lows from the N-E Atlantic, which were obtained by matching mesoscale cyclone tracks from the reanalysis ERA-5 with polar lows listed by the Norwegian meteorological institute (STARS-dataset). ERA-5 reproduced most (92%) of the polar lows.

The classification reveals that polar lows develop in four different vertical shear configurations. These are characterised by the vertical shear angle that provides the angle between the thermal wind vector and the direction of the background flow. We show that the shear angle organises the dynamics of the systems. This confirms the usefulness of the categorisation into forward and reverse-shear polar lows in order to describe the dynamical configuration. We further expand this categorisation by right and left-shear polar lows that propagate towards colder and warmer environments, respectively. Systems in all four shear categories are all intensifying by moist baroclinic instability. Systems that develop by a hurricane-like mechanism are not found.

1 Introduction

Polar lows (PLs) are intense mesoscale cyclones that occur in the extended winter season at high latitudes (Renfrew, 2015). They develop at locations where the polar air mass is advected over open water, situations generally called marine cold-air outbreaks (Rasmussen and Turner, 2003).

PLs are one of the major natural hazards in the polar region, due to their gale-force wind (Wilhelmsen, 1985), large amount of snow fall (Harrold and Browning, 1969), low visibility, high waves (Orimolade et al., 2016), and potential for icing on ships and airplanes (Samuelsen et al., 2015).

Due to the small scale, typically 100 - 500km in diameter (Rojo et al., 2015) and short lifetime, often 6 - 48h, PLs are challenging to observe and to predict (Businger and Reed, 1989). Their sudden and unexpected appearance may have caused the capsizing of numerous vessels in the past (Wilhelmsen, 1981). Today, the numerical-weather prediction (NWP) is sophisticated enough to simulate these systems (e.g. Yanase et al., 2004; Claud et al., 2004). The models do, however, have issues predicting the exact location and intensity of PLs (e.g. Føre et al., 2012; Stoll et al.).

The analysis of NWP models for PL situations is complicated by the fact that PLs appear in very different forms (Rojo et al., 2015). The scientific community has not yet come to a consensus regarding a unified conceptual model describing their development (Rasmussen and Turner, 2003). This study provides a suggestion for such a conceptual model.

Two main concepts have been suggested in order to explain the intensification of PLs. One describes polar lows as baroclinic disturbances of a smaller scale than synoptic mid-latitude cyclones (e.g. Harrold and Browning, 1969; Reed, 1979; Reed and Duncan, 1987). The other explains PL development as convectively driven by latent heat release, similar to tropical cyclones (e.g. Rasmussen, 1979; Emanuel and Rotunno, 1989), either by the CISK (conditional instability of second kind) or WISHE (wind induced surface heat exchange) closure.

Multiple studies indicate that PLs may best be explained by a combination of the two concepts. Sardie and Warner (1983) argued that neither dry baroclinic, nor pure CISK modes grow fast enough at the same scales of observed

polar lows, by using a three-layer, two-dimensional, quasi-geostrophic model. Instead, the growth rate and scale could be explained by a moist baroclinic development. Also, Terpstra et al. (2015) demonstrated that interplay of baroclincity and diabatic effects can lead to rapid intensification, which would not be created if only one of the two processes was active.

Yanase and Niino (2007) simulated the growth of disturbances by dry baroclinic instability and by CISK in an idealised marine polar air mass by using a 5-km-resolution non-hydrostatic model. They found the fastest intensification in an environment with high baroclincity supported by latent heat release. The vortex in these environments developed a comma-shaped cloud, which is typical for extra-tropical, baroclinic cyclones. In experiments without a temperature gradient, an axis-symmetric vortex developed, which resembles a tropical cyclone, but with slow growth rates. However, this axis-symmetric vortex, which is different to a vortex in a baroclinic environment, was very sensitive to the form of the initial disturbance.

In general, Yanase and Niino (2007) found a smooth transition in the polar-low dynamics with varying baroclinicity. For this reason, the existence of a "polar-low spectrum" ranging from comma-shaped "pure baroclinic", to spirali-form "pure-convective" systems was suggested in the 1980s (p.157 Rasmussen and Turner, 2003). The contribution from baroclinicity and latent heat release to the intensification varies from case to case within the "spectrum", and even during the lifetime of single systems.

Bracegirdle and Gray (2008) note that most PLs occupy a hybrid between the extremes in the "spectrum". We, however, question whether the extremes of the "polar-low spectrum" are actually occurring. PLs that appear to be hurricane-like in their mature stage were often described to initially develop by baroclinic instability (e.g. Nordeng and Rasmussen, 1992; Føre et al., 2012). Also, a PL developing dry-baroclinically without latent heat release has to our knowledge not been observed.

The orientation of the baroclinic background field as compared to the mean flow varies between PLs (Rasmussen and Turner, 2003). Some PLs are observed in forward shear environments (e.g. Reed and Blier, 1986; Hewson et al., 2000) similar to typical mid-latitude cyclones, although in the polar air mass and not at the polar front. Other PLs develop in reverse shear environments (e.g. Reed, 1979; Bond and Shapiro, 1991; Nordeng and Rasmussen, 1992). Duncan (1978) defined forward and reverse shear environments by a vertical shear angle close to $0°$ and $180°$, respectively. The vertical shear angle is given by the angle between the vectors of the tropospheric mean wind and the thermal wind. The thermal wind vector is along isotherms with the cold side to its left (in the northern hemisphere). Due to the thermal wind relation, the thermal wind expresses the change of the horizontal wind with height, i.e. the vertical shear. Hence the thermal wind vector is equivalent to the vertical shear vector.

We mainly use the term of the vertical shear vector since it describes the way this vector is determined in this study. PLs in a forward shear can be understood as having the cold air on their left side as seen in propagation direction and warm air on their right side. The opposite is the case for reverse shear situations. Hence, each shear situation can be interpreted to develop along one side of a cold-air outbreak.

Terpstra et al. (2016) categorised PLs from the STARS dataset (description later) into forward and reverse shear cases. They found an approximately similar amount of both types and some characteristic differences. PLs in a forward (reverse) shear environment were mainly propagating eastward (southward), had an associated upper-level (lower-level) jet, and were associated to a deep-baroclinic zone (an occluded low). Reverse-shear systems were observed to have considerably higher turbulent heat fluxes and larger temperature differences between the sea surface and 500hPa, i.e. a lower static stability than forward-shear systems.

The categorisation of PLs appears to be useful for deriving some general aspects of different PLs. Many attempts have been made to derive PL classifications that describe their dynamics (e.g. Businger and Reed, 1989; Rasmussen and Turner, 2003; Bracegirdle and Gray, 2008). The division into forward and reverse shear types has turned out to be useful (Terpstra et al., 2016). However, this categorisation may not be the most accurate when it comes to distinguish between PL types, and other ways might exist. Furthermore, the shear angle does not distinguish between baroclinically- and convectively-driven systems, hence it cannot measure whether a "polar-low spectrum" exists.

In this study, we investigate differences and similarities within PLs. We categorise PLs based on sub-synoptic meteorological fields around the PL. This categorisation is performed by self-organising maps (SOM, see Section 2.5) without an *a-priori* determination of a variable used for the categorisation. The identification of typical configurations in the meteorological fields can reveal the underlying intensification mechanisms of the PLs.

In order to perform this categorisation, we need two components: a list of PL cases, and an atmospheric dataset of sufficient quality to resolve the sub-synoptic environment around the PLs. Multiple case studies of PLs have been performed in the past and an important amount of knowledge has been deducted from these (e.g. Harrold and Browning, 1969; Bond and Shapiro, 1991; Bracegirdle and Gray, 2009). However, to achieve some general aspects, a representative amount of cases has to be examined. The STARS (Sea Surface Temperature and Altimeter Synergy for Improved Forecasting of Polar Lows) dataset is an operationally updated list of PLs collected by the Norwegian meteorological institute (MET) for the Nordic Seas since November, 1999 (Noer and Lien, 2010). It is likely the most well-accepted list of PL cases, and multiple studies are based on it (e.g. Laffineur et al., 2014; Zappa et al., 2014; Rojo et al., 2015; Terpstra et al., 2016; Smirnova and Golubkin, 2017; Stoll et al., 2018).

In order to apply the SOM categorisation, we need an atmospheric dataset of sufficient quality to resolve the sub-synoptic environment around the PLs. Only recently atmospheric reanalyses have become sophisticated enough to simulated PLs. In the third version of the ECMWF reanalysis, ERA-40, Laffineur et al. (2014) identified 6 out of 29 STARS PLs, whereas they detected already 13 of these PLs from the fourth version of the ECMWF reanalysis, ERA-Interim. More studies have estimated the amount of represented STARS PL by ERA-Interim to 48% Smirnova and Golubkin (2017), 55% (Zappa et al., 2014), 60% (Michel et al., 2018) and 69% (Stoll et al., 2018). Theses studies applied different detection methods for the PLs within ERA-Interim and utilised different versions of STARS dataset. The ability of the latest version of the ECMWF reanalysis, ERA-5, to simulate PLs has not yet been investigated. However, some studies have shown that atmospheric models with a comparable horizontal resolution as ERA-5 are capable to produce most PL cases (Smirnova and Golubkin, 2017; Stoll et al., 2018). Here we show that ERA-5 reproduces almost all cases from the STARS dataset.

By analysing a whole list of PLs as represented in ERA-5, we investigate the following main research questions:

- – What are the typical configurations of the meteorological fields around PLs?

- – Can an existing PL classification be confirmed or should a different one be considered?

- – What are the pertinent intensification mechanisms?

This study is structured as follows: The ensuing section introduces the utilised data and methods. Section 3 describes the typical arrangements of the meteorological fields around PLs and discuss these in connection to a useful classification. Section 4 analyses the PL intensification mechanism. Finally, Section 5 provides a conclusion and discussion of the main results.

2 Methods

2.1 Polar low list

This study is based on a recent version of the STARS dataset that has been published by Rojo et al. (2019), in the following referred to as the Rojo list. It includes the location and time of PLs detected from AVHRR satellite images that were listed in STARS dataset from MET between November 1999 and March 2019 in the North Atlantic (Noer and Lien, 2010)

In addition to the STARS dataset, the Rojo list includes the cloud morphology for each detected PL time step, and in situations of multiple PLs connected to one PL event, the list includes the location of each individual centre as described in Rojo et al. (2015), whereas the STARS dataset only provides the centre of the major PL during the PL event.

The Rojo list includes 3848 PL time steps of 420 PLs centres for 262 PL events of which 183 PL events feature a single PL centre and the remaining 79 PL events have multiple PLs, with most commonly 2 - 4 centres, but reaching up to 9 PL centres per event. (However, the 9 centres did not occur simultaneously.)

The Rojo list includes individual time steps of each PL centre when AVHRR satellite images were available. Hence, the time interval between observations is irregular between 30 minutes and up to 12 hours, and the list lacks the genesis and lysis time of some PLs.

2.2 Polar low tracks in ERA-5

In order to investigate the development of the PLs on the Rojo list, we analyse 4D-meteorological fields centred around these PLs. Fields from the European Centre for Medium-Range Weather Forecasts (ECMWF) state-of-the-art reanalysis version 5 (ERA-5) were chosen (ECMWF, 2018-07). The reanalysis provides data from 1979 to near-present at hourly time resolution. The underlying model has a spectral truncation of T639 in the horizontal plane, which is equivalent to a grid spacing of about 30km, and 137 hybrid levels in the vertical direction, of which approximately 47 are below 400hPa, which is the typical height of the tropopause at high latitudes. In this study, data are obtained at a lat × long grid of 0.25° × 0.5° within 50° - 85° N and 40° W - 65° E, which includes all time steps from the Rojo list. We chose a coarser grid spacing for the longitudes as they converge towards the pole. For our analysis, we use data from surface variables and from the pressure levels at 925, 850, 700 and 500hPa.

To analyse the development of the PLs, tracks covering their full lifetime are required at a high temporal resolution. We apply the mesoscale tracking algorithm developed by Watanabe et al. (2016) to ERA-5 to obtain tracks at an hourly resolution and retain the tracks that match with the systems from the Rojo list.

The tracking procedure is based on local maxima in the relative vorticity at 850hPa. The procedure applies a linkage between consecutive time steps within a distance of 100km relative to the steering location. This location is derived from the propagation of the PMC centre with the steering wind that is defined as the average wind of the 700 and 1000hPa level within a radius of 200km around a centre of the PMC.

We tune the parameters in the tracking algorithm of Watanabe et al. (2016) since our objective is somewhat different. In this study, we aim to obtain good matches to the cases from the Rojo list, whereas Watanabe et al. (2016) attempted to detect all, and only, PMCs. The algorithm is modified as follows:

- – A land mask is not applied, as some PLs partly propagate over land areas.

– A uniform filter of 60km radius is applied to the vorticity field, as this considerably reduces artificial splitting of PLs and smoothes the tracks.

– In connection to the vorticity smoothing, the vorticity thresholds for the detection are also reduced as compared to Watanabe et al. (2016): The threshold for the vortex peak $\zeta_{max,0}$ is reduced from 2 to $1.5 \cdot 10^{-4} \mathrm{s}^{-1}$, and the threshold for the vortex area $\zeta_{min,0}$ from 1.5 to $1.2 \cdot 10^{-4} \mathrm{s}^{-1}$.

– Synoptic-scale disturbances defined by Watanabe et al. (2016) are labelled but not excluded, as by visual inspection plenty of the correctly-matched systems from the Rojo list were classified as synoptic-scale disturbances by the PMC algorithm. Since we only focus on the systems from the Rojo list that are included in ERA-5, and the systems included in the Rojo list were defined to be PLs by operational meteorologists, an additional filter for synoptic-scale disturbances is not required here.

All tracks that have a distance of less than 150km to at least one PL time step from the Rojo list are regarded as matches. Sometimes several tracks match the same PL in the Rojo list, but due to the vorticity smoothing this is rather seldom. Multiple matches to the same PL from the Rojo list are found to have two reasons: 1. ERA-5 features a multiple PL of which only one is included in the Rojo list. 2. The tracking algorithm produces several track segments of the same PL, which do not overlap in time. This occurs mainly if the location of the vorticity maximum moves within an area of high vorticity, e.g. a frontal zone. In these cases, it is tested whether two track segments can be merged. They are merged if the time gap between the two segments is less than 6 hours, and if the extrapolation of one track segment over the time gap includes the other segment within a distance of 150km. This merging was applied for 93 PL centres.

Finally, some tracks are excluded, either if their lifetime is shorter than 5 hours, or if they are on land for most of their lifetime. The latter is here defined as the initial, middle, and final time steps of the PL occurring on land. Other land exclusion methods were tested and give similar results. In addition, a track is not included twice if it matches with two Rojo centres, which happens when ERA-5 captures only one of the centres of a multiple PL event from the Rojo list.

Applying this procedure, a total of 374 PL centres with 13,221 hourly time steps that are associated to 240 different PL events remain in our dataset. Hence, 240 of the 262 PL events (92%) from the Rojo list are reproduced in ERA-5. This expresses that ERA-5 includes most PL events and the applied tracking and matching procedure is successful. From an older version of the STARS dataset with 138 PLs with a lifetime of at least 6 hours, Stoll et al. (2018) detected 107 (80%) of which 94 (69% of the 138) had at least one time step over open water. In that study, matching was performed

within a distance of 250km, whereas here, the distance is reduced to 150km. Also Michel et al. (2018) detected about 60% of the STARS PLs in ERA-Interim with an automatic tracking procedure. Our detection rate indicates that ERA-5 is advanced as compared to its predecessor ERA-Interim when it comes to capturing PL cases.

2.3 Polar-low centred grid

In this study, we take a PL-centred perspective. Horizontal meteorological fields from ERA-5 for each individual time step of a PL track are transformed into a PL centred grid. The cells of the PL-centred grid (black dots in Figure 1) are derived from the location of the vorticity centre and the propagation direction of the PL. To obtain the propagation direction, we apply a smoothing on the PL track points due to several reasons: The tracks can feature bumpy behaviour due to the positions coinciding with the discrete spacing of the grid. In addition, the location of the vorticity maximum can sometimes change within an area of higher vorticity, such as a frontal zone. At low propagation speed, variable propagation directions can occur which influence the rotation of the PL-centred grid.

For the track smoothing, we use a cubic spline interpolation with a smoothing parameter of 0.001 for every PL track (De Boor et al., 1978). The spline interpolation is a compromise between the desire to stay close to the actual PL location and to obtain smooth tracks. The smoothing parameter should be in the range [0,1], where 0 is equivalent to a straight line least-square fit, and 1 to a cubic spline interpolation that lays the smoothed track through all track points. After testing different smoothing parameters, the chosen parameters was found to be a good compromise. An example of a smoothed track is presented in Figure 1.

The PL-centred grid has an extent of 1000×1000km, and a grid spacing of 25km, which is approximately the grid spacing of ERA-5. Since the typical diameter of the PLs is estimated to be between 150 and 600km (Rojo et al., 2015, and Fig. 8), this grid covers the PL and its sub-synoptic environment. The meteorological fields from ERA-5 are linearly interpolated onto the PLCG (see Fig. 1).

The PL-centred grid is only derived for time steps, where it is fully covered within the chosen ERA-5 boundaries. This lead to a reduction from 13,221 to 12,695 PL time steps, which removes 4 of the 374 PL centres for their complete lifetime. Most of the excluded time steps occur at the end of the PL lifetime. Hence, this exclusion has only a small influence on our analysis of the PL intensification.

2.4 Parameter preparation

The investigation of the PL dynamics is mainly based on PL-centred, horizontal fields at different atmospheric levels. However, for the comparison of PLs some parameters are deduced from the PL environment. These parameters are
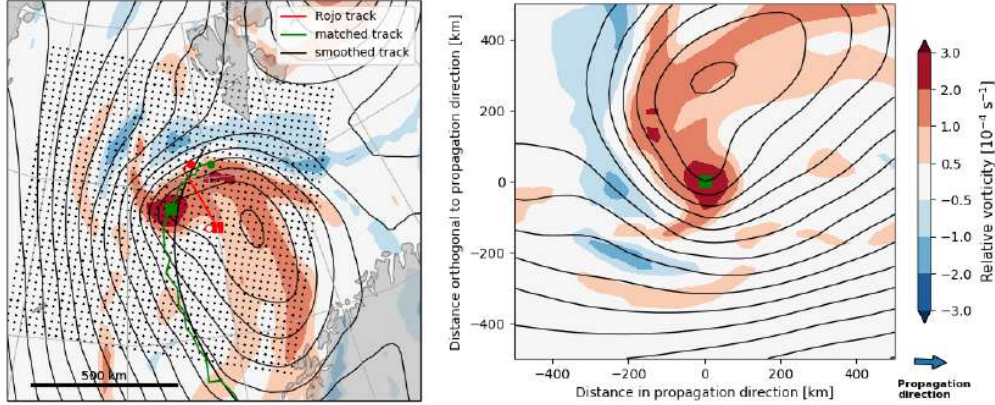
Figure 1. (Left) Relative vorticity (shading) and geopotential height (contours, spacing 10m) at 850hPa for 20 March 2001 01:00 UTC. The track of polar low number 10 from the Rojo list is shown in red. The matched track is depicted in green. The present location at this time is indicated by squares. The smoothed track for determination of the propagation direction is depicted in black. The propagation direction of the PL at this time is southward. The location of the grid cells of the polar-low centred grid are denoted by black dots. (Right) Same fields as for (left) in the polar-low centred grid, constructed such that the polar-low centre is in the middle (green square) and the propagation direction is rightward.

mainly calculated as the mean within a distance of 250km to the PL centre from ERA-5 data. This length scale is the typical radius of a PL. For the near-surface wind speed the local maximum is determined. For parameters that are prone to be highly influenced by either sea-ice cover or topography, such as surface turbulent heat fluxes, only grid cells over open ocean are included for the calculation of the local mean.

Parameters that may need some clarification or that are computed from ERA-5 variables are explained in the following.

The medium-level **cloud cover** in ERA-5 is defined as the cloud cover between the levels with $0.45 < \sigma < 0.8$ where σ is the fraction of the pressure of a given level and the surface pressure. Hence medium-level cloud cover is approximately between 800 - 450hPa.

The large-scale **precipitation** is generated by the microphysics scheme of ERA-5. It is computed from atmospheric fields at spatial scales resolved by the model. Convective precipitation is generated by the convective scheme of the model, which presents convection at smaller spatial scales than the model grid cells (ECMWF, 2018-07).

The **Brunt-Väisälä frequency**, N, is estimated from the potential temperature, θ, at two pressure levels with geopotential height, z. In this study the levels are chosen to be at 500 and 925hPa. Different levels were tested and give similar results.

$$N = \sqrt{\frac{g}{\theta}\frac{\partial\theta}{\partial z}} \approx \sqrt{\frac{g}{(\theta_1+\theta_0)/2}\frac{\theta_1-\theta_0}{z_1-z_0}} \qquad (1)$$

The **horizontal temperature gradient** is computed as follows

$$|\nabla_h T| = \sqrt{\left(\frac{\partial T}{\partial x}\right)^2 + \left(\frac{\partial T}{\partial y}\right)^2} \qquad (2)$$

The **vertical shear vector** in the horizontal wind is computed by the difference in the mean wind vectors at 500 and 925hPa,

$$d\boldsymbol{u} = (du, dv) = (\overline{u_{500}} - \overline{u_{925}}, \overline{v_{500}} - \overline{v_{925}}). \qquad (3)$$

Means, indicated by an over bar, are computed within a distance of 250km around the PL centre for the given time step. The upper-level (500hPa) is considerably higher than the level chosen by Terpstra et al. (2016) (700hPa). We demonstrate that the dynamics involved in the PL span the entire troposphere and hence we consider it most reasonable to apply these. We tested deviations in the pressure levels used for the computation and obtained qualitatively similar results.

The **vertical shear strength** is calculated by the length of the shear vector divided by the mean vertical distance of the two pressure surfaces,

$$\frac{d\boldsymbol{u}}{dz} = \frac{\sqrt{du^2 + dv^2}}{\overline{z_{500}} - \overline{z_{925}}}. \qquad (4)$$

This procedure is different from that applied by Terpstra et al. (2016), who calculated the difference in the horizontal wind speed between two levels. For situations where the horizontal wind vector rotates with height at the same wind speed, the method of Terpstra et al. (2016) results in zero shear strength. Differently, the definition applied here produces the strength of the differential vector.

The **shear angle**, α, is derived from the angle between the mean horizontal wind vector, $\overline{\boldsymbol{u}} = (\overline{u}, \overline{v})$, and the shear vector, $d\boldsymbol{u}$,

$$\alpha = [\alpha_m - \alpha_s] \,(\mathrm{mod}\ 360°) \tag{5}$$

$$\text{with} \quad \alpha_m = \arctan\left(\frac{\overline{u}}{\overline{v}}\right), \quad \alpha_s = \arctan\left(\frac{du}{dv}\right) \tag{6}$$

The mean wind vector is obtained from the 850 and 700hPa levels. The mean of these two levels is chosen, since it gives a good approximation for the propagation of the PLs, as we show later. It could also be derived from a singular level between 850 and 700hPa.

Note, that the shear angle by this computation takes values between 0 and 360° and not only between 0 and 180° as in Terpstra et al. (2016). We will show that situations with a shear angle of 90° are different from an angle of -90°.

In contrast to Duncan (1978) and Terpstra et al. (2016), we do not use the gradient in the thickness of an atmospheric layer to determine the thermal wind vector. However, applying their computation of the thermal wind vector gives similar results as the vertical shear vector utilised in this study.

2.5 Self-organising maps (SOM)

Kohonen et al. (2001) developed the SOM method for displaying typical patterns in high-dimensional data. The patterns, also referred to as nodes, are ordered in a 2-D array with neighbouring nodes being more similar to each other than nodes with a longer distance in the array. Kohonen et al. (2001) originally developed the method for artificial neural networks, but it has been extensively applied in many fields of science in the last years, including climate data analysis (e.g. Nygård et al., 2019).

The size of the node array has to be subjectively determined for the dataset at hand. It is typically decided after some testing. Here, the final choice is an array of 3×3 nodes. For our data set, larger arrays appear to mainly display additional details of minor interest. On the other hand, smaller arrays merges nodes that we want to discuss individually. In our case the SOM method reduces 12,695 PL-centred fields to 3×3 typical fields of the same spatial dimension as each individual PL-centred field.

We apply the package described in Wehrens et al. (2007) for the computation. Here follows a short description of the SOM method: Initially, 3×3 nodes are randomly chosen from 9 PL-centred fields. During the training phase, iteratively the PL-centred fields are compared to each node by measuring the Euclidean distance in the fields. The most similar node to the field of a given time step is adjusted, and so is to a smaller degree also neighbouring nodes in the 3×3 grid. Eventually the SOM nodes become ordered, despite the fact that they were randomly initiated. Also, each of the 12,695 time steps (from the input data) is assigned to one SOM node with the highest similarity.

Multiple meteorological fields in the PL-centred grid of the 12,695 time steps were tested for their application in the SOM algorithm. A comparison of these and reasoning that we chose the temperature anomaly field at 850hPa for further analysis is provided in the supplementary material. The temperature anomaly field of each time step is here defined by $T'(x,y) = T(x,y) - \mathrm{mean}_{x,y} T(x,y)$, where $T(x,y)$ is the PL-centred temperature field at one time step and $\mathrm{mean}_{x,y} T(x,y)$ the mean temperature within the PL-centred grid of the individual time step. In this way the information concerning a PL time step occurring in a warm or cold environment is removed, which would otherwise dominate the SOM analysis, and the temperature gradient fields are instead apparent.

Some of time steps within each node can be associated with genesis, mature and lysis situations of the PL. The mature stage of the PL is here defined as the time step with the maximum filtered relative vorticity at 850hPa. A given PL can occupy several SOM nodes during its lifetime. This evolution can be tracked through the SOM matrix. Evolution mainly occurs to neighbouring SOM nodes, since neighbours in the SOM matrix are most similar. Sometimes PLs develop back and forth between nodes, which expresses that the system is in a state between two nodes. This back and forth development is removed since it does not express a development of the system.

3 Typical polar low configurations

In this section we present the typical configurations of the meteorological fields around the PLs from the STARS dataset.

3.1 SOM matrix

The SOM algorithm deduces the temperature anomaly fields at 850hPa from the 12,695 PL time steps to a matrix of 3×3 SOM nodes presented in shadings in Figure 2. The SOM method is useful to condense the variability in the dataset to an interpretable size. The fraction of the PL time steps associated to each node is expressed by the number in parenthesis. The nodes display horizontal temperature fields with different strength and orientation of the gradients as seen from the propagation direction of the PLs, which is displayed towards the right.

Nodes in the corners are the most extremes by construction of the SOM algorithm and hence show highest horizontal temperature gradients. Nodes on opposing sides of the matrix display temperature anomaly fields that are most different from each other. The SOM matrix displays that the gradient in the temperature field around PLs takes all possible orientations as compared to the propagation direction.

PLs represented by SOM nodes 1 and 9 propagate approximately along the horizontal temperature gradient at 850hPa
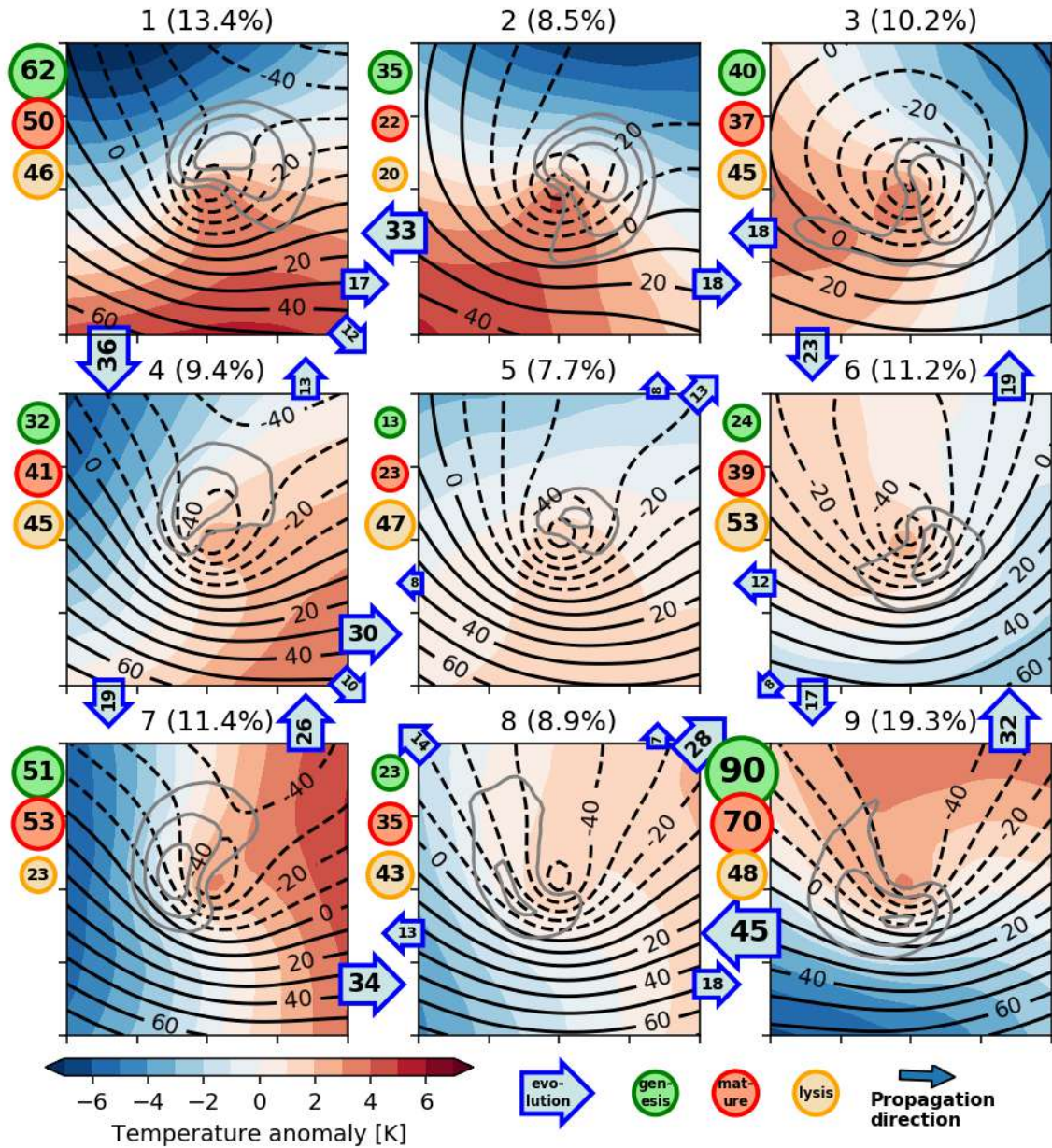
Figure 2. The self-organising map (SOM) of the temperature anomaly field at 850hPa for all time steps associated to the PLs in a PL-centred grid. Displayed is the composite of the 850hPa temperature anomaly (shading), 850hPa geopotential height anomaly (black contours) and medium-level cloud cover (grey contours at 0.7, 0.8 and 0.9) associated to the SOM nodes. The subtitle number labels the SOM nodes and the percentage displays the fraction of all time steps represented by the respective node. Green, red and yellow coloured circles indicate the number of genesis, mature and lysis PL stages within each node. The numbers in the arrows indicate the amount of shifts between two nodes. Arrows with numbers smaller than 5 are not displayed.

with the cold side to its left and right, respectively. These represent the classical forward and reverse shear situations, respectively (e.g. Forbes and Lottes, 1985; Terpstra et al., 2016). We show this in the next subsection. PLs in node 3 are propagating towards colder environments and hence this node is assigned the name "cold-ward propagation". The opposite is present in node 7 with systems propagating towards warmer environments, and therefore called "warm-ward propagation". The others nodes typically display intermediate states between the nodes in the corners with weaker temperature gradients.

The composite of the geopotential height anomalies at 850hPa associated to each SOM node is displayed in black contours of Figure 2. The geopotential height field expresses the horizontal flow in the PL environment. The composite in the 850hPa geopotential height associated with the different SOM nodes are similar. They express that PLs are typically a trough of a synoptic-scale low-pressure anomaly located to its left-hand side as seen in propagation direction. All nodes have only a weak closed contour in the geopotential height at 850hPa at the PL centre. The circulation is somewhat more closed for node 3. The geostrophic flow at 850hPa in the environment of the PL is approximately parallel to the propagation direction of the PL.

In order to test the variability in the background flow, the SOM algorithm is also applied to the 850hPa geopotential height anomaly field (see supplementary material). This confirms that the PLs are mid-level troughs of different strength and angle of the trough axis. In general the PLs show little variability in the patterns of the mid-level flow.

Also in the relative vorticity at 850hPa, the PLs show little variability in the shape, which is revealed from the application of the SOM algorithm to this variable (supplementary material). The PLs are circular to elliptical vorticity maxima with differential strength around the PL centre which fast decay on a length scale of approximately 150km. Hence it appear that the PLs are secondary cyclones embedded in a large-scale flow. Neither the thermal field nor the environmental flow are axis-symmetric relative to the PL centre, as is the case for tropical cyclones. Instead, we argue later that PLs are non-axis-symmetric baroclinic disturbances.

The flow expressed by the geopotential height field is a superposition of the large-scale flow and the circulation associated to the PL. Hence, the PL intensifies the large-scale flow on one side and weakens it on the other side. All nodes have the highest associated wind speed at 850hPa to the right-hand side of the PL centre as seen in the propagation direction. This is visible by the closely-spaced geopotential contours in Figure 2. In contrast, most of the nodes have rather weak winds on the left-hand side of the PL centre. Hence, the location of the strongest horizontal wind at 850hPa associated to the PLs is largely determined by the propagation direction and little effected by the orientation of the thermal field.

Figure 2 also depicts the composite of the medium-level cloud cover associated to each node in grey contours. Each node has a distinct location with increased cloud cover, which indicates the region in which the main updrafts occur. The updrafts are a result of configuration of the environmental flow. Hence, the cloud configuration indicates that each node represents a specific flow pattern. The composite of the medium-level cloud has a comma shape for all nodes, with a different orientation of the cloud. It is typically located at the warm front on the cold side of the PL centre.

3.2 Connection to the vertical wind shear

By the thermal wind relation the horizontal temperature gradient is connected to the vertical shear of the horizontal wind. The vertical shear vector, which is equivalent to the thermal wind vector, displays the change of the horizontal wind vector with height. The vertical shear vector is orientated along isotherms with the cold air to its left and warm air to its right hand side in the northern hemisphere. The mean horizontal wind vectors within a distance of 250km to the PL centre at different atmospheric levels associated to each of the SOM nodes are displayed in the hodographs in Figure 3. The change of the wind vector with height is expressed by the vertical shear vector. The distribution of the vertical shear vectors within each node is depicted by the windroses in Figure 3.

In node 1 and 2 the cold air is to the left as seen from the propagation direction of the PL (Fig. 2). The angle between the mean wind and the vertical-shear vector is small (Figure 3, typically $0° \pm 30°$). Hence node 1 and 2 display the classical forward shear situations. The mean horizontal wind and the vertical-shear vector are almost parallel and the horizontal wind speed increases with height in propagation direction (hodograph in Fig. 3). For forward shear situations, the SOM-mean, area-mean wind vector at 500hPa has a strength of more than $16\mathrm{ms}^{-1}$ at 500hPa, but less than $5\mathrm{ms}^{-1}$ at 925hPa (see Figure 3). A calm mean wind vector indicates that the wind vectors within the area, which is a circle with 250km radius, cancel each other. This happens since the circulation is closed and the background flow is negligible near the surface (see Fig. 7. The median value in the most intense 10m wind speed is $15.5\mathrm{ms}^{-1}$ for these nodes, which is strong but somewhat lower than for other shear situations (Fig. 5, discussion later).

In node 9 the opposite to node 1 and 2 is the case. PLs within node 9 are of the classical reverse shear types. The cold air is to the right as seen from propagation direction and hence the vertical-shear vector is opposite to the propagation direction. The shear angle is typically between $160° \pm 30°$. This lead to a reduction of the speed of the mean wind vector with height. Therefore the strength of the mean wind vector at 500hPa is only around $3\mathrm{ms}^{-1}$, whereas the strength of the mean wind vector at lower levels is high ($\approx 12\mathrm{ms}^{-1}$ at 925hPa). Hence reverse shear situations are characterised by
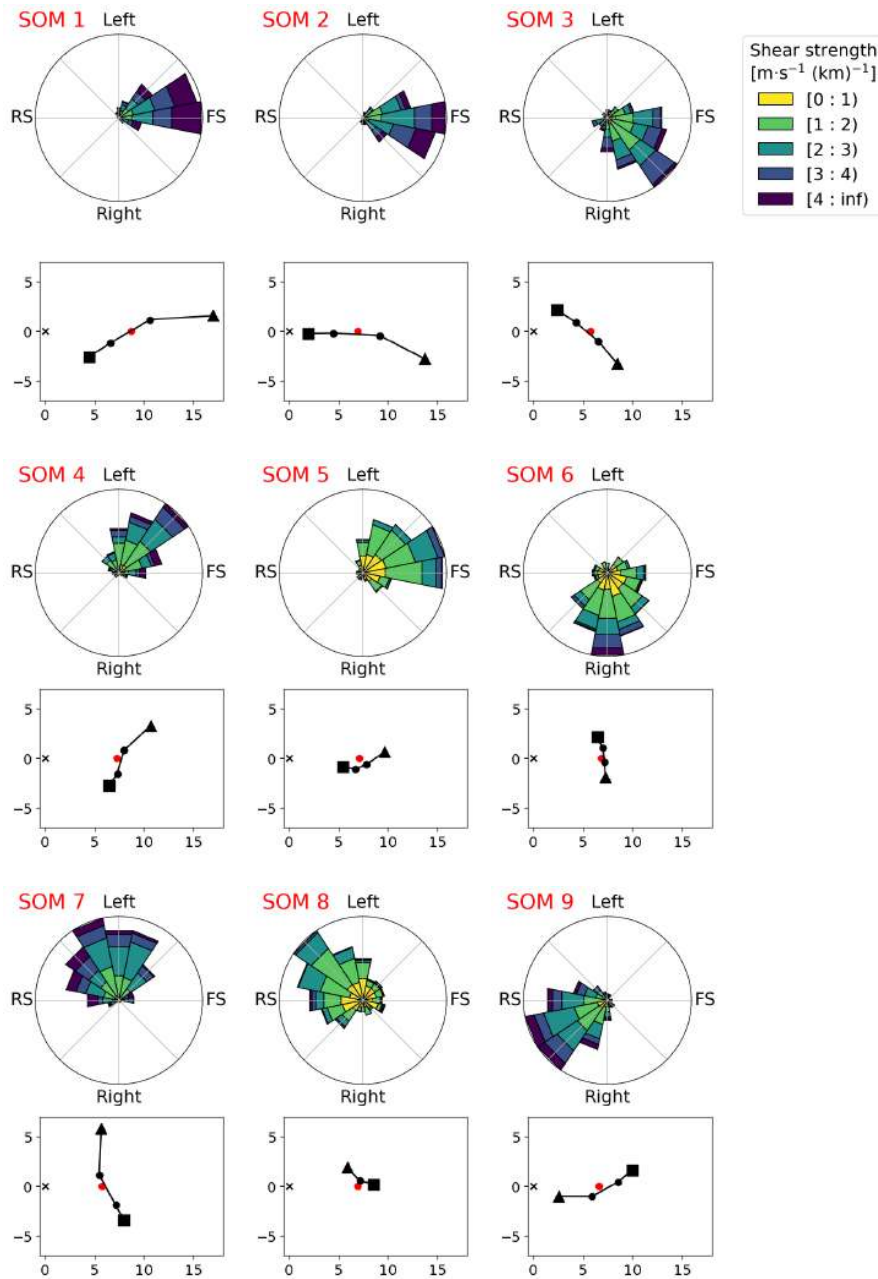
Figure 3. Distribution of the vertical shear vector (wind roses) and the mean hodograph (lower plot) associated to each SOM node. Wind roses: The vertical wind shear vector is calculated as the difference in the mean wind vectors at 925 and 500hPa (Eq. 4. The vertical shear angle is calculated as the deviation from the propagation direction of the PL (Eq. 5). A shear angle of $0°$ which indicates forward shear (FS) is displayed towards the right. Shear angles of 90, 180 and $270°$ represent right-shear, reverse-shear (RS) and left-shear conditions, respectively. Hodographs: The origin is marked by a "x". The square, two circles and triangle mark the wind vector of the 925, 850, 700 and 500hPa, respectively, as mean within a distance of 250km around the PL. The wind vectors are rotated into propagation direction, which is displayed towards the right. The red dot denotes the mean propagation vector of the PLs within the SOM node. Units on the x and y-axis are ms^{-1}. Mean wind vectors close to 0 can be caused by a closed horizontal circulation.

an almost closed upper-level circulation and a strong near-surface trough (see Fig. 7). Similar to this, Bond and Shapiro (1991) and Terpstra et al. (2016) observed that reverse shear systems are often accompanied by a strong low-level jet.

Node 3 and 7 have shear angles closer to 90° which indicate a rotation of the horizontal wind vector with height. PLs in node 3 are propagating towards colder environments and the vertical wind shear is towards the right as seen from the propagation direction with a forward tendency (Figure 3, typically around 45±20°. The veering, a clockwise turn of the wind vector with height, is also a clear indication of the associated warm-air advection. Node 7 shows the opposite to node 3, PLs are propagating towards warmer environments with vertical wind shear to the left compared to the propagation direction (Figure 3, typically around -110±30°). This backing, a anti-clockwise rotation of the wind vector with height, is an indication of cold-air advection.

For the "corner nodes" the most frequent shear angle is anticlockwise (=cyclonically) rotated by 20 - 45°as compared to the idealistic categories forward, reverse, left and right shear, which would have shear angles of 0, 180, 90 and -90°, respectively. However, the large-scale temperature gradient, envisioned from the composites of the environmental thermal fields at 850hPa around the PLs (Fig. 2, appears to be approximately parallel or orthogonal to the propagation direction. It can also be anticipated that the PL cyclonically rotates the thermal field by approximately 20 - 45°around the PL centre. This rotation induces a cyclonic "bias" of the vertical shear angle. However, the directional shear categories should not be interpreted as being strictly bounded since intermediate situations exist. It is also shown later that the PLs often change the vertical shear angle during their lifetime.

Node 4 which can be interpreted as an intermediate situation between the node 1 and 7, the shear angle also takes intermediate values (-50± 20°). In the remaining nodes (5, 6 and 8) the horizontal temperature gradient, which determines the vertical shear strength, is small (Fig. 3 and 5) and hence the angle of the vertical shear is of less importance. The mean wind vectors of these nodes at different heights are almost uniform (Fig. 3), which indicates a quasi-barotropic alignment of the flow.

3.3   Location of the nodes

We now investigate the typical location and propagation direction of the time steps associated to each node within the Nordic Seas (Fig. 4).

PLs in forward shear situations, node 1 and 2, are mainly occurring between Svalbard and the Norwegian mainland in an eastward and N-E-E-ward flow. The cold-ward propagation systems (node 3) appear mainly in the Barents Sea in an north-eastward flow. Reverse shear systems (node 9) are mainly located in the Norwegian Sea in a S-S-W-ward flow. The typical location and propagation directions of these two PL types is in accordance with (Terpstra et al., 2016). Warm-

ward propagation situations (node 7) occur in a S-E-ward flow, mainly on the west-side of Svalbard. Systems in an intermediate situation between forward shear and warm-ward propagation (node 4) are occurring mainly between Svalbard and Norway in an S-E-ward flow. Systems in the remaining SOM nodes (5, 6 and 8), which are considered to mainly represent mature or dissipating stages of PLs, are mainly located downstream to the neighbouring nodes in the corners. These remaining nodes often occur close to the coast of Norway where the flow is directed such that the PLs are about to make landfall.

In general, the location and propagation direction associated to each of the SOM nodes is rather confined. Hence, the orientation of the thermal field expressed by each node is closely linked to a compass direction. This suggests that only certain configurations of the flow and the thermal field within the North Atlantic are favourable for PL development. In another ocean basin, the preferred propagation directions to the different shear situations may likely be different.

3.4   Evolution between patterns

Only a minority of the PLs is associated to the same SOM node for its whole lifetime (value?). Typically PLs change between SOM nodes during its development. This evolution is displayed by the blue arrows in Figure 2, where the number expresses the amount of transitions from one to the other node connected by the arrow.

The evolution between the SOM nodes is often associated to a change in the propagation direction of the PL. This is supported by the distinct propagation direction of PL time steps within each node. The propagation direction is mainly determined by the orientation of the synoptic scale flow. If the synoptic-scale flow in which the PL is embedded changes direction, this effects the orientation of the thermal field in relation to the flow. We show later that the dynamical evolution in all nodes with a high temperature gradient is similar.

Still, we can learn some more from the evolution pathways, especially combined with the information on how many systems within each SOM node are in the genesis, mature and lysis stage, which is displayed by green, red and yellow arrows, respectively, in Figure 2.

At initial times (green circles) the PLs are most frequent in the SOM nodes in the corners. These situations are associated to a large horizontal temperature gradient (as will be presented later). Of the in total 370 PLs, forward (node 1+2: (62+35)/370 = 26%) and reverse shear (node 9: 24%) are the dominant initial situations. However, also cold-ward (node 3: 11%) and warm-ward propagation (node 7: 14%) are often genesis situations. The SOM nodes with a small associated temperature gradient (5, 6 and 8) are only seldomly initial, but more frequently lysis situations. Hence one conclusion is that PLs are evolving in the SOM matrix more frequently from nodes with high to low baroclinicity than the opposite.
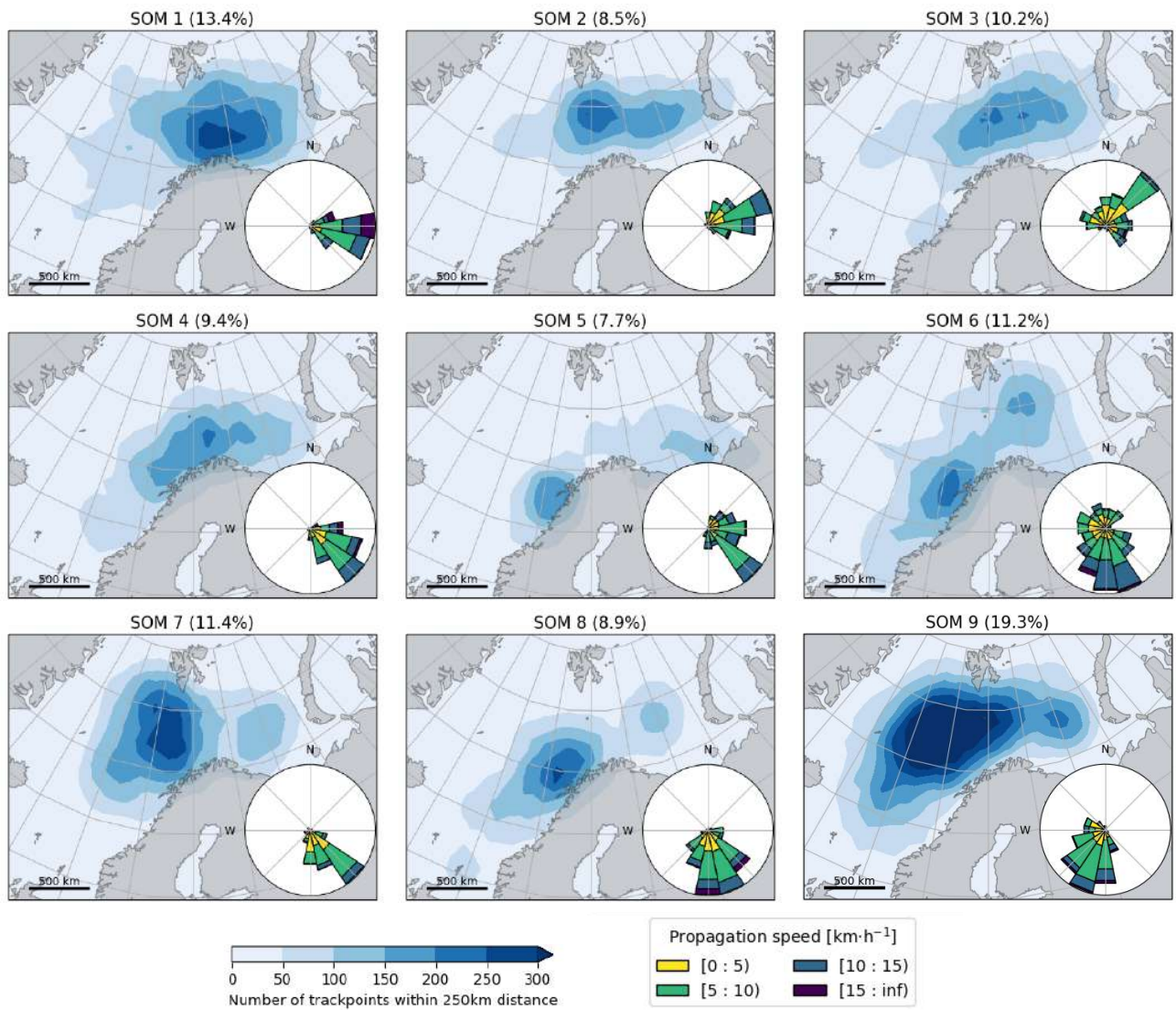
Figure 4. Track density of the time steps associated to each SOM node. The windroses depict the distribution in the propagation direction and speed of the time steps associated to each node.
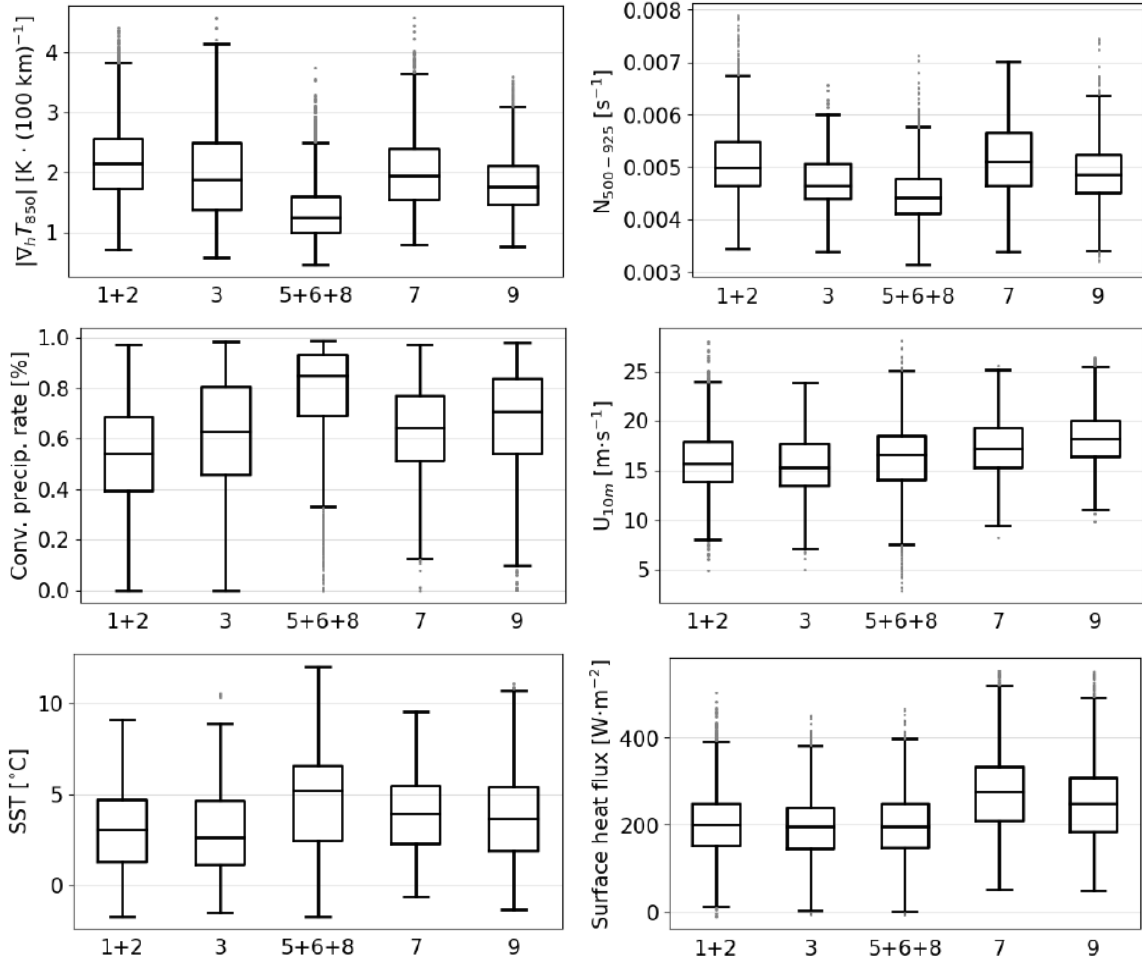
Figure 5. Box plots presenting the distributions in different parameters for all time steps attributed to the SOM nodes presented in Figure 2. SOM nodes 1+2, and 5+6+8 are presented together since the parameter distributions are similar. The mean of the parameter within 250km distance to the centre is calculated with some exceptions. For the 10m wind speed the maximum is obtained. For the computation of the mean in the static stability, sea-surface temperature and surface heat fluxes, grid cells that are covered by land or sea-ice are excluded.

3.5 Characteristics of the individual patterns

Now the characteristics of PL time steps associated to the different SOM nodes are investigated by comparing parameters in their PL environments.

5   The strength of the baroclinicity can be inferred from the strength of the vertical wind shear in Figure 3. The vertical shear strength is by the thermal wind balance tight to the horizontal temperature gradient. The horizontal temperature gradient is, however, more easily directly assessed by the vi-

10 sual inspection of a synoptic weather map than the vertical shear strength. The mean horizontal temperature gradient at 850hPa is large for the SOM nodes in the corners (including node 2) with median values around 2.0K per 100km (Fig. 5). This expresses again that PLs in these nodes are occurring

15 in an highly baroclinic environment. Especially the forward-

shear situations (node 1+2) have very high temperature gradients (median 2.1 per 100km). It is somewhat lower for the reverse-shear situations (median 1.8K per 100km).

     The baroclinic development in the corner nodes is supported by a low static stability ($N \approx 0.005\mathrm{s}^{-1}$, Fig. 5) as 20 compared to typical atmospheric values in synoptic-scale baroclinic environments. They are twice as high as in the baroclinic instability analysis in Vallis (2017).

     In situations of forward shear and warm-ward propagation the atmosphere is somewhat more stable (node 1+2 and 7, 25 medians $N =0.0050$ and $0,0051\mathrm{s}^{-1}$) than in situations of reverse shear and cold-ward propagation (SOM 3 and 9, median 0.0048 and 0.0047s^{-1}). The nodes with weak baroclinic growth rate (5, 6 and 8, median 2.3K per 500km) have considerably lower static stability than the other nodes (median 30

$N = 0.0044\text{s}^{-1}$). This might be an indication that convection is more importance for PLs in these nodes.

For these nodes (5+6+8) also the rate of convective precipitation of the total precipitation is high (Fig. 5, median at 85%). However, the rate of the total precipitation in the mean around the system is low for all SOM nodes with median values between 5.0 and 6.4 mmd^{-1} (not shown). It is hence questionable that latent heat release in convection could be a singular mechanism leading to the intensification of the PLs within these SOM nodes. In contrast, for the SOM nodes with a high horizontal temperature gradient (1 - 3, 7, 9) convective and large-scale precipitation accounts for approximately 60% and 40%, respectively. Large-scale precipitation is presumably caused by slantwise frontal ascent, which is characteristic for baroclinically-driven systems (e.g. Harrold and Browning, 1969). This supports that the nodes with a high thermal gradient express a baroclinic development.

The distributions in the maximum 10m wind speed in the vicinity of the system are rather similar between the SOM nodes. Situations of forward shear and cold-ward propagation have a somewhat lower maximum wind speed (median $\approx 15.5\text{ms}^{-1}$) than situations of reverse shear (median $\approx 18.2\text{ms}^{-1}$) and warm-ward propagation (median $\approx 17.2\text{ms}^{-1}$). This is a consequence of the vertical shear. In reverse shear situations the mean flow is strong at low levels and decreases with height (Fig. 3). The induced circulation of the PL intensifies the low-level flow on the left-hand side in propagation direction of the PL (see also Fig. 7) which leads to strong low-level winds. Surface friction reduces the wind near the surface, such that a low-level jet is present. For forward shear situations, the mean wind vector is weak at low levels (Fig. 3) and hence the intense near-surface wind is mainly caused by the polar-low induced circulation (see also Fig. 7) and somewhat weaker than for reverse shear situations.

The sea-surface temperature in the vicinity of the PLs is colder for situations in forward shear and cold-ward propagation (median 3.1 and 2.6°C , respectively, Fig. 5), warmer for situations in reverse shear and warm-ward propagation (median 4.0 and 3.7°C , respectively), and highest for situations with a low baroclinicity; especially node 8 has a median SST of 5.7°C . This can be explained by the typical location of PLs in the different nodes (Fig. 4). Node 1 - 3 occur at more northerly locations and nodes 5, 6 and 8 often close to the Norwegian coast where the water is warmed by the Norwegian ocean current. Hence different sea-surface temperatures are mainly an artefact of the different typical location of the nodes.

The turbulent heat fluxes at the surface are highest for the node expressing warm-ward propagation (node 7, median 276Wm^{-2}, Fig. 5) and also high for reverse-shear situations (node 9, median 250Wm^{-2}). They are lower for situations of forward shear and cold-ward propagation (median 202 and 196Wm^{-2}, respectively). This might be associated to stronger near-surface winds and a warmer sea surface for sit-

uations associated to SOM nodes with high than with low surface fluxes. The SOM nodes associated with a weak baroclinicity have surface fluxes comparable to forward shear situations (median 200Wm^{-2}).

3.6 Connection to cloud morphologies

Rojo et al. (2019) labelled the cloud morphology of every time step in their list by inspection of IR satellite images.

Figure 6 shows that within the nodes with a high baroclinicity (1, 2, 3, 7 and 9) comma-shaped clouds are the most frequent cloud form. 51% of the labelled time steps by Rojo et al. (2019) within these nodes are comma clouds, 32% spirali-form clouds, 5% wave-type clouds, 2% Merrygo-round systems and remaining 10% were labelled differently.

In the nodes with a low baroclinicity (5, 6 and 8) the spirali-form clouds are most dominant. 52% of the labelled time steps were assigned to be of spirali-form, 30% of comma-form, 4% wave-like, 3% Merry-go-round systems and again 10% of other form.

This supports the result of Yanase and Niino (2007) from idealised simulations that the cloud form is connected to the baroclincity of the environment. However, the nodes with a low baroclincity have little resemblance with a nearly axissymmetric spiral system as simulated by Yanase and Niino (2007). These nodes rather resemble the occlusion stage of a baroclinic development (Fig. 2) with a quasi-geostrophic alignment of the flow (Fig. 3).

In the nodes with high baroclinicity the spirali-form cloud was still recognised in approximately one third of the situations. It could be hypothesised that some of these are developing baroclinically but rather following the cyclogenesis with a warm seclusion, as suggested by the Shapiro-Keyser model (Shapiro and Keyser, 1990). In later stages of this model the cloud signature resembles a spiral. This would be an alternative hypothesis to the "hurricane-like" PLs that are mainly driven by latent heat release.

4 Baroclinic intensification mechanism

In this section the flow patterns in the baroclinic SOM nodes (1, 3, 7 and 9) are presented. We argue that in all these SOM nodes moist baroclinic instability is acting, although the upper and low-level fields have different orientations in the nodes.

For the assessment of dry baroclinic instability, we display the composite fields associated to the baroclinic SOM nodes in the temperature anomaly at 850hPa, the SLP and the geopotential height at 500hPa (first column in Figure 7). The role of diabatic effects is examined by the composite fields of the precipitation, the total column water vapour and the transport vector of the latter (second column in Figure 7). The surface sensible and latent heat fluxes, together with the
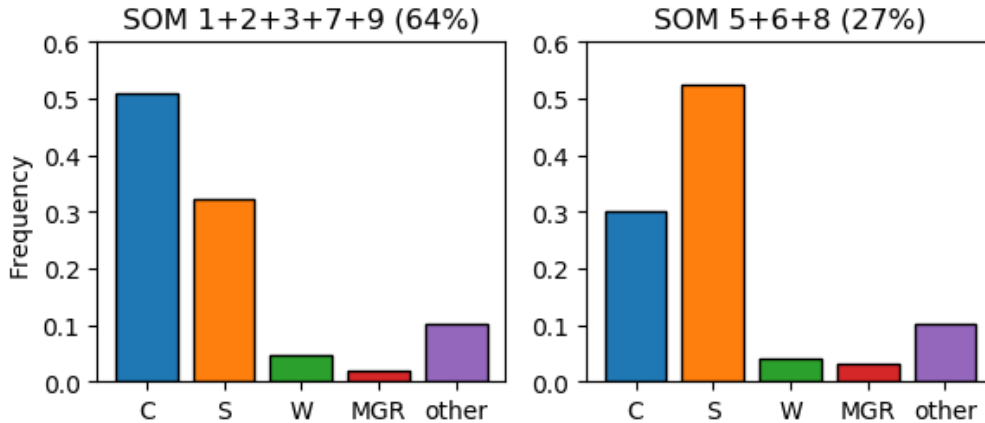
Figure 6. The frequency distribution of the cloud morphologies labelled by Rojo et al. (2019) within the baroclinc SOM nodes (left) and the less baroclinc nodes (right). The cloud morphologies are: C = Comma shaped, S = Spiraliform, W = Wave system, MGR = Merry-go-round. The number in percentage expresses the share of time steps included in the nodes. Node 4 is not included since it is considered as an intermediate stage. It includes the remaining 9% of the time steps.

near-surface wind vector are displayed (last column in Figure 7) to investigate their role.

4.1 Different baroclinic arrangement

In the following, we discuss the baroclinic arrangement within the nodes in the corners of the SOM matrix.

For forward shear PLs (node 1) the arrangement of the temperature field and the upper- and lower-level flow field (Fig. 7) resembles a small version of a mid-latitude baroclinic cyclone, that develops in the polar front (e.g. Dacre et al., 2012). For node 2 the fields appear similar to node 1 with a slight clockwise rotation. Forward shear situations show in the composite a closed near-surface circulation at the location of the PL centre and a trough within an UL jet in the rear (left in the figure) of the centre. Hence the tilt of the low pressure anomaly with height is in the opposite direction to the vertical-shear vector, which is displayed as a small insert in the upper-right corner.

Cold-ward propagation or right-shear situations (node 3) are in the composite characterised by a closed LL vortex of considerably strength and an UL flow towards the right (and in propagation direction) with a remarkable trough axis on the left-hand side of the centre (Fig. 7). This leads to a left-ward vertical tilt of the low pressure anomaly as seen from propagation direction. Reverse shear systems (node 9) are in the composite characterised by an intense low-level trough and a weak UL closed circulation which is centred ahead of the LL trough. Warm-ward propagation, or left-shear situations (node 7) are in the composite characterised by a LL trough in a flow directed to the front-right and an UL trough in a flow directed to the front-left. Hence, an approximately 90°cyclonic rotation of the trough axis with height. The UL pressure anomaly is located to the right of the PL centre,

where the gradient in the geopotential height at 500hPa is highest.

For all of the baroclinic SOM nodes the vertical tilt of the low pressure anomaly with height is in the opposite direction to the vertical-shear vector. This is characteristic for acting baroclinic instability. In the following we describe the positive feedback between the upper- and lower-level pressure perturbations that leads to a mutual intensification.

The low-level circulation causes warm-air advection down the environmental thermal gradient in the sector in the direction of the vertical-shear vector. This is in the following referred to as the warm sector. For forward (reverse) shear this is ahead of (behind) the PL as seen from propagation direction. For cold-ward (warm-ward) propagation the warm sector lies to the right (left) side of the PL track. Analogously, the low-level circulation causes cold-air advection up the environmental thermal gradient in the sector behind the vertical-shear vector (cold sector). Hence, the low-level temperature advection is arranged to baroclinically generate eddy available potential energy (see first term of equation 5 in Terpstra et al. (2015)).

This low-level differential temperature advection amplifies the UL low pressure anomaly since it reduces the atmospheric thickness in the sector of cold-air advection, which is situated beneath the UL perturbation. The opposite is the case in the sector of warm-air sector.

The UL disturbance causes a downstream diverging flow. The divergence is located above the near-surface low pressure anomaly and hence leads to a further reduction of the pressure. The diverging flow initiates ascending motion. This leads to the production of relative vorticity vortex stretching and tilting (not shown) which further intensifies the low-level circulation.
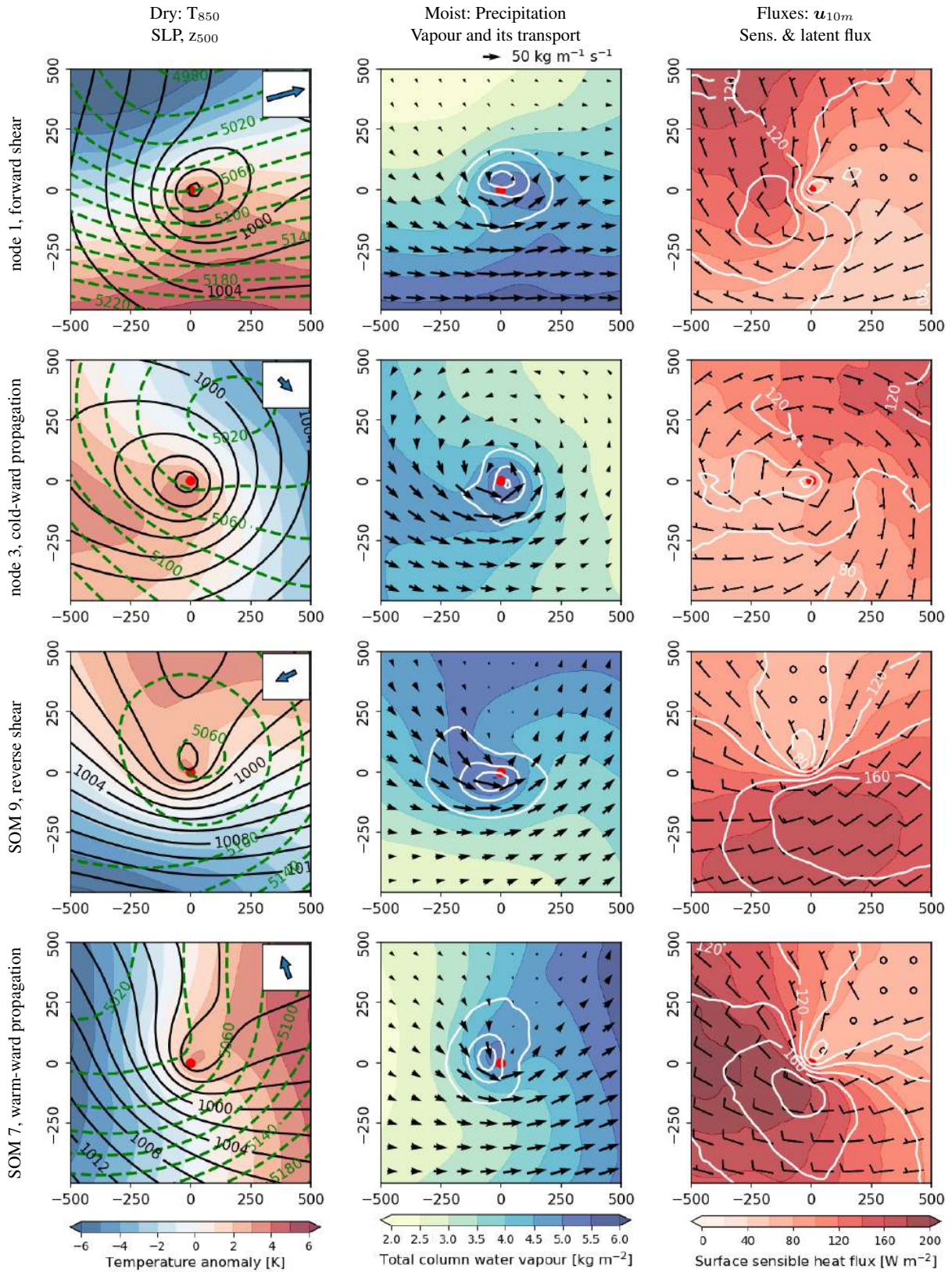
Figure 7. Composites of meteorological fields at different atmospheric levels (columns) associated to SOM nodes 1, 3, 9 and 7 (rows) for situations of increasing vorticity. First column: temperature anomaly at 850hPa (shadings), sea-level pressure (black contours, 2hPa spacing) and geopotential height at 500hPa (green contours, spacing 20m). The inset shows the mean of the vertical shear vector within the SOM node (compare to Fig. 3). Second column: Total column water vapour (shadings), total precipitation (contours, $0.2\,\mathrm{mmh^{-1}}$ spacing) and transport of the total column water vapour (arrow, the strength is scaled according to the length of the arrow above the upper panel). Third column: 10m wind vectors (quivers), surface sensible heat flux (shading) and surface latent heat flux (contours, spacing $20\mathrm{Wm^{-2}}$).

Hence, a mutual intensification of the upper and lower perturbation is acting in all baroclinic SOM nodes. The perturbations efficiently interact due to a low vertical stability (in average of the PLs covered by the STARS dataset) through the whole troposphere (up to around 400hPa). This suggest that the baroclinic development spans the whole troposphere. This in turn suggests that the baroclinic intensification is seldom just confined to low levels, as suggested in a case study by Mansfield (1974). For reverse shear systems, the upper-level circulation is rather weak but still couples with the low-level trough (see green contour of node 9 in Fig. 7). This is noteworthy since reverse-shear PLs were sometimes described develop in a low-level baroclinic zone (e.g. Terpstra et al., 2016).

Most PLs within the here analysed STARS dataset experience a considerable horizontal temperature gradient for at least parts of their lifetime (Fig. 8). The lifetime-maximum in 850hPa of the mean temperature gradient around the is typically 2.2K per 100km (median). Only 10% of the systems encounter a smaller temperature gradient than 1.4K per 100km during their whole life time, which is still a reasonable gradient to induce baroclinic waves. It would reduce the growth rate obtained in Section 4.3 by approximately one third. Hence, we conclude that the majority of the PLs are embedded in a baroclinic zone at least for parts of their life time.

4.2   Diabatic contribution

Most of the precipitation occurs at the warm front, in the sector between the the vertical-shear vector and its left side as seen from the PL centre (Fig. 7). This is also the location of the increased cloud cover with a comma-shaped form (Fig. 2). The latent heat release acts to further increase the positive temperature anomaly in the warm sector. Hence diabatic heating generates eddy available potential energy (Terpstra et al., 2015).

The arrows in Fig. 7 display the transport of the total column water vapour. For all shear situations moisture is advected from the warm side of the PL into the area of precipitation. Note the PLs are propagating to the right in the figure. This has to be considered to interpret the system-relative moisture transport. In situations of forward shear (node 1) and warm-ward propagation (node 7) the PL is propagating towards the warm and moist sector. In situations of reverse shear (node 9) and cold-ward propagation (node 3) the moisture is advected into the area of precipitation from the rear of the PL.

The surface sensible and latent heat fluxes together with the near-surface wind vector are displayed in Figure 7. The highest sensible heat fluxes occur on the cold side of the PL, i.e. in the cold-air outbreak. Strong heating on the cold side and less heating on the warm side leads to a negative diabatic generation of eddy available potential energy, and therefore dampens the PL intensification.

Latent heat fluxes are roughly co-located to the sensible heat fluxes, but occur further downstream where the air mass is already heated and has therefore an higher capacity to hold water vapour. The highest moisture fluxes occur in the cold sector. They occur rather downstream than upstream to the location of the precipitation. To reach the location of the precipitation, this moisture must be advected around the PL which requires some time. We therefore hypothesise that this moisture has a limited short-term effect on the intensification of the PL. The latent heat fluxes in the warm sector give an additional source of moisture, however it appears that most of the water vapour is transported from the environmental warm side of the PL into the area of precipitation.

These results on the distribution of the heat fluxes however do not contradict that the fluxes are important to create an environment in which PLs can grow. Sensible heat fluxes from the sea-surface into the polar air mass produce an air mass of low static stability. A low static stability is required for the disturbances to intensify at the observed growth rate (next section). Without latent heat fluxes, the polar air mass in which the PL develops would be rather dry. The diabatic contribution from latent heat release is, however, supporting the fast intensification of the PLs (e.g. Sardie and Warner, 1983; Terpstra et al., 2015).

4.3   Scale considerations

In this section, we determine the growth rate and size of the fastest growing mode following dry baroclinic instability theory (e.g. p.354ff Vallis, 2017). These have been determined in other studies (e.g. Mansfield, 1974), however with considerably different parameters as found here within the PL environments. The growth rate of the fastest growing mode is given by

$$\sigma_{max} = 0.3 \frac{f}{N} \frac{\partial \boldsymbol{u_s}}{\partial z}. \tag{7}$$

The wavelength of this mode is $\lambda_m = 3.9 L_d$ with the deformation radius $L_d = \frac{NH}{f}$. The diameter of an low pressure system (d_σ) can be understood to constitute of half a wavelength, hence $d_\sigma \approx 2\frac{NH}{f}$.

Typical values of the included parameters are deduced from the PL environments of the baroclinic SOM nodes: $N \approx 0.005 \text{s}^{-1}$ (Fig. 5), $\frac{du}{dz} \approx 2 \cdot 10^{-3} \text{s}^{-1}$ (the shear strength in Fig. 3) the height of the tropopause $H \approx 7 \text{km}$ (see appendix) , and $f \approx 1.4 \cdot 10^{-4} \text{s}^{-1}$ for 70° N.

Inserting these values result in growth rate $\sigma_{max} \approx 1.7 \cdot 10^{-5} \text{s}^{-1} \approx 1.5 \ (\text{day})^{-1}$, and a diameter of the PL by dry baroclinic instability of $d_\sigma \approx 500 \text{km}$.

Hence, the growth rate by dry baroclinic instability in the PL environment is approximately one order of magnitude higher than for typical mid-latitude cyclones (e.g. Vallis, 2017). The growth rate by dry-baroclinic theory is large, but still to small to explain the intensification of PLs within frac-
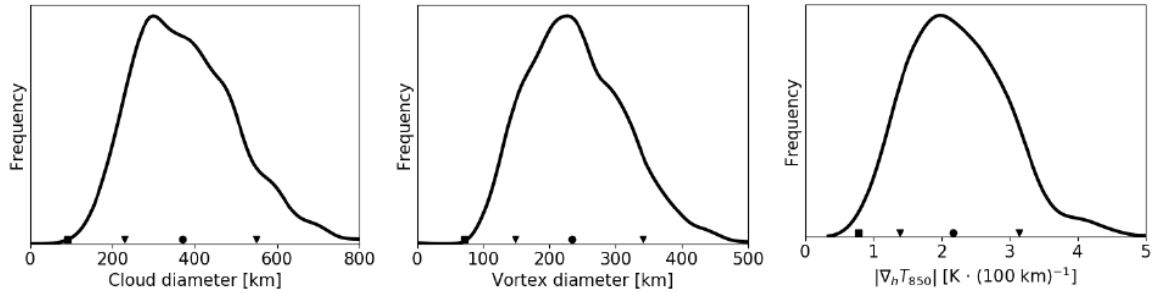
Figure 8. (Left, centre) Distribution of the diameter of the all PL time steps. (Left) from the cloud diameter attributed by Rojo et al. (2019), and (centre) estimated from the diameter derived from the vortex area from the tracking algorithm by Watanabe et al. (2016). (Right) Distribution of lifetime maximum in the mean horizontal temperature gradient within a distance of 250km to the PL centre. The square denotes the minimum value, the dot the median and the triangles the 10th and 90th percentiles of the distributions. The curves are computed with a Gaussian kernel.

tions of a day. Hence, the release of latent heat is required to further increasing the growth rate (e.g. Terpstra et al., 2015).

However, the diameter of the systems predicted from dry-baroclinic theory is somewhat larger than the observed PL diameter. The typical diameter, estimated from the size of the cloud signature by Rojo et al. (2019) is between 230 - 550km (10th and 90th percentile) with the median value being around 370km (Fig. 8 left). The cloud size estimated for the medium-level comma-shaped clouds of SOM 1, 3, 4 and 9 is around 300km. The diameter, estimated by the vortex area derived during the tracking procedure is typically between 150 - 340km with the median diameter around 235km.

This shows that the typical PL diameter ($d_{PL} \approx 300$km) is considerable smaller, but of the same magnitude, than the diameter estimated by dry baroclinic instability theory ($d_\sigma \approx 500$km). Multiple studies (Sardie and Warner, 1983; Yanase and Niino, 2007, e.g.) have shown that the wavelength of the fastest growing mode is considerably smaller if the baroclinic model include latent heat release, parametrized by slantwise convection and/or CISK, than for dry baroclinic environments.

The release of latent heat constraints the size of the updrafts and hence lead to a reduction of the wavelength of fastest growing mode. A diabatic contribution is observed in all of the baroclinic SOM patterns. Hence, we conclude that only the inclusion of latent heat release, even though the rate of total precipitation is small as compared to other intense cyclones, can explain the considerably smaller size of the PLs than predicted by dry baroclinic theory.

For the baroclinic SOM nodes, around 60% of the precipitation is of "convective" and 40% of "large-scale" type (Fig. 5). This gives an indication that a mixture of large-scale, slantwise convection associated to moist baroclinicity and convective precipitation, associated to CISK is occurring during the development. Hence we suggest that the majority of the PLs develop by a moist baroclinic mechanism with the inclusion of the CISK mechanism.

The rate of convective precipitation is in the median around 50% for forward shear situations and in the median approximately 66% for reverse shear situations. Hence CISK appears more important in the latter than the former. In the SOM nodes representing the later PL stages (5, 6 and 8), almost all of the precipitation is of convective type, which indicates that PLs often develop from a more moist baroclinic situation into a convective situation.

5 Discussion and conclusion

In this study, we classify PLs by the structure of the local meteorological fields in order to investigate their dynamical mechanisms. For this purpose, the SOM algorithm is applied on the temperature anomaly fields at 850hPa of the PL environment. The analysis reveals that the investigated PLs can be explained by moist baroclinic instability in different configurations.

The different configurations can be expressed by the vertical shear angle, the angle between the propagation direction of the PL and the vertical-shear vector, which is equivalent to the thermal-wind vector. Hence, the classification into forward and reverse-shear PLs as suggested by Duncan (1978) is confirmed to successfully distinguish between typical configurations. The classification by Duncan (1978) is a linear classification with shear angles from 0 to 180°. However, since PLs with shear angles of 90 and -90° appear different to each other and to the forward and reverse shear cases, we expand the linear classification to span a whole cycle of shear angles between -180 and 180°. This expansion includes two new shear types, left and right-shear, which have an associated shear angle of approximately -90 and 90°, respectively. Left-shear PLs propagate into warmer environments. Hence we refer to them as "warm-ward propagating PLs". The warm-ward propagation is associated to predominantly cold-air advection in the environment, which induces backing (left-ward rotation) of the horizontal wind vector with

height. Therefore, warm-ward propagating PLs can be interpreted to develop at the leading edge of a cold-air outbreak. The opposite is the case for right-shear PLs, also referred to as "cold-ward propagating PLs". These PLs can be interpreted to occur when warmer air is advected into the polar air mass.

The shear angle of a given PL is often varying during its lifetime. This is mainly associated to a directional change of the synoptic-scale flow as compared to the thermal field. A change of the shear angle during the life cycle of a PL is influencing the dynamical configuration, but does not change the acting intensification mechanism, which is baroclinic instability independent of the shear angle. A deep baroclinic structure is observed for all shear situations. The configuration of the relevant dynamical features contributing to the PL intensification is organised by the vertical-shear vector. Therefore, the classification of the PLs based on their environmental thermal fields is successful to reveal the development mechanism.

The vertical axis of the location of the low-pressure anomaly is tilted in the opposite direction relative to the vertical shear vector (Fig. 7). In forward and reverse shear conditions, the vertical axis of the low pressure anomaly is tilted backward and forward, respectively. In right (left) shear condition the pressure tilt is left- (right-)ward. Due to little variability between the PLs in the mid-level flow - PLs are typically mid-level troughs - the wind shear leads to characteristic upper- and lower-level flow patterns for each shear type (Fig. 7).

Latent heat release mainly develops along the warm front and forms a typical comma-shaped cloud in the sector between the direction of the vertical-shear vector and its left side. The diabatic heating in the warm sector supports the baroclinic development. It appears that most of the moisture that is released in the comma cloud originates from the warm side of the PL, whereas the direct influence of the surface latent heat flux is limited (Fig. 7).

The direct effect of surface sensible heat flux is to dampen the cyclogenesis. However, both fluxes are of importance to prepare the environment in which the PLs can develop. The sensible heat flux creates an environment of a very low static stability ($N \approx 0.005\mathrm{s}^{-1}$). This is approximately half the value typically considered for baroclinic disturbances in mid-latitudes (e.g. Vallis, 2017). Also other studies investigating the growth of PLs apply considerably higher values for the static stability (e.g. $N \approx 0.01\mathrm{s}^{-1}$ in Terpstra, 2014). Dominantly, the combination of a low static stability and a high vertical wind shear, which is equivalent to a large horizontal temperature gradient, favour high growth rates and small disturbance scales of dry-baroclinic waves in the typical PL environments. Additionally, a higher Coriolis parameter and a low tropopause at high than at mid-latitudes further increase the growth rates and decrease the disturbance scales.

In order to explain that the observed growth rates of PLs are larger and the disturbance scales of PLs are smaller than explained by dry-baroclinic theory, the release of latent heat by condensation must be taken into account. This was also suggested for example by Sardie and Warner (1983); Terpstra et al. (2015). The release of latent heat acts to constrain and strengthen the updrafts, which reduces the length scale and fastens the intensification. Considerable amount of precipitation is observed at the warm front in all shear situations. We therefore suggest that moist-baroclinc development is the dominant mechanism leading to the intensification of a majority of the PLs from the investigated list.

We find no evidence for hurricane-like PLs. Nearly axissymmetric systems that intensify purely by latent heat release cannot be confirmed by our analysis, also when other variables for the classification were applied. This indicates that a "PL spectrum" expressing variable PL cyclogenesis ranging from comma-shaped baroclinic systems to spirali-form, hurricane-like types (Rasmussen and Turner, 2003) is not useful. However, it might be that the resolution of the nonhydrostatic ERA-5 model is not sufficient for representing the hurricane-like PL cases. The investigation of PLs simulated by a high-resolution model, for example by the Arctic reanalysis CARA, could provide clarity in this matter.

As hurricane-like development appears unable to explain the spirali-form cloud structure, what is then causing the remarkable cloud spirals of some PLs? From our analysis it appears that most PLs develop in a high baroclinic zone for at least parts of their lifetime. Our analysis reveals that most of the precipitation occurs at the warm front. The PLs typically develop a warm core, as found by almost every case study (e.g. Bond and Shapiro, 1991; Nordeng and Rasmussen, 1992; Føre et al., 2011). These characteristics are typical for the baroclinic cyclogenesis following the Shapiro-Keyser life cycle (Shapiro and Keyser, 1990). In this model, the cyclone forms a warm seclusion with a spirali-form cloud structure at the mature stage. Hence, PLs with spirali-form clouds might be described following the Shapiro-Keyser cyclogenesis, as was argued for one PL case study by Hewson et al. (2000). Studies on high-resolution datasets that have the capability to reveal the arrangement and evolution of the fronts associated to the PLs will reveal the validity of this hypothesis..

To summarise; PLs are well described as secondary, mesoscale cyclones embedded in a synoptic-scale flow, already noted by Dannevig in 1954. The synoptic-scale flow can take any orientation as compared to the thermal field and hence a continuous spectrum of environmental shear orientations are found in which PLs may baroclinically develop. In contrast, typical synoptic cyclones are embedded in the planetary flow, which has a well defined North - South temperature gradient, implying that these cyclones are predominantly of forward shear type (e.g. Dacre et al., 2012).

References

Bond, N. A. and Shapiro, M.: Polar lows over the Gulf of Alaska in conditions of reverse shear, Monthly weather review, 119, 551–572, 1991.

Bracegirdle, T. J. and Gray, S. L.: An objective climatology of the dynamical forcing of polar lows in the Nordic seas, International Journal of Climatology, 28, 1903–1919, 2008.

Bracegirdle, T. J. and Gray, S. L.: The dynamics of a polar low assessed using potential vorticity inversion, Quarterly Journal of the Royal Meteorological Society, 135, 880–893, 2009.

Businger, S. and Reed, R. J.: Cyclogenesis in cold air masses, Weather and Forecasting, 4, 133–156, 1989.

Claud, C., Heinemann, G., Raustein, E., and McMurdie, L.: Polar low le Cygne: satellite observations and numerical simulations, Quarterly Journal of the Royal Meteorological Society, 130, 1075–1102, 2004.

Dacre, H., Hawcroft, M., Stringer, M., and Hodges, K.: An extratropical cyclone atlas: A tool for illustrating cyclone structure and evolution characteristics, Bulletin of the American Meteorological Society, 93, 1497–1502, 2012.

De Boor, C., De Boor, C., Mathématicien, E.-U., De Boor, C., and De Boor, C.: A practical guide to splines, vol. 27, springer-verlag New York, 1978.

Duncan, C.: Baroclinic instability in a reversed shear-flow, Meteorological Magazine, 107, 17, 1978.

ECMWF: ERA5 data documentation, https://confluence.ecmwf.int/display/CKB/ERA5+data+documentation, 2018-07.

Emanuel, K. A. and Rotunno, R.: Polar lows as arctic hurricanes, Tellus A, 41, 1–17, 1989.

Forbes, G. S. and Lottes, W. D.: Classification of mesoscale vortices in polar airstreams and the influence of the large-scale environment on their evolutions, Tellus A: Dynamic Meteorology and Oceanography, 37, 132–155, 1985.

Føre, I., Kristjánsson, J. E., Saetra, Ø., Breivik, Ø., Røsting, B., and Shapiro, M.: The full life cycle of a polar low over the Norwegian Sea observed by three research aircraft flights, Quarterly Journal of the Royal Meteorological Society, 137, 1659–1673, 2011.

Føre, I., Kristjánsson, J. E., Kolstad, E. W., Bracegirdle, T. J., Saetra, Ø., and Røsting, B.: A 'hurricane-like' polar low fuelled by sensible heat flux: high-resolution numerical simulations, Quarterly

Journal of the Royal Meteorological Society, 138, 1308–1324, 2012.

Harrold, T. and Browning, K.: The polar low as a baroclinic disturbance, Quarterly Journal of the Royal Meteorological Society, 95, 710–723, 1969.

Hewson, T., Craig, G., and Claud, C.: Evolution and mesoscale structure of a polar low outbreak, Quarterly Journal of the Royal Meteorological Society, 126, 1031–1063, 2000.

Kohonen, T., Schroeder, M., Huang, T., and Maps, S.-O.: Springer-Verlag New York, Inc., Secaucus, NJ, 43, 2001.

Laffineur, T., Claud, C., Chaboureau, J.-P., and Noer, G.: Polar lows over the Nordic Seas: Improved representation in ERA-Interim compared to ERA-40 and the impact on downscaled simulations, Monthly Weather Review, 142, 2271–2289, 2014.

Mansfield, D.: Polar lows: The development of baroclinic disturbances in cold air outbreaks, Quarterly Journal of the Royal Meteorological Society, 100, 541–554, 1974.

Michel, C., Terpstra, A., and Spengler, T.: Polar Mesoscale Cyclone Climatology for the Nordic Seas Based on ERA-Interim, Journal of Climate, 31, 2511–2532, 2018.

Noer, G. and Lien, T.: Dates and Positions of Polar lows over the Nordic Seas between 2000 and 2010, Met. no report, 16, 2010, 2010.

Nordeng, T. E. and Rasmussen, E. A.: A most beautiful polar low. A case study of a polar low development in the Bear Island region, Tellus A, 44, 1992.

Nygård, T., Graversen, R. G., Uotila, P., Naakka, T., and Vihma, T.: Strong dependence of wintertime Arctic moisture and cloud distributions on atmospheric large-scale circulation, Journal of Climate, 32, 8771–8790, 2019.

Orimolade, A., Furevik, B., Noer, G., Gudmestad, O., and Samelson, R.: Waves in polar lows, Journal of Geophysical Research: Oceans, 121, 6470–6481, 2016.

Rasmussen, E.: The polar low as an extratropical CISK disturbance, Quarterly Journal of the Royal Meteorological Society, 105, 531–549, 1979.

Rasmussen, E. A. and Turner, J.: Polar lows: Mesoscale Weather Systems in the Polar Regions, Cambridge University Press: Cambridge, UK, 2003.

Reed, R. J.: Cyclogenesis in polar air streams, Monthly Weather Review, 107, 38–52, 1979.

Reed, R. J. and Blier, W.: A Case Study of Comma Cloud Development in the Eastern Pacific, Monthly Weather Review, 114, 1681–1695, https://doi.org/10.1175/1520-0493(1986)114<1681:ACSOCC>2.0.CO;2, 1986.

Reed, R. J. and Duncan, C. N.: Baroclinic instability as a mechanism for the serial development of polar lows: a case study, Tellus A, 39, 376–384, 1987.

Renfrew, I.: SYNOPTIC METEOROLOGY | Polar Lows, in: Encyclopedia of Atmospheric Sciences (Second Edition), edited by North, G. R., Pyle, J., and Zhang, F., pp. 379 – 385, Academic Press, Oxford, second edition edn., https://doi.org/https://doi.org/10.1016/B978-0-12-382225-3.00317-0, 2015.

Rojo, M., Claud, C., Mallet, P.-E., Noer, G., Carleton, A. M., and Vicomte, M.: Polar low tracks over the Nordic Seas: a 14-winter climatic analysis, Tellus A, 67, 2015.

Rojo, M., Noer, G., and Claud, C.: Polar Low tracks in the Norwegian Sea and the Barents Sea from 1999 un-

til 2019, https://doi.org/10.1594/PANGAEA.903058, https://doi.org/10.1594/PANGAEA.903058, supplement to: Rojo, Maxence; Claud, Chantal; Noer, Gunnar; Carleton, Andrew M (2019): In Situ Measurements of Surface Winds, Waves, and Sea State in Polar Lows Over the North Atlantic. Journal of Geophysical Research: Atmospheres, 124(2), 700-718, https://doi.org/10.1029/2017JD028079, 2019.

Samuelsen, E. M., Løset, S., and Edvardsen, K.: Marine icing observed on KV Nordkapp during a cold air outbreak with a developing polar low in the Barents sea., Proceedings of the 23rd International Conference on Port and Ocean Engineering under Arctic Conditions; 2015 Jun 14–18; Trondheim, Norway, 2015.

Sardie, J. M. and Warner, T. T.: On the Mechanism for the, Development of Polar Lows, Journal of the Atmospheric Sciences, 40, 869–881, 1983.

Shapiro, M. A. and Keyser, D.: Fronts, jet streams and the tropopause, in: Extratropical cyclones, pp. 167–191, Springer, 1990.

Smirnova, J. E. and Golubkin, P. A.: Comparing polar lows in atmospheric reanalyses: Arctic System Reanalysis versus ERA-Interim, Monthly Weather Review, 2017.

Stoll, P. J., Valkonen, T., Graversen, R. G., and Noer, G.: A well-observed polar low analysed with a regional and a global weather-prediction model, Quarterly Journal of the Royal Meteorological Society.

Stoll, P. J., Graversen, R. G., Noer, G., and Hodges, K.: An objective global climatology of polar lows based on reanalysis data, Quarterly Journal of the Royal Meteorological Society, 2018.

Terpstra, A.: Dynamical perspectives on the formation and intensification of polar lows, 2014.

Terpstra, A., Spengler, T., and Moore, R. W.: Idealised simulations of polar low development in an Arctic moist-baroclinic environment, Quarterly Journal of the Royal Meteorological Society, 141, 1987–1996, 2015.

Terpstra, A., Michel, C., and Spengler, T.: Forward and reverse shear environments during polar low genesis over the North East Atlantic, Monthly Weather Review, 144, 1341–1354, 2016.

Vallis, G. K.: Atmospheric and oceanic fluid dynamics, Cambridge University Press, 2017.

Watanabe, S.-i. I., Niino, H., and Yanase, W.: Climatology of polar mesocyclones over the Sea of Japan using a new objective tracking method, Monthly Weather Review, 144, 2503–2515, 2016.

Wehrens, R., Buydens, L. M., et al.: Self-and super-organizing maps in R: the Kohonen package, Journal of Statistical Software, 21, 1–19, 2007.

Wilhelmsen, K.: The polar low near the Norwegian coast, 1981.

Wilhelmsen, K.: Climatological study of gale-producing polar lows near Norway, Tellus A, 37, 451–459, 1985.

Yanase, W. and Niino, H.: Dependence of polar low development on baroclinicity and physical processes: An idealized high-resolution numerical experiment, Journal of the Atmospheric Sciences, 64, 3044–3067, 2007.

Yanase, W., Fu, G., Niino, H., and Kato, T.: A polar low over the Japan Sea on 21 January 1997. Part II: A numerical study, Monthly Weather Review, 132, 1552–1574, 2004.

Zappa, G., Shaffrey, L., and Hodges, K.: Can polar lows be objectively identified and tracked in the ECMWF operational analysis and the ERA-Interim reanalysis?, Monthly Weather Review, 142, 2596–2608, 2014.